



ANNUAL REPORT 2019

Institut für Kernphysik · COSY

Jül-4423

Annual Report 2019

Institut für Kernphysik / COSY

DIRECTORS AT THE IKP

Experimental Hadron Structure (IKP-1):

Experimental Hadron Dynamics (IKP-2):

Theory of the Strong Interactions (IKP-3/IAS-4):

Large-Scale Nuclear Physics Equipment (IKP-4):

Prof. James Ritman

Prof. Hans Ströher (managing director 2018-19)

Prof. Ulf-G. Meißner

Dr. Ralf Gebel (managing director 2020-21)

EDITORIAL BOARD

Dr. Ralf Gebel

Prof. Frank Goldenbaum

Dr. Dieter Grzonka

Prof. Christoph Hanhart

Dr. Volker Hejny

Dr. Andro Kacharava

Prof. Andreas Lehrach

Prof. Livia Ludhova

Prof. Ulf-G. Meißner

Prof. James Ritman

Susan Schadmand, Ph.D. habil.

Dr. Thomas Sefzick

Prof. Hans Ströher

Dr. Raimund Tölle

Cover picture: Logos of existing and future accelerator facilities (COSY, ELENA, FAIR/GSI, HBS and HESR), projects (STRONG2020) and collaborations (ATHENA, Borexino, CBM, CLAS, CPEDM, GlueX, HADES, JEDI, JUNO, JuSPARC, LENPIC, OSIRIS, PANDA, PAX, QCD (SFB110) and WASA), in which the Institut für Kernphysik is involved.

Contents

Preface	vi
1 Experimental Activities for FAIR	1
1.1 The PANDA Experiment at FAIR	1
1.2 KOALA Experiment at HESR	5
1.3 The PANDA Cluster-Jet Target	6
1.4 Detector Tests for the CBM and HADES Experiments	7
2 Storage Ring Based EDM Search	8
2.1 Introduction	8
2.2 Results for Beam-Based Alignment at COSY	9
2.3 Measurement of Beam Oscillations of a Mismatched Waveguide RF Wien Filter	10
2.4 Commissioning of the JEDI Polarimeter	10
2.5 Simulations for the Prototype EDM Storage Ring	11
2.6 Plans for Proton Spin-Coherence-Time Measurements	12
2.7 Search for Axions/ALPs at COSY via Oscillating EDMs	12
3 Neutrino Physics	13
3.1 Borexino	13
3.2 JUNO	16
4 Accelerator Research	17
4.1 Introduction	17
4.2 COSY Operation	17
4.3 Control System Upgrade	18
4.4 Improved Tune Monitoring	18
4.5 Injector	19
4.6 Progress of the HESR	20
5 Further Activities	23
5.1 GlueX at Jefferson Lab	23
5.2 Polarized Molecules	23
5.3 Laser-Plasma Acceleration	24
6 Theoretical Investigations	24
6.1 Introduction	24
6.2 Ab Initio Nuclear Thermodynamics	25
6.3 An Update on Fine-Tunings in the Triple-Alpha Process	26
6.4 Implications of an Increased ${}^3_{\Lambda}\text{H}$ Binding Energy	26
6.5 Refined Predictions for the Spin Partners of the $Z_b(10610)$ and $Z_b(10650)$	27
6.6 Kaon Photoproduction and the Λ Decay Parameter α_{-}	28
6.7 Addressing Ergodicity Issues in Low-Dimensional Lattice Calculations	28
A Beam Time at COSY in 2019	30
B Committees	32
B.1 CBAC – COSY Beam Time Advisory Committee	32
B.2 Committee Service	32
C Publications – Journal Articles	34
D Talks and Colloquia	39
D.1 Conference and Workshop Contributions	39
D.2 Colloquia	47

E Academic Degrees	49
E.1 Dissertation / PhD Theses	49
E.2 Master Theses	49
E.3 Bachelor Theses	49
F Awards	51
G Third Party Funded Projects	52
H Collaborations	53
I Conferences and Outreach Activities (Co-)Organized by the IKP	54
I.1 Georgian-German Science Bridge: 2nd QUALI-Start-Up Science Lectures in Jülich	54
I.2 Georgian-German Science Bridge: Outreach Activity	54
I.3 Decyphering Strong Interaction Phenomenology through Precision Hadron Spectroscopy	54
I.4 The 2019 Workshop of the APS Topical Group for Hadronic Physics	55
I.5 Helmholtz - DIAS International Summer School "Quantum Field Theory at the Limits: from Strong Fields to Heavy Quarks "	55
I.6 Four Day Particle Physics Academy and One Training Program for High School Teachers	55
I.7 Further Events (Co)-Organised by Members of the Institute	56
I.8 Colloquium in Honour of the 80 th Birthday of Prof. Dr. K. Kilian	56
J Teaching Positions	57
K Personnel	58
L Individual Contributions	61
FAIR Related Experimental Activities	63
Storage Ring Based EDM Search	79
Neutrino Physics	92
Accelerator Research	100
Further Activities	122

Preface

During 2019 it became apparent that it is not feasible to implement the 2018 decisions by the Boards of Forschungszentrum Jülich (FZJ) and Helmholtzzentrum für Schwerionenforschung (GSI) concerning "TransFAIR" (i.e. the transfer of IKP from FZJ to GSI to secure its competences for the community). Thus, in the autumn 2019 meetings, new decisions were taken, which essentially request to have a viable plan by early 2020. For the IKP personnel this delay continues to generate significant uncertainty.

2019 was also characterized by the preparation for the Strategic Review of the Helmholtz Association in the Research Field "Matter", which took place in January 2020. The scientific projects of IKP – hadron physics, symmetry investigations, neutrino physics and accelerator research – are already affiliated with GSI, and it remains to be seen how they will (be able to) develop in future.

As far as our scientific activities are concerned, the year 2019 provided a number of significant achievements:

- The JEDI collaboration has conducted a very successful test measurement at COSY demonstrating the feasibility to search for Dark Matter particles (axions, axion-like particles) via oscillating electric dipole moments (EDM): while a magnetic storage ring is unsuitable for precision static EDM searches because the precession due to the magnetic dipole eliminates any effect, it would create a resonance condition for an oscillating EDM at the right frequency.
- The CPEDM collaboration has prepared a detailed feasibility study for a "Storage Ring to Search for Electric Dipole Moments of Charged Particles" as background information for the European Strategy for Particle Physics (ESPP) Update in 2020 and submitted it to the arXiv. It outlines the strategy for the storage-ring EDM project from COSY to an all-electric ring with clock-wise and counter clock-wise polarized proton beams for ultimate precision.
- The Borexino collaboration has completed a comprehensive geo-neutrino analysis of data taken with the Borexino detector at Gran Sasso (Italy) between December 2007 and April 2019, resulting in a total of about 50 events. This corresponds to an estimated radiogenetic heat of approximately 25 TW from ^{238}U and ^{232}Th in the earth mantle.
- In a recent experiment the production of HD Molecules with well-defined nuclear spins has been demonstrated. When electron and nuclear spins of hydrogen and deuterium atoms are preselected, these isotopes can recombine into HD molecules with well-defined nuclear spins in all possible combinations, reaching nuclear polarization values up to 80%.
- An important milestone for the PANDA/HADES Phase-0 experiment was reached by completing the construction of the new straw tracker station STS1, thereby enabling tracking for forward going particles up to $\theta = 6.5^\circ$. Together with HADES this system will be used to measure radiative decays of excited hyperons and can later be adapted for use in the PANDA forward spectrometer.

Significant progress and milestones can also be reported for the accelerators HESR and COSY:

- The pre-assembly of the dipole magnets for the HESR has been completed. All 42 dipole magnets that do not need to be adapted to an experiment have been delivered to the interim storage hall near GSI in Darmstadt.
- The construction of all octants of the yoke for the large solenoid magnet of the PANDA detector was manufactured at the Russian company BINP. The integration into the HESR lattice is under preparation.
- Novel input and output coupling structures were developed for stochastic cooling with correction signals which amplified by state-of-the-art power amplifiers based on GaN technology. They have been successfully commissioned and are in use at COSY for test experiments with the PANDA cluster target.
- A new beam polarimeter (JePo), based on modular LYSO scintillators, has been installed in COSY, replacing the venerable EDDA detector. JePo will be mainly exploited for the EDM investigations of the JEDI collaboration.

In August, we celebrated the 80th birthday of our former director Kurt Kilian with a scientific colloquium, which was attended by his former colleagues, his friends and family. We are very happy that Kurt is frequently dropping in at IKP.

Let me conclude by thanking all of the IKP members for their contributions to the success (and viability) of the institute.

Jülich, March 2020

Hans Ströher

1 Experimental Activities for FAIR

1.1 The PANDA Experiment at FAIR

The future Facility for Antiproton and Ion Research (FAIR), which is currently under construction, will be one of the largest accelerator facilities in the world giving access to new experiments to gain insights into the structure of matter and the evolution of the universe.

The antiProton ANnihilation at DArmstadt (PANDA) experiment is one of the main experiments of FAIR. It will utilize an intense anti-proton beam with excellent momentum resolution provided by the High Energy Storage Ring (HESR) to perform precision measurements up to a beam momentum of 15 GeV/c to improve the understanding of Quantum Chromo Dynamics.

One way to gain a deeper insight into the mechanisms of QCD in the non-perturbative regime is to understand the excitation spectrum of baryons. So far, experimental studies focused on the nucleon excitation spectrum, while there is nearly no knowledge on the excitation spectra of double and triple strange baryons. The available information is mostly from bubble chamber experiments with low statistics. PANDA will be the ideal tool to improve the knowledge of excited hyperons due to the high production cross section in antiproton-proton collisions, which allows PANDA to surpass the available statistics within a few weeks of measurement.

One prerequisite for the measurement of hyperons but also for the reconstruction of excited charmonium states is the precise measurement of the flight path of charged particles. For this purpose four different sub-detectors are used within PANDA: a Micro Vertex Detector (MVD) surrounding the interaction point, a Straw Tube Tracker (STT) consisting out of more than 4000 gas filled straw tubes and 3 layers of GEM detectors in the central spectrometer and a Forward Tracking System (FTS) consisting out of straw tubes as well in the forward-spectrometer.

The design and the production of the STT is one of the responsibilities of the IKP for the PANDA experiment. Beam tests of prototypes have been performed and the analysis of the achieved data confirmed the excellent spatial resolution of the system which surpasses the design goals. A first real test of the system will be the usage of one of the PANDA tracking stations made out of STT straw tubes in the HADES experiment, which was prepared in the last year.

The reconstruction of charged tracks within a complex detector system like PANDA requires the development of highly specialized tracking algorithms. Here conventional tracking algorithms like Hough transformations are competing with more modern approaches as artificial neural networks. At the moment it is not clear which one outmatches the other, therefore both are under development for the two different parts of the PANDA detector.

Study to Determine Spin Parity Quantum Numbers of Dedicated Ξ Resonances in $\bar{p}p \rightarrow \bar{\Xi}^+ \Lambda K^-$

Due to the limited statistics only few excited hyperon states are known by their mass and width and even less is known about their quantum numbers. A partial wave analysis (PWA), in which the complex amplitudes of certain processes are extracted to investigate the dynamics of these processes, allows the mass and width of the resonances as well as their spin and parity quantum numbers to be determined.

Here a study to determine the quantum numbers of the Ξ resonances $\Xi(1690)^-$ and $\Xi(1820)^-$ with the Partial Wave Interactive Analysis Software (PAWIAN) is presented. Up to now, PAWIAN has not been used on a final state containing both Ξ and Λ baryons. Therefore, in a first step only single resonances are investigated. Since in experiments not only contributions from Ξ resonances in the ΛK^- system are expected, but also Λ^* and Σ^{*0} resonances in the $\bar{\Xi}^+ K^-$ system, a study of events including also a contribution from $\bar{p}p \rightarrow \bar{\Lambda}(1890)\Lambda$ has been performed.

PAWIAN gives the possibility to generate events based on a user-defined decay model. The software tool uses an event-based maximum likelihood fit, which is however very time consuming for a high statistics data sample. As a starting point a data set with 3,000 events for both $\Xi(1690)^-$ and $\Xi(1820)^-$ has been generated. The normalization of the fit is done by Monte-Carlo Integration. Therefore, a reference data set containing 10,000 phase-space distributed events of the reaction $\bar{p}p \rightarrow \bar{\Xi}^+ \Lambda K^-$ has also been generated.

The beam momentum is chosen to be $p_{\bar{p}} = 4.6 \text{ GeV}/c$, which corresponds to a center-of-mass energy of about 100 MeV above the $\bar{\Xi}^+ \Xi(1820)^-$ production threshold.

In addition to the single Ξ resonances, a data set including the reaction $\bar{p}p \rightarrow \bar{\Lambda}(1890) \Lambda$ has been generated. Here, the spin parity quantum numbers $J^P = 3/2^+$ of the $\bar{\Lambda}(1890)$ are chosen according to the values given by the Particle Data Group. Figure 1 shows the Dalitz plot for a generated $\Xi(1690)^-$ ($J^P = 1/2^+$) data sample including $\bar{\Lambda}(1890)$. The Ξ resonance is observable as a vertical band in the Dalitz plot while the $\bar{\Lambda}(1890)$ appears as broad horizontal band.

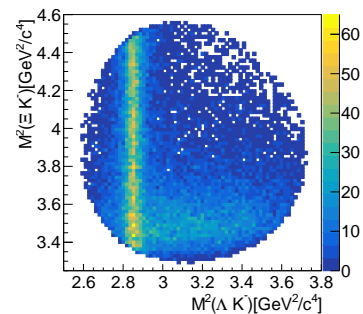


Figure 1: Dalitz plot for a generated data sample containing a $\Xi(1690)^-$ (vertical band) and a $\bar{\Lambda}(1890)$ resonance (horizontal band).

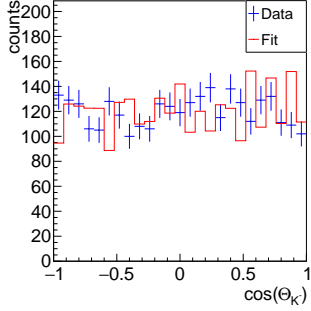


Figure 2: Angular distribution of K^- in the reference frame of the resonance. The generated $1/2^+$ distribution is shown in blue while the fitted $3/2^+$ distribution is shown in red.

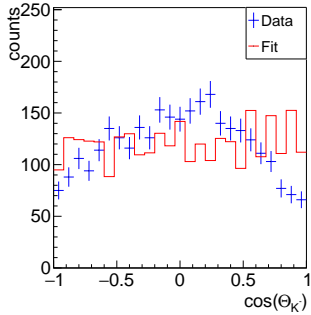


Figure 3: Angular distribution of K^- in the reference frame of the resonance. The generated $3/2^+$ distribution is shown in blue while the fitted $1/2^+$ distribution is shown in red.

The main question to be answered is whether it is possible to determine the quantum numbers of the Ξ resonances with PAWIAN. For this purpose, the data sets described in the previous section have been generated with different quantum numbers: $1/2^+$, $1/2^-$, $3/2^+$ and $3/2^-$. This choice of spin and parity quantum numbers is motivated by the values given by the Particle Data Group. The sample generated has been successively fit with all other hypotheses using a multi-dimensional fit.

The hypothesis selection is based on the Aikake Information Criterion (AIC). Here, the results are compared by the ΔAIC value with $\Delta AIC = AIC_i - AIC_{\min}$.

A hypothesis is assumed to be suitable for values $\Delta AIC < 2$, whereas hypothesis with $\Delta AIC > 10$ are excluded.

As a first step the single resonance cases are investigated. For $\Xi(1690)^-$ the angular distribution of the K^- in the rest frame of the resonance does not show significant differences for all fitted hypotheses as can be seen for example in Figure 2 showing the angular distribution of the generated $1/2^+$ and the fitted $3/2^+$ hypothesis. However, the angular distribution for the generated $3/2^+$ and fitted $1/2^+$ (see Figure 3) shows that in this case it is possible to differentiate the spin values based on the distribution. The same statement can be made for all other 1-dimensional variables.

Table 1: Fit Results for $\Xi(1690)^-$ obtained with the multi-dimensional fit. For each generated J^P hypothesis (gen. hyp), the ΔAIC values of all fitted hypotheses (fit) are listed. In all cases, the correct fit hypothesis is preferred by the fit ($\Delta AIC = 0$), whereas the wrong fit hypotheses can be excluded ($\Delta AIC > 10$).

gen. hyp ↓	fit →			
	$1/2^+$	$1/2^-$	$3/2^+$	$3/2^-$
$1/2^+$	0	36.7	55.9	124.6
$1/2^-$	77.2	0	80.8	371.0
$3/2^+$	159.8	179.7	0	128.7
$3/2^-$	113.6	276.9	71.6	0

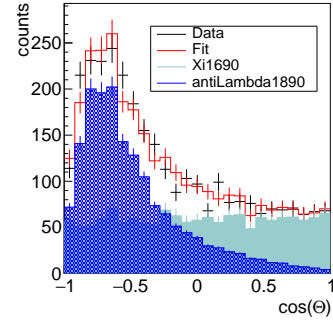


Figure 4: Angular distribution of K^- . The generated $1/2^+$ distribution is shown in black while the fitted $1/2^+$ distribution is shown in red. The contribution of $\Xi(1690)^-$ is shown in green and the contribution of $\bar{\Lambda}(1890)$ in blue.

Although it is not possible to determine the spin and parity quantum numbers from one of the 1-dimensional variables, the fit results obtained with the multi-dimensional fit prefer the true hypothesis, in each case. As an example, the results of the multi-dimensional fit for $\Xi(1690)^-$ are summarized in Table 1. The wrong hypotheses are all excluded by $\Delta AIC > 10$. For $\Xi(1820)^-$ the results are not as clear as for $\Xi(1690)^-$. Here, the fit results prefer the true hypothesis for all generated cases, but at least one of the other hypotheses have a $\Delta AIC < 6$.

The obtained results for $\Xi(1690)^-$ including the crossed channel show that the true hypothesis achieved the best fit result. As an example, Figure 4 shows the angular distribution of the K^- for $\Xi(1690)^-$ with a generated and fitted $1/2^+$ hypothesis. Figure 5 shows the reconstructed Dalitz plot for a fitted $1/2^+$ hypothesis. Here, the $\Xi(1690)^-$ is clearly observable as vertical band. Nevertheless, it is not possible to make a clear statement if other hypotheses can be safely excluded since the statistics used for the fit are too low. For some cases regarding $\Xi(1820)^-$ with included crossed channel, it is even not possible to exclude wrong hypotheses.

The presented study shows that the determination of the spin and parity quantum numbers J^P of dedicated Ξ resonances with PAWIAN is possible in general. The inves-

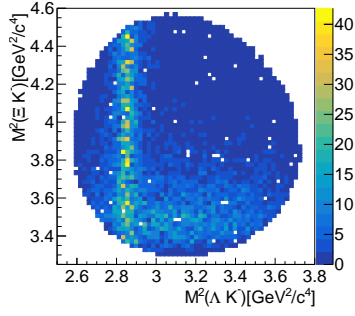


Figure 5: Reconstructed Dalitz plot for $\Xi(1690)^-$ with a fitted $1/2^+$ to a generated $1/2^+$ hypothesis.

tigation of data sample including a single narrow Ξ resonance shows that the input values of the quantum numbers can be reproduced. The fit results are obtained from 3,000 generated events. But data samples with at least a factor 10 higher statistics are needed. However, the fit of data sets with high statistics requires a high computing time.

Including an additional resonance in the crossed channel, here $\bar{\Lambda}(1890)$, leads to results which are not as significant as for the case of the single resonances.

With an assumed cross section in the order of a microbarn and a reconstruction efficiency of about 5 % PANDA will produce about 19000 reconstructed excited hyperon states per day at the beginning of the experiment.

The PANDA Straw Tube Tracker

The calibration and track reconstruction of the PANDA central Straw Tube Tracker (STT) were further developed with data from the beamtest campaign conducted in 2018. A STT test system was exposed to proton and deuteron beam from COSY, covering a beam momentum range from about 0.6 to 2.5 GeV/c in order to emulate similar particle energy-loss measurements in the PANDA experiment. The STT calibration includes the determination of the individual tube position, the wire position inside the individual tube¹, and the parametrised isochrone radius - drift time relation. The calibration steps are done iteratively, using the reconstructed tracks and calculating the position deviations for the straw hits. It was checked that a common (global) calibration is sufficient and can be used for all individual data sets with different particle species and momentum. Fig.6 shows the final resolution obtained for all data sets. For nearly minimum ionising protons at 2.5 GeV/c a spatial resolution of about 125 μm is achieved, far better than the design goal of 150 μm . Strongly ionising particles with lower particle velocities (p/Mc) can be measured with even better spatial resolutions of about 100 μm . More details about the calibration methods can be found in an individual report.

¹The gravitational sag of the wires leads at half length of the horizontally aligned tubes to a wire displacement from the center axis which is then further increased by the electric field. Maximum deviations of less than 200 μm were measured for all individual tubes.

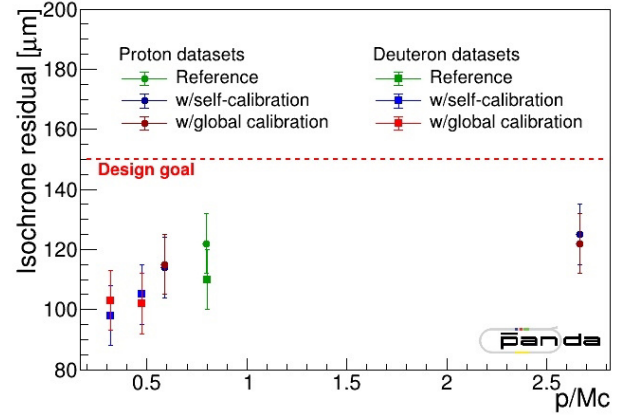


Figure 6: Spatial resolution of reconstructed proton and deuteron tracks with particle momenta ranging from 0.3 to 2.65 GeV/c. The differences between the data sets with a common, global calibration and individual data set calibrations are negligible, i.e. less than 5 μm .

The PANDA Phase-0 Straw Tracker Station in the HADES Experiment

A main activity in 2019 was the construction and completion of the new Straw Tracker Station STS1 for the combined PANDA/HADES experiment. HADES is a well-established experiment for hadron physics studies and will start an early FAIR Phase-0 experiment program at the SIS 18 synchrotron at FAIR. The physics program consists of proton scattering on protons or nuclear targets (A). In particular, the study of hyperon structures by measuring radiative hyperon decays ($p + p(A) \rightarrow Y + X \rightarrow \Lambda e^+ e^- + X$, with Y=any hyperon, X=rest) is of interest and well connected to the PANDA physics program. For the Phase-0 experiment, the HADES spectrometer will be upgraded by a dedicated detection system consisting of two straw tracker stations and a RPC detector in the very forward region, covering the polar angle range from about 0.5° to 6.5° for particle track reconstruction.

The STS1 station (see Fig.7) consists of 704 straws arranged in 16 modules, each with 32 straws, and 4 center modules with 48 straws each and featuring a $8 \times 8 \text{ cm}^2$ hole for the direct beam. The layout and dimensions of the modules were adjusted to the PANDA Forward Tracker to allow a later use of the 32 straw modules in the PANDA Tracker Stations FT3 and FT4. For setting up and pre-testing the STS1 the data-acquisition system was installed and updated. The same DAQ system will be also used for the PANDA-STT system. After finishing the functional system tests, the STS1 will be installed in the HADES spectrometer at GSI in early spring 2020 and followed by a test beamtime of the upgrade HADES spectrometer in early June.

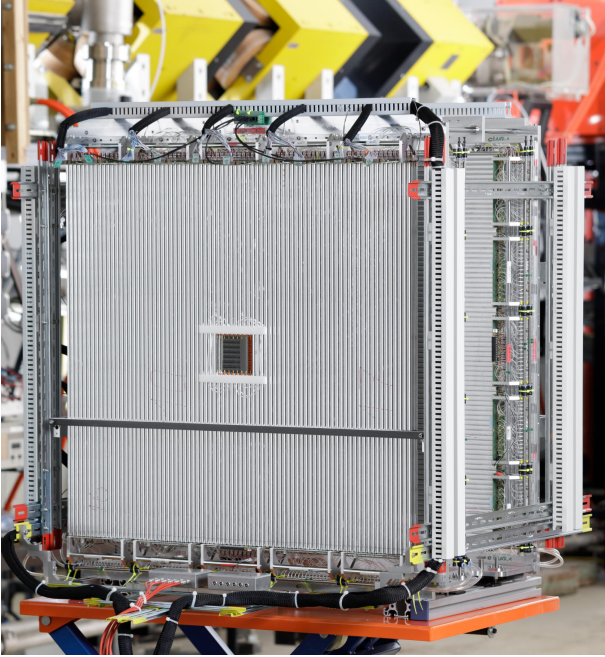


Figure 7: Photograph of the new Straw Tracker Station STS1 in front of COSY quadrupoles (in yellow) in the COSY-TOF test beam area.

Track reconstruction of charged particles

The reconstruction of charged tracks in the various different tracking detectors is an ambitious goal and it is not clear which approach is the best one to achieve the highest efficiency, accuracy and purity in the shortest time. Therefore different tracking algorithms for the central spectrometer as for the forward spectrometer are under development.

The first algorithm developed is specialized on the reconstruction of tracks in the Straw Tube Tracker (STT). The STT measures which straw was hit and, in addition, the drift time of the generated charge in the straw tube. With this information it is possible to improve the hit-resolution perpendicular to the straw tube to $150 \mu\text{m}$. The algorithm is based on a Hough transformation, where for each hit all possible tracks are calculated. The track parameters are collected in a histogram, the so called Hough space. Hits belonging to the same track are described by the same track parameters and therefore fill the same bin in the Hough space. The possible tracks per hit are calculated by using the Apollonius problem, which is the mathematical description of finding a circle that is tangential to three other circles. The Apollonius problem enables the possibility to use the additional drift time information. Currently, the algorithm uses 2 hits and the origin for the calculation. An example for a Hough space for one track is shown in Figure 8. The black crosses and circles indicate the hit points and rings of equal drift time (isochrones). The grey circle represents the particle track found by the algorithm. The entries of the Hough space are visualized as points col-

ored by a color scheme from blue to black depending on the number of entries per bin.

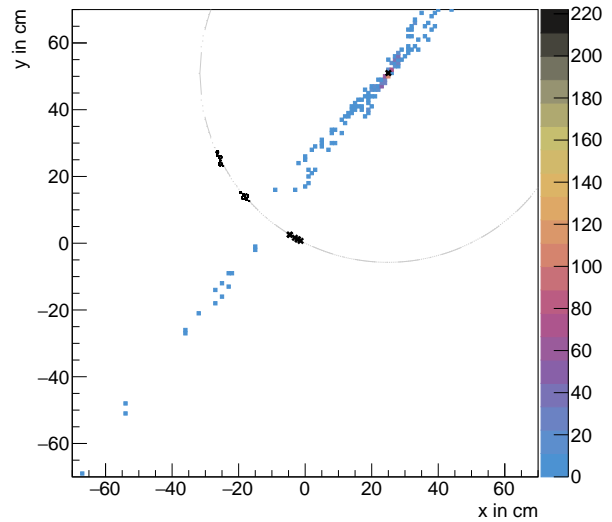


Figure 8: Example for a Hough space for one track.

To improve the performance of the Hough transformation, different data preselection methods are performed. The first method is based on a cellular automaton, which uses the neighborhood relations of the close-packing of the STT. Neighboring hits which unambiguously result from just one track are collected in tracklets. These tracklets are used for the Hough transformation to extract the track parameters. The second method uses the assumption that hits belonging to the same track have a continuous azimuth angle. By filling all azimuth angles in a histogram, different tracks can be preselected by dividing the data in subsectors depending on the azimuth angle. The Hough transformation is then applied to the preselected data. Due to losses of hits or crossing tracks the preselections can divide particle tracks in several tracklets. These tracklets have to be merged in the final step. The quality of a track finding algorithm is often measured by two quantities. The first one is the track finding rate of reconstructible tracks, the second one is the ghost ratio. The track finding rate is defined as the ratio of found tracks to all reconstructible tracks. Here reconstructible tracks are defined as tracks which have more than three hits in the Micro Vertex Detector (MVD) or more than five hits in all central tracking detectors (MVD, STT and GEM). The ghost ratio is the fraction of wrongly found tracks to all reconstructible tracks. Currently, the track finding algorithm described above is able to find 84.9 % of all reconstructible primary tracks and has a ghost ratio of 20.6 %.

For the forward spectrometer, where the charged tracks are measured in front of, inside and behind a dipole magnetic field, two different algorithms based on artificial neural networks are under development. As PANDA is a

fixed target experiment, most of the produced particles at PANDA will have a forward boost. Therefore it is of crucial importance to have an efficient, robust and fast track reconstruction algorithm at the forward part of the experiment in the FTS stations. Machine learning algorithms could make a great contribution to the tracking problem due to their capability to model complex and non-linear data dependencies.

Two different approaches have been developed for track reconstruction out of hits in the FTS based on artificial neural networks.

The first one is a local method. In this approach an Artificial Neural Network (ANN) is trained to accept coordinates from hit pairs as an input and outputs a probability that the pair is on the same track or not. The output probability should be close to 1 if the hit-pair belongs to the same track, otherwise the hits belong to different tracks. Hit pairs are connected to tracks if the probability(hit_1, hit_2) passes the probability cut, and probability(hit_2, hit_3) also passes the probability cut, then hit_1, hit_2 , and hit_3 are all on the same track. Two different neural networks are applied, one for the tracking stations outside of the magnetic field (FTS1, FTS2, FTS5, and FTS6) and one for the tracking stations inside the magnetic field (FTS3, and FTS4). A Recurrent Neural network (RNN) is used to build the full tracks out of the track segments found by the ANN.

The second approach is a global method. Here Graph Neural Networks (GNNs) are applied for particle tracking. GNNs are a relatively new class of deep learning architectures which can deal effectively with irregular data structures (non-Euclidean data). The primary task of the GNN is to associate detector elements together by classifying the edges of the graph. The graph is constructed so that the nodes are the hits recorded by the detector and the edges are connections of the hits between adjacent detector layers. In the input graphs, node features are the hit coordinates. The network output is an edge probability, that is 1 if two hits come from the same track, and 0 otherwise. The probability output can be used exactly like the first method to connect hits together. An example of an input graph is shown in Fig. 9, and an output graph is shown in Fig. 10.

Two performance metrics were measured to judge the performance of the proposed methods. The purity was defined as the fraction of hits in one track coming from the correct particle, and the efficiency defined as the ratio of the number of reconstructed tracks to the number of all simulated tracks. For the local method purity is ranging from 85% to almost 100% depending on the momentum and the number of tracks per event. For the global method purity is always above 90%. Efficiency for both methods is about 75% for low momentum tracks, and about 95% for high momentum tracks.

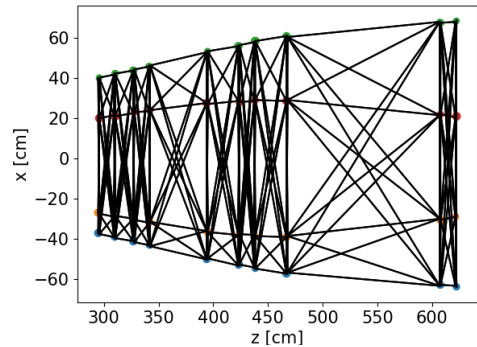


Figure 9: An example of an input graph, where hit coordinates (colored points) represent node features (x,z), and the black lines represent graph edges.

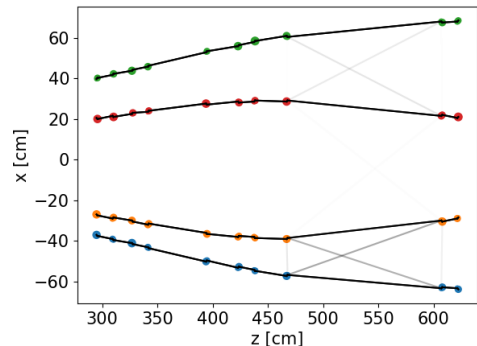


Figure 10: An example of an output graph. Black lines represent output probability of 1, while faded lines represent a number smaller than 1, so by setting a threshold for probability, track candidates can be formed.

1.2 KOALA Experiment at HESR

The KOALA experiment will study antiproton-proton elastic scattering at small momentum transfers at HESR. Since the evaluation of the pure Coulomb differential cross section, which is proportional to $1/t^2$, is unambiguous, a measurement in the region of Coulomb dominance would determine the $\bar{p}p$ luminosity in an independent way and allow parameters of the $\bar{p}p$ interaction to be extracted. The idea of KOALA is to measure the scattered beam antiprotons at forward angles with fast timing detector and the recoil target protons near 90° with energy detectors. Thus, a large range of t distribution, i.e. [0.0008–0.1] GeV^2 can be reconstructed.

Prior to the measurement of $\bar{p}p$ elastic scattering at HESR, the method as well as the KOALA detector will be verified by measuring pp elastic scattering at COSY, since pp and $\bar{p}p$ elastic scattering have the same kinematics. The full KOALA setup in Fig. 11 has been built and installed at COSY for the commissioning experiment. The recoil detector is about 90 cm away from the interaction point. The forward detector is located at $z=4.6$ m downstream of the interaction point.

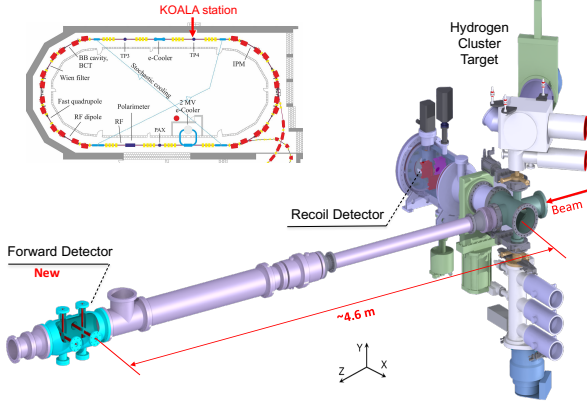


Figure 11: The full KOALA setup at COSY

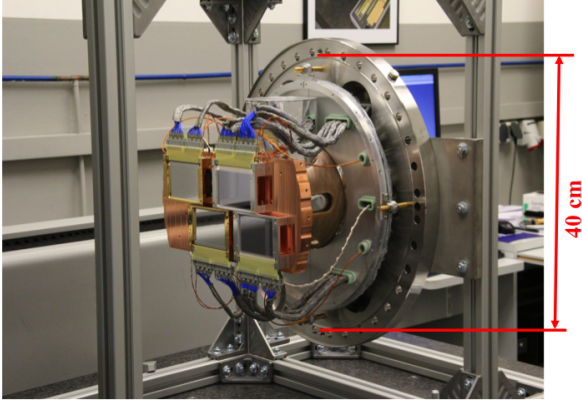


Figure 12: A KOALA recoil detector consists of 2 silicon and 2 germanium strip sensors

A picture of the recoil detector as used for the commissioning is shown in Fig. 12. Two silicon strip sensors with dimensions of 76.8 mm (length) x 50 mm (width) x 1 mm (thickness) have been placed at about 90 cm from the target to cover the recoil angles, $\alpha=0^\circ-15.7^\circ$. Each silicon detector has 64 strips with 1.2 mm pitch. In addition, two germanium strip detectors with 5 and 11 mm thickness have been set up in 2 rows as well. Both germanium detectors have 67 readout strips with a strip pitch of 1.2 mm in a sensitive area of 80.4 mm (length) x 50 mm (width).

The forward detector consists of 4 pairs of scintillators, which have been located symmetrically at up, down, left and right of the beam axis. Each pair has been sequentially installed in the vacuum tube along beam axis with a distance of 20 cm each other. The scintillator bars have the form of an isosceles trapezoidal with dimensions of (10x20) mm (bases) x 90 mm (height) x 6 mm (thickness) and cover the polar angle of $0.37^\circ-1.2^\circ$.

The full setup of KOALA has been installed at COSY for commissioning. Data have been collected with proton beam momenta of 2.5, 2.8, 3.0 and 3.2 GeV/c. One

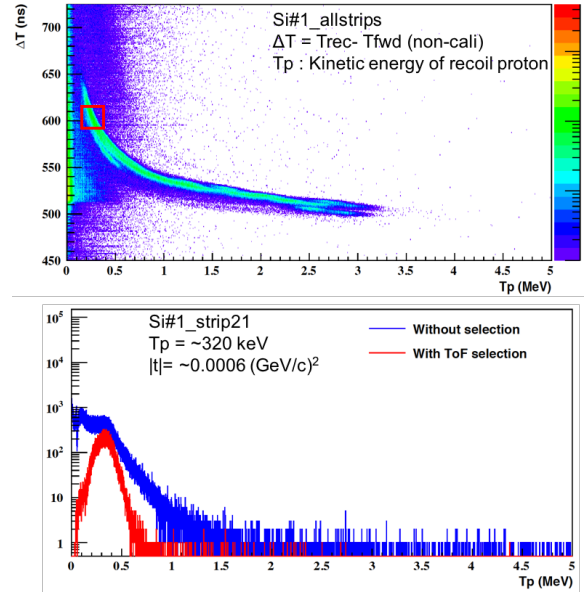


Figure 13: The upper plot shows the ΔT versus recoil proton energy distribution; The red and blue distributions in the lower plot show the events on a single strip of the silicon detector with and without (time of flight) ToF information, respectively.

of the highlight results is the coincidence measurement, which works perfectly between the recoil and forward detectors. Fig. 13 shows a data sample at a beam momentum of 3.0 GeV/c. The upper plot shows the distribution of the ToF versus the kinetic energy of the recoil protons. It indicates a clear recoil proton band. With the implementation of a coincidence cut, pure elastic events can be selected and the background can be significantly suppressed. The red and blue histograms at the lower plot indicate the event distribution with and without this coincidence, respectively. The distribution on the specific strip has a peak around 320 keV, which corresponds to t of 0.0006 GeV 2 . The preliminary result is very promising to verify the detector concept. The KOALA experiment will be performed at HESR as soon as the antiproton beam will be available.

1.3 The \bar{P} ANDA Cluster-Jet Target

The \bar{P} ANDA experiment at the future accelerator facility FAIR will use a cluster-jet target for a major part of the planned experimental program. This target was built up and thoroughly tested at Münster laboratories where it was operated on a daily basis. In summer 2018 it was transferred to COSY at Forschungszentrum Jülich for an extensive series of measurements on beam-target interaction and vacuum studies in a close to \bar{P} ANDA geometry under real accelerator conditions.

Already from the beginning, the \bar{P} ANDA cluster-jet target at the former WASA experiment location at COSY (cf. Fig. 14) showed an excellent performance and a sta-

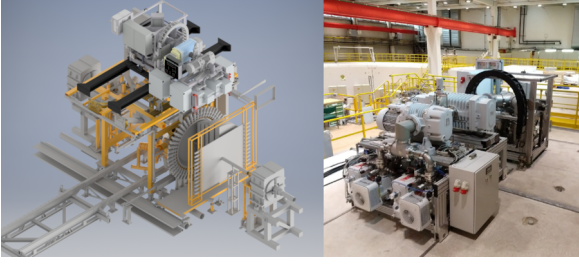


Figure 14: *Left*: CAD drawing of the $\bar{\text{P}}\text{ANDA}$ cluster-jet target with the WASA forward detector. *Right*: Installation of the $\bar{\text{P}}\text{ANDA}$ cluster-jet target on top of the COSY ring ceiling.

ble target thickness of more than 2×10^{15} atoms/cm² in a distance of more than 2m from its nozzle, which corresponds to the later $\bar{\text{P}}\text{ANDA}$ interaction point.

In addition to its performance, the $\bar{\text{P}}\text{ANDA}$ cluster-jet target is perfectly embedded into the new COSY control system with the EPICS based slow control system. This makes it possible to control the jet target, e.g., in dependence of the COSY cycle time or super cycle experiment number. Also all relevant target parameters and measurements are saved into the COSY archiver appliance.

Two beam times in 2019 were used to study in detail the interaction of the COSY proton beam and the cluster-jet beam. It was shown that the influence of the proton beam on small clusters has a small, but measurable, effect on the accelerator vacuum (cf. Fig. 15). A systematic study of this effect with larger clusters and different beam currents is planned for upcoming COSY beam times and is of highest interest for studies on the vacuum situation at HESR/FAIR in presence of a cluster-jet beam. Further-

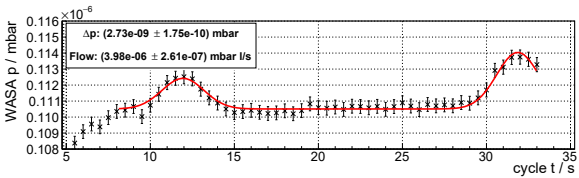


Figure 15: Vacuum pressure at the WASA IP as function of the time-dependent horizontal COSY beam position. The pressure increase is given by ion-beam induced cluster evaporation, resulting in a maximum pressure for full beam-target overlap.

more, studies on the COSY beam lifetime with different COSY beam currents and different cluster-jet target thicknesses were performed. It was shown that envisaged beam lifetimes of more than 30 minutes with target thicknesses desired by the $\bar{\text{P}}\text{ANDA}$ experiment are possible using the installed stochastic cooling system for HESR, which is currently installed in part at COSY.

Of special interest for the $\bar{\text{P}}\text{ANDA}$ experiment is a stable and well known beam quality, e.g. for precise energy scans of resonances. Intensive beam quality measurements were done 2019 using the $\bar{\text{P}}\text{ANDA}$ cluster-jet

target, the stochastic cooling and the COSY Schottky detector. It was successfully shown that the mean value of the nominal COSY beam momentum of 3.0 GeV/c varies even at larger target thicknesses only in the order of $\delta p/p \sim 10^{-6}$ (cf. Fig. 16) with a stable momentum spread of $\Delta p/p \approx 10^{-4}$.

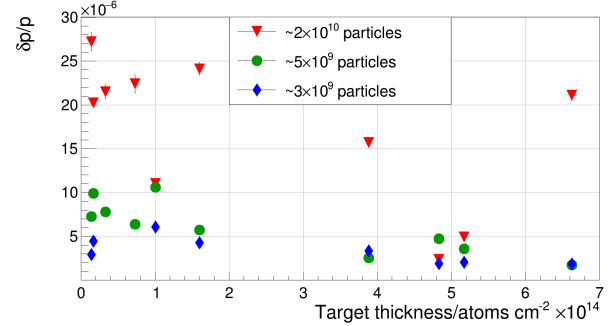


Figure 16: Mean COSY beam momentum as function of the $\bar{\text{P}}\text{ANDA}$ cluster-jet target thickness and for different numbers of stored particles in COSY. The red triangle markers at 5×10^{14} show that the optimal adjustment of the stochastic cooling concerning beam particle number and target thickness is important for best results.

In upcoming beam times at COSY it will be continued to investigate the beam quality, lifetime and vacuum conditions of COSY in presence of the $\bar{\text{P}}\text{ANDA}$ cluster-jet target at different target settings. Of special interest are these measurements in cooperation with the stochastic cooling at COSY, but also the 2 MV electron cooler studies at COSY benefit from the state of the art, high thickness $\bar{\text{P}}\text{ANDA}$ target for performance measurements. Furthermore, the influence of new and optimized vacuum chambers for the $\bar{\text{P}}\text{ANDA}$ target on the accelerator vacuum will be tested.

1.4 Detector Tests for the CBM and HADES Experiments

High-intensity proton beam extracted from COSY has been used for testing prototype detectors of the CBM experiment at FAIR and the HADES experiment at SIS-18 relevant for its operation in the FAIR phases 0 and 1.

CBM Silicon Tracking System Module

The CBM experiment has entered a phase in which the main detector system test activity has been shifted to the mCBM (“miniCBM”) demonstrator experiment at GSI/SIS-18. mCBM became operational late 2018. Specific detector investigations, however, are still well placed in different beam campaigns for mCBM, e.g. using the focused “pencil beams” at COSY.

A test carried out in the JESSICA cave at COSY in November 2019 addressed a newly assembled CBM-STS module, shown in Fig. 17, comprising a further developed

front-end electronics board (FEB-8) with the new ASIC version STS-XYTER v2.1 and new low-voltage regulation. This was the first operation of a fully functional and noise-optimized STS module in beam. The module was mounted onto a carbon fiber support ladder and installed on a frame in a mobile test station. It was operated with specific power regulating and distributing electronics and a full prototype CBM data-driven read-out chain, along with a scintillating fiber hodoscope. The test focused on scanning the sensor position with respect to the proton beam ($p = 2.7 \text{ GeV}/c$, $E_{kin} = 1.92 \text{ GeV}$) to raster the sensors segmented active area and map out its response at various front-end electronics settings and different beam intensities at known beam energy. The targeted STS system noise of around $1000 e^-$ was demonstrated. Detailed analysis of the data taken is in progress to yield robust signal calibration and thus the signal-to-noise ratio, together with the particle detection efficiency in the small test system of STS module and the fiber tracking telescope.

The results contributed to concluding the ASIC Engineering Design Review in December 2019 and will give important input to the CBM module series production readiness procedure scheduled for 2020.

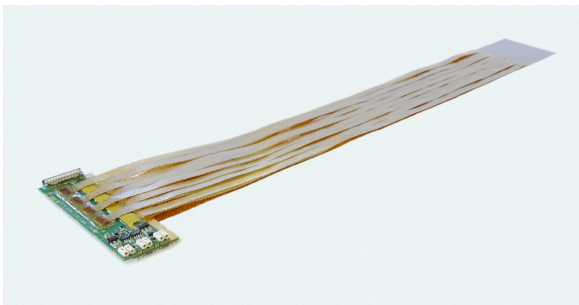


Figure 17: Detector module of the CBM STS as used in the test at COSY.

HADES Ultra-Fast Silicon Detectors

The HADES experiment has been equipped with a diamond detector system in close distance upstream of the target serving the start-time measurement for particle time-of-flight measurement. Also silicon detectors with a high doping concentration, operated in a controlled-avalanche regime, allow for fast signal collection with especially short signal rise times. This feature and their availability through standard production techniques makes them suitable as forthcoming start-timing detectors in the HADES and CBM experiments. In parallel to the CBM silicon detector module test, ultra-fast silicon detectors (UFSD) were arranged on the beam table in the JESSICA cave, in combination with a Mini Drift Chamber (MDC) developed for HADES. The USFS-MDC setup allowed evaluating the chamber's drift velocity map inside drift cells of new geometry, along with its spatial resolution. The timing properties of the UFSDs

themselves was studied with a pair of such silicon sensors alone.

The small station of two UFSD strip sensors of $50 \mu\text{m}$ strip pitch used is illustrated in Fig. 18. The readout was realized with custom-built discrete electronics providing two stages of amplification, together with two discriminator systems (NINO, PADIWA) and a TRB3 based TDC system. The particle rates were between 7 and 10 kHz per strip. The detectors were operated in ambient air without additional cooling. The precision of the start-time measurement achieved for pairs of channels yields $81 \text{ ps}/\sqrt{2} \approx 58 \text{ ps}$.

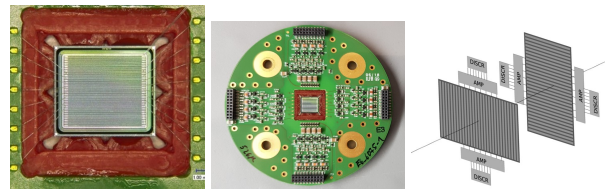


Figure 18: Prototypes of Ultra-fast silicon detectors, single-sided segmented into micro strips and arranged in a two-coordinate test system.

2 Storage Ring Based EDM Search

2.1 Introduction

In October 2010, early in the second period of the Programme-oriented-Funding (PoF-II) of the Helmholtz Association, a Scientific Advisory Council, chaired by Stephan Paul (TU Munich), strongly endorsed our plans to investigate the possibilities of a search for Electric Dipole Moments (EDM) of charged particles (proton, deuteron) in storage rings. Almost 10 years later, the subsequently founded JEDI collaboration at COSY has accomplished substantial achievements for key accelerator technologies as well as in measurement techniques. Within an ERC Advanced Grant (srEDM) of the European Union, a deuteron-EDM precursor experiment is currently being set-up at COSY. A first measurement was carried out in 2018 and is currently being analyzed. In the meanwhile, both the experimental equipment and the accelerator are further optimized towards a second run in 2021.

After establishing the CPEDM collaboration together with CERN scientists, this progress has culminated in a report *Storage Ring to Search for Electric Dipole Moments of Charged Particles - Feasibility Study*², which summarizes the current knowledge and the inferred strategy. The critical next step will be a prototype EDM ring, running at low energies, to establish key issues which cannot be demonstrated with COSY, and to perform a first direct proton-EDM measurement. JEDI and CPEDM are

²available as [arXiv:1912.07881](https://arxiv.org/abs/1912.07881) and soon to be published as a CERN Yellow Report

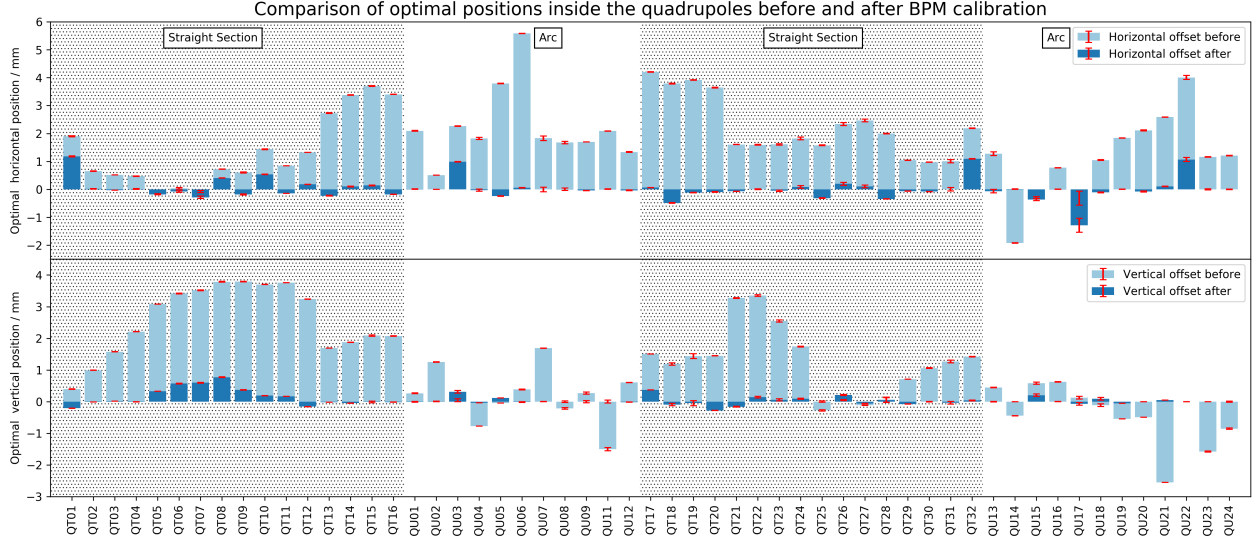


Figure 19: Optimal positions inside the quadrupoles before (light blue) and after (dark blue) the calibration of the BPMs with the beam-based alignment. The optimal positions are now significantly closer to zero and nearly all within the 0.2 mm alignment specifications.

well on the way towards a detailed Technical Design Report for this demonstrator ring. One requirement, a sufficiently large spin coherence time for protons, is addressed by a recent proposal.

In parallel, a further application of these developments, namely the search for axions or axion-like particles (ALPs), has been successfully demonstrated.

In the following sub-sections, these achievements are discussed in more detail.

2.2 Results for Beam-Based Alignment at COSY

In order to have a good orbit in COSY it is needed to go through the centers of the quadrupoles. This way the beam does not see additional magnetic fields from being displaced inside the quadrupoles, which will influence the spin rotation and thereby the electric dipole moment (EDM) measurement and make it difficult to compare simulations with actual measurements.

The beam-based alignment method allows us to measure the positions of the magnetic centers of the quadrupoles relative to the electric centers of the beam position monitors (BPMs). It then makes it possible to calibrate the zero of the BPMs to the position where the beam passes through the center of the quadrupoles.

For the beam-based alignment measurement one needs to modify the current of one individual quadrupole. This was not an intended mode of operation in COSY and also was not possible without additional hardware, as four quadrupoles are always powered by one main power supply. In order to overcome that difficulty four new source-sink power supplies have been acquired and connected in parallel to the individual quadrupole to be studied. This

allows to modify the current through one quadrupole by adding or bypassing a fraction of the current for only that magnet. In order to determine the magnetic center of a quadrupole, i.e. optimal position, one has to find the point where it does not steer the beam. The amount of how much it influences the orbit at a position in the accelerator can be seen in Eq. (1), with $\Delta x(s)$ being the orbit change at position s in the accelerator, Δk the change in quadrupole strength, $x(s_0)$ the position of the beam with respect to the magnetic center of the quadrupole, and the other parameters the usual accelerator parameters (magnetic rigidity $B\rho$, length of quadrupole ℓ , quadrupole strength k , betatron tune ν , beta function β and betatron phase ϕ at the measurement position s or the quadrupole position s_0 , respectively).

$$\Delta x(s) = \frac{\Delta k \cdot x(s_0) \ell}{B\rho} \frac{1}{1 - k \frac{\ell \beta(s_0)}{2B\rho \tan \pi \nu}} \times \frac{\sqrt{\beta(s)} \sqrt{\beta(s_0)}}{2 \sin \pi \nu} \cos[\phi(s) - \phi(s_0) - \pi \nu] \quad (1)$$

From the equation one can see that if one is in the center of the quadrupole ($x(s_0) = 0$) and varies the strength (Δk) then the beam does not move and one is at the optimal position. This position is searched for all the quadrupoles in the ring (see Fig. 19) and then the BPMs were recalibrated so that the new zero of the BPM is when the beam passes centrally through the quadrupole.

This new calibration of the BPMs now shifts the optimal positions in the quadrupoles to zero or closer to zero, as there are more quadrupoles than BPMs in the ring. Overall it is a very good improvement and if one now corrects towards a zero orbit one actually passes through the centers of the quadrupoles.

2.3 Measurement of Beam Oscillations of a Mismatched Waveguide RF Wien Filter

A novel device, acting as a beam transparent and transverse spin rotator, a waveguide RF Wien Filter, has been constructed and implemented in COSY to realize the next step towards the measurement of the deuteron EDM in a magnetic storage ring.

The waveguide Wien filter is operated under the so-called *matched condition*. In this mode of operation, the electric and magnetic fields generated in the device produce equally large electric and magnetic forces that act on the stored particles which corresponds ideally to a vanishing Lorentz force F_L and consequently, to a non-oscillating beam. In order to ensure this mode of operation, a novel technique to determine the amplitude of the beam oscillations has been established and tested.

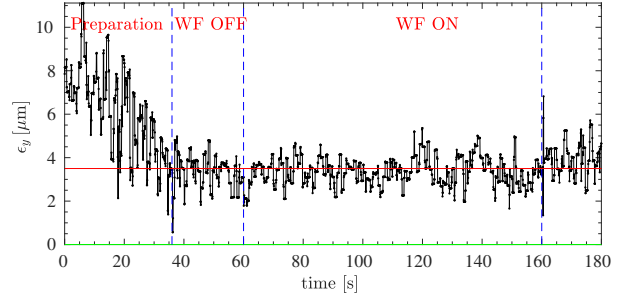
As a consequence of the flexible control circuit of the waveguide RF Wien filter, the device can induce oscillations of the beam on purpose by carefully mismatching the impedance, and these oscillations can then be measured using the aforementioned technique. Matching and mismatching the RF Wien filter, is performed by adjusting its driving circuit, particularly the variable load. The load part consists of an impedance matching network and a fixed high-power water-cooled resistor $R_f = 25 \Omega$, where the larger part of the RF power is dissipated. The matching network is of (C-C-L) L-type. It consists of a fixed air coil with a nominal design value of $28.8 \mu\text{H}$, verified by measurements in the frequency range from 630 kHz to 1.6 MHz. The variable capacitors C_L and C_T are vacuum-based, each ranging from 50 pF to 980 pF. They permit to reach the intended impedance value to match the waveguide Wien filter.

Figure 20 shows the measured value of vertical beam oscillations denoted by ϵ_y . Panel (a) of Fig. 20 shows the measured value of ϵ_y at the matched point, described by $C_L = 716.27$ pF, and $C_T = 507.78$ pF. In this case, switching on the RF Wien filter shows no effect on the measured value of ϵ_y .

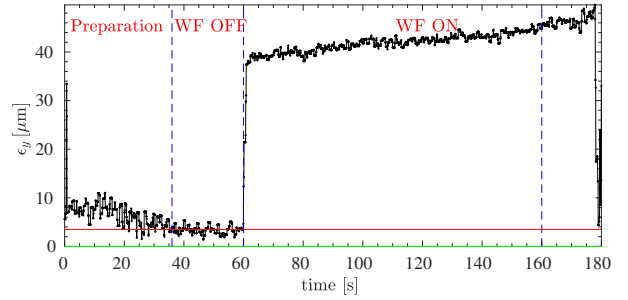
Panel (b) shows ϵ_y at a mismatched point, described by $C_L = 907.79$ pF, and $C_T = 885.58$ pF. One can see clearly the effect of mismatched fields on the beam leading to the jump in ϵ_y when the RF Wien filter is switched on. Now, performing the measurements for each *possible* combination of C_L and C_T results in a Lorentz force map, shown in Fig. 21. The net power was maintained constant at a level of 600 W for the entire map.

2.4 Commissioning of the JEDI Polarimeter

The search for a charged-particle EDM using a polarized beam confined in a storage ring requires a polarimeter optimized for high efficiency, large analyzing power, and stable operating characteristics. With typical beam momenta near 1 GeV/c, the scattering of protons or deuterons from a carbon target into forward angles be-



(a) Measured oscillation amplitude ϵ_y at the matched point with $C_L = 716.27$ pF, and $C_T = 507.78$ pF.



(b) Measured oscillation amplitude ϵ_y at a mismatched point with $C_L = 907.79$ pF, and $C_T = 885.58$ pF.

Figure 20: Two measurements of the oscillation amplitudes ϵ_y as a function of time in a cycle.

comes a nearly optimal choice for an analyzing reaction. Superior energy resolution is needed for clean and reproducible event triggers and high speed readout allowing large event rates is necessary for excellent statistical precision and sensitivity. Consequently, the JEDI collaboration has decided to design and build a dedicated modular new polarimeter for precision measurements, based on the inorganic scintillator material LYSO (Lutetium-yttrium oxyorthosilicate).

After a careful design, optimization and test phase at an external beamline of COSY the JEDI polarimeter (JePo) has recently been installed into the storage ring. It replaces the venerable EDDA detector, which was one of the earliest experimental installations in COSY. Since then its plastic scintillator system was used as the beam polarimeter for JEDI and other experiments. More recently, it was joined by the forward detector system of the WASA detector. The JePo concept exploits LYSO modules ($3 \times 3 \times 8 \text{ cm}^3$), individually coupled to modern large area silicon photosensor (SiPM) arrays, which are operating at low voltage. The detector system has radial symmetry and an almost unhindered view onto the target inside the COSY ring, realized by a very thin vacuum window. This makes the polarimeter very efficient for up-down and left-right asymmetry measurements, which constitute the basis for the determination of the beam polarization.

During fall 2019, the polarimeter consisting of 52 modules was assembled at the COSY ring. Figure 22 shows the final installation with vertical and horizontal targets

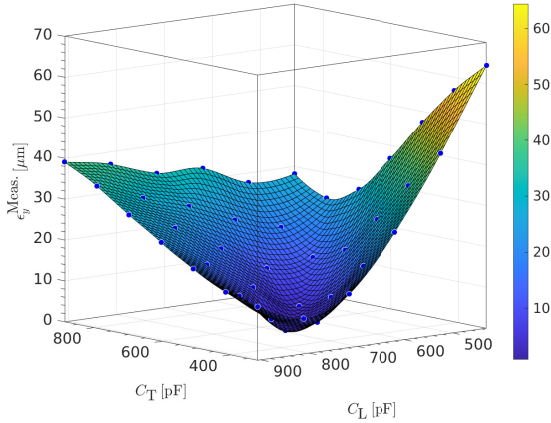


Figure 21: The measured oscillation amplitudes ϵ_y map as a function of C_L and C_T with an average constant power in the RF Wien filter of (600 ± 25) W at each point of the map.

using magnetic feed-throughs. During one week of beam time the polarimeter has been tested with vertically polarized deuteron beam as well as unpolarized cycles. Detector modules, voltage supply, and the target control system showed the desired performance.

In future upgrades, Rogowsky beam positioning coils will be added at the entrance and exit flanges of the polarimeter to monitor the beam crossing through the detector. This will improve our control over systematic errors for the asymmetry measurement.

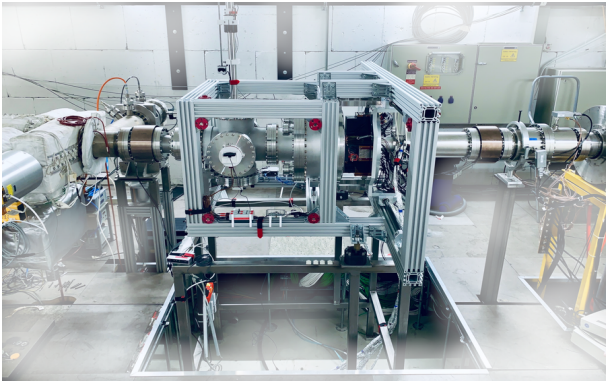


Figure 22: The picture of JEDI polarimeter (JePo) installed in the COSY ring.

2.5 Simulations for the Prototype EDM Storage Ring

A conceptual design has been made for a combined E/B-prototype ring (PTR) based on the requirements and limitations of electric and magnetic bending elements. Specifically the magnetic flux density of the magnet

should be roughly 33 mT. The corresponding E-field is about 7 MV/m (see Fig. 23).

A detailed investigation of the required field strength and distribution resulted in the following boundary conditions.

- The design of the magnetic field provides the required field homogeneity level. A highly uniform magnetic dipole field can be reached by a $\cos(\theta)$ distribution of the conductors (see Fig. 23, right). Care was taken to keep this level up for the entire magnet comprising the stray fields. This leads to a design in which the return paths of the conductor follow the same $\cos(\theta)$ principle (see Fig. 23, left).
- The gradient magnetic field due to the curvature has been cancelled by the introduction of a small tilt angle of the upper conductors in the cross section and an opposite angle for the lower ones in the cross section.
- The magnet has a power consumption of about 43 kW. The current density in the conductor is about 2.6 A/mm^2 . This seems to be feasible if water cooling of the conductors is provided. The mass of the copper conductors for a single magnet amounts to about 3000 kg. The magnet can be accommodated outside the vacuum tube.
- The electric field can be generated by a conventional plate capacitor inside the vacuum tube with rounded Rogowski-type ends for better field homogeneity (see Fig. 23).
- The homogeneity of the fields in the cross section reaches a similar level as the magnetic fields. Homogeneity investigations have been carried out in terms of larger gap widths and higher plates.
- Same as for the magnetic field, electric field gradients due to the curvature can be cancelled, in this case by giving the surfaces of the capacitor plates slightly convex or concave shapes. This procedure is suggested to reduce the requirements on dedicated electric quadrupoles, which have been envisaged to reduce the effect of gradients. The additional expenditure for the manufacture of such shapes is presumably not much higher because of the curvature of the capacitor.
- The magnetic field plot can be read as the local inverse gap distance of the capacitor plates if local matching of normalized electric and magnetic fields is required. This recipe can be followed up to small magnetic field values until larger capacitor gaps become impractical. If the matching has to be pursued even for the low-field region in between dipole magnets, either capacitors at stepped potential values have to be stacked along the trajectory direction, or small additional dipole magnets have to keep up a small value of the field in between, keeping the gap width at acceptable levels.

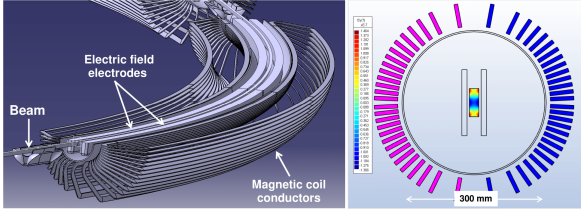


Figure 23: Shown on the left is a cutaway drawing of the prototype ring in the $\vec{E} \times \vec{B}$ version. A side view of the lower half of a 45° bend element is shown. The electrodes have a gap of 60 mm. The magnetic coil conductors (single, $4 \times 4 \text{ mm}^2$ copper bars) produce a highly uniform “cosine-theta” dipole field. Shown on the right is a transverse section displaying an end view of the magnet coil, as well as a field map of the good magnetic field region.

Beam and spin simulations towards a prototype ring are presently performed. A lattice optics with different focusing strengths is studied in detail. Estimations of beam losses in the prototype ring for different lattices are performed by using analytical formulas. These tasks are carried out, to minimize systematic errors, enhance beam lifetime and spin coherence time, by optimizing the lattice optics.

This conceptual design study can only be considered as a first step towards the realization of an E/B prototype ring. Severe engineering efforts have to be undertaken to cast the preliminary design described into a solid design ready for manufacturing. During this procedure, the design presented here may have to be adapted to mechanical and electrical requirements.

2.6 Plans for Proton Spin-Coherence-Time Measurements

For several years the JEDI collaboration has performed a number of experiments on prolonging and understanding the spin coherence time (SCT) of cooled and bunched deuterons at a beam momentum of $p = 970 \text{ MeV}/c$. It has been shown that sextupole configurations leading to small chromaticities in the horizontal and vertical plane result in long SCTs in the order of $\tau = 1000 \text{ s}$. In order to achieve this result a number of tools have been developed to measure the spin coherence time as well as the spin tune and to phase-lock the spin precession to an external rf resonator (rf solenoid, rf Wien filter). All the experimental work was accompanied by theoretical studies and lattice simulations of spin and particle tracking.

The long term strategy for EDM searches utilizing storage rings foresees a step-wise plan using an intermediate prototype ring running polarized protons as a demonstrator for key technologies for an electric ring as well as for frozen spin, and has as a final goal a high precision all-electric storage ring for protons with counter-rotating beams. For these proposed measurements a successful realization of a long spin coherence time also for protons

is a mandatory requirement. Furthermore, it will verify theoretical predictions of simulation codes and the credibility of the theoretical calculations for the proton case. Therefore, we want to start a similar program for protons as we had it for deuterons in the past once the precursor experiment has been finished.

A number of things suggest that the proton is the more challenging case, including the increased size of the anomalous moment (and the speed of precession in the COSY ring), the greater abundance of machine and imperfection resonances, and greater complications with the landscape of chromaticity leading to shorter polarization lifetimes. This also means that more polarimeter statistics acquired in shorter times will be needed to follow the proton spin manipulations: the recently installed JEDI polarimeter will provide rate capabilities of 10^6 s^{-1} and more.

2.7 Search for Axions/ALPs at COSY via Oscillating EDMs

Originally, the axion was introduced to resolve the strong CP problem in QCD. If they exist, axions or axion-like particles (ALPs) would be also viable candidates for dark matter. Axions, when coupled with gluons, induce oscillations in the nuclear electric dipole moment d_n which can be described as $d_n(t) = d_0 + d_1 \cos(\omega_a t + \phi_a)$ where ω_a , the oscillation frequency, is related to the axion mass m_a with $\omega_a = m_a c^2 / \hbar$.

A search for axions in a magnetic storage ring makes use of an interaction between the induced oscillating EDM and the resulting torque in the motional electric field. In the resonant case, when the oscillation frequency matches the spin precession frequency of a beam polarized in the ring plane, a net rotation out of the ring plane can be observed. This rotation speed can be calibrated to yield the oscillating EDM d_1 value and, thus, the corresponding axion-gluon coupling factor.

This works under the following assumptions: the axion is coherent in space, causing all beam particles along the ring to oscillate together, the axions are dense enough to be detected whenever a measurement is done, and the axion maintains coherent in time long enough for the resonance to be measured. In addition, the phase ϕ_a that relates oscillations induced by the axion field and the spin precession, is arbitrary and modulates the size of the effect.

In spring 2019, the JEDI Collaboration conducted a proof of principle experiment at COSY using a $0.97 \text{ GeV}/c$ in-plane polarized deuteron beam. The machine was operated on the fourth harmonic in order to store four bunches simultaneously. While rotating the polarization direction from vertical into the horizontal plane by means of an RF solenoid, two of these four bunches acquire a nearly orthogonal polarization. A combination of these bunches then allows the detection of axions with any phase.

Prior to the rotation into the horizontal plane the beam was electron cooled and sextupole field corrected to

maintain the in-plane polarization of the beam for the length of the storage time. Depolarization of the beam would reduce the size of the jump. For the measurement of the polarization the WASA Forward Detector was used.

After the beam preparation, the revolution frequency of the ring was varied in slow ramps (see Fig. 24). It is important to note that a scan in revolution frequency is analogous to a scan in spin precession frequency.

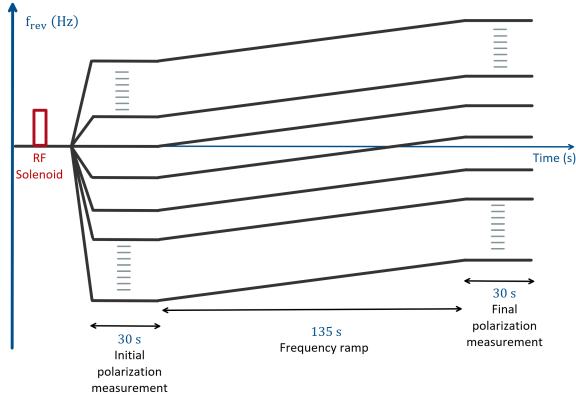


Figure 24: Schematic diagram of the scanning process (see text). The horizontal axis is time and vertical axis is the revolution frequency of the machine. The red rectangle marks the time of the RF solenoid operation.

For statistical purposes, the polarization was measured for a period of 30 s before and after the slow ramp. The difference in the average initial and final polarization was calculated to test for a change in vertical polarization. The scans deliberately overlapped by about 10% so as not to miss an axion near either end of the scan.

As a test to our experimental method, an RF Wien filter with a sideways magnetic field was set to a fixed frequency and the machine frequency was scanned to cross this resonance. This produced a polarization jump similar to the one that would be produced by an axion. As the phase between the machine and the RF Wien filter was kept random (like the axion phase), jumps varied in size and direction. Such a "test" was also helpful for the calibration of jumps from the axion search.

Over 100 scans with different initial frequencies were completed during the beam time, covering a frequency range of 1.2% around a spin tune frequency of 121 kHz. Each scan setting was repeated 8 times and checked twice with unpolarized beam. A detailed analysis of the data is underway.

This proof of principle experiment demonstrates the feasibility of a search for axion/ALPs by scanning the machine frequency for a resonance between an axion-induced oscillating EDM and the spin.

3 Neutrino Physics

The neutrino group is specialized in low-energy neutrino physics with liquid-scintillator (LS) based detectors. Borexino (Sec. 3.1), the world's radio-purest 280 tons LS detector in the Laboratori Nazionali del Gran Sasso in Italy is taking data since 2007, focused on solar neutrinos, geoneutrinos, and searches for rare processes in coincidence with astrophysical events. JUNO (Sec. 3.2) will be the first multi-kton LS detector currently under construction in Jiangmen, China. German groups are leading the construction of the 20 tons OSIRIS detector (Sec. 3.2) that will monitor the level of radio-purity of the LS during the several months long period of filling the JUNO central detector.

3.1 Borexino

Solar Neutrino Analysis

After the publication of the latest solar neutrino results concerning the comprehensive measurement of all components of the pp -chain solar neutrinos (pp , ${}^7\text{Be}$, pep , and ${}^8\text{B}$) in 2018 in Nature³, the collaboration was preparing 2 more technical papers, dealing with a detailed description of the analysis in the lower and in the higher energy window separately. The details of the low-energy analysis considering the measurement of pp , ${}^7\text{Be}$, and pep neutrinos and setting the upper limit on CNO cycle neutrinos were published in October 2019⁴, while the details of the ${}^8\text{B}$ and hep neutrino analyses in the high energy window is imminent for submission to PRD in early 2020.

The low-energy analysis strategy is based on a multivariate fit approach which takes into account two energy spectra, the so called Three-Fold Coincidence (TFC) subtracted and TFC-tagged ones. The TFC technique was developed to tag ${}^{11}\text{C}$ cosmogenic background that decays into β^+ and has a too long lifetime to be simply vetoed. A fit example of the TFC-subtracted spectrum is shown in Fig. 25. In the multivariate fit approach, additional pulse shape and radial distributions of events from the TFC-subtracted spectrum are included. The former is exploited to disentangle the contribution of the remaining positron events from ${}^{11}\text{C}$, while the latter helps to constrain the external background. The newly published PRD paper provides many technical details of this analysis, as event selection cuts, backgrounds, TFC technique, e^+/e^- discrimination technique, likelihood of the multivariate fit, the Monte Carlo based and analytical description of the detector response, sensitivity studies, as well as more technical details about the final results. As an example we show the distribution of the e^+/e^- pulse shape variable in Fig. 26, which is important for the achievement of a 5σ significance of pep neutrino observation demonstrated in the likelihood profile shown in Fig. 27.

³Comprehensive measurement of pp -chain solar neutrinos, *Nature* 562 (2018) 496

⁴Simultaneous precision spectroscopy of pp , ${}^7\text{Be}$, and pep solar neutrinos with Borexino Phase-II, *Phys. Rev. D* 100 (2019) 082004

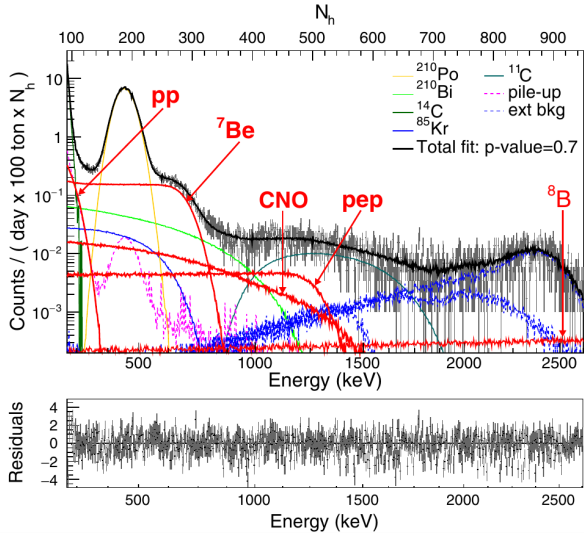


Figure 25: Example of the fit of the Borexino Phase-2 TFC-subtracted energy spectrum showing the data (grey), the total fit (black), and the spectral shapes of different signal (solar neutrinos shown in red) and background components.

Substantial effort is currently ongoing towards a possibility to observe for the first time the solar neutrinos from the so called CNO cycle. This fusion process should have a minor contribution in the Sun, but should be a dominant process powering heavy stars. The prerequisite of such a measurement is the identification of methods with which it would be possible to constrain the ^{210}Bi contamination of the LS. The expected Borexino sensitivity based on the Phase 3 (2016+) data is promising, thanks to the thermal stability of the detector achieved by its thermal isolation and an active temperature control blocking the convection currents inside the detector.

Search for Non-Standard Neutrino Interactions

The precise understanding of the Borexino energy spectrum allows us to set limits on non-standard interactions (NSI) of neutrinos, in particular flavor-diagonal neutral current interactions that modify the $\nu_e e^-$ and $\nu_e \tau^-$ couplings using Borexino Phase II data. The analysis has been performed assuming the solar neutrino fluxes from the Standard Solar Model both in the high and in the low metallicity hypothesis. The solar neutrino interactions in Borexino are measured through the neutrino-electron scattering reaction. The predicted recoiled electron distributions depend on the energy spectra of solar neutrinos, energy-dependent neutrino oscillation probability P_{ee} , and the differential cross sections $d\sigma_\alpha/dT_e$ of the neutrino-electron elastic scattering ($\alpha = e, \mu, \tau$; T_e = kinetic energy of the electron). The functions P_{ee} and $d\sigma_\alpha/dT_e$ depend again on the chiral neutrino-electron couplings $g_{\alpha L(R)}$. In some theories NSI are predicted by

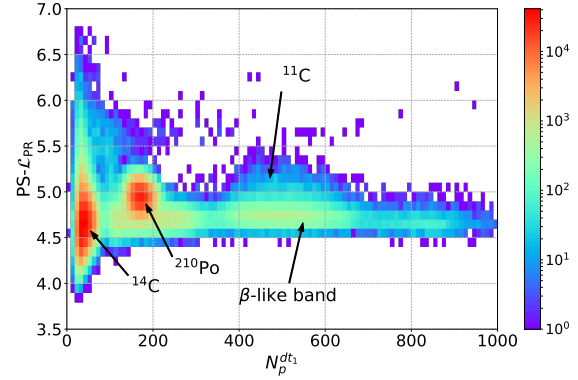


Figure 26: Distribution of the pulse shape variable $PS-L_{PR}$ (based on the likelihood of a position reconstruction algorithm) as a function of the N_p^{dt1} energy estimator (practically number of triggered PMTs, 500 corresponds to about 1 MeV) for Borexino Phase 2 events. This variable is used to further constrain ^{11}C (β^+) events from β^- -like band containing also solar neutrino signals.

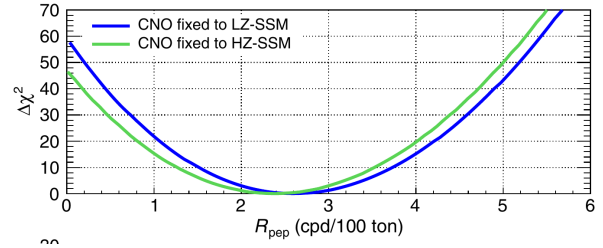


Figure 27: $\Delta\chi^2$ profile for the pep neutrino interaction rate as measured by Borexino.

a linear modification of the $g_{\alpha L(R)}$ couplings, as for example $\epsilon_\alpha^{L(R)}$ constants added to the $g_{\alpha L(R)}$. No indications for new physics were found at the level of sensitivity of the detector and constraints on the $\epsilon_\alpha^{L,R}$ parameters were set (see Fig. 28). The article has been submitted in the Journal of High Energy Physics.

Muon Seasonal Variation

A study on the modulation of the cosmic muon signal using 10 years of data from Borexino was published in the Journal of Cosmology and Astroparticle Physics in February 2019⁵. The paper presented the seasonal variation of the muon rate and its correlation with atmospheric temperature variations. A seasonal modulation with a period of (366.3 ± 0.6) days and a relative amplitude of $(1.36 \pm 0.04)\%$ was observed. This is shown in Fig. 29. The cosmogenic neutron production rate was also found

⁵Modulations of the cosmic muon signal in ten years of Borexino data, J. Cosm. Astrop. Phys. 02 (2019) 046

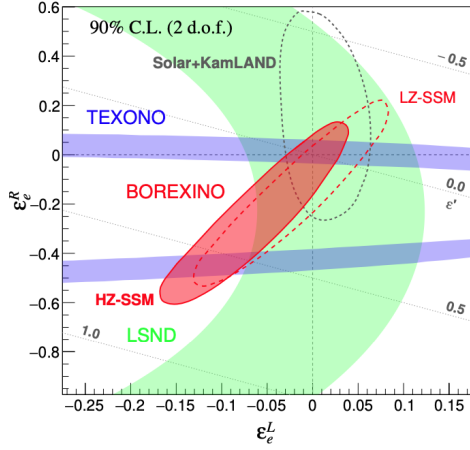


Figure 28: Allowed region for parameters of the NSI of neutrinos in the ϵ_e^R versus ϵ_α^L plane obtained by Borexino compared to other experiments.

to show seasonal modulation which was in phase with the muons. The effective temperature coefficient α_T correlated with the kaon-to-pion production ratio in the atmosphere was extracted to be (0.90 ± 0.02) and a positive correlation of the muon flux with the atmospheric temperature was shown. In addition, an evidence for the long-term modulation of the muon flux with a period of ~ 3000 days with a maximum in June 2012 was presented.

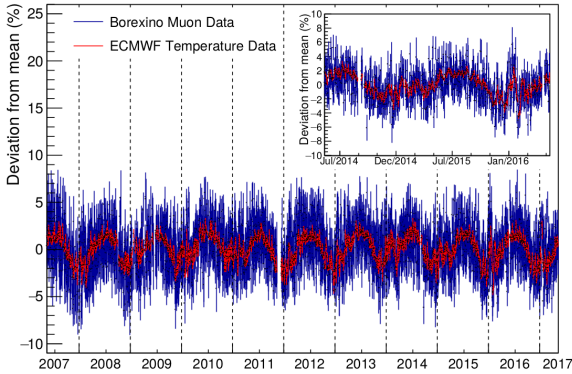


Figure 29: Borexino muon seasonal variation data. Daily percent deviations of the cosmic muon flux and the effective atmospheric temperature from the mean in ten years of data. The insert shows a zoom for two years from May 2014 to May 2016.

Geoneutrinos

Borexino released a new update on the geoneutrino measurement with improved analysis techniques using the data from December 2007 to April 2019. These results were presented at the TAUP conference in Japan and a long paper *Comprehensive geoneutrino analysis with Borexino* was submitted to Physical Review D in September 2019. The paper presented a geoneu-

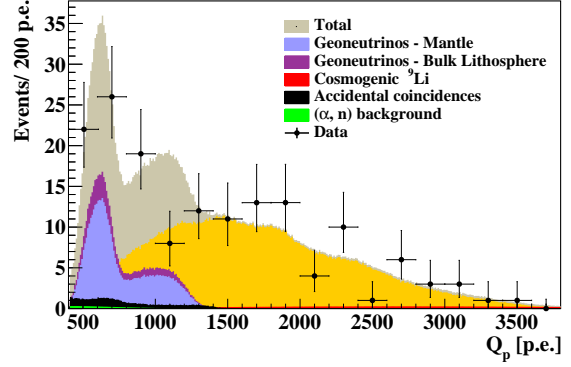


Figure 30: Borexino spectral fit of 154 Inverse Beta Decay candidates to extract the mantle signal after constraining the contribution of the bulk lithosphere.

trino measurement using 3263 days of data taken between December 2007 and April 2019. The reported exposure represents an increase by a factor of two over a previous Borexino analysis from 2015, thanks to an improved data selection that included an enlarged fiducial volume and sophisticated cosmogenic vetoes. By observing $52.6_{-8.6}^{+9.4}$ (stat) $_{-2.1}^{+2.7}$ (sys) geoneutrinos from ^{238}U and ^{232}Th , a geoneutrino signal of $47.0_{-7.7}^{+8.4}$ (stat) $_{-1.9}^{+2.4}$ (sys) TNU with $_{-17.2}^{+18.3}\%$ total precision was obtained. The null-hypothesis of observing a geoneutrino signal from the mantle was excluded at a 99.0% C.L. for the first time, exploiting detailed knowledge of the local crust near the experimental site. The corresponding spectral fit of the selected 154 candidates is shown in Fig. 30. Measured mantle signal of $21.2_{-9.0}^{+9.5}$ (stat) $_{-0.9}^{+1.1}$ (sys) TNU corresponds to the production of a radiogenic heat of $24.6_{-10.4}^{+11.1}$ TW (68% interval) from ^{238}U and ^{232}Th in the mantle. Assuming 18% contribution of ^{40}K in the mantle and $8.1_{-1.4}^{+1.9}$ TW of total radiogenic heat of the lithosphere, the Borexino estimate of the total radiogenic heat of the Earth is $38.2_{-12.7}^{+13.6}$ TW, which corresponds to the convective Urey ratio of $0.78_{-0.28}^{+0.41}$. This is compatible with different geological predictions, however there is a $\sim 2.4\sigma$ tension with those Earth models which predict the lowest concentration of heat-producing elements in the mantle. In addition, by fitting the data with a constraint on the number of expected reactor antineutrino events, the existence of a hypothetical georeactor at the center of the Earth having a power greater than 2.4 TW at 95% C.L. was excluded. Particular attention was given to the description of all analysis details which should be of interest for the next generation geoneutrino measurements using liquid scintillator detectors.

Search for Low-Energy Neutrinos from Astrophysical Sources

In September 2019 we presented at the TAUP conference in Japan several results about possible neutrino and an-

antineutrino fluxes from astrophysical sources. A corresponding paper was submitted to Astroparticle Physics. Experimental constraints on the diffuse supernova $\bar{\nu}_e$ fluxes were obtained in the previously unexplored region below 8 MeV. Model-independent upper limits in the energy range 1.8 - 16.8 MeV on antineutrino fluxes from unknown sources were set, improving previous Borexino results, on average, by a factor 2.5. We also searched for $\bar{\nu}$ in the solar neutrino flux and got a limit for a solar $\bar{\nu}_e$ flux of $384 \text{ cm}^{-2}\text{s}^{-1}$ (90% C.L.), assuming an undistorted solar ^8B neutrinos energy spectrum, that corresponds to a transition probability $p_{\nu_e \rightarrow \bar{\nu}_e} < 7.2 \times 10^{-5}$ (90% C.L.) for $E_{\bar{\nu}_e} > 1.8$ MeV. At lower energies, by investigating the spectral shape of elastic scattering events, we achieved a new limit on solar ^7Be - ν_e conversion into $\bar{\nu}_e$ of $p_{\nu_e \rightarrow \bar{\nu}_e} < 0.14$ (90% C.L.) at 0.862 MeV. We also investigated solar flares as possible neutrino sources and obtained the strongest up-to-date limits on the fluence of neutrinos of all flavors below 3 MeV. We also excluded an intense solar flare as the cause of the observed excess of events in run 117 of the Cl-Ar Homestake experiment.

3.2 JUNO

The Jiangmen Underground Neutrino Observatory (JUNO) is a multi-purpose, liquid scintillator-based neutrino experiment, proposed in 2008 to determine the Neutrino Mass Hierarchy (MH) by detecting reactor antineutrinos. The detection mechanism exploits the inverse beta-decay (IBD) reaction, where an antineutrino interacts with a proton and generates a positron plus a neutron. The detector site has been chosen in order to achieve the best sensitivity to this measurement. The JUNO complex is currently under construction in China, with a rock overburden above the experimental hall of around 700 m, and is located 53 km away from both Yangjiang and Taishan nuclear power plants. The end of construction is scheduled for 2021.

Beside the main goal of the neutrino mass hierarchy identification, additional measurements are accessible to the detector. The reactor antineutrino flux can be exploited for a measurement of the solar oscillation parameters θ_{12} and Δm_{21}^2 with a sub-percent accuracy, which would represent the most precise measurement in the neutrino solar sector. Supernovae neutrinos can also be observed in case of a stellar explosion, inferring important information on the burst process at the source. The fine energy resolution can also be exploited to observe the solar neutrino flux, by means of elastic scattering on electrons. Other sources potentially accessible to JUNO are constituted by geoneutrinos, generated in radioactive decays inside the Earth, and atmospheric neutrinos, produced after Cosmic Rays interactions in the atmosphere. Exotic searches include non-standard interactions, sterile neutrinos, and search for proton decay and dark matter annihilation signals. The IKP group is involved in the development of the reconstruction methods and sensitivity studies. In order

to address the neutrino MH issue, the non-linearity response in the measured positron energy needs to be known to a precision of less than 1%. A model is being developed in the group to describe the positron energy non-linearity, based on the electron non-linearity model. The model includes the description of several processes, such as the scintillation mechanism, the positron annihilation with the associate gamma photon emission, and the subsequent Compton scatterings. Besides a possible publication of these results on their own, they are also being used in a new publication on the updated JUNO sensitivity to Neutrino MH, which is currently under development in the JUNO collaboration.

The JUNO liquid scintillator will contain a non-negligible amount of the radioactive isotope ^{14}C , which can not be removed due to its chemical similarity to the major isotope ^{12}C . Pile-up of these events can worsen the sensitivity to the neutrino MH. The techniques of identification of such pile up events are currently studied in the group. They have also led to a new and precise vertex reconstruction algorithm.

Reconstruction techniques based on machine-learning algorithms are also developed in the group, with the application in waveform, energy, and position reconstructions, as well as in the pulse shape event discrimination. A new PhD student and a postdoc who joined the group in the 2nd half of 2019 have further broadened the physics spectrum of the group, being specialized in the search for Proton decay and in the atmospheric neutrino analysis, respectively.

The OSIRIS Detector

The radio-purity of the LS in JUNO is crucial for the success of the experiment and the collaboration has set stringent limits on the targeted radio-purity levels. For the neutrino MH-analysis a concentration of ^{238}U and ^{232}Th less than 10^{-15} g/g of LS is required, while for the solar neutrino analysis this requirement is one order of magnitude tighter. The purpose of the OSIRIS (Online Scintillator Internal Radioactivity Investigation System) detector is to monitor whether the LS meets these requirements during the whole process of filling the 20 ktons of LS into the JUNO central detector. OSIRIS can contain 20 tons of LS and the samples from each purification badge will be constantly flowing through it.

The principle of measuring the levels of ^{238}U and ^{232}Th contamination lies in identification of the fast time-coincident decays of the isotope pairs ^{214}Bi - ^{214}Po and ^{212}Bi - ^{212}Po , respectively. In addition, OSIRIS will be able to measure the ^{14}C concentration down to a $^{14}\text{C}/^{12}\text{C}$ ratio of 10^{-17} at 90% confidence level.

OSIRIS is mainly developed by the German part inside the JUNO collaboration. The responsibility of the IKP group is the development of the source calibration system. The radioactive sources will be employed with the help of the ACU (Automatic Calibration Unit) kindly provided by the Daya Bay collaboration. A substantial effort

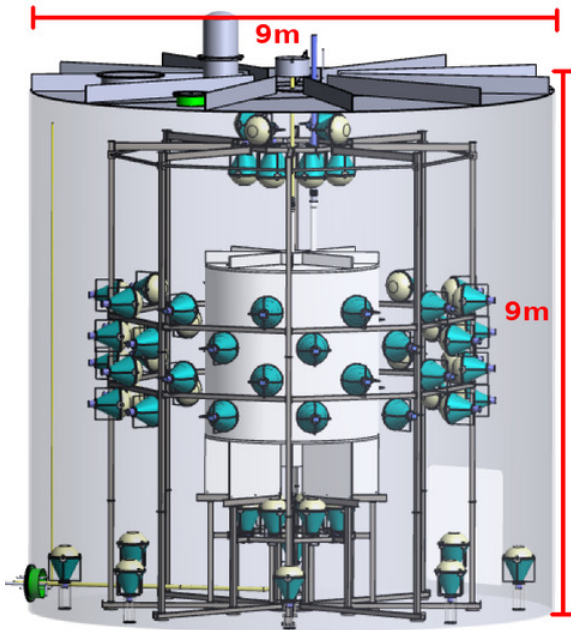


Figure 31: The OSIRIS detector design.

is ongoing in order to adapt the unit in OSIRIS and to plan the whole calibration procedure with a minimal risk of the contamination of the LS.

The OSIRIS detector design, consisting of two optically separated vessels, is shown in Fig. 31. The inner vessel is an acrylic cylinder with a diameter and height of 3 m each. It holds the scintillator and is observed by 64 20"-PMTs. These PMTs are held by a steel frame which is fully contained in the outer vessel. Due to the purpose of OSIRIS to constantly monitor the LS quality, it has an inlet on the top and an outlet in the bottom of the inner vessel: both equipped with a diffuser to ensure an equal distribution of the scintillator in the vessel.

The outer vessel is a stainless steel cylinder filled with water, which serves as a buffer volume to shield against external radioactivity from the surrounding rock. It is equipped with additional 12 20"-PMTs that will detect the Cherenkov light from cosmogenic muons.

The readout design of the PMTs will use a novel approach. To maximize the quality of the signal, the readout electronics as well as the digitizer is placed directly inside the base of the PMT. This enables better impedance matching of the PMT base and therefore a higher quality of the signal. The analogue-to-digital converter chip was developed in the ZEA-2 institute of FZJ. OSIRIS will run with a trigger-less readout scheme. The waveforms from individual PMTs will be sent, together with a synchronized time stamp, to the outside DAQ system. Here, a dedicated software will sort the waveforms (based on their time-stamps) and will build the "offline trigger". The IKP group is involved in the development of the latter.

The group was also involved in the construction of the OSIRIS Monte Carlo. Worth to mention is the imple-

mentation of the biasing mechanism for an efficient simulation of the external background, previously applied by the Borexino collaboration.

The tool for the estimation of the OSIRIS sensitivity as radio-activity monitor was also developed here and was used to determine the optimal detector design parameters, as is the number of PMTs, their distance to the inner vessel, or to estimate the impact of different radioactive contaminants.

4 Accelerator Research

4.1 Introduction

Major efforts at IKP-4 are aiming at progress in (i) controlling all synchrotron properties of COSY that affect the analysis of systematic errors for the search for an electric dipole moment, (ii) finalizing the design and mechanical work for the HESR, which is the biggest German in-kind contribution to FAIR apart from the buildings, and (iii) supporting the activities for the High Brightness Neutron Source at Forschungszentrum Jülich. For HESR several work packages are nearly finished and are focussing now on assembly and documentation. The delivery of the main dipole magnets (except the 4 special dipole magnets for the SPARC collaboration) is complete. For more details see section 4.6.

4.2 COSY Operation

As the feasibility study of the EDM search is a common endeavour of both machine and experimental physicists, the task is shouldered by the COSY operating crew and the JEDI collaboration working in close collaboration. A major part of the work covered by the COSY operating crew is the migration from the Tcl/Tk-based control system which is not quite maintenance friendly, to Control System Studio (CSS) utilizing EPICS. Additionally, the BPM control system hardware has been changed to the LIBERA system which is selected for use at FAIR.

The upgrades aim towards better beam control e.g. beam orbit, tune, and chromaticity control improvements. The upgrade of the BPM electronics introduced automatic in-situ gain calibration, automatic orbit correction and feedback algorithms. A significant part of the work is the transition towards a faster and less restrictive magnet control. It further includes improved tune measurement tools. Ultimately the control of all systems will be centralized around EPICS enabling ease of operation, automation and setup of additional services. Continuous work on migration of accelerator sub-systems to EPICS and adding relevant data to the central archiving service allows for real-time data analysis and significantly shortens the time needed for failure location and correction which helps improving the accelerator systems.

All measures described above together with the geodetic

survey followed by the mechanical adjustment of magnets to 0.2 mm alignment accuracy allowed for achieving a RMS orbit deviation less than 0.3 mm in both planes.

4.3 Control System Upgrade

EPICS (Experimental Physics and Industrial Control System) is an open-source, modular, flexible, and scalable control system. It provides a framework for server-client nodes on top of standard network infrastructure via the Channel Access protocol. Notable clients are Control System Studio for GUI deployment and the EPICS Archiver appliance for status and data logging. Accessibility of the orbit correction magnets via the new control system allows us to use new algorithms for optimization or automation, e.g. orbit correction or beam based alignment. New algorithms are envisaged to be integrated in the control system, e.g. automated orbit response matrix measurements or injection optimization. Sub-systems already accessible via EPICS include:

- Beam current monitor
- Schottky diagnostics
- Tune monitors
- 100 kV electron cooler
- 2 MeV electron cooler
- Neutral particle detectors
- Orbit monitoring and control
- Beam loss monitors
- Beam profile monitoring systems
- Beam spill monitors in the extraction beam lines

The level of integration varies. Dedicated GUIs have been developed providing highly optimized display of relevant data. The control system upgrade is done in close collaboration with Cosylab, a leading industry partner.

Data Archiving The central archiver service makes it possible to store EPICS-based machine and experimental data over an extended period of time. Therefore it is possible to review the machine performance based on actual values read back from numerous sub-systems. This also helps disentangling complex dependencies, like component failures affecting multiple systems. Data can be stored until the final data processing of experiments was performed, which can be in some cases years after the experiment took place.

Save and Restore The Save-and-Restore feature allows storing and restoring of all EPICS-based machine control parameters at any time. This is not only helpful for the change of the flat-top energy of the accelerator, but also new systems can be easily integrated. In addition, the GUI reports mismatches as they occur, helping in the discovery of faulty machine states.

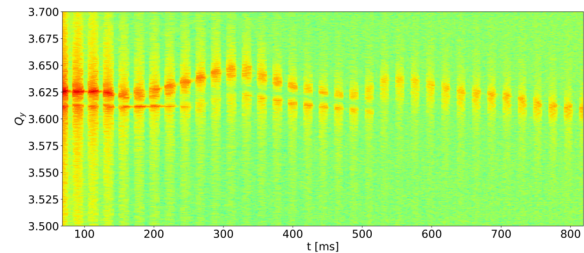


Figure 32: Evolution of vertical tune during acceleration.

Alarming Within the EPICS framework an alarming feature is implemented. While regular alarming is usually only shown in the respective GUI, where the values are shown, a central alarming server is available. This server collects all alarms centrally and displays them on a central GUI, with the possibility of further notification methods. The implementation is now prepared and the possibility of integrating the up to now used alarming within the new EPICS based system is investigated.

4.4 Improved Tune Monitoring

The new fast tune system provides a fast, robust and reliable tune measurement for bunched beams in COSY. The LIBERA beam position processors are used to measure the beam position for each particle bunch individually. While exciting betatron oscillations of the beam the horizontal and vertical tune is extracted from the beam position data by means of a Fourier analysis. The amplitude peak is clearly visible in the resulting spectrum and fitted by a Gaussian. The fit of the measured data directly leads to the fractional tune, q or $(1 - q)$. This allows for a fast tune measurement with milliseconds time resolution and tune precision of three digits. The system is capable of continuous tune monitoring, which is most helpful during acceleration of polarized beams. The beam is excited with low power for typically a few milliseconds. Thus the impact on the beam is kept to a minimum.

Fig. 32 shows the evolution of the vertical betatron tune during acceleration of a deuteron beam to 970 MeV/c. The beam excitation was pulsed to minimize emittance blow up. The user interface is being extended to make this view available routinely.

The fast tune system features:

- Highly configurable beam excitation
- Minimal beam disturbance
- Optional background suppression
- Data taking from multiple BPMs for enhanced robustness
- Support for coupled tunes and multi-bunch-mode
- High level data integrity and plausibility checks for better reliability
- Live tune resonance diagram

The tunes of unpolarized deuteron beams were repeatedly measured during the ramp to track its behaviour during acceleration. Furthermore, tune measurements were carried out at the end of machine cycles after most of the polarized beam had been extracted onto an internal target. This was possible despite the low remaining beam intensity of several 10^8 particles. Still, the variation of the measured tunes over the single BPMs was smaller than $6 \cdot 10^{-4}$ in the horizontal, and $3 \cdot 10^{-4}$ in the vertical plane. Currently we are also preparing a standard tool for chromaticity measurements based on the fast tune system. The beam momentum will be changed by means of frequency jumps using the RF-cavity. Using several tune measurements before and after each jump, we can then calculate the chromaticity automatically. The high precision of the fast tune system will allow for a precise chromaticity measurement.

A detailed report on the fast tune project can be found in the individual contributions at the end of this report.

4.5 Injector

JULIC The Isochron Cyclotron JULIC serves as injector for COSY, providing particle beams of 45 MeV protons and 75 MeV deuterons both polarized and unpolarized. Since beginning of the High Brilliance neutron Source (HBS) project a series of experiments using beams directly from the cyclotron started. Those experiments are carried out at the former Big Karl hall at the low energy irradiation place NESP (NiederEnergieStrahlPlatz). In that beamline an additional pair of quadrupole magnets and diagnostic elements have been installed and taken into operation.

High Brilliance Neutron Source Scientific research with neutrons is mostly done at reactor or spallation neutron sources. In recent years available reactor sources have been being decommissioned and just a few new spallation sources are being built. The possibility to perform neutron scattering experiments is going to decline. Compact Accelerator based Neutron Sources (CANS) operating at low ion energies (below 100 MeV) are an effective and very cost efficient way to offer neutrons. The HBS project is therefore developing such a CANS. In order to be competitive to modern neutron sources, the whole chain from neutron production, neutron moderation up to the transport system needs to be optimised. In this framework, the HBS team performed two important experiments at the COSY facility in 2019. One experiment investigated the neutron yield by bombarding target materials relevant for CANS e.g. beryllium, vanadium and tantalum with protons at various energies. The available databases for the neutron production cross sections indicated that beryllium and vanadium are good target materials at ion energies below 20 MeV whereas tantalum is a better target at higher energies. However, these databases are rather inaccurate. The performed experiment showed that vanadium is under-performing and

beryllium is the better target material regarding the neutron yield at lower energies. Additionally, the cross over to a tantalum target for maximising the neutron yield happens at higher energies. The second experiment investigated the moderator efficiency of a mesitylene based cold moderator system and the extraction mechanism into a neutron transport system. By lowering the temperature of the mesitylene moderator, the neutron energy spectra shifted to lower energies. The peak maximum could be changed from 1.5 Å at room temperature to 3.0 Å at 22 K increasing the intensity at higher wavelengths (> 10 Å) by a factor of ten. The possibility to place the optical elements close to the moderator enables the capture and transport of a large phase-space volume. The calculated brightness for thermal and cold neutron energies is therefore competitive to modern research reactors. The experiments done at the COSY facility showed that the concept of a high power CANS as developed within the HBS project is competitive to other sources and can be used to perform demanding neutron scattering experiments.

Radiation effect tests and isotope production investigations at JULIC In 2019 nine radiation hardness tests and nuclide production investigations have been performed at the cyclotron JULIC.

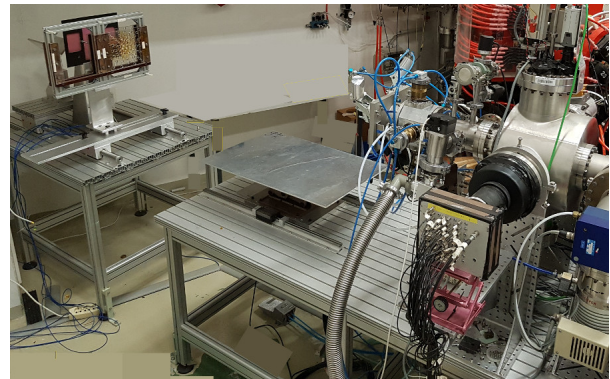


Figure 33: IndustrieBestrahlungsPlatz (IBP). Beam is coming from the right hitting the devices on the left side.

Aims of these hardness tests are to prove the functionality of integrated circuits in harsh radiation environment, check for material degeneration due to radiation or measure the nuclide production cross-section for medical applications. With respect to the type of irradiation, the span of beam currents varies between low nA to $\sim 10 \mu\text{A}$ or particle fluences ranging from 10^{11} p/cm² up to 10^{14} p/cm² and can last for some minutes up to several hours. Two target stations, the Industrie-Bestrahlungs-Platz IBP and the INM-target chamber are installed at JULIC for these purposes. Users of the irradiation facilities are Fraunhofer INT, PANDA@FAIR, ESS, the Institute of Neuroscience and Medicine (INM-5) as well as the Institute of Energy and Climate Research (IEK-4). Radiation hardness tests for space application done in collaboration with Fraunhofer INT only need a small fluence of some

10^{11} protons respectively H^- -Ions per cm^2 . In a run, a series of devices, mounted on a carrier board with 15×15 cm^2 . at the Industrie-Bestrahlungs-Platz (IBP) are under irradiation at the same time. This test bench was also used for PANDA, checking electric devices, which are foreseen to be operated at the accelerator facility FAIR. Fig. 33 shows the IBP test bench.

To monitor and control the fluence and homogeneity during the ongoing irradiation up to 12 PTW® Farmer Ionization Chambers and 2 PTW® Bragg Peak Chambers are available and can be connected to a PTW MULTIDOS Multichannel dose meter. The probes are mounted right beside the electronic components on the carrier board. The data visualization and acquisition is done with Labview®-Programs recording all dosimetry-data as well as other important data like humidity, temperature and pressure. All data are stored in files and can be processed later.

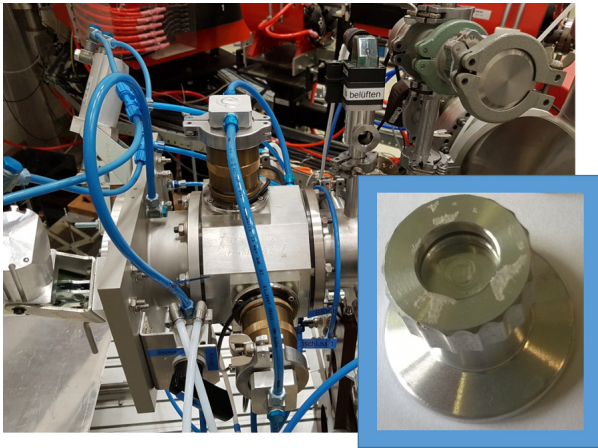


Figure 34: INM-Target chamber with target holder (enlarged in the inset). The diameter of the target is 7mm.

The nuclide production cross section measurements are done at the INM-target chamber (Fig. 34) installed at an external beamline of the cyclotron. In 2019 three measurements together with INM-5 took place. For these irradiations a beam of 200 nA is focused onto the target with 7mm diameter. The duration of these experiments is typically 30-60 min. To calculate the production cross-section later on, a precise measurement of the beam current on the target is done with a Beam Current Integrator mod. 2000AEC from TRI and an Ortec Dual Counter mod. 995.

In case of investigations, concerning changes of material properties due to radiation, the necessary particle fluence is far higher, up to 10^{14} p/cm². These investigations take place at both target stations depending on the size of the devices. Several material tests have been done for PANDA to check, if the lightweight construction structures will withstand 15 years of operation at FAIR without damages. These tests have been performed with 100 nA for several hours irradiation time at the IBP-test stand while investigations on the damages inside tungsten due

to high dose irradiation, asked for by IEK-4 was done inside the INM-target chamber. To verify simulations of the radiation damage a tungsten target was irradiated with $\sim 1 \mu A$ for 50 hours .

4.6 Progress of the HESR

Introduction

IKP is leading the international consortium which is dedicated to build the HESR. It is strongly supported by colleagues from the Central Institutes for Engineering and Analytics (ZEA) of the Research Center Jülich. About 68% of the total project investment money could be either spent or bound by contract.

According to the project schedule the ground breaking for the HESR tunnel is planned for 2021, the release of the buildings to users (e.g. HESR) to the beginning of 2023, and the start of the commissioning of the facility to the beginning of 2024. This schedule depends upon the progress of the construction of the buildings: The contract for construction of the buildings of p-LINAC, CR, and HESR is scheduled to be awarded during 2020.

The collaboration in the field of accelerators between Jülich and Darmstadt now saturated on a high level. In addition to the routinely exchange of information with architects and planners of the building infrastructure, regular meetings with our colleagues at FAIR are meanwhile well established in the fields of component identification, installation planning, detail planning of cabling, identification of synergies for component design and component acquisition etc.

Workpackage Magnets

All main dipole magnets and quadrupole magnets are delivered to Jülich. 42 of the dipole magnets are fiducialized and assembled with a heating-jacket covered vacuum chamber. Each chamber is NEG coated, filled with dry nitrogen and closed with metallic seals to allow a storage until the HESR tunnel will be available for moving in the components. The hydraulic lifting system shown in Fig. 35, which allows replacing the vacuum chamber on site in the HESR tunnel has been tested successfully.

Four main dipole magnets are waiting in Jülich to be assembled with a dedicated vacuum chamber for the SPARC collaboration (Stored Particles Atomic Physics Research Collaboration). Modified chambers with inlet and outlet for a LASER beam have to be used. These chambers are currently being NEG-coated at GSI, Darmstadt, before they will be sent to Jülich for pre-assembly. The pre-assembly of the quadrupole units in the arc sections will start as soon as the beam position monitors (BPMs) and the ion clearing chambers are delivered by their respective manufacturers. The girders for the quadrupole units are already delivered together with handling and stiffening equipment which allow to align all the magnets on the girder already during pre-assembly. The handling structures will remain on the girder until



Figure 35: HESR main dipole magnet with accessories for lifting the upper yoke for maintenance purposes. The cycle of lifting and lowering the upper yoke can be watched online⁷.



Figure 36: Left: Injection dipole magnet with electrical and cooling water connections, deflection angle 7° . Right: Injection septum with screen on the right hand side for shielding the circulating beam. The rectangular opening is for the pipe of the incoming beam. Deflection angle is 3.817° for each of the 2 septa.

the final unloading from the truck is done. During a test transport on the road the alignment was not degraded noticeably.

The correction magnets (steerers and sextupoles) are continuously delivered by our Romanian partner for magnet fabrication. These magnets are scheduled to be completely delivered by the end of 2020.

The injection dipole magnet and the 2 injection septa were delivered to Jülich. Their vacuum chambers and girders are being designed, see Fig. 36

Work Package Power Converters

The specification for the acquisition of the 2 main dipole power converters is finalized now. It will be used for the call for tender once we know a realistic date for delivery, i.e. the HESR buildings must be contracted. During the last months, 30 power converters were delivered by our Romanian partners. Due to a bottle neck in personnel it was not possible to perform the required electromagnetic

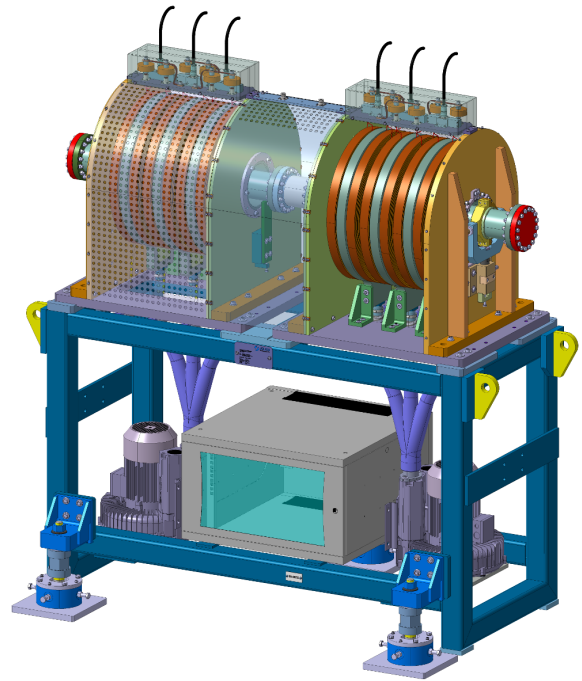


Figure 37: 3D model of one HESR cavity as basis for the in-house production. The gap in the middle is surrounded by two resonators. The protective covers are shown in transparent colour. The cover of the resonator on the right side is removed to allow an unobstructed view on the ferrite coils (brown) and the air guidance elements (light green). Note the fans in the lower part of the girder.

compatibility measurements which are part of the site acceptance test. This activity will start in early Q1/2020.

Work Package RF System

The mechanical design of the cavity was finalized, see Fig. 37. The production started in the in-house workshops. Nearly all hardware of the full system is already on site. The gap in the middle is surrounded by two resonators. The ferrite disks are air-cooled to allow feeding by transistor amplifiers. They are operated in push-pull mode. Two cavities will be built.

Work Package Injection (Kickers with Pulsers)

All kicker magnets are now assembled on their individual base plates. They will operate in vacuum. There will be two tanks to house 2 magnets each. The first of these tanks has been delivered to the manufacturer of the injection system. FZJ personnel installed the tank there with vacuum pump and heating jackets. The first two magnets are being installed into that tank. Fiducialisation is scheduled for Q1/2020. The assembly of the second series tank is scheduled to start in Q2/2020. Delivery together with the pulsers will happen once magnetic and vacuum measurements for the factory acceptance test are performed. The site acceptance test is scheduled before the end of 2020.

⁷<https://seafile.ikp.kfa-juelich.de/f/2647099ba22140008e47>

Work Package Beam Diagnostics

Beam position monitor (BPM) The BPM fabrication could be released after presentation of a prototype. Electrical behavior and geometry had been analyzed. One side of the BPM is produced with beam pipes of different lengths. The development of the fixed gain head amplifier for the BPM electrodes is finished. The complete chain of BPM, head amplifier, A110 amplifier, and Libera beam position processor is prepared for testing at COSY. After successful test the production of the head amplifiers and additional supporting equipment will be launched.

In the meantime, the test stand for measuring the electrical properties of each BPM could be automatized. Other tests with a prototype, like the general behavior of the BPM, low intensity measurements with the current of the first injected bunch being simulated, could be performed as well.

Beam loss monitor system (BLM) First BLM detectors for the system have been assembled at GSI. For 2020 a test at COSY during regular beam operation is planned. Therefore, a FESA/LSA control system setup will be installed at COSY to ensure the full capability with the future FAIR facility.

Beam current transformer (BCT) The BCTs for the HESR have been delivered end of 2019. A DC and a fast current transformer (FCT) are foreseen. Especially the FCT will be tested, as a position dependence is expected, as well as a droop for the comparably long pulses expected in the HESR. In order to calculate the beam current as precisely as possible from the measured values, these properties have to be known. It is planned to use the same test stand as for the BPMs.

Ion clearing (IC) The IC chambers are still in production. In 2019 only a prototype chamber was delivered. The electron beam welding seam along the race-track shaped cross section of the chamber seems to be the main difficulty for the producer. High voltage supplies for the beam loss monitors arrived and were mounted into racks.

Viewer A viewer for the end of the injection path has been designed and tested. Now it is cleaned and will be assembled for storage. The mechanical design of the viewers for the circulating beam is finalized (see Fig. 38) and in-house production started. When the viewer is in parking position, an RF cage will electrically close the opening in the beam pipe. The mechanical design of the 2 scraper assemblies is finished. Tendering is being prepared.

Ionization beam profile monitor (IPM) The IPM design work is continued. The final mechanical design is expected in Q2/2020.

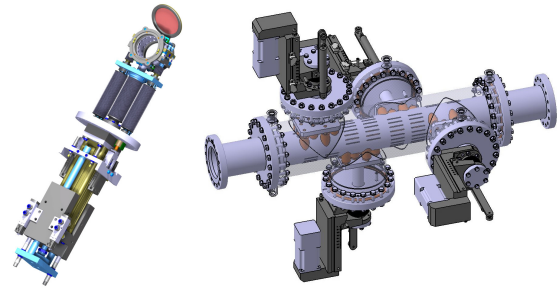


Figure 38: Left: Viewer with RF cage. Right: Scraper module with vertical and horizontal jaws and drives. Transparent beam pipe allows view on the RF cover with inner diameter of the normal beam pipe.

In addition the high voltage power supplies for the ionization beam profile monitor, the ion clearing and the beam loss monitor system has been delivered and are being tested.

Work Package Vacuum, Space Management

The work is now focussing on finalizing the mechanical layout of each vacuum section: Girders are being designed together with handling and transportation tools, beam pipes are being defined to close the vacuum chambers all around the ring depending on the class of beam pipes (fixed end, floating end, rigid for transmitting position information etc.). The design of the heating jackets is also a major effort. Goal is to award the biggest contracts in 2020.

Work Package Stochastic Cooling

The production of the pickup and kicker tanks is finished. The focus now is shifted on the pre-assembly of each tank to its own girder with water manifolds, amplifier connections etc. Detailed descriptions of the assembly steps are being recorded. All power amplifiers are in Jülich now.

Optical fiber lines are very attractive to transmit broadband RF-signals over a wide distance. They are easy to install, have low attenuation and zero dispersion. But standard fibers have some disadvantages: the signal speed is only about 60% of speed of light and these lines have a high temperature-gradient. An alternative are hollow fiber lines, where the light is guided in a hollow core which is surrounded by a microstructured cladding. Two 50m long lines of such fiber were installed as transmission-lines between pickup and kicker at COSY. They were successfully operated in both transverse cooling systems. Sometimes small periodical changes in amplitude and phase were observed sometimes not. This is probably caused by vibrations. Influences on the cooling process were not detected. A decision about the realization of the feedback line (coaxial line or optical fiber) is being prepared.

Work Package Experiment Integration

The chicane dipole magnets (Fig. 39) were delivered to Jülich and have been accepted. Girders and vacuum chambers are being designed. The specification of the compensation solenoid is being prepared to order the solenoid within 2020. Details of the interfaces between experiment and HESR are continuously monitored and optimized. Changes with a wider impact on the FAIR project planning are launched using the formal change request procedure.



Figure 39: Chicane dipole magnet, connection side

5 Further Activities

5.1 GlueX at Jefferson Lab

GlueX is a particle physics experiment located in Hall D of the Thomas Jefferson National Accelerator Facility (JLab). Hall D is dedicated to the operation of the large-acceptance detector GlueX for experiments with a broad-band, linearly-polarized photon beam produced by 12 GeV electrons from the CEBAF accelerator.

The primary purpose of the GlueX experiment is to better understand the nature of confinement in quantum chromodynamics (QCD) by identifying a spectrum of hybrid and exotic mesons generated by the excitation of the gluonic field binding the quarks. Such mesonic states are predicted to exist outside of the well-established quark model, but none have been definitively identified by previous experiments. The wider scope extends to a broad high-statistics survey of known light mesons up to and including J/ψ .

The IKP-1 group has joined the GlueX collaboration in June 2019, with the aim of studying radiative decays (both real and virtual) of mesons and baryons. Radiative decays reveal the structure of hadrons and can be driven by e.g. quantum anomalies and final-state interactions. Measurements of the electromagnetic transition form factors in the low mass, time-like regime can be accessed by Dalitz decays. They enable studies of the evolution of the

transition form factors from the space-like to the time-like region.

The analysis of experimental data on meson decays using the existing and upcoming data sets from Hall D takes advantage of the charged particle and photon detection capabilities of the existing and upgraded GlueX detector and, possibly, dilepton reconstruction. Furthermore, the plan is to study radiative decays of excited hyperons in K_L induced reactions. These studies will concentrate in particular on states with multiple strangeness.

5.2 Polarized Molecules

The development of polarized storage-cell gas-targets like at ANKE or PAX has shown that the polarized hydrogen/deuterium atoms inside can recombine in H_2/D_2 molecules. Depending on the surface materials, the temperature and the magnetic fields the nuclear polarization of the atoms is at least partially preserved in the molecules. In recent experiments a polarized atomic beam source (ABS) was fed with hydrogen and deuterium molecules at the same time. Beside the 'pure' molecules H_2 and D_2 even HD molecules were produced and their polarization was measured with a Lamb-shift polarimeter separately. Depending on the equipment of the transition units of the ABS it is now possible to polarize the hydrogen and deuterium beam atoms independently from each other. Therefore, it is possible to produce the HD molecules in any of the possible spin isomers, i.e. the proton and deuteron spins of the molecule are determined separately. In Fig. 40 a Lyman-spectra of the Lamb-shift polarimeter is shown for HD molecules, when hydrogen atoms in the hyperfine substate $|m_J = +1/2, m_I = -1/2\rangle$ and $| -1/2, -1/2\rangle$ recombine with deuterium atoms in the substates $| +1/2, -1\rangle$ and $| -1/2, -1\rangle$ on a Fomblin surface. Thus, the HD molecules are found in the spin isomer $|m_{I(D)} = -1, m_{I(H)} = -1/2\rangle$ where both spins are anti-parallel to an external magnetic field. In a next step these highly polarized HD molecules will be frozen on a cold surface at the end of the storage cell. As solid ice the polarization lifetime of the HD is known to be very long, i.e. up to years. Thus, the polarized molecules can be collected and stored so that they can be used for further experiments. E.g. polarized HD molecules might be useful for precision spectroscopy of HD^+ ions to avoid the hyperfine broadening in laser spectroscopy or as polarized molecule for the search of the electric dipole moment of both nucleons. Another option is the use of these polarized molecules as target for laser-acceleration experiments to produce polarized proton and deuteron beams in the several MeV range or as polarized fuel for nuclear fusion reactors to increase the energy output.

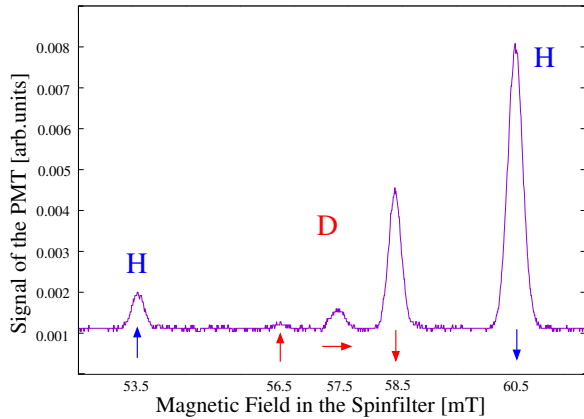


Figure 40: Lyman- α spectrum of HD molecules after recombination on a Fomblin surface. The nuclear polarization deduced from this spectra is $P_z = -0.77 \pm 0.01$ for the proton and $P_z = -0.79 \pm 0.01$ and $P_{zz} = +0.69 \pm 0.01$ for the deuteron in the HD.

5.3 Laser-Plasma Acceleration

Introduction

FZJ is very active in the field of laser-plasma interaction with matter, accommodating local and regional research teams from a wide range of disciplines, including condensed matter physics, materials science, structural biology, accelerator technology, plasma and nuclear physics. The Short-Pulsed Particle and Radiation Center (JuSPARC) will become an interdisciplinary center for collaborative research using ultra-short pulsed photons.

In its first stage, it comprises four driving laser systems, which are outlined in: JuSPARC — The Jülich Short-Pulsed Particle and Radiation Center⁸. The first stage (JuSPARC I), which already started early 2019, produces ultra-short pulsed photons. These beams are generated employing the radiation from a high-power, short-pulse laser using nonlinear up conversion for photon production.

In a second stage, the generation of ultra-short pulsed photons with ultra-high repetition rate and later on with higher energies is planned, including the production and handling of polarized hadron beams. Preparatory work is already performed based on the long-term experience of IKP. FZJ extended his plans in this field under the umbrella of the research and development platform for accelerator technology ATHENA (Accelerator Technology HELmholtz iNfrAstructure).

Experiments with Polarized Beams

One unexplored field of particle acceleration is the motion of particle spins in huge magnetic fields inherently present in relativistic plasmas. In the framework of the

⁸Journal of large-scale research facilities, 6, A138, <http://dx.doi.org/10.17815/jlsrf-6-174>

JuSPARC facility and the ATHENA consortium, Laser-driven generation of polarized proton and ^3He -ion beams in combination with the development of advanced target technologies is being pursued. Novel target technologies will be employed at different laser facilities.

Experiments are in preparation for the PHELIX (Petawatt Hoch-Energie Laser für SchwerIoneneXperimente) laser facility at GSI in Darmstadt and the 10 Petawatt laser facility SULF (Shanghai Super-intense Ultrafast laser Facility). A pre-polarized ^3He gas-jet target will be utilized for the experiments at PHELIX. For the experimental realization of a polarized proton beam in the GeV regime at SULF, a pre-polarized target based on an HCl gas jet is under construction at IKP. Finally, these targets can also be utilized in the future stages of JuSPARC with laser intensities from the roughly hundred Terawatt up to the Petawatt level.

This development is strongly connected to ATHENA_{hadron}: Development of polarized targets for proton and ion acceleration. Besides the FZJ cooperation partner PGI-6, JSC, IKP-2 and IKP-4, also HHU Düsseldorf is involved.

Simulation of Polarized Beam Acceleration

In order to predict the degree of beam polarization from a laser-driven plasma accelerator, particle-in-cell simulations including spin effects have been carried out. For this purpose, the Thomas-BMT equation, describing the spin precession in electromagnetic fields, has been implemented into the VLPL (Virtual Laser Plasma Lab) code from the Institut für Theoretische Physik, HHU Düsseldorf. By implementing spin effects in a 3D-PIC simulation code, theoretical predictions on the proton spin behavior during laser-driven plasma acceleration can be made.

The simulations are carried out on the Jülich supercomputers in close cooperation of IKP-4, PGI-6, JSC and HHU Düsseldorf.

6 Theoretical Investigations

6.1 Introduction

The IKP theory group studies the strong interactions in their various settings — spanning topics in hadron structure and dynamics, the nuclear many-body problem, symmetry tests in Quantum Chromodynamics (QCD), physics beyond the Standard Model and strongly correlated electronic systems. The first focus of the theory group is the formulation and application of effective field theories for precision hadron and nuclear physics based on the symmetries of QCD. The second focus is related to high performance computing in nuclear, hadronic and condensed matter physics, spear-headed by the work on nuclear lattice simulations. Since July 2012, the group is heavily involved in the activities of the collaborative research center “Symmetries and the emergence of

structure in QCD” (CRC 110) together with researchers from Bonn University, TU München, Ruhr-Universität Bochum, IHEP/CAS (Beijing, China), ITP/CAS (Beijing, China) and Peking University (China). This CRC is presently in its second funding period (until 06/2020). Some of the high-lights of these activities are discussed in the following.

6.2 Ab Initio Nuclear Thermodynamics

The equation of state of strongly interacting matter is one of the central topics in contemporary nuclear physics, as it plays an important role in the early universe, heavy-ion reactions and the generation of gravitational waves in violent neutron star mergers. We have performed *ab initio* calculations based on nuclear lattice effective field theory (NLEFT) using a leading-order pionless EFT interaction as used in our study of the essentials of nuclear binding. Despite the simplicity of the interaction, the ground-state energies and charge radii of the light and medium-mass nuclei are well reproduced, as well as the zero-temperature equation of state of pure neutron matter. When applied to zero-temperature neutral symmetric nuclear matter, we obtain $\rho_0 = 0.205 \text{ fm}^{-3}$ and $E/A = -16.9 \text{ MeV}$ at the saturation point. The lattice simulations are performed using auxiliary-field Monte Carlo. In this work, we use a novel algorithm called pinhole trace algorithm (PTA) to efficiently compute the canonical partition function $Z(\beta)$, and the expectation value of any observable O , $Z_O(\beta)$, on the lattice. The pinhole trace algorithm is an extension of the pinhole algorithm introduced in our earlier work to sample the spatial positions and spin/isospin indices of the nucleons. The new feature is that we also perform a quantum mechanical trace over all possible states. In this work we perform simulations on a $6 \times 6 \times 6$ cubic lattice with a spatial lattice spacing $a = 1/150 \text{ MeV}^{-1} = 1.32 \text{ fm}$, such that the corresponding momentum cutoff is $\Lambda = \pi/a \simeq 470 \text{ MeV}$. The temporal lattice spacing is $a_t = 1/2000 \text{ MeV}^{-1}$. We impose twisted boundary conditions along the x -, y - and z - directions. The twist angles are averaged over all possible values by Monte Carlo sampling to remove the fictitious finite-volume shell effect. As the first application of the PTA, we study the nuclear liquid-vapor phase transition by examining the finite-temperature equation of state for symmetric nuclear matter with equal numbers of protons and neutrons and the Coulomb interaction is neglected. In Fig. 41 we present the calculated chemical potential and pressure isotherms. Each point represents a separate simulation. The temperature T covers the range of $10 \text{ MeV} \leq T \leq 20 \text{ MeV}$ and the nucleon number A varies from 4 to 144, which corresponds to densities from 0.008 fm^{-3} to 0.2 fm^{-3} . These settings allow us to explore the whole region relevant to the nuclear matter liquid-vapor phase transition. All the Monte Carlo errors for μ are smaller than 0.02 MeV and not shown explicitly in Fig. 41. Based on the lattice results, we map the whole μ - ρ - T equation of state in this area

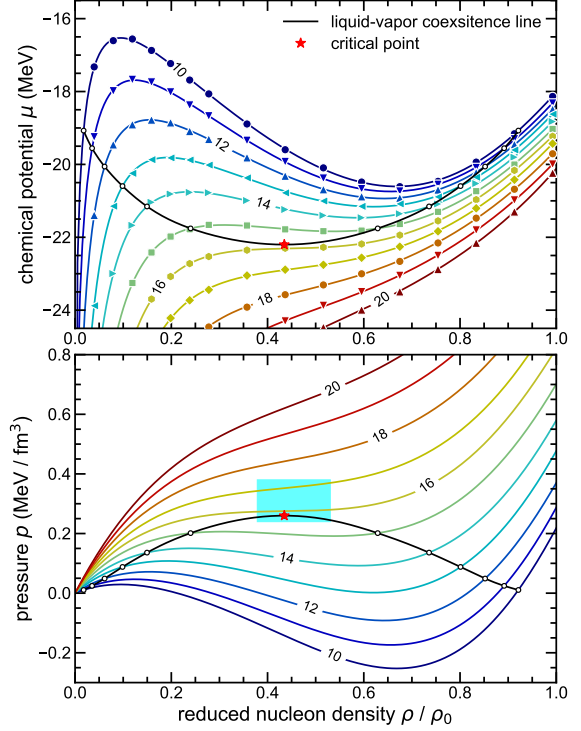


Figure 41: Upper panel: The μ - ρ isotherms of symmetric nuclear matter. The nucleon densities are re-scaled against the saturation density ρ_0 . The symbols represent the lattice results, the error bars are smaller than the symbols. The connecting lines are interpolations. The numbers are the corresponding temperatures. The temperature differences between adjacent isotherms are 1 MeV. The black line denotes the liquid-vapor coexistence line derived from the Maxwell construction. The red star denotes the calculated critical point. Lower panel: The p - ρ isotherms. The cyan square marks the empirical critical point extracted from experiment.

using interpolation. The critical point is then deduced from solving the equations $d\mu/d\rho = d^2\mu/d\rho^2 = 0$. The uncertainties in the critical values are estimated by propagating the simulation and interpolation errors. We found the critical temperature, density, and chemical potential to be $T_c = 15.80(1.6) \text{ MeV}$, $\rho_c = 0.089(18) \text{ fm}^{-3}$, and $P_c = 0.26(3) \text{ MeV/fm}^3$, respectively. The liquid-vapor coexistence line is determined through the Maxwell construction of each isotherm and depicted as a solid black line in Fig. 41. In the lower panel of Fig. 41 we show the deduced p - ρ isotherms, the corresponding liquid-vapor coexistence line and the critical point. The calculated critical pressure is $P_c = 0.260(3) \text{ MeV/fm}^3$. For comparison, we also draw the critical point extracted by analyzing the cluster distributions in heavy-ion collisions. We expect that the quality of both ρ_0 and ρ_c calculations can be improved by including higher-order corrections.

6.3 An Update on Fine-Tunings in the Triple-Alpha Process

The triple-alpha process, whereby evolved stars create carbon and oxygen, is believed to be fine-tuned to a high degree. Such fine-tuning is suggested by the unusually strong temperature dependence of the triple-alpha reaction rate at stellar temperatures. This sensitivity is due to the resonant character of the triple-alpha process, which proceeds through the so-called ‘‘Hoyle state’’ of ^{12}C with spin-parity 0^+ . The Hoyle state is located about 7.7 MeV above the groundstate and just 380 keV above the triple-alpha threshold. The question of fine-tuning can be studied within the *ab initio* framework of nuclear lattice effective field theory, which makes it possible to relate *ad hoc* changes in the energy of the Hoyle state to changes in the fundamental parameters of the nuclear Hamiltonian, which are the average light quark mass m_q and the electromagnetic fine-structure constant. In this work, we have updated the effective field theory calculation of the sensitivity of the triple-alpha process to small changes in these fundamental parameters. This is driven by various recent developments in particle and astrophysics. In particular, we consider recent high-precision lattice QCD calculations of the nucleon axial coupling g_A and its quark mass dependence, various recent simulations of S-wave nucleon-nucleon scattering at unphysical pion masses as well as new and more comprehensive results from stellar simulations of the production of carbon and oxygen, considering also the dependence of element generation on the star’s metallicity Z . While the updated stellar simulations allow for much larger *ad hoc* shifts in the Hoyle state energy than previously thought, see Fig. 42, recent lattice QCD results for the nucleon S-wave singlet and triplet scattering lengths now disfavor the ‘‘no fine-tuning scenario’’ for the light quark mass m_q , see also Fig. 42.

6.4 Implications of an Increased $^3_\Lambda\text{H}$ Binding Energy

Hyperons are possibly a significant component of neutron stars. Their appearance could alter basic properties of neutron stars, e.g. the maximal possible mass. Therefore, the determination of reliable hyperon-nucleon (YN) interactions is currently of very high interest. But the few available ΛN and ΣN scattering data do not allow one to determine the spin and angular dependence of the YN force. Indeed, the binding and excitation energies of hypernuclei are often utilized as further constraints for the determination of YN interactions. One of the most important examples is $^3_\Lambda\text{H}$ which has already been used for many years to fix the relative strength of the ΛN interactions in the $^3\text{S}_1$ and $^1\text{S}_0$ states. Therefore, the STAR collaboration’s new value of the Λ separation energy of $^3_\Lambda\text{H}$ of 410 ± 120 keV has attracted a lot of attention. It is significantly higher than the previously accepted value of 130 ± 50 keV. This motivated us to study the implications of such an increased separation energy for YN in-

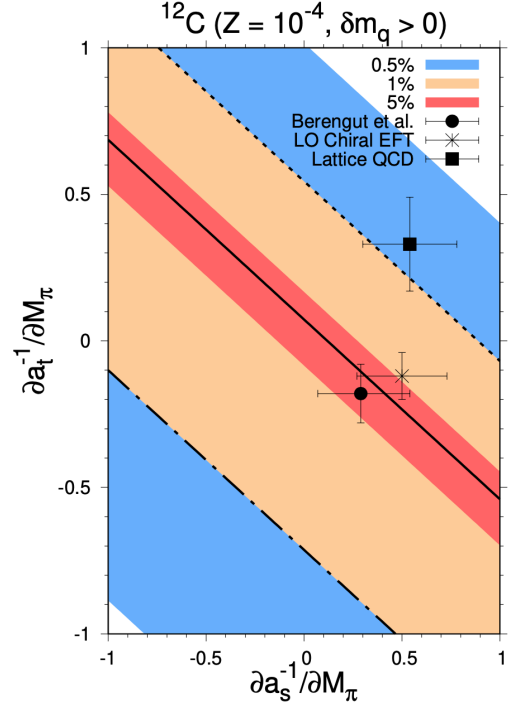


Figure 42: ‘‘Survivability plots’’ based on the new stellar simulations based on the production of ^{12}C in a low metallicity (Z) star. The various bands correspond to changes in the light quark mass by 5%, 1% and 0.5% (inside out), in comparison to a determination from BBN (circle), leading order chiral EFT (cross) and a combination of lattice QCD results (box) for the quark mass dependence of the inverse singlet (s) and triplet (t) NN scattering lengths.

teractions and to predict the consequences for other light hypernuclei.

Based on our next-to-leading-order (NLO) chiral YN interactions, a combined analysis is possible. The interactions are consistent with the symmetries of QCD and describe all available low energy YN data perfectly. With regard to the strength of the Λ - Σ transition, two versions are available, NLO13 and NLO19, and each of them has been realized with four different regulators. These eight parameterizations of the YN force are all equivalent for the ΛN and ΣN systems. Different predictions for hypernuclei therefore indicate the size of possible three-baryon forces (3BF) and are a measure of the theoretical uncertainty. The original implementations are also consistent with the old $^3_\Lambda\text{H}$ separation energy of 130 keV. We could show for the example of NLO19 that the YN forces can be adjusted to accommodate larger $^3_\Lambda\text{H}$ Λ separation energies without compromising the agreement with the YN data. The resulting forces NLO19a, NLO19b and NLO19c lead to an increased magnitude of the $^1\text{S}_0$ ΛN scattering length of -4.0 fm, -4.5 fm and -5.0 fm, respectively. The predictions for the $^3_\Lambda\text{H}$ Λ separation between 280 and 470 keV also encompass the new STAR measurement.

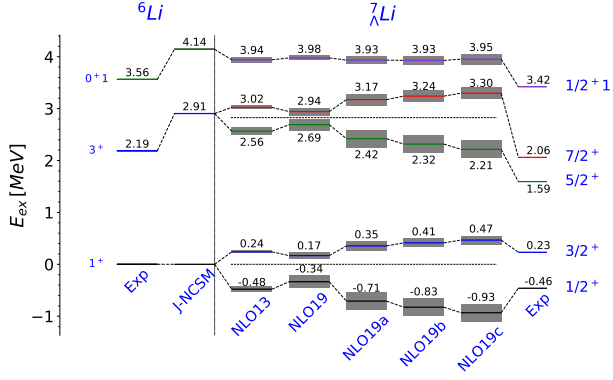


Figure 43: Comparison of the excitation spectrum of ${}^7_\Lambda\text{Li}$ using different YN interactions. The uncertainties are indicated by the grey bands. The dashed lines show the centroids for each spin doublet.

We then used the interactions to predict separation energies for ${}^4_\Lambda\text{He}$. Interestingly, the increase in the magnitude of the 1S_0 scattering length led to an increased Λ separation energy for the 0^+ state but to a decrease of the 1^+ state which improves the agreement with the empirical values.

For systems with more than four baryons, we rely on the Jacobi-no core shell model (J-NCSM) and similarity renormalization group (SRG) evolved interactions. These are again equivalent for the YN systems. The major part of the 3BFs due to SRG can be taken into account by employing SRG such that ${}^5_\Lambda\text{He}$ is correctly predicted. In Fig. 43, we compare our results for the excitation spectrum of ${}^7_\Lambda\text{Li}$. Clearly, the doublet spacings are increased. Surprisingly, the centroids of the doublets are not affected by the changes. Similarly to the ground state separation energy of ${}^7_\Lambda\text{Li}$, the modified interactions slightly impairs the agreement of the doublet spacings with experiment. Nevertheless, our results show that an increased hypertriton binding energy can be consistent with the binding energies of other light hypernuclei.

The work exemplifies that the Jacobi-NCSM allows us to analyse separation energies for several hypernuclei including also YN data. With the expected new experimental results at FAIR, J-PARC, Jlab and other facilities, we will therefore be able to devise realistic and reliable YN interactions.

6.5 Refined Predictions for the Spin Partners of the $Z_b(10610)$ and $Z_b(10650)$

Amongst the large number of states found recently in spectroscopy studies in the heavy quarkonium mass ranges charged states that decay into final states containing a heavy quark and a heavy antiquark are special, since they contain at least four quarks. In the recent years our group studied $Z_b(10610)$ and $Z_b(10650)$, isovector $J^{PC} = 1^{+-}$ states, located very close to the $B\bar{B}^*$ and

$B^*\bar{B}^*$ threshold, respectively, in great detail employing an effective field theory designed analogously to what is used in the two-nucleon sector. This treatment calls for the inclusion of the one-pion exchange (OPE) and two momentum-independent counter terms at leading order. A study of the Z_b line shapes revealed, however, some unexpected features:

- While in the two nucleon system the static OPE is a good approximation, in the doubly heavy sector retardation effects are potentially significant.
- For energies near the $B^*\bar{B}^*$ threshold, the relative momentum in the $B\bar{B}^*$ system is about 500 MeV overcoming the usual suppression of D -waves.
- The data does not show any signature of a transition of the $Z_b(10650)$ to the $B\bar{B}^*$ channel.

Especially the last item appears to be irritating, since the OPE induces a strong $B^*\bar{B}^*(S) \rightarrow B\bar{B}^*(D)$ transition that leaves a sizeable structure in the data that cannot be absorbed into the leading order counter terms. Moreover, the very same transition shows a strong dependence on the regulator employed to render the Lippman Schwinger Equation well defined. The latter observation calls for promoting an $S - D$ counter term to leading order. Once this is done both problems just mentioned get solved: We get an excellent description of the data and all regulator dependence is gone. The corresponding fit is called fit 1 below. Moreover, we found that the inclusion of momentum-dependent $S - S$ counter terms as well as the η -exchange did not modify the pole locations significantly. This fit is called fit 2 in what follows.

While the main effect of the pion exchange gets largely reduced by promoting the $S - D$ counter term, the OPE still leaves an imprint in observables. Since the $S - D$ transitions effectively induce a strong momentum dependence into the interaction, contrary to expectations now two-hadron resonances can also appear closely above a threshold. This happened in our analysis not only for the $Z_b(10650)$ but especially for the siblings of the Z_b states, the so-called W_{bJ} ($J = 0, 1, 2$) states: These are spin symmetry partners of the Z_{bS} with quantum numbers J^{++} . As an example in Fig. 44 we show our predictions for the line shapes of the W_{b0} states, the higher (lower) one being a member of the same spin multiplet as the $Z_b(10650)$ ($Z_b(10610)$). The poles of fit 1 (fit 2), in the figure shown as red (black) solid line, are for the lower W_{b0} ($-8.5 \pm 2.8 + i(1.5 \pm 0.2)$) ($(2.3 \pm 4.2) - i(16 \pm 3)$) MeV and for the higher one ($-1.2 \pm 0.1 - i(0.7 \pm 0.3)$) ($(-1.3 \pm 0.4) - i(1.7 \pm 0.5)$) MeV relative to the $B\bar{B}$ and the $B^*\bar{B}^*$ threshold, respectively. Experimentally the W_{bJ} states can be searched for at Belle II in radiative decays of excited vector bottomonia. Such a test of the theoretical predictions is feasible and will provide deeper insights into how QCD forms multi-quark states.

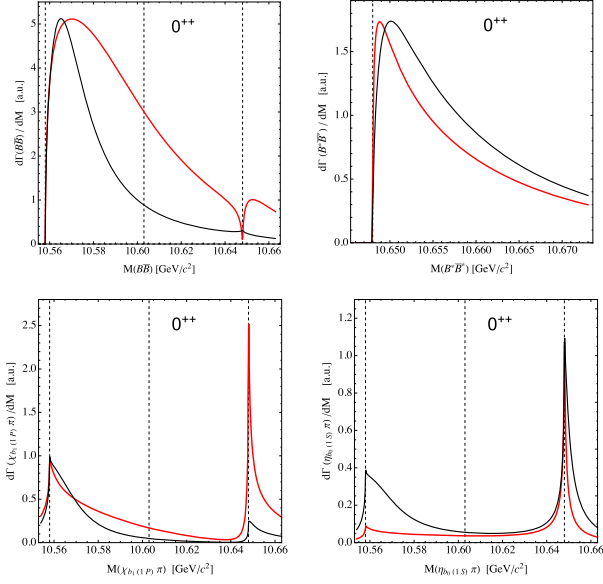


Figure 44: Predicted line shapes in the 0^{++} channel. Upper panel: The line shapes in the $B\bar{B}$ and $B^*\bar{B}^*$ channels. Lower panel: The line shapes in the $\chi_{b1}(1P)\pi$ and $\eta_b(1S)\pi$ channels. The red and black lines show the results for the fits 1 and 2, respectively, and the vertical dashed lines indicate the position of the $B\bar{B}$, $B\bar{B}^*$ and $B^*\bar{B}^*$ thresholds.

6.6 Kaon Photoproduction and the Λ Decay Parameter α_-

The asymmetry parameter α_- of the weak decay $\Lambda \rightarrow p\pi^-$ is a fundamental quantity in hadron physics. Its actual value plays a key role in the exploitation of the so-called self-analyzing nature of the Λ decay for determining its polarization in experiments. Due to parity violation the decay $\Lambda \rightarrow p\pi^-$ is not isotropic but correlated to its spin and exhibits an angular distribution of the form $I(\theta) \propto 1 + \alpha_- P \cos\theta$, with P being the polarization of the Λ . Thus, a measurement of the distribution allows one to determine that polarization, provided that α_- is known. Clearly any revision of α_- implies automatically a change in the deduced value for P , for all past experiments. Additionally, in combination with α_+ from $\bar{\Lambda}$ decay α_- provides a measure for matter-antimatter asymmetry. Finally, the weak decay parameter also affects the decay parameters of the Ξ and Ω baryons.

The actual value of α_- as given by the Particle Data Group (PDG), 0.642(13), seemed to be well established. Indeed, it had been accepted and used for over 40 years. However, recently the BESIII collaboration reported a new value, which is with 0.750(9)(4) some 17 % higher than the previous one. It was extracted from an analysis of the angular distributions of the Λ (and $\bar{\Lambda}$) decay in the reaction $J/\psi \rightarrow \Lambda\bar{\Lambda}$.

This sizable and certainly unexpected change motivated us to investigate whether a larger value for α_- as sug-

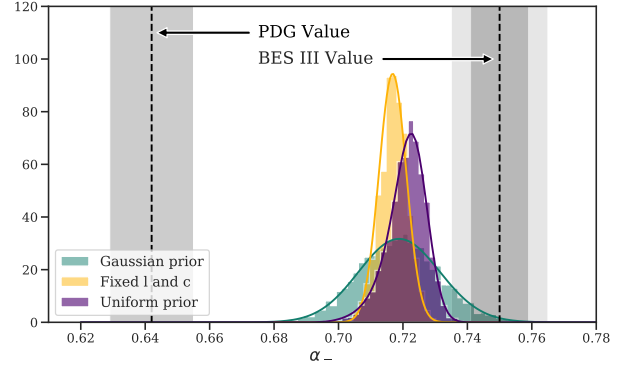


Figure 45: Results for α_- based on our statistical analysis, for different assumptions (priors) on the beam polarization calibration. Dark grey vertical bands represent statistical uncertainty; the additional light grey bands on the BESIII result represent systematic uncertainty.

gested by the BESIII analysis is supported by other and independent experimental information too. Clearly, an independent determination of the asymmetry parameter would be highly desirable. With that aim in mind we examined the reaction $\gamma p \rightarrow K^+\Lambda$ where extensive measurements of various polarization observables have been presented recently by the CLAS Collaboration at JLab. In this case one can make use of identities that connect the polarization observables for pseudoscalar meson photoproduction, known as the ‘‘Fierz identities’’. These identities allow one to determine not only the polarization observables but also α_- from a careful analysis of the angular distributions.

The value for α_- obtained in our study is 0.721(6)(5). The result is corroborated by multiple statistical tests, see Fig. 45, showing that our new value yields the best description of the data in question. Obviously our analysis supports the new BESIII finding that α_- is significantly larger than the previous PDG value. Any experimental quantity relying on the value of α_- should therefore be re-considered.

6.7 Addressing Ergodicity Issues in Low-Dimensional Lattice Calculations

The Hubbard model arises naturally when electron-electron interactions are added to the tight-binding descriptions of many condensed matter systems. For instance, the two-dimensional Hubbard model on the honeycomb lattice is central to the *ab initio* description of the electronic structure of carbon nanomaterials, such as graphene. Such low-dimensional Hubbard models are advantageously studied with Markov chain Monte Carlo methods, such as Hybrid Monte Carlo (HMC). HMC is the standard algorithm of the lattice gauge theory community, as it is well suited to theories of dynamical fermions. As HMC performs continuous, global updates

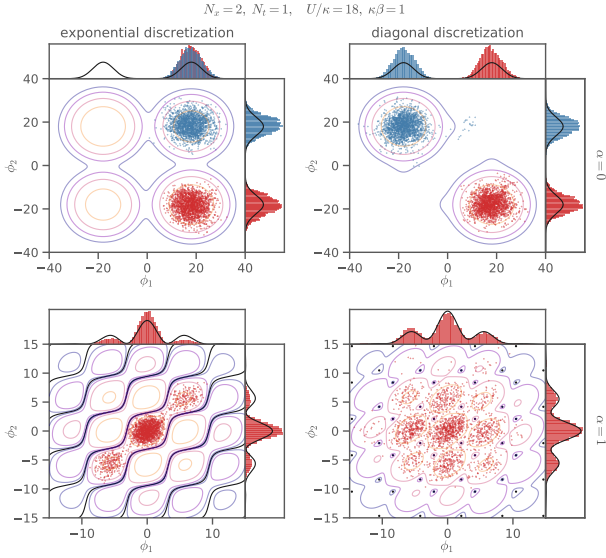


Figure 46: Examples of different discretizations (exponential vs. diagonal, $\alpha = 0, 1$) and the generated background fields via HMC. Blue and red points correspond to different HMC runs. With the exception of the lower right panel, all others show HMC generated results that are “trapped”, and thus ergodicity was violated. The results from the lower right panel, exhibiting no ergodicity violations, were obtained from a fermion operator developed by researchers of IAS-4/IKP-3.

of the lattice degrees of freedom, it provides superior scaling with system size relative to local updating methods. A potential drawback of HMC is its susceptibility to ergodicity problems due to so-called exceptional configurations, for which the fermion operator cannot be inverted. This causes the distribution of generated background fields during an HMC simulation to become very multi-modal, with each mode largely separated from one another. Domain walls can also occur that separate out different topologically distinct regions of the background field (see Fig. 46). Either situation requires exponential time for HMC to “tunnel” between the modes, which leads to an ergodicity problem. Therefore the Markov chain cannot probe all relevant regions of phase space, and this in turn makes observables calculated from Monte Carlo suspect. Indeed, such ergodicity problems have been found in certain formulations of HMC simulations of the Hubbard model, and this has led to an “abandonment” of HMC in the condensed matter community in favour of algorithms that utilize simpler local sampling schemes but have much weaker scaling to avoid ergodicity issues.

By analyzing the symmetries of the two-dimensional system in detail, members of IAS-4/IKP-3 have addressed this issue of ergodicity directly and clarified under what conditions ergodicity is maintained or violated in HMC simulations of the Hubbard model. In particular, they studied how different lattice formulations of the fermion operator lead to ergodicity issues, and how others avoided

it. Here the geometry and symmetry of the system and its discretization played key roles. Somewhat counterintuitively, it was determined that ergodicity became violated in discretizations with *more* symmetry.

The gained insight into the relationship between ergodicity violation and the symmetries of the system allowed the researchers to formulate a fermion operator which is both computationally convenient and free of ergodicity problems, albeit lacking some of the full symmetries of the original system. However, the researchers also devised a new form of HMC, one that employs “ergodicity jumps” between the largely separated modes, enabling all modes to be sampled with their correct respective weights. This form of HMC allowed them to use the original fully symmetric fermion operator without any ergodicity violations, and in addition retain the superior scaling with system size.

A Beam Time at COSY in 2019

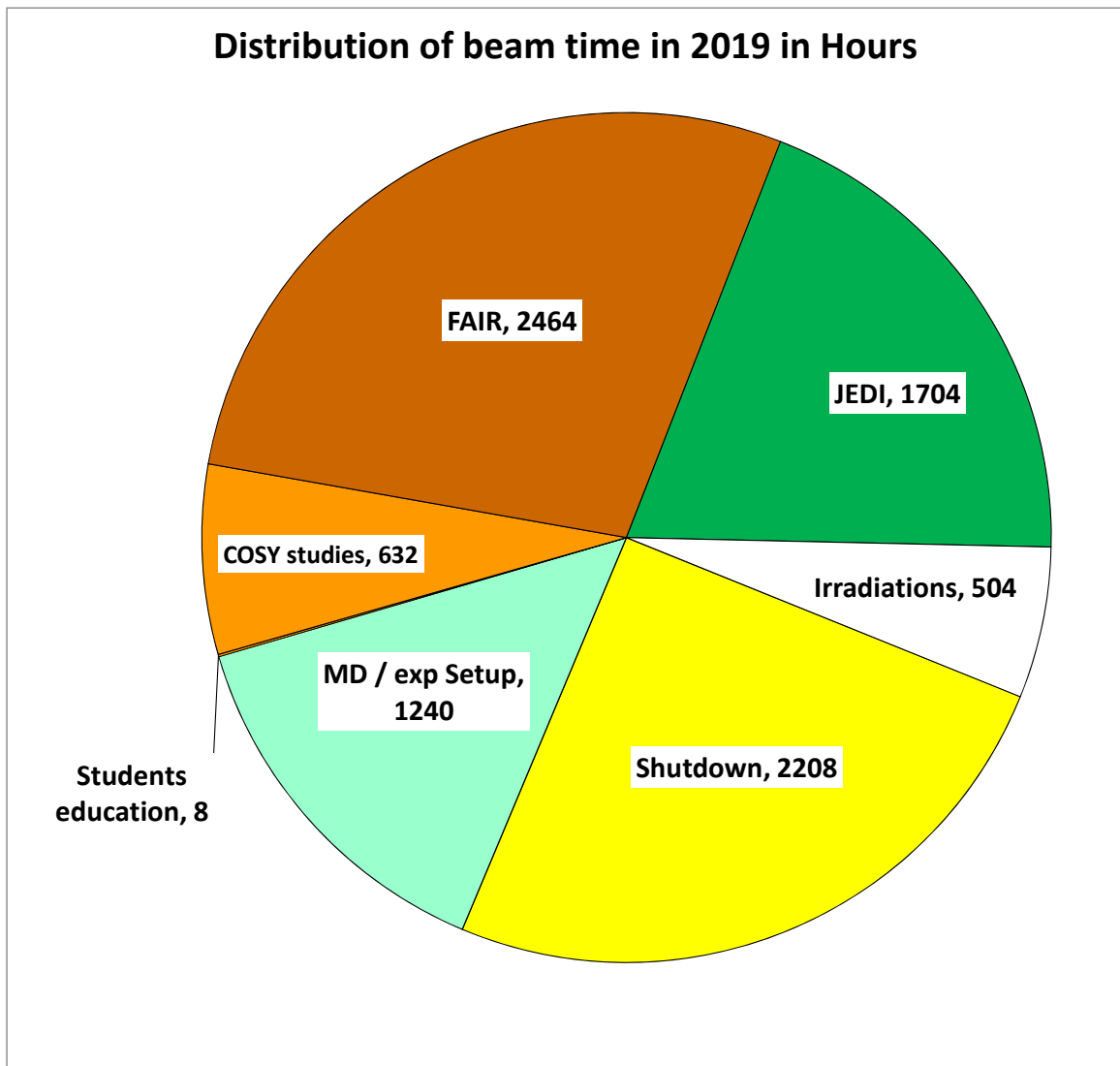


Figure 47: COSY beam-time statistics in 2019.

The distribution of user weeks and maintenance/shutdown periods is listed in Table 2.

Table 2: Overview COSY user beam time and EDM/FAIR weeks in 2019.

Date	Experiment	Duration	Reaction, experiment #
1.01.19.–20.01.19	Maintenance	3 weeks	
28.01.–03.02.	COSY	1 week	beam optics studies, Exp. A005.4
04.02.–10.02.	EDM (JEDI)	1 week	JEDI beam based alignment, Exp. A015
18.02.–24.02.	FAIR (STT)	1 week	FAIR straw tube tracker, Exp. D002.3
04.03.–10.03.	FAIR (KOALA)	1 week	FAIR KOALA, Exp. D005.2
11.03.–17.03.	FAIR (Clust.)	1 week	FAIR Cluster Jet Target, Exp. D009
18.03.–31.03.	Maintenance	2 weeks	
08.04.–28.04.	EDM (JEDI)	3 weeks	EDM Spin dyn. & Axion EDM, Exp. E007.1 & E008.1
06.05.–12.05.	EDM (JEDI)	1 week	EDM Polarimetry, Exp. E002.6
20.05.–26.05.	FAIR (CBM)	1 week	CBM measurements COSY Exp. D004.6
03.06.–09.06.	COSY	1 week	beam optics studies, Exp. A005.4
10.06.–16.06.	COSY	1 week	Orbit feedback, Exp. A014.1
17.06.–04.08.	Maintenance	7 weeks	
24.06.–30.06.	HBS	1 week	HBS Exp. A010.5 (within Maintenance)
12.08.–18.08.	COSY	1 week	stochastic cooling, Exp. A001.8
19.08.–25.08.	FAIR (Clust.)	1 week	FAIR Cluster Jet Target, Exp. D009.3
26.08.–01.09.	FAIR (KOALA)	1 week	FAIR KOALA, Exp. D005.2
04.09.–06.09.	COSY	3 days	RWTH students education
09.09.–15.09.	FAIR (Lumi)	1 week	FAIR Luminosity, Exp. D011
16.09.–22.09.	HBS	1 week	High Brilliance Source HBS, Exp. A013.1
23.09.–13.10.	EDM (JEDI)	3 weeks	JEDI beam based alignment, Exp. A015.1
21.10.–27.10.	EDM (JEDI)	1 week	EDM Polarimetry, Exp. E002.7
04.11.–10.11.	FAIR (CBM)	1 week	CBM measurements COSY Exp. D004.7
18.11.–24.11.	COSY	1 week	stochastic cooling, Exp. A001.9
25.11.–01.12.	COSY	1 week	electron cooling, Exp. A002.6
02.12.–08.12.	FAIR (KOALA)	1 week	FAIR KOALA, Exp. D005.3
09.12.–15.12.	COSY	1 week	Radiation hardness measurements, D012
16.12.–31.12.	Maintenance	2 weeks	
user weeks 2019		26 weeks	
maintenance		14 weeks	
EDM		9 weeks	
FAIR		9 weeks	

B Committees

B.1 CBAC – COSY Beam Time Advisory Committee

Prof. K. Aulenbacher	Universität Mainz, Germany
Prof. O. Kester	TRIUMF, Canada
Prof. C.J. Schmidt	GSI Darmstadt, Germany
Prof. T. Stöhlker	HI-Jena, Jena, Germany
Prof. M. Weber (chair)	KIT, Karlsruhe, Germany

B.2 Committee Service

O. Felden	- WTR (Scientific and Technical Council), FZ-Jülich GmbH, Germany
F. Goldenbaum	- Chair of the PANDA at FAIR collaboration board
	- WTR (Scientific and Technical Council), FZ-Jülich GmbH, Germany
	- Scientific Secretary of COSY Beam Advisory Committee (CBAC), FZ-Jülich GmbH, Germany
J. Haidenbauer	- Theory advisory Group PANDA
C. Hanhart	- Theory advisory Group PANDA
	- Particle Data Group
R. Gebel	- International Organising Committee of the 22nd International Conference on Cyclotrons and their Applications CYC2019 in Cape Town, South Africa
V. Hejny	- WTR (Scientific and Technical Council), FZ-Jülich GmbH, Germany
A. Lehrach	- Institutional representative in the European Network for Novel Accelerators (EuroNNAc)
	- Coordination, support and enhancement of training activities for accelerators in Europe in the EU-Projekt ARIES (Accelerator Research and Innovation for European Science and Society)
	- International Advisory Committee of the 4th European Advanced Accelerator Concepts Workshop (EAAC2019), La Biodola Bay, Isola d'Elba, Italy
	- Subtopic Speaker of the HGF Programme "Matter and Technologies", Accelerator Research and Development (ARD), Subtopic 2
	- Member of the Management, Topic ARD, HGF Programme "Matter and Technologies"
	- Member of the JuDocs Council, FZ-Jülich GmbH, Germany
U.-G. Meißner	- Selection Committee for the Chinese participants of the Lindau Noble Prize Winners meeting, DFG & NSFC
	- Scientific Advisory Committee of the Collaborative Research Center (SFB) 1245, "Nuclei: From fundamental interactions to structure and stars", TU Darmstadt
	- German/DFG delegate of NuPECC
	- Project coordinator, Regional Doctoral Program in Theoretical and Experimental Particle Physics (Bonn, Jülich, Siegen Tiflis, Yerevan), funded by Volkswagen Stiftung
	- Spokesperson of the Collaborative Research Center SFB/TR-110 "Symmetries and the Emergence of Structure in QCD"
	- Theory advisory Group PANDA
	- Particle Data Group
A. Nogga	- WTR (Scientific and Technical Council), FZ-Jülich GmbH, Germany
D. Prasuhn	- International Advisory Committee of the COOL Conferences (Beam Cooling)
J. Ritman	- Co-Chair of the MESON biannual conference series
	- Chair of the Scientific Advisory Committee for FAIR-CZ
S. Schadmand	- Jefferson Lab User Organization (JLUO) Board of Directors
	- Workshop Program Committee of the APS Topical Group on Hadronic Physics (GHP)

- R. Stassen - Member of the Machine Advisory Committee for NICA (Nuclotron-based Ion Collider fAcility), Joint Institute for Nuclear Research (JINR), Dubna, Russia
- T. Stockmanns - Computing coordinator PANDA
- H. Ströher - IAB KIU (Int. Advisory Board Kutaisi Int. University, Georgia)
 - ISPC (Int. Spin Physics Committee)
 - NuPECC (Nuclear Physics European Collaboration Committee)

C Publications – Journal Articles

1. Y. Ünal and U. Meißner
Chiral constraints on the isoscalar electromagnetic spectral functions of the nucleon from leading order vector meson couplings
Phys. Lett. B **794** 103 - 108 (2019)
2. Y. Ünal and U. Meißner
A note on scalar meson dominance
Chinese Phys. C **43** 103105 - (2019)
3. N.R. Acharya *et al.*
Constraints on disconnected contributions in $\pi\pi$ scattering
J. High Energ. Phys. **2019** 165 (2019)
4. P. Adlarson *et al.*
Examination of the production of an isotensor dibaryon in the $pp \rightarrow pp\pi^+\pi^-$ reaction
Phys. Rev. C: Nucl. Phys. **99** 025201 (2019)
5. A. Agadjanov, U. Meißner and A. Rusetsky
Nucleon in a periodic magnetic field: Finite-volume aspects
Phys. Rev. D **99** 054501 (2019)
6. M. Agostini *et al.*
Simultaneous precision spectroscopy of p p , Be 7 , and p e p solar neutrinos with Borexino Phase-II
Phys. Rev. D **100** 082004 (2019)
7. M. Agostini *et al.*
Modulations of the cosmic muon signal in ten years of Borexino data
J. Cosmol. Astropart. P. **2019** 046 - 046 (2019)
8. D. Alfs *et al.*
Drift chamber calibration and particle identification in the P-349 experiment
Eur. Phys. J. Web of Conferences **199** 05017 - (2019)
9. D. Alfs *et al.*
Design of a detector to study $S = -2$ baryon interactions induced by stopped antiproton annihilation
Eur. Phys. J. Web of Conferences **199** 05023 - (2019)
10. M.N. Anwar, Y. Lu and B. Zou
 $\chi_b(3P)$ multiplet revisited: Hyperfine mass splitting and radiative transitions
Phys. Rev. D **99** 094005 (2019)
11. V. Baru *et al.*
Remarks on the heavy-quark flavour symmetry for doubly heavy hadronic molecules
Eur. Phys. J. C **79** 46 (2019)
12. V. Baru *et al.*
Spin partners $W b J$ from the line shapes of the $Z_b (10610)$ and $Z_b (10650)$
Phys. Rev. D **99** 094013 (2019)
13. M. Burrows *et al.*
Ab initio folding potentials for nucleon-nucleus scattering based on no-core shell-model one-body densities
Phys. Rev. C: Nucl. Phys. **99** 044603 (2019)
14. M. Büscher *et al.*
Polarized proton beams from a laser-plasma accelerator
Int. J. Mod. Phys. A **34** 1942028 - (2019)
15. Q.B. Chen *et al.*
Behavior of the collective rotor in nuclear chiral motion
Phys. Rev. C: Nucl. Phys. **99** 064326 (2019)

16. L. Dai *et al.*
A Study on the Correlation Between Poles and Cuts in $\pi\pi$ Scattering
Commun. Theor. Phys. **71** 1309 - (2019)
17. V. Dallas *et al.*
Bifurcations between turbulent states in a two-dimensional shear flow
Phys. Rev. Fluids **1** 19 (2019)
18. D. Djukanovic, J. Gegelia and U. Meißner
Derivation of spontaneously broken gauge symmetry from the consistency of effective field theory II: Scalar field self-interactions and the electromagnetic interaction
Phys. Lett. B **788** 436 - 441 (2019)
19. M. Du, F. Guo and U. Meißner
Implications of chiral symmetry on S -wave pionic resonances and the scalar charmed mesons
Phys. Rev. D **99** 114002 (2019)
20. M. Durante *et al.*
All the fun of the FAIR: fundamental physics at the facility for antiproton and ion research
Phys. Scr. **94** 033001 - (2019)
21. I. Engin *et al.*
Laser-induced acceleration of Helium ions from unpolarized gas jets
Plasma Phys. Contr. F. **61** 115012 (2019)
22. E. Epelbaum *et al.*
Few- and many-nucleon systems with semilocal coordinate-space regularized chiral two- and three-body forces
Phys. Rev. C: Nucl. Phys. **99** 024313 (2019)
23. E. Epelbaum *et al.*
Reply to the Comment by Manuel Pavon Valderrama on “How (not) to renormalize integral equations with singular potentials in effective field theory”
Eur. Phys. J. A **55** 56 (2019)
24. J. Ferretti *et al.*
The baryo-quarkonium picture for hidden-charm and bottom pentaquarks and LHCb Pc(4380) and Pc(4450) states
Phys. Lett. B **789** 562 - 567 (2019)
25. J. Gegelia and U. Meißner
Vacuum energy in the effective field theory of general relativity
Phys. Rev. D **100** 046021 (2019)
26. J. Gegelia and U. Meißner
Vacuum energy in the effective field theory of general relativity. II. Inclusion of fermions and a comment on the QCD contribution
Phys. Rev. D **100** 124002 (2019)
27. K. Grigoryev *et al.*
Electrostatic deflector studies using small-scale prototype electrodes
Rev. Sci. Instrum. **90** 045124 - (2019)
28. D. Grzonka *et al.*
Search for polarized antiproton production
Hyperfine Interact. **240** 22 (2019)
29. D. Grzonka *et al.*
Polarization analysis of \bar{p} produced in pA collisions
Eur. Phys. J. Web of Conferences **199** 05013 - (2019)
30. Y. Guan *et al.*
Observation of Transverse $\Lambda/\bar{\Lambda}$ Hyperon Polarization in e^+e^- Annihilation at Belle
Phys. Rev. Lett. **122** 042001 (2019)

31. F. Guo *et al.*
Isospin breaking decays as a diagnosis of the hadronic molecular structure of the P_c (4457)
Phys. Rev. D **99** 091501 (2019)
32. Z. Guo *et al.*
Towards a precise determination of the scattering amplitudes of the charmed and light-flavor pseudoscalar mesons
Eur. Phys. J. C **79** 13 (2019)
33. J. Haidenbauer and U. Meißner
In-medium properties of a ΞN interaction derived from chiral effective field theory
Eur. Phys. J. A **55** 23 (2019)
34. J. Haidenbauer and U. Meißner
Phenomenological view on baryon-baryon potentials from lattice QCD simulations
Eur. Phys. J. A **55** 70 (2019)
35. J. Haidenbauer
Coupled-channel effects in hadron-hadron correlation functions
Nucl. Phys. A **981** 1 - 16 (2019)
36. L. Hlophe *et al.*
Deuteron- α scattering: Separable versus nonseparable Faddeev approach
Phys. Rev. C: Nucl. Phys. **100** 034609 (2019)
37. A. Hützen *et al.*
Polarized proton beams from laser-induced plasmas
High Power Laser Sci. Eng. **7** e16 (2019)
38. D.G. Ireland *et al.*
Kaon Photoproduction and the Λ Decay Parameter α_{-}
Phys. Rev. Lett. **123** 182301 (2019)
39. L. Jokhovets *et al.*
Improved Rise Approximation Method for Pulse Arrival Timing
IEEE T. Nucl. Sci. **66** 1942 - 1951 (2019)
40. A.B. Kaliyar *et al.*
Measurements of branching fraction and direct C P asymmetry in $B^{\pm} \rightarrow K_S^0 K_S^0 K^{\pm}$ and a search for $B^{\pm} \rightarrow K_S^0 K_S^0 \pi^{\pm}$
Phys. Rev. D **99** 031102 (2019)
41. B. Kardan, HADES Collaboration and J. Ritman
Collective flow and correlations measurements with HADES in Au+Au collisions at 1.23 AGeV
Nucl. Phys. A **4** 431-434 (2019)
42. J.B. Kim *et al.*
Search for C P violation with kinematic asymmetries in the $D^0 \rightarrow K^+ K^- \pi^+ \pi^-$ decay
Phys. Rev. D **99** 011104 (2019)
43. E. Kou *et al.*
The Belle II Physics Book
Prog. Theor. Exp. Phys. **2019** 123C01 (2019)
44. H. Krebs, E. Epelbaum and U. Meißner
Nuclear Electromagnetic Currents to Fourth Order in Chiral Effective Field Theory
Few-body systems **60** 31 (2019)
45. S. Krieg *et al.*
Accelerating Hybrid Monte Carlo simulations of the Hubbard model on the hexagonal lattice
Comput. Phys. Commun. **236** 15-25 (2019)
46. P. Lenisa *et al.*
Low-energy spin-physics experiments with polarized beams and targets at the COSY storage ring
Eur. Phys. J. Techn. Instrum. **6** 2 (2019)

47. N. Li *et al.*
Galilean invariance restoration on the lattice
Phys. Rev. C: Nucl. Phys. **99** 064001 (2019)
48. Y.B. Li *et al.*
First Measurements of Absolute Branching Fractions of the Ξ_c^0 Baryon at Belle
Phys. Rev. Lett. **122** 082001 (2019)
49. B. Lu *et al.*
Essential elements for nuclear binding
Phys. Lett. B **797** 134863 - (2019)
50. P. Lu *et al.*
Observation of $B^+ \rightarrow p\bar{\Lambda}K^+K^-$ and $B^+ \rightarrow \bar{p}\Lambda K^+K^+$
Phys. Rev. D **99** 032003 (2019)
51. L. Ma, Q. Wang and U. Meißner
Double heavy tri-hadron bound state via delocalized π bond
Chinese Phys. C **43** 014102 - (2019)
52. L. Ma, Q. Wang and U. Meißner
Trimeson bound state $B B B^*$ via a delocalized π bond
Phys. Rev. D **100** 014028 (2019)
53. U. Meißner
Charmante Verletzung
Phys. J. **18** 22 (2019)
54. J. Pang *et al.*
Energy shift of the three-particle system in a finite volume
Phys. Rev. D **99** 074513 (2019)
55. J. Ritman and H. Ströher
Precision resonance energy scans with the PANDA experiment at FAIR – Sensitivity study for width and line-shape measurements of the X(3872)
Eur. Phys. J. A **55** 42 (2019)
56. W. Schott *et al.*
Towards a first measurement of the free neutron bound beta decay detecting hydrogen atoms at a through-going beamtube in a high flux reactor
Eur. Phys. J. Web of Conferences **219** 04006 (2019)
57. C. Seng and U. Meißner
Toward a First-Principles Calculation of Electroweak Box Diagrams
Phys. Rev. Lett. **122** 211802 (2019)
58. I.S. Seong *et al.*
Search for a Light $C P$ -odd Higgs Boson and Low-Mass Dark Matter at the Belle Experiment
Phys. Rev. Lett. **122** 011801 (2019)
59. D. Severt, U. Meißner and J. Gegelia
Flavor decomposition of the pion-nucleon σ -term
J. High Energ. Phys. **2019** 202 (2019)
60. B. Singh *et al.*
Technical design report for the \bar{P} ANDA Barrel DIRC detector
J. Phys. G **46** 045001 - (2019)
61. V. Tselyaev *et al.*
Low-energy $M 1$ excitations in $Pb 208$ and the spin channel of the Skyrme energy-density functional
Phys. Rev. C: Nucl. Phys. **99** 064329 (2019)
62. T. Vonk, F. Guo and U. Meißner
Aspects of the QCD Θ -vacuum
J. High Energ. Phys. **2019** 106 (2019)

63. S. Watanuki *et al.*
Measurements of isospin asymmetry and difference of direct C P asymmetries in inclusive $B \rightarrow X_s \gamma$ decays
Phys. Rev. D **99** 032012 (2019)
64. M.K. Weikum *et al.*
EuPRAXIA - a compact, cost-efficient particle and radiation source
AIP Conf. Proc. **2160(1)** 040012 (2019)
65. H. Witała *et al.*
Application of Semilocal Coordinate-Space Regularized Chiral Forces to Elastic Nd Scattering and Breakup
Few-body systems **60** 19 (2019)
66. J. Wynen *et al.*
Avoiding ergodicity problems in lattice discretizations of the Hubbard model
Phys. Rev. B **100** 075141 (2019)
67. Y. Yusa *et al.*
Measurement of time-dependent C P violation in $B^0 \rightarrow K_s^0 \pi^0 \pi^0$ decays
Phys. Rev. D **99** 011102 (2019)

D Talks and Colloquia

D.1 Conference and Workshop Contributions

1. F. Abusaif
Development of beam position monitors for storage rings
DPG spring meetings, München 2019, München, Germany: 2019-03-17 - 2019-03-22
2. M. Agostini *et al.*
Solar Neutrino Results and Future Opportunities with Borexino
XIII International Conference on Beauty, Charm and Hyperon Hadrons, Lisbon, Portugal: 2018-06-17 - 2018-06-23
3. D. Alfs, D. Grzonka and J. Ritman
Status of the analysis for the search of polarization in the antiproton production process
DPG-Frühjahrstagung, München, Germany: 2019-03-17 - 2019-03-22
4. Z. Bagdasarian
Borexino: Latest Results and Future Opportunities
Lomonosov Conference on Elementary Particle Physics, Moscow, Russia: 2019-08-22 - 2019-08-28
5. Z. Bagdasarian
Borexino''s guide into the solar core and neutrinos
Deutschen Physikalischen Gesellschaft Spring Meeting, Aachen, Germany: 2019-03-25 - 2019-03-29
6. J. Baggemann *et al.*
Internally-cooled target design to achieve high power density in a CANS target
International Meeting of the Union for Compact Accelerator-driven Neutron Sources, Paris, France: 2019-07-08 - 2019-07-11
7. V. Baru *et al.*
Properties of $Z_b(10610)$ and $Z_b(10650)$ from an analysis of experimental line shapes
9th International Workshop on Charm Physics, Novosibirsk, Russia: 2018-05-21 - 2018-05-25
Eur. Phys. J. Web of Conferences 202 06012 -
8. V. Baru *et al.*
Exotic molecular states in the decays of vector bottomonia
The 12th International Workshop on e^+e^- Collisions from Phi to Psi, Novosibirsk, Russia: 2019-02-25 - 2019-03-01
Eur. Phys. J. Web of Conferences 212 02002 -
9. V. Baru *et al.*
Heavy-quark spin-symmetry partners of $Z_b(10610)$ and $Z_b(10650)$ molecules
International Workshop on e^+e^- Collisions from Phi to Psi, Mainz, Germany: 2017-06-26 - 2017-06-29
Eur. Phys. J. Web of Conferences 218 08005 -
10. V. Baru, C. Hanhart and A.V. Nefediev
X(3915) as a tensor $D^*\bar{D}^*$ molecule
International Workshop on e^+e^- Collisions from Phi to Psi, Mainz, Germany: 2017-06-26 - 2017-06-29
Eur. Phys. J. Web of Conferences 218 08004 -
11. T. Brückel *et al.*
The High Brilliance Neutron Source (HBS) Project
International Meeting of the Union for Compact Accelerator-driven Neutron Sources, Paris, France: 2019-07-08 - 2019-07-11
12. P. Doege *et al.*
Target Concept for the High Brilliance Neutron Source
International Meeting of the Union for Compact Accelerator-driven Neutron Sources, Paris, France: 2019-07-08 - 2019-07-11
13. I. Drachnev *et al.*
REVIEW ON SOLAR NEUTRINO STUDIES BOREXINO
Eighteenth Lomonosov Conference on Elementary Particle Physics, Moscow, Russia: 2019-08-22 - 2019-08-28

14. R.W. Engels
The Jülich Setup for Storage Cell Characterisation
LHCSpin Project-Workshop, Italien, Italien: 2019-07-15 - 2019-07-17
15. R.W. Engels
Advantages of Nuclear Fusion with Polarized Fuel - Polarized Fusion
Prefer-Workshop, Russia, Russia: 2019-06-04 - 2019-06-06
16. R.W. Engels *et al.*
Advantages of Nuclear Fusion with Polarized Fuel
23rd International Spin Physics Symposium, Ferrara, Italy: 2019-09-10 - 2019-09-14
17. R.W. Engels *et al.*
Production and Storage of Polarized H₂, D₂ and HD Molecules
23rd International Spin Physics Symposium, Ferrara, Italy: 2019-09-10 - 2019-09-14
18. W. Esmail, T. Stockmanns and J. Ritman
Machine Learning for Track Finding at PANDA
Connecting the Dots and Workshop on Intelligent Trackers (CTD/WIT2019), Valencia, Spain: 2019-04-02 - 2019-04-05
arXiv:1910.07191
19. W.A. Esmail, T. Stockmanns and J. Ritman
Electromagnetic decay of excited Hyperons at HADES
DPG-Frühjahrstagung, München, Germany: 2019-03-17 - 2019-03-22
20. O. Felden *et al.*
Recent Extensions of JULIC for HBS Investigations
22th Cyclotron 2019, Capetown, South-Africa: 2019-09-22 - 2019-09-27
21. C. Genster *et al.*
Development of the OSIRIS detector simulation and its sensitivity study
Deutsche Physikalische Gesellschaft, Aachen, Germany: 2019-03-25 - 2019-03-29
22. A. Gillitzer *et al.*
Perspectives for Ξ Baryon Spectroscopy in $\bar{p}p$ Collisions with the PANDA Detector
DPG-Frühjahrstagung, München, Germany: 2019-03-17 - 2019-03-22
23. J. Golak *et al.*
Radiative pion capture in 2 H, 3 He and 3 H
15th International Workshop on Meson Physics, Cracow, Poland: 2018-06-07 - 2018-06-12
Eur. Phys. J. Web of Conferences 199 05005 -
24. D. Gotta
Strong-interaction effects in light antiprotonic atoms
Workshop on antiproton-nucleus interactions and related problems, ECT Trento, Italy: 2019-06-17 - 2019-06-21
25. D. Gotta
25 years of ultimate-resolution exotic atom X-ray spectroscopy
Physics of Fundamental Symmetries and Interactions, Villigen, Switzerland: 2019-10-21 - 2019-10-25
26. A. Göttel *et al.*
Calibrating OSIRIS - a radioactivity monitor for JUNO
Deutsche Physikalische Gesellschaft, Aachen, Germany: 2019-03-25 - 2019-03-29
27. D. Guffanti *et al.*
Perspectives for CNO neutrino detection in Borexino
5th International Solar Neutrino Conference, Dresden, Germany: 2019-06-11 - 2019-06-14
28. D. Guffanti *et al.*
Results from Borexino on solar and geo-neutrinos
The 39th International Conference on High Energy Physics, Seoul, Korea: 2018-07-04 - 2018-07-11

29. Y. Guo *et al.*
Searching for Proton Decay in JUNO
DFG Research Unit JUNO Meeting, Garching, Germany: 2019-10-09 - 2019-10-11
30. T. Gutberlet *et al.*
The High Brilliance Neutron Source (HBS) Project
DPG-Frühjahrstagung der Sektion Materie und Kosmos, TU München, Germany: 2019-03-17 - 2019-03-22
31. T. Gutberlet *et al.*
Bringing Neutrons to the User - The Jülich HBS Project for accelerator based neutron sources
International Meeting of the Union for Compact Accelerator-driven Neutron Sources, Paris, France: 2019-07-08 - 2019-07-11
32. T. Gutberlet *et al.*
Bringing Neutrons to the User - The Jülich HBS Project for accelerator based neutron sources
DPG-Frühjahrstagung der Sektion Kondensierte Materie, Universität Regensburg, Germany: 2019-03-31 - 2019-04-05
33. T. Gutberlet *et al.*
Neutrons for today and tomorrow - The HBS Project for compact accelerator based neutron sources
Workshop on Efficient Neutron Sources, Paul Scherrer Institut, Switzerland: 2019-09-02 - 2019-09-05
34. T. Gutberlet *et al.*
Making ESS a success - A landscape of European accelerator based neutron sources
23rd meeting of the International Collaboration on Advanced Neutron Sources, Chattanooga, Tennessee, USA: 2019-10-13 - 2019-10-18
35. T. Gutberlet *et al.*
Neutrons for today and tomorrow - The HBS Project for compact accelerator-based neutron sources
Workshop SCANS - A Compact Accelerator-Driven Neutron Source for Scandinavia?, Institute for Energy Technology, Kjeller, Norway: 2019-12-16 - 2019-12-17
36. J. Haidenbauer
Baryon-baryon interactions and the quest to constrain them by measuring correlation functions
Workshop on Hadron Interactions and Polarization from Lattice QCD, Quark Model, and Heavy Ion Collisions, Kyoto, Japan: 2019-03-25 - 2019-04-05
37. J. Haidenbauer
Antiproton-proton interaction from chiral effective field theory
ECT* Workshop on Antiproton-Nucleus interactions, Trento, Italy: 2019-06-17 - 2019-06-21
38. J. Haidenbauer
Hyperon-nucleon interactions: Recent developments
Workshop on Femtoscopy, Munich, Germany: 2019-09-12 - 2019-09-13
39. J. Haidenbauer
Assorted aspects of hyperon physics
Theia-Strong2020 Workshop, Speyer, Germany: 2019-11-25 - 2019-11-29
40. J. Haidenbauer
Hyperon-nucleon interaction in few- and many body systems
3rd EMMI Workshop, Wroclaw, Poland: 2019-12-02 - 2019-12-06
41. C. Hanhart
Doubly heavy hadronic molecules: Concepts and Tools
Exotic Hadron Spectroscopy 2019, York, United Kingdom: 2019-12-12 - 2019-12-13
42. C. Hanhart
Perspectives to understand the XYZ states
The 12th International Workshop on the Physics of Excited Nucleons, Bonn, Germany: 2019-06-10 - 2019-06-14
43. C. Hanhart
Theory of hadronic molecules applied to the XYZ states
International Workshop on e+e- Collisions from Phi to Psi, Mainz, Germany: 2017-06-26 - 2017-06-29
Eur. Phys. J. Web of Conferences 218 08002 -

44. S. Harabasz, HADES Collaboration and J. Ritman
Multi-differential pattern of low-mass e+e- excess from s NN = 2.4 GeV Au+Au collisions with HADES
 27th International Conference on Ultrarelativistic Nucleus-Nucleus Collisions (Quark Matter), Venice, Italy: 2018-05-13 - 2018-05-19
 Nucl. Phys. A 982982 771 - 774
45. A. Hützen *et al.*
POLARIZED PROTON BEAMS FROM LASER-INDUCED PLASMAS
 13th International Computational Accelerator Physics Conference,, Key West, USA: 2018-10-20 - 2018-10-24
46. L. Huxold *et al.*
A Lamb-Shift Polarimeter for \vec{H}_2 and \vec{D}_2 Molecules
 23rd International Spin Physics Symposium, Ferrara, Italy: 2019-09-10 - 2019-09-14
47. P. Kampmann and L. Ludhova
Reduction of the 14C-background in the JUNO experiment
 7th Symposium on Symmetries in Subatomic Physics, Aachen, Germany: 2018-06-10 - 2018-06-15
 Hyperfine Interact. 240 3
48. P. Kampmann
Status and Physics of the JUNO experiment
 19th Lomonosov conference, Moscow, Russia: 2019-08-22 - 2019-08-28
49. P. Kampmann *et al.*
Reduction of the 14C background in the JUNO experiment
 Deutsche Physikalische Gesellschaft, Aachen, Germany: 2019-03-25 - 2019-03-29
50. B. Kardan, HADES Collaboration and J. Ritman
Collective flow and correlations measurements with HADES in Au+Au collisions at 1.23 AGeV
 27th International Conference on Ultrarelativistic Nucleus-Nucleus Collisions (Quark Matter), Venice, Italy: 2018-05-13 - 2018-05-19
51. C. Käseberg
ELECTROSTATIC DEFLECTOR DEVELOPMENT or an EDM storage ring
 DPG-Frühjahrstagung 2019, München, Germany: 2019-03-17 - 2019-03-22
52. I. Keshelashvili *et al.*
A new approach: LYSO based polarimetry for the EDM measurements
 18th International Conference on Calorimetry in Particle Physics, Eugene, USA: 2018-05-21 - 2018-05-25
 J. Phys.: Conf. Ser. 11621162 012029 -
53. G. Kornakov, HADES Collaboration and J. Ritman
Sub-threshold strangeness production measured with HADES
 27th International Conference on Ultrarelativistic Nucleus-Nucleus Collisions (Quark Matter), Venice, Italy: 2018-05-13 - 2018-05-19
 Nucl. Phys. A 982982 803 - 806
54. S. Kumaran
Borexino: Improvements of the latest geoneutrino results
 Neutrino Geoscience 2019, Prague, Czech Republic: 2019-10-21 - 2019-10-23
55. S. Kumaran and L. Ludhova
Towards the Improved Geoneutrino Measurement with Borexino
 Workshop on Observatory Synergies for Astroparticle physics and Geosciences, Paris, France: 2019-02-11 - 2019-02-12
56. S. Kumaran
Analysis Strategies for the Updated Geoneutrino Measurement with Borexino
 Topics in Astroparticle and Underground Physics, Toyama, Japan: 2019-09-09 - 2019-09-13
57. S. Kumaran and L. Ludhova
Updated Geoneutrino Measurement with the Borexino Detector
 DPG Spring Conference, Aachen, Germany: 2019-03-25 - 2019-03-29

58. S. Kumaran and L. Ludhova
Analysis Strategies for the Updated Geoneutrino Measurement with Borexino
 Neutrino Geoscience 2019, Prague, Czech Republic: 2019-10-21 - 2019-10-23
59. A. Lai *et al.*
Characterization of the Strip Front-End ASIC of the PANDA MVD with the JDRS
 DPG-Frühjahrstagung, München, Germany: 2019-03-17 - 2019-03-22
60. A. Lehrach
Overview and Highlights FZJ
 5th Annual Matter and Technologies Meeting, Jena, Germany: 2019-03-05 - 2019-03-07
61. A. Lehrach
Polarized Beams from Laser-Plasma Accelerators
 4th European Advanced Accelerator Concepts Workshop, La Biodola Bay, Isola d'Elba, Italy: 2019-09-15 - 2019-09-21
62. L. Ludhova
Neutrino tomography I. Geoneutrinos: a new tool to study the Earth
 Workshop on observatory synergies for astroparticle physics and geoscience, Paris, France: 2019-02-11 - 2019-02-12
63. L. Ludhova
Low-energy Neutrino Physics with Liquid Scintillator Detectors
 18th Lomonosov Conference on Elementary Particle Physics, Moscow, Russia: 2017-08-24 - 2017-08-30
64. L. Ludhova
Updated geoneutrino measurement with Borexino
 16th International Conference on Topics in Astroparticle and Underground Physics, Toyama, Japan: 2019-09-09 - 2019-09-13
65. E. Mauerhofer *et al.*
The High-Brilliance Neutron Source (HBS) Project - Perspectives for Neutron Activation Analysis
 Seminar on Activation Analysis and Gamma Spectrometry, TUM Maschinenwesen Garching, Germany: 2019-02-24 - 2019-02-27
66. E. Mauerhofer *et al.*
The High-Brilliance Neutron Source (HBS) Project - Perspectives for Neutron Activation Analysis
 2nd International Conference on Radioanalytical and Nuclear Chemistry, Budapest, Hungary: 2019-05-05 - 2019-05-10
67. U. Meißner
Nuclear physics from lattice simulations
 The first workshop of Southern Nuclear Science Computing Center, Guangzhou, China: 2019-01-08 - 2019-01-09
68. U. Meißner
Breaking and restauration of symmetries in NLEFT
 ENST program on "Symmetry breaking and symmetry preserving schemes: how to efficiently grasp collective correlations in mesoscopic many-body systems?", Saclay, France: 2019-05-13 - 2019-05-17
69. U. Meißner
Theory of baryon resonances
 The 12th International Workshop on the Physics of Excited Nucleons, Bonn, Germany: 2019-06-10 - 2019-06-14
70. U. Meißner
Nuclear lattice effective field theory
 Summer School on "Frontiers in Lattice QCD," Peking University, Beijing, China: 2019-06-24 - 2019-07-12
71. U. Meißner
Introduction to effective field theories for strong interactions
 Summer School on "Low-Energy Strong Interactions", Beijing, China: 2019-08-24 - 2019-08-28

72. U. Meißner
Lectures on Chiral Perturbation Theory
School and Workshop "Frontiers of QCD", Tbilisi, Georgia: 2019-09-24 - 2019-09-28
73. U. Meißner
Theory of hadron resonances
School and Workshop "Frontiers of QCD", Tbilisi, Georgia: 2019-09-24 - 2019-09-28
74. U. Meißner
Theory of hadron resonances
Workshop on "Universal physics in Many-Body Quantum Systems - From Atoms to Quarks", Trento, Italy: 2019-10-07 - 2019-10-11
75. U. Meißner
Precision predictions
Joint ECFA-NuPECC-APPEC Seminar, Orsay, France: 2019-10-14 - 2019-10-16
76. U. Meißner
Towards heavy nuclei in nuclear lattice effective field theory
Workshop on "New generation nuclear density functionals", Beijing, China: 2019-11-18 - 2019-11-22
77. L. Miramonti *et al.*
Recent results on pp-chain solar neutrinos with the Borexino detector
Prospects in Neutrino Physics, NuPhys2018, London, United Kingdom: 2018-12-19 - 2018-12-21
78. F. Müller
Measurement of dC vector analyzing power and cross sections at COSY for EDM polarimetry
23rd International Spin Physics Symposium, Ferrara, Italy: 2018-09-10 - 2018-09-14
79. P. Niedermayer *et al.*
Electron Cooling Experiments with 2.4 GeV/c proton beam at COSY
DPG-Frühjahrstagung, München, Germany: 2019-03-18 - 2019-03-22
80. P. Niedermayer *et al.*
Recent Developments and Experimental Results From Electron Cooling of a 2.4 GeV/c Proton Beam at COSY
12th Workshop on Beam Cooling and Related Topics, Novosibirsk, Russia: 2019-09-23 - 2019-09-27
81. A. Nogga
Charge-symmetry breaking in light hypernuclei based on chiral and similarity renormalization group-evolved interactions
13th International Conference on Hypernuclear and Strange Particle Physics, Portsmouth, VA, USA: 2018-06-24 - 2018-06-29
82. Ö. Penek and L. Ludhova
Analytical Multivariate Studies in the Borexino Solar Neutrino Analysis
DPG Frühjahrstagungen Aachen, Aachen, Germany: 2019-03-25 - 2019-03-29
83. Ö. Penek, L. Ludhova and Borexino Collaboration
Measurement of pp-chain Solar Neutrinos with Borexino
WIN2019 The 27th International Workshop on Weak Interactions and Neutrinos, Bari, Italy: 2019-06-02 - 2019-06-08
84. A. Pocar *et al.*
Solar Neutrino Physics with Borexino
The 15th International Workshop on Tau Lepton Physics, Amsterdam, The Netherlands: 2018-09-24 - 2018-09-28
85. V. Poncza
Search for Electric Dipole Moments at COSY in Jülich - Spin tracking simulations using Bmad
DPG-Frühjahrstagung 2019, München, Germany: 2019-03-17 - 2019-03-22
86. V. Poncza
Search for electric dipole moments at COSY in Jülich - spin tracking simulations using Bmad
10th International Particle Accelerator Conference, Melbourne, Australia: 2019-05-19 - 2019-05-25

87. V. Poncza and A. Lehrach
Search for Electric Dipole Moments at COSY in Jülich - Spin-Tracking Simulations using BMAD
 10th International Particle Accelerator Conference, Melbourne, Australia: 2019-05-19 - 2019-05-25
88. E. Prencipe *et al.*
Search for four- and six-quark exotics with charm and strange quark content
 DPG-Frühjahrstagung, München, Germany: 2019-03-17 - 2019-03-22
89. E. Prencipe
X, Y, Z Search at Belle II
 9th International Workshop on Charm Physics, Novosibirsk, Russia: 2018-05-21 - 2018-05-25
 Eur. Phys. J. Web of Conferences 202 01001 -
90. J. Pretz
Towards a Storage Ring Electric Dipole Moment Measurement
 DPG Tagung, Aachen, German: 2019-03-25 - 2019-03-29
91. J. Pütz *et al.*
Study of $\bar{p}p \rightarrow \bar{\Xi}^+ \Lambda K^-$ with the PANDA Detector
 The 12th International Workshop on the Physics of Excited Nucleons, Bonn, Germany: 2019-06-10 - 2019-06-14
92. B. Ramstein *et al.*
Time-Like Baryon Transitions studies with HADES
 15th International Workshop on Meson Physics (MESON), Krakau, Polen: 2018-06-07 - 2018-06-12
 Eur. Phys. J. Web of Conferences 199199 01008 -
93. M. Redchuk
Comprehensive measurement of pp-chain solar neutrinos with Borexino
 European Physical Society Conference on High Energy Physics, Ghent, Belgium: 2019-07-10 - 2019-07-17
94. M. Redchuk
Improved approach of monitoring the effective quantum efficiency of Borexino photomultipliers
 DPG Frühjahrstagung (Spring Meeting), Aachen, Germany: 2019-03-25 - 2019-03-29
95. V. Reva *et al.*
COSY Experience of Electron Cooling
 12th Workshop on Beam Cooling and Related Topics, Novosibirsk, Russia: 2019-09-23 - 2019-09-27
96. M. Rimmler *et al.*
Proton beam multiplexing and pulse distribution concepts for the High Brilliance Neutron Source HBS
 DPG-Frühjahrstagung der Sektion Materie und Kosmos, TU München, Germany: 2019-03-17 - 2019-03-22
97. M. Rimmler
Proton Beam Multiplexer Developments for Multi-Target Operation at the High-Brilliance Neutron Source HBS
 8th International Meeting of the Union for Compact Accelerator-driven Neutron Sources, UCANS-8, Paris, France, 8 Jul 2019 - 10 Jul 2019, Paris, France: 2019-07-08 - 2019-07-10
98. S. Ropertz, C. Hanhart and B. Kubis
Scalar isoscalar form factors for energies above 1 GeV
 9th International Workshop on Charm Physics, Novosibirsk, Russia: 2018-05-21 - 2018-05-25
 Eur. Phys. J. Web of Conferences 202 06002 -
99. S. Schadmand
Electromagnetic Transition Form Factors of the η and ω Mesons
 DPG-Frühjahrstagung, München, Germany: 2019-03-17 - 2019-03-22
100. S. Schadmand
Electromagnetic Transition Form Factors of Light Mesons
 Proceedings of the 8th International Conference on Quarks and Nuclear Physics (QNP2018), Tsukuba, Japan: 2018-11-13 - 2018-11-17

101. M. Schever
The Jiangmen Underground Neutrino Observatory
 Deutsche Physikalische Gesellschaft, Aachen, Germany: 2019-03-25 - 2019-03-29
102. V. Shmakova
Progress toward the first measurement of the deuteron Electric Dipole Moment at COSY
 DPG-Frühjahrstagung 2019, Aachen, Germany: 2019-03-25 - 2019-03-29
103. N. Shurkhno and R. Stassen
Control of stochastic cooling systems
 12th International Workshop on Beam Cooling, Novosibirsk, Russia: 2019-09-23 - 2019-09-27
104. S. Siddique
SIMULATION OF PROTOTYPE PROTON EDM STORAGE RING
 DPG-Frühjahrstagung 2019, München, Germany: 2019-03-17 - 2019-03-22
105. T. Stockmanns
PandaRoot – the simulation and reconstruction framework of PANDA
 ICTP-SAIFR/FAIR Workshop on Mass Generation in QCD, Sao Paulo, Brazil: 2019-02-25 - 2019-03-01
106. A. Thampi *et al.*
Study of the invariant mass system in the $J/\Psi\phi$ in B decays and continuum with BaBar and Belle combined data sets
 DPG-Frühjahrstagung, München, Germany: 2019-03-17 - 2019-03-22
107. D.K. Toporkov *et al.*
Status of the Polarized Molecular Source
 23rd International Spin Physics Symposium, Ferrara, Italy: 2019-09-10 - 2019-09-14
108. A. Vishneva *et al.*
Limit on the effective magnetic moment of solar neutrinos using Borexino data
 5th International Solar Neutrino Conference, Dresden, Germany: 2018-06-11 - 2018-06-14
109. T. Wagner
Beam Based Alignment at the Cooler Synchrotron (COSY)
 "Matter and the Universe" Days 2019, Hamburg, Germany: 2019-02-14 - 2019-02-15
110. T. Wagner and J. Pretz
Beam-based Alignment at the Cooler Synchrotron (COSY)
 10th International Particle Accelerator Conference, Melbourne, Australia: 2019-05-19 - 2019-05-24
111. T. Wagner
Beam-based Alignment at COSY
 DPG Frühjahrstagung 2019, München, Germany: 2019-03-17 - 2019-03-22
112. T. Wagner
Beam-based alignment at the Cooler Synchrotron (COSY)
 10th International Particle Accelerator Conference, Melbourne, Australia: 2019-05-19 - 2019-05-24
113. M. Weikum *et al.*
Status of the Horizon 2020 EuPRAXIA Conceptual Design Study
 10th International Particle Accelerator Conference, Melbourne, Australia: 2019-05-19 - 2019-05-24
114. M. Wurm *et al.*
Solar Neutrino Spectroscopy in Borexino
 5th International Solar Neutrino Conference, Dresden, Germany: 2019-06-11 - 2019-06-14
115. Y. Xu and L. Ludhova
Machine learning methods for JUNO Experiment
 PHYSTAT-nu 2019, CERN, Switzerland: 2019-01-22 - 2019-01-25
116. Y. Xu *et al.*
Event Reconstruction with Machine Learning methods in JUNO
 Deutsche Physikalische Gesellschaft, Aachen, Germany: 2019-03-25 - 2019-03-29

117. P. Zakalek *et al.*
Neutron production and moderation for a High Brilliance Neutron Source (HBS)
 Second Scientific Workshop of the Program "From Matter to Materials and Life, HZDR Dresden, Germany: 2019-02-13 - 2019-02-15
118. P. Zakalek *et al.*
High-Brilliance Neutron Source Project
 14th Int. Conf. on Heavy Ion Accelerator Technology, Lanzhou, China: 2018-10-22 - 2018-10-26
119. Y. Zhou and H. Xu
Towards the final setup of KOALA experiment
 DPG-Frühjahrstagung, München, Germany: 2019-03-17 - 2019-03-22

D.2 Colloquia

1. J. Haidenbauer
Hyperon-nucleon interaction in few-body systems and in heavy ion collisions
 Darmstadt, Germany: 2019-06-06 -
2. A. Lehrach
Overview and highlights FZJ
 5th Matter and Technologies Days, Jena, Germany: 2019-03-05 - 2019-03-07
3. A. Lehrach
The COSY Synchrotron
 Interest in a low momentum beam at CERN, Jülich, Germany: 2019-03-01
4. L. Ludhova
Solar neutrino spectroscopy with Borexino
 Ferrara, Italy: 2019-12-12 - 2019-12-13
5. L. Ludhova
Geoneutrinos
 Garching, Germany: 2019-10-10 - 2019-10-10
6. L. Ludhova
Observation of neutrinos from the Sun and the Earth in Borexino
 GSI-FAIR Colloquium, GSI, Germany: 2019-04-30 - 2019-04-30
7. L. Ludhova
Low-energy neutrino physics with Borexino
 Colloquium at Shanghai Jiao-Tong University, Shanghai, China: 2019-01-25 - 2019-01-25
8. U. Meißner
Precision Predictions
 Colloquium, Institute of Theoretical Physics, Chinese Academy of Sciences: 2019-11-20
9. U. Meißner
Nuclear Physics as Precision Science
 GSI-FAIR-Colloquium, GSI, Darmstadt: 2019-01-15
10. U. Meißner
Threshold pion photoproduction - with an eye on Reinhard's contribution
 Festkolloquium zum 60. Geburtstag von Reinhard Beck, Universität Bonn: 2019-06-14
11. U. Meißner
Nucleons on a Lattice: Symmetry Breaking and Restoration
 Colloquium, Saclay, Germany: 2019-05-17
12. U. Meißner
Nuclear Physics as Precision Science
 Physics Department Colloquium, Stony Brook, USA: 2019-04-30

13. Ö. Penek
Measurement of pp-chain Solar Neutrinos with Borexino
 Seminar on Solar Neutrino Physics, University of Strasbourg, Strasbourg, France: 2019-04-11 - 2019-04-11
14. J. Pretz
Physik und Musik - Vom Gartenschlauch zur Posaune
 Nacht der Wissenschaft, Duesseldorf, Germany: 2019-09-13
15. J. Pretz
Physik und Musik - Vom Gartenschlauch zur Posaune
 CAMPUS Talks, ARD alpha, Muenchen, Germany: 2019-06-04 - 2019-06-04
16. F. Rathmann
Electric Dipole Moment Searches using Storage Rings
 Symposium Opening EDM Lab Bonn, Bonn, Germany: 2019-03-22 - 2019-03-22
17. S. Schadmand
An update on $\omega \rightarrow \pi^0 e^+ e^-$ analysis from g12
 hadron spectroscopy session CLAS collaboration meeting, Jefferson Lab, Newport News, USA: 2019-03-05 - 2019-03-08
18. H. Ströher
Electric Dipole Moments (EDM)
 Hamburg, Deutschland: 2019-02-14 - 2019-02-15
19. H. Ströher
Static and Oscillating Electric Dipole Moments
 Wuppertal, Germany: 2019-05-27 - 2019-05-27
20. H. Ströher
Das Nukleon (Proton, Neutron) Was wir darüber wissen (und was nicht)
 Bonn, Germany: 2019-06-14 - 2019-06-14
21. H. Ströher
Static and Oscillating Electric Dipole Moments
 Krakau, Polen: 2019-06-26
22. H. Ströher
Why is the World the Way it is?
 Abasha, Georgia: 2019-08-22 - 2019-08-22
23. H. Ströher
What is GGSB - 15 years on?
 Tbilisi, Georgia: 2019-09-27 - 2019-09-27
24. T. Wagner
Accurate position calibration of beam position monitors in storage rings
 16th SPARC Topical Workshop, Jena, Germany: 2019-09-09 - 2019-09-13
25. A. Wirzba
Electric Dipole Moments of Light Nuclei in Chiral Effective Field Theory
 Orsay, France: 2019-01-31 - 2019-01-31

E Academic Degrees

E.1 Dissertation / PhD Theses

1. A. Aksentev
2D Frozen spin method of searching for the deuteron EDM in a storage ring
National Research Nuclear University "MEPhI", Moscow
2. S. Basile
Development of a high-precision LYSO polarimeter for the EDM search at the COSY storage ring
University of Ferrara
3. C. Genster
Soft- und Hardwareentwicklung für die Flüssigszintillator-Detektoren der nächsten Generation JUNO und OSIRIS
Software and hardware development for the next-generation liquid scintillator detectors JUNO and OSIRIS
RWTH Aachen University
4. J. Michaud
Effect of electrostatic deflectors and associated fringe fields on spin coherence time for the measure of the proton electric dipole moment in a storage ring
Université Grenoble Alpes
5. F. Müller
Polarimeter Development for Electric Dipole Moment Measurements in Storage Rings
Universitätsbibliothek RWTH Aachen

E.2 Master Theses

1. M. Abuladze
Monte Carlo Simulation for the JEDI Polarimeter (JePo) Performance
Free University of Tbilisi
2. B. Alberdi
Optimization of Injection in COSY
RWTH Aachen
3. M. Beyss
Detection and Analysis of Recombination Rates during Electron Cooling at COSY
RWTH Aachen
4. C. Kaeseberg
Electrostatic Deflector Development for Electric Dipole Moment Measurements at Storage Rings
RWTH Aachen
5. C. Käseberg
Electrostatic Deflector Development for Electric Dipole Moment Measurements at Storage Rings
RWTH Aachen
6. S. Kroon
Towards CNO measurement with Borexino: ^{210}Bi homogeneity in the liquid scintillator
RWTH Aachen

E.3 Bachelor Theses

1. L. Bayer
Consistent extraction of the rho parameters from various reactions
Bonn
2. S. Clausen
Herstellung von Speicherzellen zur Rekombination von polarisierten Molekülen
FH Aachen, Campus Jülich

3. A. Heinrich
Optimization of electric deflectors for a storage ring experiment
RWTH Aachen
4. P. Niedermayer
Charakterisierung der Kühdynamik des 2MeV Elektronenkühlers am Beschleuniger COSY
FH Aachen
5. H. Smitmanns
Further measurements of the recombination of nuclear polarised hydrogen atoms into molecules on different surfaces
FH Aachen, Campus Jülich

F Awards

H. Ströher The medal of Georgian public figure and philanthropist Akaki Khoshtaria (contribution to the development of GGSB project)

A. Kacharava The medal of Georgian writer-academician Konstantine Gamsakhurdia (contribution to the development of GGSB project)

R. Stassen Dieter-Möhl-Medal for his pioneering work in the field of the cooling of particle beams

S. Kumaran Best poster prize at the TAUP 2019 conference in Japan about the geoneutrino measurement of Borexino.

J. Slim The Friedrich Wilhelm prize of the RWTH Aachen for excellent doctoral thesis 2019

G Third Party Funded Projects

Project	Responsible/Contact	Funded by
Untersuchung von exotischen 4-Quark Zuständen	E. Prencipe	DFG
PGSB: Experimental tests of time-reversal	H. Ströher	BMBF
Bestimmung der Neutrino-Massenhierarchie	L. Ludhova	DFG
(CASCADE) Computational Science for Comp	T. Luu, U. G. Meißner	HGF
SFB/TRR 110 Quantenchromodynamik TP A01	J. Haidenbauer	DFN/SFB, NFSC
SFB/TRR 110 Quantenchromodynamik TP B03	C. Hanhart	DFN/SFB, NFSC
SFB/TRR 110 Quantenchromodynamik TP B06	A. Nogga	DFN/SFB, NFSC
SFB/TRR 110 Quantenchromodynamik TP Z01	U. G. Meißner	DFN/SFB, NFSC
SFB/TRR 110 Quantenchromodynamik TP Z02	C. Hanhart	DFN/SFB, NFSC
SFB/TRR 110 Quantenchromodynamik TP B09	T. Luu, U. G. Meißner	DFN/SFB, NFSC
PANDA/ Straw Tube Tracker	J. Ritman	Industrieprojekt mit der GSI GmbH
PANDA/ Micro Vertex Detector	J. Ritman	Industrieprojekt mit der GSI GmbH
HESR - Dipole und Quadrupole	R. Tölle	Industrieprojekt mit der FAIR GmbH
HESR - sonstige Magnete	J. Böker	Industrieprojekt mit der FAIR GmbH
HESR - Netzgeräte	M. Retzlaff	Industrieprojekt mit der FAIR GmbH
HESR - Hochfrequenz	R. Stassen	Industrieprojekt mit der FAIR GmbH
HESR - Injektion	R. Tölle	Industrieprojekt mit der FAIR GmbH
HESR - Strahldiagnose	V. Kamerzhiev	Industrieprojekt mit der FAIR GmbH
HESR - Vakuum	F. Esser	Industrieprojekt mit der FAIR GmbH
HESR - Stochastische Kühlung	R. Stassen	Industrieprojekt mit der FAIR GmbH
HESR - Panda-Integration	D. Prasuhn	Industrieprojekt mit der FAIR GmbH
AVA MSCA ITN	D. Grzonka	EU
Unit Costs TA1	D. Grzonka	EU (STRONG2020)
Travel and Subsistance for Users TA	D. Grzonka	EU (STRONG2020)
Transnational Access to COSY TA1	D. Grzonka	EU (STRONG2020)
JRA2-FTE@LHC:	F. Rathmann	EU (STRONG2020)
Fixed Target Experiments at the LHC		
JRA3-PrecisionSM:	S. Schadmand	EU (STRONG2020)
Precision Tests of the Standard Model		
JRA7-HaSP:	C. Hanhart	EU (STRONG2020)
Light-and heavy-quark hadron spectroscopy		
JRA12-SPINFORFAIR: Spin for FAIR	F. Rathmann	EU (STRONG2020)
srEDM ERC Advanced Grant Management	H. Ströher	EU
srEDM ERC Advanced Grant Research	H. Ströher	EU
ATHENA _h (Accelerator Technology HELmholtz iN-frAstructure)	A. Lehrach	HGF

H Collaborations

- ATHENA Accelerator Technology Helmholtz Infrastructure
(https://www.athena-helmholtz.de/home/index_eng.html)
- Belle-II (B(meson) to lepton lepton (v.2))
(<https://www.belle2.org>)
- Borexino (Boron solar neutrino experiment, LNGS, Italy)
(<http://borex.lngs.infn.it>)
- CBM (Compressed Baryonic Matter)
(<https://www.gsi.de/work/forschung/cbmnqm/cbm.htm>)
- CLAS (CEBAF Large Acceptance Spectrometer, JLab, USA)
(<https://www.jlab.org/Hall-B/clas-web>)
- CPEDM (Electric Dipole Moments, CERN)
(<http://pbc.web.cern.ch/edm/edm-org.htm>)
- ELENA (CERN) (Extra Low Energy Antiproton ring)
(<https://espace.cern.ch/elena-project/SitePages/Home.aspx>)
- GlueX (The GlueX experiment, JLab, USA)
(<https://www.jlab.org/Hall-D/>)
- HADES (High Acceptance DiElectron Spectrometer)
(<https://www-hades.gsi.de>)
- HBS (High Brilliance Neutron Source)
(https://www.fz-juelich.de/jcms/jcms-2/EN/Forschung/High-Brilliance-Neutron-Source/_node.html)
- JEDI (Jülich Electric Dipole moment Investigation, COSY)
(<http://collaborations.fz-juelich.de/ikp/jedi>)
- JUNO (Jiangmen Underground Neutrino Observatory, Jiangmen, China)
(<http://juno.ihep.cas.cn>)
- JuSPARC (Jülich Short-Pulsed Particle and Radiation Center)
(<https://jusparc.fz-juelich.de/>)
- LENPIC (Low Energy Nuclear Physics International Collaboration)
(<http://www.lenpic.org/>)
- PANDA (Anti-Proton Annihilation at Darmstadt, FAIR)
(<https://panda.gsi.de>)
- PAX (Polarized Antiproton eXperiments, COSY)
(<http://collaborations.fz-juelich.de/ikp/pax>)
- PDG (Particle Data Group)
(pdg.lbl.gov)
- STRONG-2020 (The strong interaction at the frontier of knowledge: fundamental research and applications)
(www.strong-2020.eu)
- WASA (Wide Angle Shower Apparatus, FRS)
(<https://www-win.gsi.de/frs/index.htm>)
- WASA (Wide Angle Shower Apparatus, WASA-at-COSY)
(<http://collaborations.fz-juelich.de/ikp/wasa/>)

I Conferences and Outreach Activities (Co-)Organized by the IKP

I.1 Georgian-German Science Bridge: 2nd QUALI-Start-Up Science Lectures in Jülich

During September 8-15, 2019, thirty students from four Georgian universities (AUG, GTU, ISU and TSU) have visited Forschungszentrum Jülich to attend the so called "QUALI-Start-Up Science Lectures" (autumn school), which were co-funded by the Georgian Ministry of Education and Science (MES) and institutes of Jülich. This was the second school of its kind in Jülich and a follow-up of two previous events in Georgia in 2013 and 2015, and the last one in Jülich, 2017. The participants had been pre-selected earlier in personal interviews at Georgian universities. The lectures were organized by the Forschungszentrum institutes: IBG, IEK, INM, IKP, PGI and ZEA. During the lectures, the students were introduced to the science conducted at the institutes and they had the chance to perform hands-on practices in laboratories. They also visited RWTH Aachen University and had the possibility to do sightseeing in Aachen and Cologne. As part of the event, twelve excellent students were selected from various scientific fields - Physics, Mathematics, Chemistry, Biology and Engineering Technology, corresponding to the mentioned FZJ institutes – which were granted additional internships of month each in Forschungszentrum Jülich. For IKP a total of 4 students were identified which will visit the institute in Jan./Feb., 2020.



Figure 48: Participants and organisers of the GGSB 2019.

I.2 Georgian-German Science Bridge: Outreach Activity

The Georgian-German Science Bridge (GGSB) project focuses on research, knowledge transfer and education. In conjunction with the latter, an expression of interest was signed in 2018 between the Ministry of Education and Science of Georgia and Forschungszentrum Jülich to also include its student laboratory JuLab. Based on this agreement, a pilot workshop for teachers and pupils was held between October 14 and 18, 2019 at Tbilisi State University (TSU). With assistance of IKP, about 60 pupils and 40 teachers from Georgian schools were introduced to the subject "Electricity (*put a spark in your electricity lessons*)" by modern didactic methods utilizing an experiment box, donated to TSU by the JuLab.



Figure 49: Participants and organisers of the Julab workshop at TSU.

I.3 Decyphering Strong Interaction Phenomenology through Precision Hadron Spectroscopy

Together with colleagues from Munich, Rome and Novosibirsk the theory department was involved in organising a four week program from October 7th through 31st, 2019, on hadron spectroscopy at the Munich Institute for Astro- and Particle Physics (MIAPP). The program brought together theorists and experimentalists actively working in the field, who summarized the status of experimental findings of the last decade as well as new theoretical ideas to identify and work on the most challenging pending problems. In the fourth week we embedded a two-day workshop on baryon spectroscopy to balance the meson dominance in the other weeks. The program has been overwhelmingly successful in gathering and stimulating fruitful discussions amongst the leading scientists in hadron spectroscopy and amplitude analysis,

representing different directions of modelling or computations.



Figure 50: Participants of the MIAPP program of hadron spectroscopy.

I.4 The 2019 Workshop of the APS Topical Group for Hadronic Physics

The biennial workshop of the GHP took place at the Sheraton Hotel in Denver, Colorado on April 10-12, 2019, immediately preceding the APS April Meeting. The workshop attendance was excellent, with 116 speakers giving presentations over the three days. The program comprised a series of eighteen plenary talks highlighting the progress made in hadronic physics over the preceding two years, together with invited and contributed parallel talks expounding in greater detail the key developments.

An important aim of the workshop was to emphasize the excitement and relevance of hadronic physics across a broad portfolio of physics activities. The plenary talks focused on the phase structure of QCD and the evolution to hadronic degrees of freedom, on the study of the structure of the nucleon, on spectroscopy as playing a key role in illuminating the degrees of freedom of QCD in the strong-coupling regime, and on the importance of the hadronic-physics program to our understanding of the Standard Model of high-energy and nuclear physics. In anticipation of a future Electron-Ion Collider, the exciting physics opportunities it would facilitate in revealing the "glue that binds us all" were outlined.

The parallel program comprised invited and contributed talks arranged into topical sessions. The topical sessions were arranged to emphasize the role of theory, experiment and computation together in constructing a faithful picture of hadronic physics.

The program and copies of the slides from all presentations are available online ⁹.

⁹<https://www.jlab.org/indico/event/282>

I.5 Helmholtz - DIAS International Summer School "Quantum Field Theory at the Limits: from Strong Fields to Heavy Quarks "

The Helmholtz International Summer School (HISS) - Dubna International Advanced School of Theoretical Physics (DIAS-TH) "Physics of Heavy Quarks and Hadrons", organized by the Bogoliubov Laboratory of Theoretical Physics of the Joint Institute for Nuclear Research together with colleagues from Jena, Dresden and the theory group, was held from July 22nd until August 2nd, 2019, in Dubna, Russia. The School covered the main topics in heavy-flavor and strong-field physics. It provided a first hand opportunity to graduate students and postdocs in high energy and high intensity physics. Leading experts in these fields presented series of lectures devoted to theoretical predictions and analyses of experimental results.



Figure 51: Participants and some lecturers of the DIAS International Summer School.

I.6 Four Day Particle Physics Academy and One Training Program for High School Teachers

In 2019 the collaborative research center "Symmetries and the emergence of structure in QCD" (CRC 110), where the theory group of IKP is heavily involved together with researchers from Bonn University, TU München, Ruhr-Universität Bochum, IHEP/CAS (Beijing, China), ITP/CAS (Beijing, China) and Peking University (China), offered for the fourth time its four day particle physics academy for high school students (with 25 participants from 10th to 13th grade) as well as a one day training program for high school teachers (23 participants) on the same topic. Venue for the former was as in all previous years the Science College Overbach in Jülich, which provides an ideal environment since housing, lab and lecture hall are all on site. After having provided already a teachers training program in Jülich, Munich and Bonn, this year it was offered in Bochum. Both

programs contained overview lectures as well as lectures on current issues in nuclear and particle physics always with special emphasis on theoretical aspects which was very much appreciated by the participants. In addition, we presented demonstration experiments to illustrate the theoretical concepts. In the course of the particle physics academy we also offered three projects to the students: In first one they got a chance to get in touch with the fundamentals of quantum mechanics, in the second they learned how to simulate numerically the trajectory of Mercury and in the third they discussed requirements of a scientific approach to philosophical issues like the anthropic principle. For both programs the feedback provided by the participants was extremely positive.



Figure 52: Participants and team of the high school student training program 2019 in front of the Science College Overbach.

I.7 Further Events (Co)-Organised by Members of the Institute

- “50. Arbeitstreffen Kernphysik”, February 2019, Schleching, Germany.
- ECT* workshop on “Antiproton-nucleus interactions and related phenomena“, June 17th - 21st, 2019, Trento, Italy.
- Bethe Forum “Multihadron dynamics in a box”, September 9th - 13th, 2019, BCTP, Bonn, Germany.
- PhD school and workshop, “Frontiers of QCD”, September 23rd-28th, 2019, Tbilisi, Georgia.
- “EPS Historical Site Inauguration and Wideröe Symposium“, RWTH’s Institute for High Voltage Technology, formerly Rogowski Institute, named Historical Site of the European Physical Society, September 30th, 2019, Aachen, Germany.

I.8 Colloquium in Honour of the 80th Birthday of Prof. Dr. K. Kilian

On August 30th, 2019, a scientific colloquium took place on the occasion of the 80th birthday of Prof. Dr. Kurt Kilian, the former director of IKP-1. After welcome greetings from Prof. James Ritman scientific lectures were given by Prof. Tord Johansson from Uppsala and Prof. Heinz Clement from Tübingen. Prof. Tord Johansson presented the achievements of the antihyperon-hyperon production experiment PS185 at the low energy antiproton ring (LEAR) operated at CERN until 1996 and Prof. Heinz Clement talked about the TOF experiment at COSY. About 50 external guests plus the IKP staff attended the colloquium which was followed by a reception and dinner for invited guests.



Figure 53: Guests at the colloquium in honour of Prof. Dr. Kurt Kilians 80th birthday.

J Teaching Positions

Institute	Name	University
IKP-1	PD Dr. A. Gillitzer	Bonn
	Prof. Dr. F. Goldenbaum	Wuppertal
	Prof. J. Ritman Ph.D.	Bochum
	S. Schadmand, Ph.D. habil.	Osaka
	Dr. T. Stockmanns	Bochum
IKP-2	Prof. Dr. D. Gotta	Köln
	PD Dr. F. Rathmann	Aachen
	Prof. Dr. L. Ludhova	Aachen
	Prof. Dr. Dr. h.c. mult. H. Ströher	Köln
	Prof. Dr. J. Pretz	Aachen
IKP-3/IAS-4	Univ. Doz. Dr. J. Haidenbauer	Graz
	Prof. Dr. C. Hanhart	Bonn
	Prof. Dr. T. Luu	Bonn
	Prof. Dr. Dr. h.c. U.-G. Meißner	Bonn
	Dr. A. Nogga	Bonn
	PD Dr. A. Wirzba	Bonn
IKP-4	Dr. O. Felden	Aachen
	Prof. Dr. A. Lehrach	Aachen

K Personnel

MSc. F. Abusaif (IKP-2)
A. Aksentev (IKP-2) (until 31st August 2019)
MSc. D. Alfs (IKP-1)
B. Alberdi (IKP-2) (until 14th October 2019)
BSc. A. Andres (IKP-2) (since 1st April 2019)
Dr. M. Anwar (IKP-3/IAS-4)
Dr. Z. Bagdasarian (IKP-2)
Dr. I. Bekman (IKP-4)
C. Berchem (IKP-TA)
Dr. E. Berkowitz (IKP-3/IAS-4) (until 31st July 2019)
M. Beyß (IKP-2) (until 14th October 2019)
Dr. C. Böhme (IKP-4)
M. Böhnke (IKP-4)
Dr. J. Böker (IKP-4)
DI N. Bongers (IKP-4)
Dr. B. Breitzkreutz (IKP-4)
P. Brittner (IKP-4)
J. But (IKP-TA)
Dr. Y. Cheng (IKP-2) (until 31st August 2019)
W. Classen (IKP-4)
M. Comuth-Werner (IKP-TA)
DI F.U. Dahmen (IKP-4)
DI N. Demary (IKP-TA)
MBA A. Derichs (IKP-1)
C. Deliege (IKP-4)
G. D'Orsaneo (IKP-2)
R. Dosdall (IKP-1)
C. Ehrlich (IKP-4)
Dr. R. Engels (IKP-2)
B. Erkes (IKP-4)
Msc. W. Esmail (IKP-1)
DI F.-J. Etz Korn (IKP-4)
Dr. O. Felden (IKP-TA)
H.-W. Firmenich (IKP-TA)
Dr. D. Frame (IKP-3/IAS-4) (since 2nd September 2019)
F. Frenzel (IKP-4)
N. Fröhlich (IKP-4)
Dr. R. Gebel (IKP-4)
Dr. C. Genster (IKP-2)
PD Dr. A. Gillitzer (IKP-1)
J. Göbbels (IKP-TA)
Prof. Dr. F. Goldenbaum (IKP-1)
MSc. A. Göttel (IKP-2)
Dr. K. Grigoryev (IKP-4)
Dr. D. Grzonka (IKP-1)
M. Gülpen (IKP-TA) (since 1st September 2019)
MSc. Y. Guo (IKP-2) (since 25th September 2019)
PD Dr. J. Haidenbauer (IKP-3/IAS-4)
A. Halama (IKP-4)
E. Hall-Brunton (IKP-TA) (since 19th August 2019)
DI S. Hamzic (IKP-4)
Prof. Dr. C. Hanhart (IKP-3/IAS-4)
T. Hahnrahts-von der Gracht (IKP-TA)
Dr. M. Hartmann (IKP-2)
DI R. Hecker (IKP-TA)
Dr. V. Hejny (IKP-2)
Dr. J.-H. Hetzel (IKP-4)
M. Holona (IKP-1)
MSc. O. Javakhishvili (IKP-2) (since 10th January 2019)
Dr. A. Kacharava (IKP-2)
Dr. V. Kamerdzhev (IKP-4)
MSc. P. Kampmann (IKP-2)
MSc. J. Kannika (IKP-1)
MSc. C. Kannis (IKP-4) (since 1st March 2019)
C. Käseberg (IKP-4) (until 14th October 2019)
A. Kelleners (IKP-TA) (since 1st November 2019)
Dr. I. Keshelashvili (IKP-2)
A. Kieven (IKP-4)
S. Kistemann (IKP-TA)
B. Klimczok (IKP-TA)
J. Knothe (IKP-TA) (until 14th September 2019)
BSc. A. Koushik (IKP-2) (since 1st October 2019)
M. Kremer (IKP-TA)
DI T. Krings (IKP-TA)
S. Kroon (IKP-2) (until 11th November 2019)
M. Küven (IKP-4)
Dr. P. Kulesa (IKP-1) (since 1st April 2019)
MSc. S. Kumaran (IKP-2)
Dr. T. Lähde (IKP-3/IAS-4)
Dr. A. Lai (IKP-1) (until 28th February 2019)
K.-G. Langenberg (IKP-4)
Prof. Dr. A. Lehrach (IKP-4)

MSc. H. Le Thi (IKP-3/IAS-4)
 C. Li (IKP-4) (until 15th January 2019)
 MSc. S. Liebert (IKP-4)
 R. Liu (IKP-2) (since 20th August 2019)
 Dr. B. Lorentz (IKP-4) (until 31st May 2019)
 MSc. K. Luckas (IKP-1) (since 1st September 2019)
 Prof. Dr. L. Ludhova (IKP-2)
 Prof. Dr. Th. Luu (IKP-3/IAS-4)
 M. Maubach (IKP-TA)
 MSc. I. Matuschek (IKP-3/IAS-4)
 J. Meisenberg (IKP-TA)
 Prof. Dr. Dr. h.c. U.-G. Meißner (IKP-3/IAS-4)
 Dr. S. Merzliakov (IKP-4)
 A. Messaaf (IKP-4) (since 1st September 2019)
 Dr. F. Müller (IKP-2)
 S. Müller (IKP-TA) (until 31st May 2019)
 Dr. A. Naß (IKP-2)
 P. Niedermayer (IKP-4) (since 22nd February 2019)
 Dr. A. Nogga (IKP-3/IAS-4)
 Msc. Ö. Penek (IKP-2)
 MSc. G. Perez-Andrade (IKP-1)(since 9th April 2019)
 BSc J. T. Peters (IKP-4)
 MSc. V. Poncza (IKP-4)
 C. Poulwey (IKP-4)
 Dr. D. Prasuhn (IKP-4)
 Dr. E. Prencipe (IKP-1)
 Prof. Dr. J. Pretz (IKP-2)
 D. Prothmann (IKP-TA)
 H. Pütz (IKP-4)
 DP J. Pütz (IKP-1)
 S. Pütz (IKP-4) (since 1st October 2019)
 PD Dr. F. Rathmann (IKP-2)
 Msc. M. Redchuk (IKP-2)
 DI K. Reimers (IKP-4)
 DI M. Retzlaff (IKP-4)
 Msc. M. Rimmler (IKP-4)
 Prof. J. Ritman (IKP-1)
 G. Roes (IKP-TA)
 Dr. B. Roy (IKP-1) (until 13th December 2019)
 D. Ruhrig (IKP-4)
 S. Saad (IKP-4) (until 30th September 2019)
 Dr. A. Saleev (IKP-2)
 Ph.D. habil. S. Schadmand (IKP-1)
 MSc. M. Schever (IKP-2) (until 30th September 2019)
 Dr. R. Schleichert (IKP-2)
 F. Scheiba (IKP-4)
 H. Schiffer (IKP-TA)
 M. Schmühl (IKP-4)
 Msc. A. Scholl (IKP-1)
 M. Schubert (IKP-4) (since 5th July 2019)
 K. Schumacher (IKP-TA) (until 30th April 2019)
 Dr. Th. Sefzick (IKP-TA)
 BSc. A. Sen (IKP-2) (since 1st June 2019)
 Dr. V. Serdyuk (IKP-1)
 Dr. G. Settanta (IKP-2) (since 15th November 2019)
 Dr. V. Shmakova (IKP-2) (since 1st March 2019)
 MSc. N. Shurkhno (IKP-4)
 R. Similon (IKP-4) (since 7th September 2019)
 DI M. Simon (IKP-4)
 H. Simonsen (IKP-TA) (until 30th April 2019)
 BSc. A. Singhal (IKP-2) (since 15th November 2019)
 H. Smitmanns (IKP-2) (until 31st March 2019)
 J. Spelthann (IKP-TA)
 D. Spölgen (IKP-2)
 Dr. R. Stassen (IKP-4)
 G. Sterzenbach (IKP-1)
 Dr. T. Stockmanns (IKP-1)
 Prof. Dr. Dr. h.c. mult. H. Ströher (IKP-2)
 MSc. A. Thampi (IKP-1)
 MSc. M. Thelen (IKP-4)
 Dr. T. Tolba (IKP-1) (until 31st August 2019)
 Dr. R. Tölle (IKP-4)
 J. Uehlemann (IKP-1)
 Dr. Y. Valdau (IKP-4)
 DI T. Vashegyi (IKP-4)
 V. Verhoeven (IKP2) (since 1st July 2019)
 BSc. M. Vitz (IKP-4) (since 1st October 2019)
 MSc. C. Vollbrecht (IKP-2) (since 16th September 2019)
 MSc. T. Wagner (IKP-2)
 L. Werth (IKP-TA) (since 1st August 2019)
 V. Wettig (IKP-TA) (since 1st September 2019)
 Dr. P. Wintz (IKP-1)

PD Dr. A. Wirzba (IKP-3/IAS-4)

K. Wolff (IKP-TA) (since 15th April 2019)

MSc. J.-L. Wynen (IKP-3/IAS-4)

Dr. H. Xu (IKP-1)

MSc. Y. Xu (IKP-2)

H. Zens (IKP-4)

Dr. Y. Zhou (IKP-1)

IKP-1 = Experimental Hadron Structure

IKP-2 = Experimental Hadron Dynamics

IKP-3/IAS-4 = Theory of the Strong Interactions

IKP-4 = Large-Scale Nuclear Physics Equipment

IKP-TA = Technical Services and Administration

L Individual Contributions

Contents

FAIR Related Experimental Activities	63
A PANDA track finding algorithm based on Hough transformations	63
Study of Excited Ξ Baryons in $\bar{p}p$ Collisions with the PANDA Detector	65
Track Finding Using Language Inspired Models	67
Self-calibration Method for the In-Beam Test of the PANDA STT	68
Preliminary Results of a Global Calibration for the PANDA STT	69
Status of a Sampling ADC Based Readout System for Straw Tube Systems	70
First Testbeam Measurements with a Multi-Layered Setup of MuPix8 Sensors for the PANDA Luminosity Detector	71
Study of SiPM Radiation Hardness with Cyclotron Beam	73
A New Package for Raw Data Unpacking in KoalaSof	74
Radiative decays of hyperons at the FAIR Phase-0 experiment of PANDA and HADES	75
Detector tests for the CBM and HADES experiments in proton beam extracted from COSY	76
PAX-project development	78
Storage Ring Based EDM Search	79
A Detailed Single Detector Analysis	79
Controlling Systematic Uncertainties in Search for an EDM in the Storage Ring	80
Spin Tune Measurements for Electric Dipole Moment Searches	81
Extraction of Azimuthal Asymmetries using Optimal Observables	82
Pellet Target Development	83
Development of Rogowski beam position monitors	84
Progress toward a direct measurement of the deuteron Electric Dipole Moment at COSY	85
Spin tune response to three-steerer bumps to aid elements alignment	86
Poster: Search for Electric Dipole Moments at COSY in Jülich – Spin-Tracking Simulations using BMAD	88
Poster: Beam-based alignment at the Cooler Synchrotron (COSY)	89
Poster: Method to search for axion-like particles at storage rings, demonstrated at COSY	90
Poster: Controlling Systematic Error In Search For An Electric Dipole Moment In The Storage Ring	91
Neutrino Physics	92
The OSIRIS source calibration system	92
iPMTs in OSIRIS	93
Improved method for obtaining effective quantum efficiency of the Borexino photomultipliers	94
Modelling liquid scintillator non-linearity in JUNO	95
Online Event Builder for OSIRIS	96
Reconstruction with Deep Learning Method in JUNO	97
Poster: Analytical Multivariate Fit and Sensitivity Studies in the Borexino Solar Neutrino Analysis	98
Poster: Updated statistics and improved analysis techniques lead to 18% precision in Borexino's geoneutrino measurement	99
Accelerator Research	100
Progress of the Lamb-shift Polarimeter for the Molecular Beam Source in Novosibirsk	100
Measurement of the nuclear polarization of pulsed H^- and D^- beams produced by the COSY polarized ion source with a Lamb-shift polarimeter	101
Production of HD Molecules in Definite Hyperfine Substates	103
A new type of laser-induced polarized proton source	104
A Fast Tune Measurement System for COSY	105
EPICS Integration Status	107
Friction force measurements in stochastic cooling	109
Drift Term Optimization Method for Adjustment of Stochastic Cooling Systems	110
Electrostatic detector studies with small-scale electrodes	112
Status Monitoring System for the Polarised Source of COSY	113
Status of the NESP beam line	114
Proton induced neutron yield measurements of different CANS targets	116
Efficiency measurements of a mesitylene based cold moderator system	118
Poster: Real time impedance monitoring for extraction magnets	119
Poster: Experimental studies of stochastic cooling system for HESR	120

Poster: Recent Extensions of JULIC for HBS investigations	121
Further Activities	122
Simulations for the proposed K-Long Facility at Jefferson Lab	122
Search for four quark exotic states with charm and strange quark content	123
Search for Exotic States with the combined BaBar and Belle Data Sets	124
P349 Antiproton Polarization Experiment. Results of 2014/15 data analysis and perspectives	125

A PANDA Track Finding Algorithm Based on Hough Transformations

A. Scholl, T. Stockmanns and J. Ritman

The main tracking detectors in the PANDA target spectrometer are the Micro Vertex Detector (MVD), the Straw Tube Tracker (STT) and Gas Electron Multiplier stations (GEM). The MVD and GEM detectors provide precise point-like position information. In contrast, the STT provides the position of the anode wire and the drift time of the electrons to the anode. This results in a cylinder (isochrone) around the center of the straw tube. Tracks of the charged particles must pass tangentially to the isochrones. Most track finding algorithms are based on hitpoints and do not use the additional isochrone information. For the STT, however, an algorithm is needed that includes this additional parameter. This work presents an approach for an algorithm that is able to deal with this challenge. It is based on a Hough transformation, in which all possible tracks are calculated for each hit. The track parameters are collected in a histogram, the so called Hough space. Hits belonging to the same track are described by the same track parameters and therefore fill the same bin in the histogram. All possible tracks per hit are calculated by solving the Apollonius problem, which is the mathematical description for finding a circle that is tangential to three other circles. By design the Apollonius problem enables the isochrone information to be used. Currently, the algorithm uses two hits and the origin for the calculation. An example for the Hough space of one track and the resulting circle is shown in Figure 1. The black crosses and

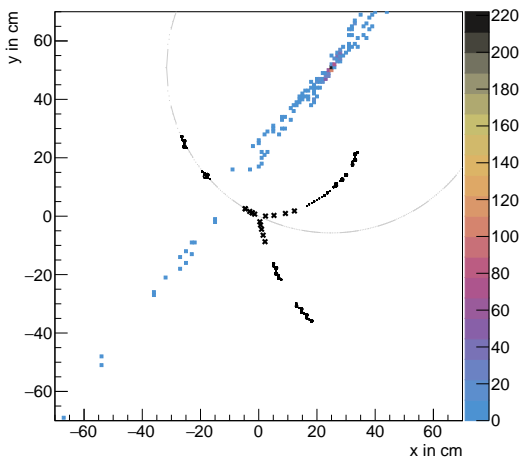


Figure 1: Example for a Hough space for one track. The hits of the MVD, STT and GEM detector are shown in black. The Hough space is represented by a histogram following the color scheme from blue to black. The found track is visualized as a gray circle.

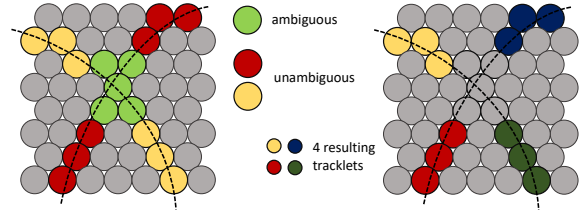


Figure 2: Illustration of the Cellular Automaton.

circles indicate the MVD hit points and the STT isochrones. Entries in the Hough space are visualized as points colored by a color scheme from blue to black depending on the number of entries per bin. The gray circle represents the particle track found by the algorithm.

To improve the performance of the Hough transformation, two different data preselection methods are performed, before the Hough transformation is applied to the data. The first one is based on a Cellular Automaton, which can be performed on the STT data. Here the neighborhood relations of the dense packing of the STT are used. Neighboring hits, which unambiguously result from just one track are collected in tracklets, as illustrated in Figure 2. In a second step these tracklets are used for the Hough transformation to extract the track parameters. Since the cellular automaton cannot be used for MVD and GEM hits, a second preselection method is used for all remaining hits not assigned by the cellular automaton. This method uses the assumption that hits belonging to the same track have a similar azimuth angle. By filling all azimuth angles in a histogram, different tracks can be preselected by dividing the data in subsectors depending on gaps in the azimuth angle distribution (see Fig. 3).

The preselections can divide particle tracks into several tracklets due to loss of hits or crossing tracks. These tracklets are merged in a final step. For this,

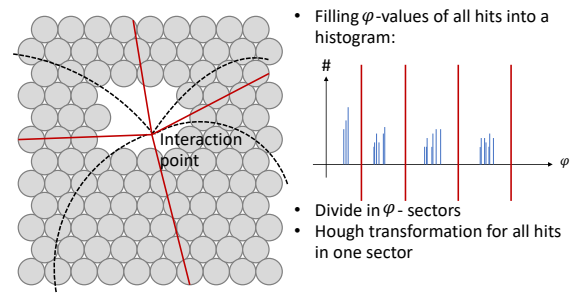


Figure 3: Illustration of the φ -gap algorithm.

three different parameters have been investigated. The first one is the relative overlapping area of two circles, the second and third one describe the difference in position and direction of the tracklets when extrapolated to their midplane. The parameters are described in more detail below.

In the ideal case with no energy loss, tracklets from the same particle track must have the same transverse momentum as well as the same flight direction and sign of its charge. The transcription of this information to the assumption, that charged particle tracks follow a circle in the x-y-plane, leads to a perfect overlap of the circle areas of both tracklets. Since different tracks have different transverse momenta using only the overlapping area leads to a wrong result for tracks with small transverse momentum. Therefore, the overlapping area needs to be normalized. This was done by dividing it by the area of the larger circle. A second method to decide if two tracklets should be merged is based on tracklets belonging to one track only have a small deviation in position and direction when propagating one tracklet to the other tracklet. For this the center plane between the two tracklets is defined and both tracklets are propagated to that plane, resulting in two points and directions at the center plane. The distance between the two points and the difference in angle between the directions is taken as a measure for the two tracks to be merged. The three merging parameters are visualized in Figure 4.

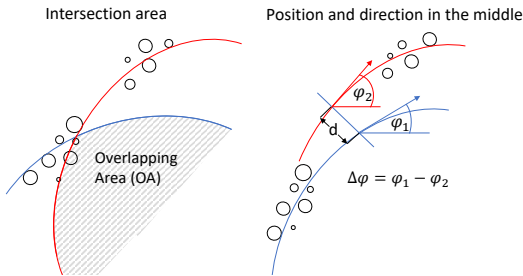


Figure 4: Parameters used to distinguish if two tracklets should be merged.

To find a good ratio of correctly merged tracklets to falsely merged tracklets a receiver operating characteristic (ROC) is used. A set of cut values is chosen with a high rate of correctly merged tracklets (true positive rate: 85.0%) and a low rate of falsely merged tracklets (false positive rate: 3.9%).

The quality of a track finding algorithm is often measured by two quantities. The first one is the probability to find a track, the second one is the ghost ratio. The track finding rate is defined as the ratio of the number of found tracks to all reconstructable tracks. The ghost ratio is the fraction of wrongly found tracks to all reconstructable tracks. Here reconstructable tracks are defined as tracks which have more than three hits in the MVD or more than five

hits in all central tracking detectors (MVD, STT and GEM). To reduce the number of falsely found tracks (ghosts) two cut conditions are included. The investigated cut parameters are the number of GEM hits in a track consisting of only GEM hits and the average number of fired neighbors per hit. To find reasonable cut values again a ROC analysis is performed for both parameters. The ROC analysis is shown in Figure 5. Here the chosen cut parameters are visualized in green. The cuts for these condi-

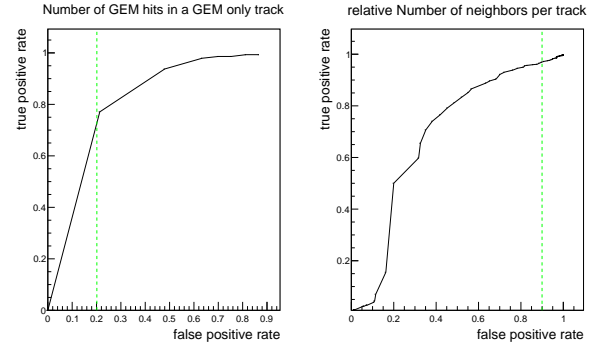


Figure 5: ROC curves for cut parameters to reduce the ghost ratio. Number of GEM hits of tracks consisting of only GEM hits on the left side, average number of neighbors per hit on the right side. The chosen cut parameters are visualized as green dashed lines.

tions need to have a low false negative rate, because the false negative rate represents the number of true tracks which are defined as ghosts. For a track finding algorithm it is more important to have a high efficiency to find true tracks than to reject ghosts. Therefore, conservative cuts have to be chosen. This is the reason why the cut of the average number of neighbors per hit is located in the upper right part of the ROC curve. So the cut to the number of GEM hits of maximum 8 GEM hits per track leads to a false negative rate of only 2.1% with a true negative rate of 36.1%. Whereas the cut to the number of neighbors of maximum 4.45 neighbors per hit leads to a false negative rate of 2.6% with a true negative rate of only 9.5%. Both cuts together lead to a decrease of the ghost ratio of 3.3 percentage points (from 23.9% to 20.6%) and a small decrease in the finding efficiency of reconstructable primary tracks of 0.3 percentage points (from 85.2% to 84.9%). The track finding rate can be divided in primary and secondary tracks. Currently, this track finding algorithm is able to find 84.9% of all reconstructable primary tracks and 57.8% of all reconstructable secondary tracks. The reason for this difference is that the algorithm currently is not designed to find secondary tracks. This will be extended in the future. The track finding algorithm has a ghost ratio of 20.6%. In the future further cut conditions will be investigated to reduce the ghost ratio.

Study of Excited Ξ Baryons in $\bar{p}p$ Collisions with the \bar{P} ANDA Detector

J. Pütz, A. Gillitzer and J. Ritman

Introduction

Understanding the excitation pattern of baryons is indispensable for a deeper insight into the mechanisms of QCD in the non-perturbative regime. Systematic studies have so far been focused on the nucleon excitation spectrum, while our knowledge on the excitation spectra of double and triple strange baryons is still rather poor. A large fraction of the inelastic $\bar{p}p$ cross section is associated to final states containing a baryon-antibaryon pair together with additional mesons, giving access to excited states both in the baryon and antibaryon channel. Combining the $\bar{p}p$ initial states with the large acceptance, the \bar{P} ANDA detector, enables a comprehensive baryon spectroscopy program in the multi-strange sector. The cross section is of the order of μb for final states containing a $\Xi^+\Xi^-$ pair, corresponding to a production rate of $\sim 10^6/\text{d}$ at a luminosity $\mathcal{L} = 10^{31}\text{ cm}^{-2}\text{ s}^{-1}$, is expected. In this study, the focus is on excited Ξ states, in particular the decay of ΛK^- or $\bar{\Lambda} K^+$ is investigated. Two different strategies for the analysis of the reaction $\bar{p}p \rightarrow \Xi^+\Lambda K^-$ and $\bar{p}p \rightarrow \Xi^-\bar{\Lambda} K^+$ are presented.

Event Generation

For this study a total of 20 million signal events were generated with the event generator EvtGen. The data sample consists of both $\Xi^+\Lambda K^-$ and $\Xi^-\bar{\Lambda} K^+$ events with a fraction of 80% resonance and 20% continuum content. If not otherwise specified, the charge conjugate process is implicitly included in the following. A beam momentum of 4.6 GeV/c has been chosen, corresponding to a center-of-mass energy of $\sqrt{s} = 3.25\text{ GeV}$, which is $\sim 300\text{ MeV}$ above the $\Xi^+\Xi^-$ production threshold. The kinematics of the decay given by the chosen beam momentum allows the population of the $\Xi(1690)^-$ and $\Xi(1820)^-$ resonances. Since there are no theoretical predictions or experimental data available, an isotropic angular distribution is used. This simplification assures that the Ξ^- and the Ξ^+ , respectively, are underlying the same detector acceptance. Furthermore the presented selection strategy is not affected by this simplification. In contrast to the Ξ^- and Ξ^+ , the Λ and $\bar{\Lambda}$ have several decay modes with a significant branching fraction. Since this study focuses on the decay of Λ ($\bar{\Lambda}$) into a $p\pi^-$ pair ($\bar{p}\pi^+$) the branching ratio $\text{BR}(\Lambda \rightarrow p\pi^-) = 63.9\%$ is set to 100% to avoid the analysis of unwanted final states. This branching ratio has been corrected in the further calculations.

Reconstruction

For this study two analysis strategies have been used. The first analysis is based on a sequential fit procedure used in most \bar{P} ANDA analyses so far. For the second analysis a full decay tree fit that was recently introduced in the PandaRoot is used. In both strategies, the event reconstruction begins with the final state particles, namely proton, \bar{p} , π^- , π^+ , K^+ and K^- , and proceeds backward through the reaction chain. Since the algorithms for track reconstruction cannot deal with secondary particles, an ideal track reconstruction algorithm has been used. To make the selection more realistic, only particles with at least 4 hits in the inner tracking detectors are selected. Ideal particle identification (PID) is used for the analysis using the sequential fit procedure. The achieved single particle reconstruction efficiency is between 61% and 87%, depending on the particle species and the production point.

The main focus in this strategy is on the reconstruction of composite state particles, namely Λ , $\bar{\Lambda}$, Ξ^- and Ξ^+ , by combining the daughter particles. Different fits, i.e. vertex fits and various kinematic fits, are performed to select the best candidate. At the final stage of the analysis, the $\Xi^+\Lambda K^-$ state, and to the $\Xi^-\bar{\Lambda} K^+$ state in the charge conjugate channel, is combined. To assure that all particles have the same origin, a vertex fit is performed on the candidate. Subsequently, a kinematic fit with 4-momentum constraint is performed on the vertex fitted candidate to match the initial four-momentum of the $\bar{p}p$ system. Candidates with a fit probability of less than 1% in both fits are rejected. However, some candidates passing these cut criteria have momenta not matching the kinematically allowed region. Therefore, an additional cut on the daughter masses is introduced. The sequential fit procedure leads to a total reconstruction efficiency of about 8% for the $\Xi^+\Lambda K^-$ and about 9% for the $\Xi^-\bar{\Lambda} K^+$ sample in the final selection both with a purity of about 98%. Since this analysis has revealed various problems in the fit routines, an additional analysis using a different fitting

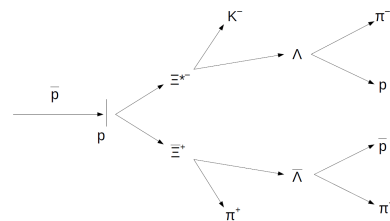


Figure 1: Systematic illustration of the decay chain.

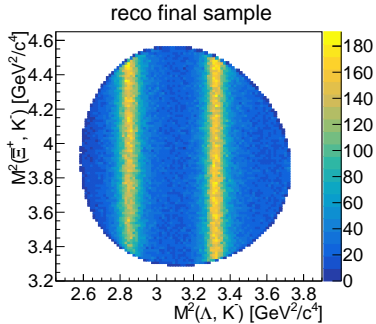


Figure 2: Dalitz plot for the final $\Xi^+\Lambda K^-$ candidates.

scheme is performed.

In the second analysis a full decay tree fit is used. In contrast to the former analysis, no PID information is used for the final state particle selection. A reconstruction efficiency between 68% and 89% is achieved for the final state particles. The selection of the composite particle candidates is only based on a mass window cut around the nominal mass to reduce the combinatorial background. Subsequently, the $\Xi^+\Lambda K^-$ ($\Xi^-\bar{\Lambda}K^+$) system is combined. The full decay tree fit is performed to the resulting candidates. Candidates with a fit probability of less than 0.01% and candidates for which the fit did not converge are rejected. This selection strategy leads to a reconstruction efficiency of 5.4% for $\Xi^+\Lambda K^-$ and 5.5% for $\Xi^-\bar{\Lambda}K^+$, and a purity of 97.7% for both samples. Figure 2 shows the Dalitz plot for the final selected $\Xi^+\Lambda K^-$ sample. Both resonances can be clearly identified as vertical bands. The mass and width of the Ξ resonances are determined by fitting two Voigt functions and a polynomial function to the invariant mass distribution of the ΛK^- or $\bar{\Lambda} K^+$ system. Figure 3 shows the invariant mass distribution of the ΛK^- system including the fitted function. The obtained fit results are summarized in Table 1. The resonance masses and the widths of the $\Xi(1690)^-$ and the $\Xi(1690)^+$ resonances are in good agreement, while the widths of the $\Xi(1820)^-$ and the $\Xi(1820)^+$ resonances deviate significantly from the input values. The reason for this deviation is being investigated.

Assuming a luminosity of $\mathcal{L} = 1 \cdot 10^{31} \text{ cm}^{-2} \text{ s}^{-1}$ during phase one of the PANDA experiment and the reconstruction efficiency of the second strategy, about 38,500 reconstructed events are expected per day.

Table 1: Fit results for the reconstructed resonance masses and widths.

particle	Mass[MeV/c ²]	Width[MeV/c ²]
$\Xi(1690)^-$	1690.0 ± 0.1	30.1 ± 0.5
$\Xi(1690)^+$	1690.2 ± 0.1	30.2 ± 0.5
$\Xi(1820)^-$	1823.0 ± 0.1	22.9 ± 0.4
$\Xi(1820)^+$	1823.1 ± 0.1	22.7 ± 0.4

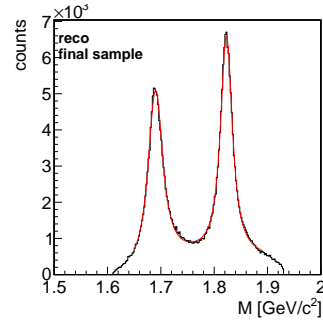


Figure 3: Invariant mass distribution (black) of the ΛK^- system. The function fitted to the distribution is shown as a red line.

Background Studies

A study of the hadronic background using the same algorithms and cuts as for both analyzes is performed. In both cases, no event out of 100 million generated events survived the applied cuts. This non-observation of background corresponds to less than 2.3 events at the 90% confidence level. Assuming a signal cross section of $\sigma_{\text{sig}} = 1 \mu\text{b}$ and a cross section of $\sigma_{\text{bg}} = 50 \text{ mb}$ for the background, a lower limit for the signal-to-background ratio and the signal significance can be estimated. For the full decay tree fit analysis, a lower limit for the signal-to-background ratio of $S/B > 19.1$ for $\Xi^+\Lambda K^-$ and $S/B > 19.5$ for $\Xi^-\bar{\Lambda}K^+$ is estimated. The signal significance is defined as

$$S_{\text{sig}} = \frac{N_{\text{sig}}}{\sqrt{N_{\text{sig}} + F_{\text{bg}} \cdot N_{\text{bg}}}}, \quad (1)$$

where N_{sig} and N_{bg} are the number of signal and background events, respectively. Since the number of generated signal and background events do not reflect the ratio between the corresponding cross sections, a scaling factor $F_{\text{bg}} \approx 6122$ is introduced, taking the correct ratio as well as the corrected branching ratio into account. The lower limit for the signal significance is then calculated to $S_{\text{sig}} > 513$ for $\Xi^+\Lambda K^-$ and $S_{\text{sig}} > 507$ for $\Xi^-\bar{\Lambda}K^+$.

Outlook

The presented work demonstrates that the experimental study of $\bar{p}p \rightarrow \Xi^+\Lambda K^-$ and $\bar{p}p \rightarrow \Xi^-\bar{\Lambda}K^+$, including also the production of resonant Ξ states, is feasible with the PANDA detector. The topology of the decay provides a significant background suppression. To reduce the model dependence, an additional study of events with a different background generator, as well as the study of, e.g. the reaction $\bar{p}p \rightarrow \bar{p}pK^-K^+\pi^-\pi^+$, could be considered.

Since the tracking algorithms in PANDA are not suitable for displaced vertices, a future study should also include the effect of a more realistic tracking algorithm.

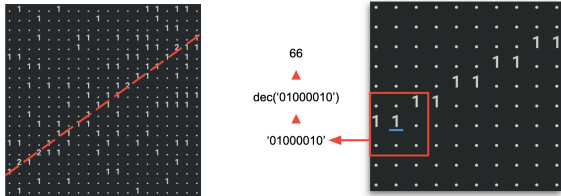
Track Finding Using Language Inspired Models

J. Kannika, T. Stockmanns and J. Ritman

Track finding is one of the processes in the track reconstruction, which is responsible for clustering the detected signals, so-called hits, into different groups of tracks. The track contains physical information of a particle that travels from one location to another location in the detector before it leaves the detector, stops or decays into further particles. This project focuses on implementing a fast track reconstruction algorithm that has higher performance than traditional tracking algorithms. Machine learning is key to this project because it can significantly reduce the computational times by prerecording all possible solutions via a training process. The recorded solutions can be easily accessed within a constant time, which is much faster than doing computations on the fly. In this work, we use language models for recognizing sequences of hits, similar to how language models are commonly used in many applications in natural language processing. The language model is a probability distribution of sequences of words built upon a text corpus. For example, we have:

I do not like green eggs and ham
I do not like them Sam I Am

If we build a language model from the text above, we can get some useful information such as $P(do|I) = 0.66$, $P(am|I) = 0.33$. These values are conditional probabilities telling that the chance for the word “I” to be followed by “do” is 66%, and to be followed by “am” is 33%. These conditional probabilities are calculated in this way $P(do|I) = \frac{\text{count}(I\ do)}{\text{count}(I)} = \frac{2}{3} = 0.66$, and $P(am|I) = \frac{\text{count}(I\ am)}{\text{count}(I)} = \frac{1}{3} = 0.33$. The calculation is based on a bigram model, which means the probabilities are calculated from the frequency of single words, and the frequency of two consecutive words. Higher-gram models such as trigram, four-gram, and so on also exist. These language models are called *n-gram* models. We created a toy data



(a) Track with background noise (b) Neighbor pattern is calculated from states of neighbor hits.

Figure 1: Toy data generator can produce hits and noise as shown in Fig. 1a and Fig. 1b. The numbers with white color indicate the number of hit or noise signals, and the dots indicate no signals.

generator which can generate hits and noise on a square lattice to test our track finding ideas. An example of data generated by the generator is shown in Fig. 1a. We built several *n*-gram models for tracking *neighbor patterns* and *moving directions*. The neighbor patterns are numbers representing states of the hits and their neighbor cells, see Fig. 1b. The numbers are calculated from states of the neighbor cells that can be treated as binary numbers. These binary numbers are then converted into decimal forms. The vocabulary of possible words for this feature is $\Sigma = \{n|n \text{ is an integer, and } 1 \leq n \leq 256\}$. Note that, the neighbor pattern 0 is ignored since we do not consider discontinuous track at this stage. We trained 2-gram, 1-skip-2-gram and 2-skip-2-gram models for this feature. The next feature is the moving directions, which are possible moving angles from one point to another neighbor point on the square lattice. The vocabulary for this feature is $\Sigma = \{0, 45, 90, 135, 180, 225, 270, 315\}$. We trained 5-gram, 10-gram and 15-gram models for this feature.

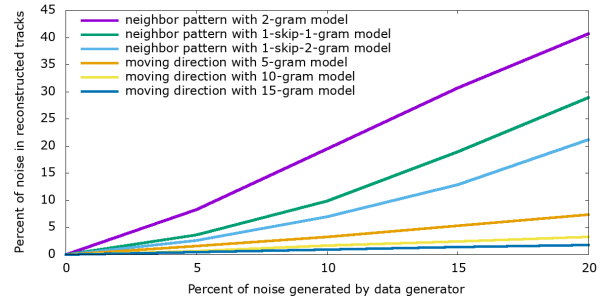


Figure 2: Results of track finding using the trained *n*-gram models to track neighbor patterns and moving directions in the presence of 0 – 20% noise.

According to results from Fig. 2, we can conclude:

- both neighbor pattern and moving direction are potential features for the track finding task,
- the 2-skip-2-gram model performs better than the 2-gram and the 1-skip-2-gram models for tracking neighbor patterns,
- the higher-gram models perform much better than the lower ones,
- the track finding time scales linearly with the number of hit points.

The next step is to study correlations between both the neighbor pattern feature and the moving direction feature by using a multi-layer perceptron. We are currently training and experimenting on the multi-layer perceptron models to see if the accuracy of the track finding task can be significantly improved compared to our previous models.

Self-calibration Method for the In-Beam Test of the PANDA STT

G. Perez-Andrade, P. Wintz and J. Ritman

The PANDA Straw Tube Tracker (STT) will be located in the solenoidal magnetic field of the Target Spectrometer and will perform charged particle tracking, momentum reconstruction and particle identification (PID) based on energy loss measurements (dE/dx) in the straw gas. In particular, $p/K/\pi$ separation in the momentum region up to ~ 0.8 GeV/c is envisaged. The STT straws will be arranged in 19 axial and 8 stereo layers enabling the 3D-reconstruction of the helical trajectories. Moreover, the self-supporting structure and close-packed straw layer modules yields a minimal material budget of 1.2% (X/X_0) [1].

In-beam measurements with a STT test system have been conducted at COSY, using proton and deuteron beams in a momentum range of $\sim 0.6 - 2.5$ GeV/c. Similar to the PANDA case, where up to 27 straw layers will be available, the test setup consisted of a stack of eight close-packed straw layers, yielding about 24 straw hits per track.

The straw calibration procedure includes: i) a fourth degree polynomial parametrization of the relation between the isochrone radius $r(t_i)$ and the electron drift time t_i , $r(t_i) = \sum P_i \times t^i$ (Figure 1), ii) the determination of the position of the straws and iii) the determination of the wire displacement from the straw axis.

The $r(t_i)$ curve is used for the track reconstruction by fitting a line tangent to all isochrones associated to a track. The best line fit is obtained through the minimization of the *track residuals*, defined as the distance from the reconstructed track to the individual isochrone radius in each hit straw. With no systematic error the residuals would be Gaussian distributed around zero. However, deviations of up to $200 \mu m$ is possible resulting from a slight wire shift from the straw center due to *e.g.* gravitational sag or misalignment. Depending on if the track crosses above or below the wire, the ionization electrons are registered with longer or shorter drift times and therefore have larger or smaller isochrone radii. The deviation is corrected by shifting the isochrone parametrization by a constant r_0 corresponding to the mean track residual. Such corrections are channel dependent and are obtained from tracks crossing above or below the straw center separately. The track reconstruction is performed again after the correction and the process is repeated until the average deviation is negligible. The spatial resolution is obtained from the width (σ) of the residual distribution. Throughout the tracking procedure the rejection of single outliers hits is performed, in order to discard signals from *e.g.* δ -electrons. The tracks residual distribution obtained after the 9th it-

eration of a proton dataset at $p_{beam} = 0.75$ GeV/c is shown in Figure 2. The values are distributed around zero with a resolution of $\sigma = 122 \mu m$. The visible tails outside the distribution can be explained by δ -electrons still remaining after the outlier rejection, indicating that a stricter rejection could be necessary.

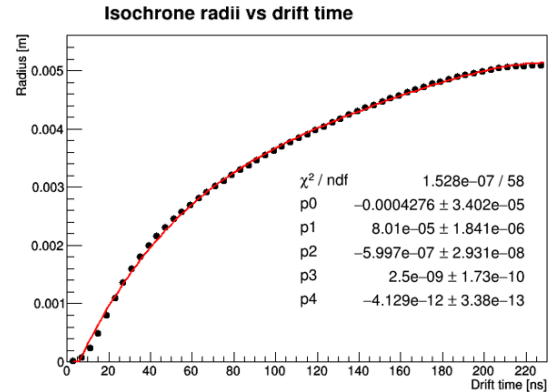


Figure 1: Isochrone radius (m) versus electron drift time (ns). The red curve shows the polynomial fit to the data points (black).

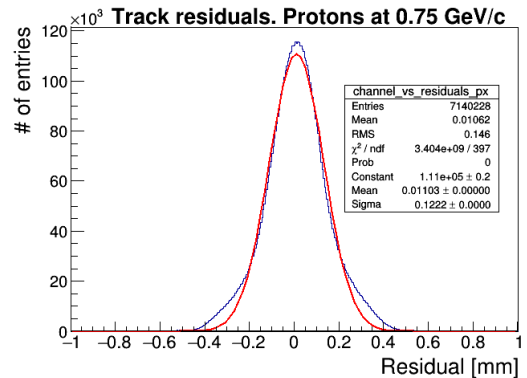


Figure 2: Track residuals distribution for a proton data set obtained after the 9th iteration showing a spatial resolution of $\sigma = 122 \mu m$. The initial spatial resolution was of $\sigma = 180 \mu m$.

The iterative process described in this report is referred to as *self-calibration* and has proven to improve the initial spatial resolution values of $\sim 190 \mu m$ to better than $130 \mu m$, surpassing the PANDA design goal resolution of $\sim 150 \mu m$.

References

- [1] PANDA COLLABORATION, Technical Design Report for the PANDA Straw Tube Tracker (2012) <https://arxiv.org/abs/1205.5441>

Preliminary Results of a Global Calibration for the PANDA STT

G. Perez-Andrade, P. Wintz and J. Ritman

Optimization of the calibration method developed for the in-beam test measurements for the PANDA-STT is in progress. Even though spatial resolutions better than the PANDA design goal of $150\ \mu\text{m}$ are already achieved with the existing self-calibration [1], its processing time depends on the number of iterations that each dataset requires to reach the optimal resolution. Moreover, the calibration parameters are obtained for each dataset independently and since at the PANDA experiment the particle momentum will be available after the track reconstruction, the ideal case is to have single dE/dx -independent calibration parameters. In addition, the latter is beneficial in the case of runs with very low statistics in specific straws. The ongoing work focuses on the simplification of the method investigating the possibility of using a common calibration for all data samples.

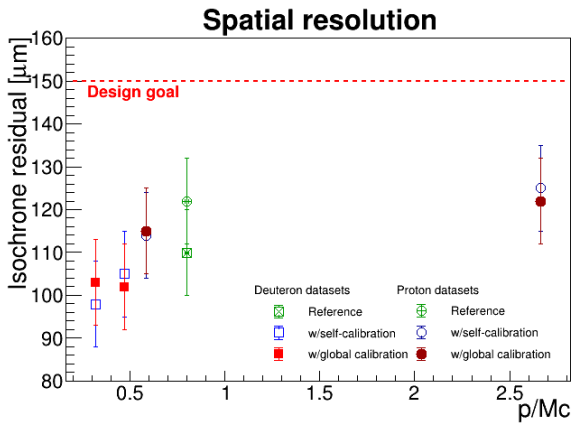


Figure 1: Spatial resolution results achieved for two proton and two deuteron datasets using self-calibration and global calibration.

Three deuteron and three proton datasets at different beam momenta have been used. The self-calibration of the chosen datasets showed that resolution values better than $130\ \mu\text{m}$ are achieved already after the fifth iteration and the value converges after the eighth iteration. Of the three datasets for each particle species, the one with the highest number of illuminated straws was chosen to be used as a *reference* for the other datasets for that same particle species. The $r(t_i)$ parametrization and the systematic deviation correction obtained from the last iteration self-calibration of the reference sample was afterwards used as the input to perform the tracking of the remaining samples without further iterations. The latter is called *global calibration*.

The spatial resolutions achieved with the self and the global calibration of the datasets together with its reference sample are shown in Figure 1. It is

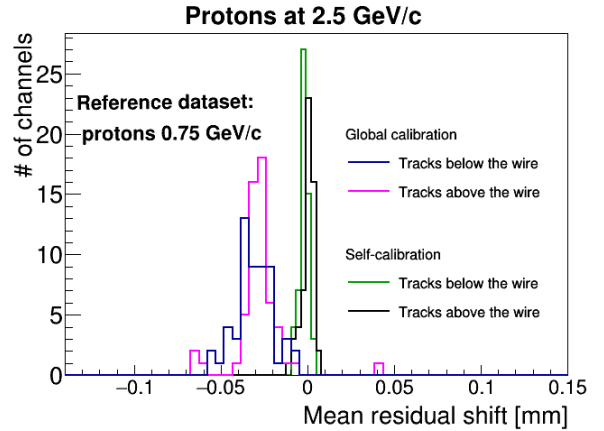


Figure 2: Track residuals obtained after the global calibration and tracking was performed in a dataset of protons at $p_{beam} = 2.5\ \text{GeV}/c$.

observed that the difference between the results obtained from both methods is smaller than $5\ \mu\text{m}$, showing that a good resolution is also achieved by the global method.

To verify that the global calibration successfully corrects the systematic error connected to the wire displacement, a comparison between the final mean track residuals obtained from the global and the self-calibration of the same proton beam dataset at $2.5\ \text{GeV}/c$ are compared in Figure 2. For this, about 9 specific straws per layer (56 in total) were selected from the most uniformly illuminated area of the setup. As expected, the mean residuals are closer to zero for the self-calibration, where most of the values are distributed around $\mu_{self_{above}} = 1\ \mu\text{m}$ and $\mu_{self_{below}} = -2\ \mu\text{m}$ for tracks above and below the straw center, respectively. On the other hand, the global calibration results in broader distributions around the mean values of $\mu_{global_{above}} = -28\ \mu\text{m}$ and $\mu_{global_{below}} = -31\ \mu\text{m}$. However, the difference between the mean values in both cases is less than $30\ \mu\text{m}$. Assuming standard error propagation, this difference worsens the overall resolution by only about $4\ \mu\text{m}$, and is considered to be negligible.

All datasets studied follow the same behaviour as the $2.5\ \text{GeV}/c$ proton beam. These comparisons show that the difference between the results achieved with the self-calibration and global calibration is minimal, supporting the possibility to adopt a common particle momentum independent calibration.

References

- [1] G. Perez-Andrade et al., Self-Calibration Method for the In-Beam Test of the PANDA STT, contribution to this annual report.

Status of a Sampling ADC Based Readout System for Straw Tube Systems

P. Kulesa¹, A. Erven², T. Hahnraaths von der Gracht¹, L. Jokhovets², H. Ohm¹,
K. Pysz³, J. Ritman¹, C. Roth², M. Schlösser², T. Seifick¹, V. Serdyuk¹, S. van Waasen², P. Wintz¹

¹IKP, Forschungszentrum Jülich, D-52425 Jülich, Germany

²ZEA2, Forschungszentrum Jülich, D-52425 Jülich, Germany

³H. Niewodniczański Institute of Nuclear Physics, PL-31342 Cracow, Poland

This report presents the status of a high-density, free-running DAQ system based on sampling ADCs (HMCAD1520) and the subsequent signal processing in an FPGA (VIRTEX7). The system has been designed for the timestamped readout of detector systems consisting of a large number of straw tube detectors. These need to deliver time information for precise particle tracking and signal charge information for energy-loss measurements and particle identification. The required parameters for the signal arrival time and signal charge can be derived continuously at hit rates up to 1 MHz per channel. A time resolution of typically 1 ns can be achieved.

The system provides more than 2000 ADC channels per readout crate for up to 250 MHz sampling frequency or 500 channels for up to 1 GHz. It is housed in a crate based on the OpenVPX standard, using a modified backplane with space for 14 payload and 2 management/controller boards.

The digital boards with ADC and FPGA are located on the front side, while the rear side is occupied by analog boards carrying compact signal amplifiers, see Fig. 1. The backplane guides analog signals into the sampling ADCs and it connects ADCs with the controllers. It also provides direct interconnections between the digital boards. The system can be run also without dedicated management/controller board and data can be transferred directly from the digital board via USB3 or SFP+ on add-on connector. The analog board shown has amplifiers with a gain of 400 and it is optimized for straw tube signals. Without any pre-amplification, analog signals from the detector are transmitted to the amplifiers via Samtec coax ribbon cables. 5 Samtec input connectors with 32 channels each deliver signals from a total number of 160 channels to each board. This setup has been used for straw tubes readout during beam times at COSY. A tracking example, together with the collected analog pulses can be seen on Fig. 2.



Figure 1: Top: The OpenVPX crate with one ADC processing board and one analog board inserted, (left) front side with processing board, (right) rear side with the preamplifier board and one Samtec 32 channel coaxial cable. Bottom: (left) The ADC board, the central FPGA is visible in the lower half of the board and the ADCs behind. (right) Preamplifier board with an adapter for direct coupling of signals into the preamplifier board.

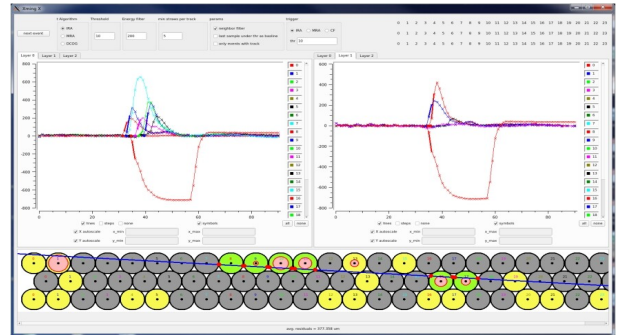


Figure 2: Straw detector signals and a sketch of a particle track passing through an array of straw tubes.

A passive analog board together with the preamplifier version with amplification factor 1 permits direct coupling of signals into the sampling ADCs to enable the system to be used as a universal tool for any kind of detector signal. For example, to examine analog signals from the PASTTREC ASIC, it delivers analog signals from each straw tube plus digital outputs from the discriminators. These measurements will permit a direct comparison of the ToT technique for signal-charge measurements with the ADC technique. Further development of the FPGA firmware for real time signal processing algorithms is in progress.

First Testbeam Measurements with a Multi-Layered Setup of MuPix8 Sensors for the PANDA Luminosity Detector*

R. Hagdorn[†], F. Feldbauer, M. Fritsch, G. Reicherz, T. Weber, Ruhr-Universität Bochum, Germany

Abstract

The goal of the PANDA Luminosity Detector (LMD) is the continuous measurement of the instantaneous luminosity as well as the determination of the integrated luminosity with a precision of at least 3%. Using multiple layers of High Voltage Monolithic Active Pixel Sensors (HV-MAPS) the luminosity is determined by measuring the tracks of elastically scattered anti-protons at small angles.

To test the parallel readout of multiple sensor prototypes several beam tests at COSY were performed. A multi-layer setup consisting of four MuPix8 sensors was used for data taking. In the obtained data, spatial and temporal correlations between the layers could be observed.

The MuPix8 Sensor Prototype

The MuPix family of chips is based on the HV-MAPS concept, combining the advantages of a monolithic design with the fast charge collection and signal generation of a fully depleted sensor by applying a high bias voltage to the substrate[1]. With a physical size of $10.8 \times 19.5 \text{ mm}^2$ the MuPix8 is the first large scale prototype. Its active area consists of 128×200 pixels with a single pixel size of $81 \times 80 \mu\text{m}^2$. It is divided into three submatrices, which use different techniques to transmit signals from the analog pixels to the readout part at the chip's periphery in order to counteract crosstalk. Since the depletion layer is only $10 \mu\text{m} - 15 \mu\text{m}$ thick, the sensor can be thinned down to $50 \mu\text{m}$, greatly reducing the amount of multiple scattering.

Testbeam with a Four Layer MuPix Telescope

Two beam tests using the four layer MuPix telescope were performed at COSY in May and September of 2019. Figure 1 shows the setup in the JESSICA hall. The four sensors were read out using a TRBv3 FPGA board[2] with one chip connected to each peripheral FPGA. From the TRB the data was sent via an ethernet connection to a control PC outside the hall. Three of the four layers were used as tracking layers with fixed threshold and HV settings. Data was taken at different threshold voltages and high voltages for the remaining layer. The goal is to determine the dependence of tracking efficiency and noise rates on those quantities.

*PANDA is supported by the BMBF

[†]rhagdorn@ep1.ruhr-uni-bochum.de



Figure 1: The MuPix8 beam telescope

During the beam time in May only matrix A of the MuPix8 was read out. Hit correlations between the pixel rows of two layers can be seen in Fig. 2. At low beam intensity the correlation plot is shown on the left. The beam was distributed evenly over the whole sensor by inserting a beam monitoring chamber in the beam's path. For the second measurement at a higher beam intensity, the row correlations clearly show a region with a reduced number of events between rows 85 and 99, since the readout state machine of the MuPix was too slow to handle the hit rate. Additionally, the monitoring chamber was removed, which resulted in a narrower beam spot, with most of the hits occurring in the upper rows.

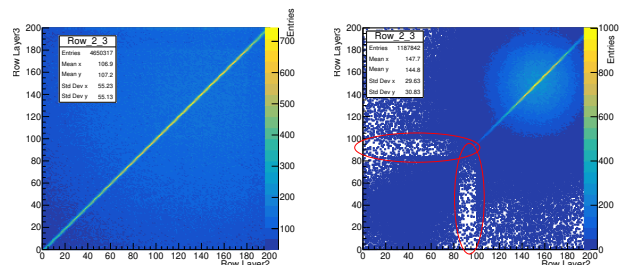


Figure 2: Row correlations between layers 2 and 3 for low (left) and high (right) beam intensity. May 2019 testbeam. Red ellipses show row bands with readout errors.

In September all three submatrices were read out. In addition, by choosing different settings for the readout state machine, the previous readout errors could be avoided (Fig. 3 left).

Between matrix A and B/C an obvious difference in hit sensitivity with respect to the threshold setting was seen (Fig. 3 right). At relatively high thresholds, a greater number of pixels in matrices B and C were insensitive to hits than in matrix A. Conversely, at lower thresholds, matrices B and C were much less affected by crosstalk than matrix A. During both beam times unshifted timestamp correlations between the

layers were seen, indicating that the timestamp counters of all four layers were set synchronously.

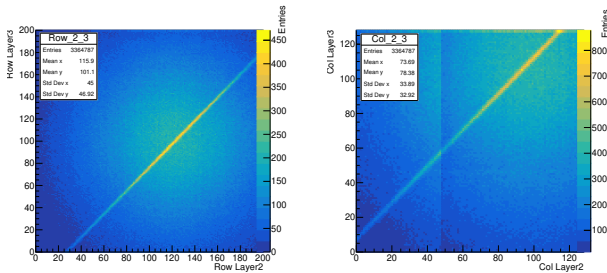


Figure 3: Row (left) and column (right) correlations between layers 2 and 3. September 2019 testbeam. Shifts along the x - and y -axes indicate a misalignment of the layers.

The test in September also showed, that our current readout firmware for the TRBv3 is incompatible with the implementation of SODAnet, which will be used as the global timing system for the final experiment. SODA compatible alternatives to the TRBv3 are currently being investigated.

Conclusion

The results from the two beam tests show that the parallel readout of four MuPix8 sensors is possible as is the readout of all submatrices of a single MuPix. Spatial and temporal correlations between the individual layers of the telescope setup have been observed. The next step is an in depth analysis of the testbeam data with respect to the efficiency and noise behaviors of the sensor at different thresholds and high voltages.

The current focus is also on finding alternatives to the use of the TRBv3 board as well as commissioning the first LMD prototype which will consist of four modules each containing four MuPix8 sensors glued to a CVD diamond carrier and bonded to flexprint cables for powering and data transmission.

References

- [1] I. Perić, “A novel monolithic pixelated particle detector implemented in high-voltage CMOS technology”, *Nucl. Instr. And Meth. A*, 582, Dec. 2007, pp. 876-885.
doi:10.1016/j.nima.2007.07.115
- [2] trb.gsi.de

Study of SiPM Radiation Hardness with Cyclotron Beam

D. Grzonka, J. Ritman, T. Sefzick, T. Tolba¹

Radiation hardness is an important topic for photo-sensors in detection systems subject to high integrated dose. The increased use of SiPMs as light readout sensors requires detailed studies of the effects of radiation exposure to their performance. A large number of studies concerning radiation hardness of SiPMs for different devices, radiation type and energy are available, but the variations in the detailed sensor structure don't allow for common statements on the SiPM performance and functionality after the exposure, which also depends on the detected signal. Motivated by the SiPM application at the barrel time of flight (barrel-ToF) detector of \bar{P} ANDA, we want to explore the radiation effects on different SiPMs that might be used for the signal readout.

The first step of these studies was to perform irradiations at the IKP cyclotron beam. SiPMs with an area of $3 \times 3 \text{ mm}^2$ from AdvanSid, Hamamatsu, KETEK and SensL were mounted in a light-tight box together with 4 dosimeters to adjust and determine the radiation dose. The first irradiation test was performed with an integrated dose of 10 Gy. The results show a drastic degradation in the light detection sensitivity of the irradiated devices, as can be seen in Fig.1 with a typical SiPM signal before and after irradiation. The dark-current increased by orders of magnitude with a high dark-count rate associated with a strong increase in the noise level from 2 mV to more than 100 mV. In addition measurements of the I-V curves before and after irradiation showed a reduction of the breakdown voltage in all SiPMs by up to about 2V. In order to observe the degradation effect

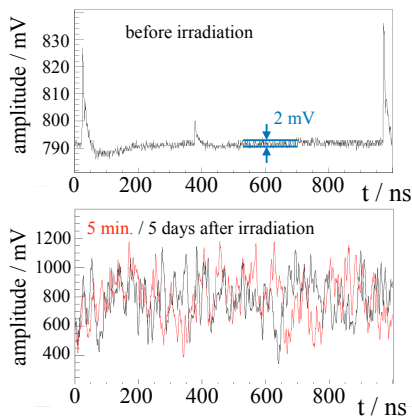


Figure 1: Typical SiPM signal before and after an irradiation with an integrated dose of 10 Gy. As example the signals from the SensL type MicroFC-30035 are shown but all tested SiPMs exhibit similar behavior. The noise was on the order of 2 mV before irradiation and increased to more than 100 mV after irradiation.

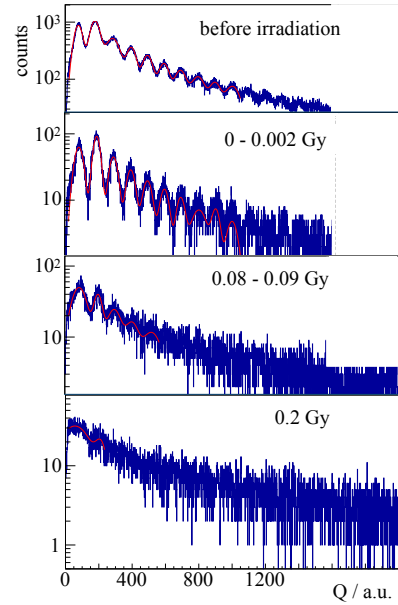


Figure 2: Distribution of the signal charge for increasing irradiation on the AdvanSid SiPM. Before irradiation the single photoelectron peaks are well separated and at an integrated dose of only 0.2 Gy the peak structure is mostly removed.

as a function of integrated dose, measurements during the irradiation were performed with a dose rate of 0.001 Gy/s. In Fig.2 the charge distribution of the AdvanSid SiPM signals is shown with increasing dose. Before irradiation the single photoelectron peaks are well separated, while already at a very low dose of 0.2 Gy the structure is nearly completely dissolved.

The studies have shown that even a very low radiation dose has a strong effect on the performance of the SiPMs which complicates the light detection at the level of a few photons. However, the irradiated SiPMs are still operational with avalanche behavior, which was tested with light pulses generated by a laser LED.

The radiation hardness studies will be continued at COSY with proton momenta up to 3 GeV/c, which is comparable to the expected radiation field in the barrel-ToF area.

References

- [1] COSY Proposal D012/D012.1, CBAC 10/11, www.ikp.fz-juelich.de/CBAC/en/cbac.shtml.

¹ current address: Universität Hamburg, Institut für Experimentalphysik, Luruper Chaussee 149, 22761 Hamburg

A New Package for Raw Data Unpacking in KoalaSoft

Yong Zhou and Huagen Xu

KoalaSoft is a simulation software framework for the KOALA experiment written in C++. It is developed based on the *FairRoot* framework[1]. The calibration, reconstruction and analysis jobs are also integrated into *KoalaSoft* thanks to the task-based design of *FairRoot*. Initially, these tasks were developed for simulation data. On the other hand, raw data from beam tests are decoded by the DAQ software called *KoalaEms*, the output format of which is not compatible with *KoalaSoft*. The same algorithms need to be implemented twice, which is not only error-prone for developing but also a big burden for maintainence.

To reuse the same tasks on both simulation and test beam data, a new package called **unpack** is developed in *KoalaSoft*. The most important class in the package is *KoaEmsSource*, which inherits *FairSource* and recognizes the EMS data format[2]. Two daughter classes from *KoaEmsSource* are also defined for network stream and disk file respectively, so that the package can be used in both online and offline analysis.

Key steps in a decoding job are illustrated in Fig.1 (faded blue). The steering class *KoaRunOnline* first reads in the channel mapping parameters with the help of *KoaEmsConfig*, and then hands over the control to the event loop defined in *KoaEmsSource*. Each step inside the loop is represented by the corresponding class as follows:

- *KoaUnpack* unpacks data from the digitization modules (TDC, QDC, ADC) in EMS. Each Instrumentation System (IS)[2] in EMS should have its own descendent from *KoaUnpack*.
- *KoaEventAssembler* retrieves the unpacked data from all modules and assembles them into a full KOALA event based on the timestamps.
- *KoaRawEventAnalyzer* analyzes the new assembled KOALA event, remaps the channel ids, fill the user-customized histograms, pushes the remapped event data to *FairRoot* data buffer and/or stores it on disk.

The data flow in the package is also shown in Fig. 1 (faded grey). The new decoded event is pushed to the task chain of *FairRoot* in the end. A task implemented in class *FairRawEventTransform* is attached immediately to transform the format into a *TCloneArray* of *digis*, which is the same as the simulation output format. All the following tasks can now access this event without limitation. In this way, the simulation and beam test analysis are merged together seamlessly.

To add more flexibility in the usage of the package, two alternative event formats are available for out-

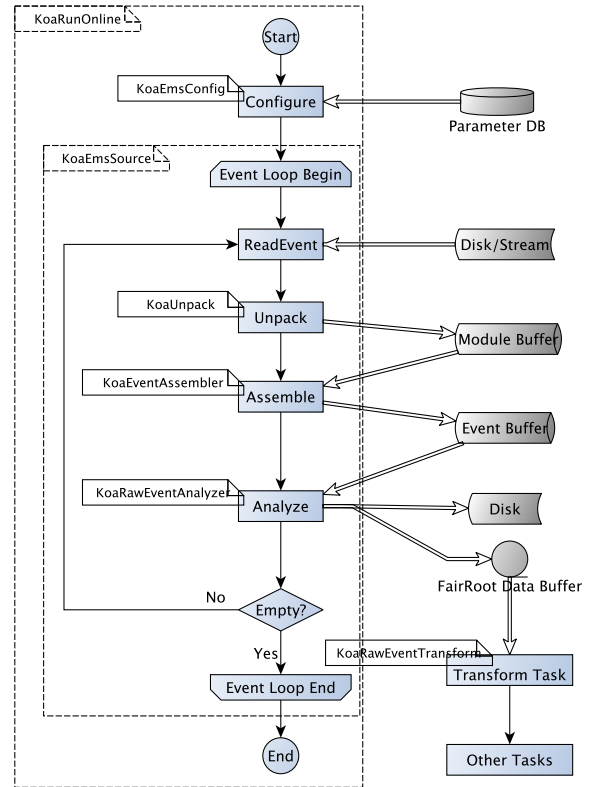


Figure 1: Key steps, important classes and the data flow in the **unpack** package

put. The first one is *module-based* format, which will be useful when setting up new EMS systems. The second one is *bloc-event* format, which simply is an aggregation of multiple arrays with detector channel id as index. This format is useful during the development of calibration algorithm.

Finally, the online program for beam test data monitoring has been redesigned based on the new package. Since the stream data from DAQ can now be injected into a full calibration, reconstruction and analysis task chain, the results of all these tasks are possible for online display as well. For this purpose, a centralized histogram server class is designed based on *THttpServer*. A task just needs to register its histograms or graphs in this server at the beginning of the run and they will show up automatically on the online display. The initial version of the program is now under active test.

References

- [1] <https://github.com/FairRootGroup/FairRoot>
- [2] K. H. Watzlawik et al. IEEE Transactions on Nuclear Science 43 (1996): 44

Radiative decays of hyperons at the FAIR Phase-0 experiment of PANDA and HADES

W. Esmail, T. Stockmanns and J. Ritman

The electromagnetic (EM) decay of excited hyperons is a very sensitive probe of its structure and it is part of the physics program of FAIR phase-0 (known as PANDA@HADES). EM decays will significantly benefit from the Forward Detector (FD) that is based on PANDA straw tubes. The FD will extend the HADES acceptance towards small polar angles between 0.5° to 6.5° , which is crucial for the hyperon reconstruction. The reaction under investigation is:

$$p(4.5\text{GeV})p \rightarrow pK^+Y^* \rightarrow pK^+(\Lambda\gamma)$$

where Y^* stands for $\Sigma(1385)$, $\Lambda(1405)$ or $\Lambda(1520)$ hyperons. The PLUTO event generator is used to generate events of this reaction at a beam kinetic energy of 4.5 GeV. The hyperon is allowed to decay via the EM transition $Y \rightarrow \Lambda\gamma$ inside PLUTO. Later in the event reconstruction process the Λ is reconstructed from its most common decay mode $\Lambda \rightarrow p\pi^-$ (BR 64%).

The first step in the signal reconstruction is the selection of events with the correct particle candidates namely p , K^+ and π^- . For this purpose an Artificial Neural Network (ANN) is used. The ANN was able to classify different classes (i.e particle species) with 97% classification accuracy.

In the second step the intermediate Λ hyperon can be reconstructed from its decay products namely p , and π^- in combination with topological cuts. The Distance of Closest Approach (DCA) between p , and π^- tracks $d_{p\pi^-}$ is expected to be small. Therefore, we require $d_{p\pi^-} < 10$ mm to reduce combinatorial background. Considering momentum and energy conservation during the Λ decay, the proton with its mass close the Λ mass, should fly almost in the same direction as the Λ , while the π^- will have a different direction. The DCA between the p track and the primary vertex $d_{p,pvtx}$ is required to be smaller than the DCA between the π^- track and the primary vertex $d_{\pi^-,pvtx}$. One last topological cut is introduced, the cosine of the angle between the spatial vector, pointing from the primary to the secondary vertex and the momentum vector of the reconstructed Λ , which should be $\cos\theta > 0.95$. Thanks to the FD, Lambdas can also be reconstructed standalone at the FD. But because no particle identification is available at the FD, a different strategy used to reconstruct Λ in the forward direction. That is, it is assumed that all tracks in the FD are p tracks. Then, all possible combinations are formed between π^- tracks from HADES and all tracks from the FD.

The DCA ($d_{p\pi^-}$) between the two tracks is calculated and pairs with $d_{p\pi^-} > 20$ mm are rejected. In addition, the cosine of the angle between the spatial vector, pointing from the primary to the secondary ver-

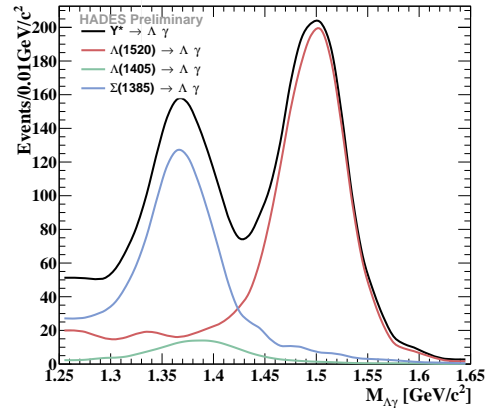


Figure 1: The invariant mass distribution of the reconstructed hyperons scaled according to the cross section.

tex, and the momentum vector of the reconstructed Λ is required to be $\cos\theta > 0.95$.

Photon candidates are identified as an energy cluster in the EMC that is spatially uncorrelated with the RPC hits. In addition to that photon candidates are required to have a velocity $\beta > 0.95$, and an energy deposition > 0.2 GeV.

Finally, the hyperon is reconstructed from the identified γ , and the combined Λ sample. A reconstruction efficiency of about 0.2% is achieved on average. Cross sections are calculated for Dalitz decays [1] and adapted for real photon decays by multiplying by a factor of α . Figure 1 shows the expected $\Lambda\gamma$ invariant mass distribution scaled to the cross section.

In addition, a study of background contributing channels is on going. Several reactions at the same beam kinetic energy mimic the signal, therefore it is necessary to introduce discriminating variables. It is expected that the $pK^+\Lambda\pi^0$ final state will be the most difficult to suppress since there is a high probability that one of the photons from the π^0 decay is not measured. The $pK^+\Lambda$ missing mass of the is one discriminating variable as the signal is expected to peak at zero (photon mass). In addition the opening angle between the Λ and γ in the hyperon rest frame (Y^*) is another discriminating variable, where the Λ and γ are expected to fly back-to-back, while the background should have flatter distribution.

References

- [1] K. Nowakowski and J. Kubo's "Feasibility studies of production and electromagnetic decay studies of hyperons for HADES", EPJ Web Conf. **199** (2019).

Detector tests for the CBM and HADES experiments in proton beam extracted from COSY

J. M. Heuser¹

High-intensity proton beam extracted from COSY has been used for testing prototype detectors of the CBM [1] experiment at FAIR and the HADES [2] experiment at SIS-18 relevant for operation in the FAIR phases 0 and 1.

CBM Silicon Tracking System Module

The CBM experiment has entered a phase in which the main detector system test activity has been shifted to the mCBM (“miniCBM”) [3] demonstrator experiment at GSI/SIS-18. mCBM became operational since late 2018. Initially being without explicit beam during SIS-18 recommissioning in December 2018, first beam delivery took place in March 2019, however limited to hours of parasitic beam from the HADES experiment as the main user then. A further beamtime for mCBM will take place at the beginning of 2020.

The March 2019 mCBM beamtime yielded plentiful information from the combined operation of detector systems: miniature/demonstrator versions of Silicon Tracking System (STS), Muon Tracking Chambers (MUCH-GEM), Ring Imaging Cherenkov Detector, Time-of-Flight system with its T0 diamond detector and RPC wall. A hadron calorimeter (Projectile Spectator Detector) has been added from the December 2019 run. The read-out was integrated in one full chain of data acquisition from the front-ends to the computing center Green Cube. Central aspect of the beamtimes is combined operation and data taking of the systems, allowing for studying various correlations ranging from data rates, as function of beam intensity and target thickness, to timing and eventually track reconstruction. With beam intensities up to 10^8 Ag ions/s and collision rates up to 10 MHz, standard CBM operation conditions and high data rates > 2.5 GByte/s peak were achieved. Detailed detector studies took place but were naturally restricted to reaching configuration readiness. Specific detector investigations are therefore still well placed in different beam campaigns than mCBM, e.g. using the focused “pencil beams” at COSY rather the particle spray from SIS-18 beams directed onto a target, with the detectors being the object to be studied and not the reference detectors.

The test carried out in the JESSICA cave at COSY in November 2019 addressed a newly assembled STS module, shown in Fig. 1, comprising a further developed front-end electronics board (FEB-8) with the new ASIC version STS-XYTER v2.1 and new low-voltage regulation. This was the first operation of a fully functional and noise-optimized STS module in beam. The module was mounted onto a carbon fiber support ladder and installed on a frame in a mobile test station. It was operated with specific power regulating and distributing electronics and a full prototype CBM data-driven read-out chain, along with a scintillating fiber hodoscope. The test focused on

scanning the sensor position with respect to the proton beam ($p = 2.7$ GeV/c, $E_{kin} = 1.92$ GeV) to raster the sensors’ segmented active area and map out its response at various front-end electronics settings and different beam intensities at known beam energy. The targeted STS system noise of around $1000 e^-$ was demonstrated (Fig. 2). Measured signal is shown in Fig. 3 depicting the beam spot for one spatial coordinate and the signal distribution for one read-out ASIC, i.e. 128 channels, all in ADC units. Detailed analysis of the data taken is in progress to yield robust signal calibration and thus the signal-to-noise ratio, together with the particle detection efficiency in the small test system of STS module and the fiber tracking telescope.

The results contributed to concluding the ASIC Engineering Design Review in December 2019 and will give important input to the CBM module series production readiness procedure scheduled for 2020.

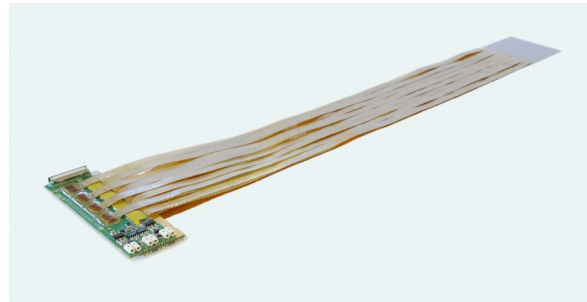


Figure 1: Detector module of the CBM STS as used in the test at COSY.

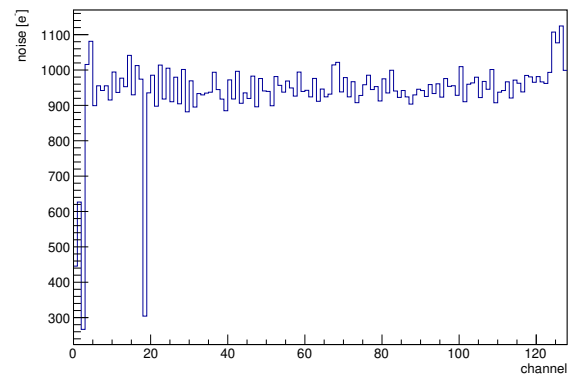


Figure 2: Noise in channels of one ASIC.

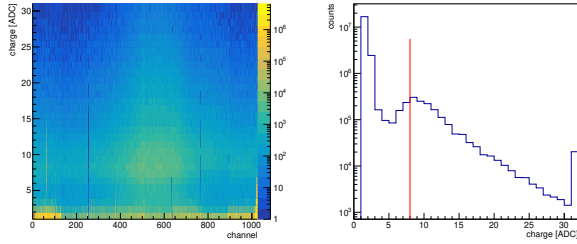


Figure 3: Beam profile seen in the channels of one sensor side (left), and signal distribution in one ASIC (right), all in ADC units before calibration.

HADES Ultra-fast Silicon Detectors

The HADES experiment has been equipped with a diamond detector system in close distance upstream of the target serving the start-time measurement for particle time-of-flight measurement [4]. Also silicon detectors with a high doping concentration, operated in a controlled-avalanche regime, allow for fast signal collection with especially short signal rise times. This feature and their availability through standard production techniques makes them suitable as forthcoming start-timing detectors in the HADES and CBM experiments. In parallel to the CBM silicon detector module test, ultra-fast silicon detectors (UFSD) [5] were arranged on the beam table in the JESSICA cave, in combination with a Mini Drift Chamber (MDC) developed for HADES. The USFS-MDC setup allowed evaluating the chamber's drift velocity map inside drift cells, along with its spatial resolution. The timing properties of the UFSDs themselves was studied with a pair of such silicon sensors alone.

The small station of two UFSD strip sensors of $50 \mu\text{m}$ strip pitch used is illustrated in Fig. 4. The readout was realized with custom-built discrete electronics providing two stages of amplification, together with two discriminator systems (NINO, PADIWA) and a TRB3 based TDC system. The particle rates were between 7 and 10 kHz per strip. The detectors were operated in ambient air without additional cooling. The time difference between strips in one and the other sensor as a function of the time-over-threshold measured per sensor is depicted in the plots of Fig. 5. The precision of the start-time measurement achieved is shown in the plot of Fig. 6 for pairs of channels, yielding $81 \text{ ps} / \sqrt{2} \approx 58 \text{ ps}$.

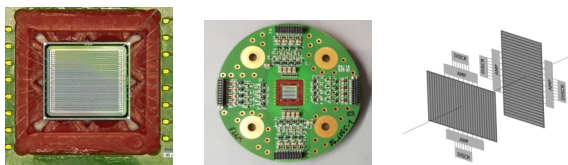


Figure 4: Prototypes of Ultra-fast silicon detectors, single-sided segmented into micro strips and arranged in a two-coordinate test system.

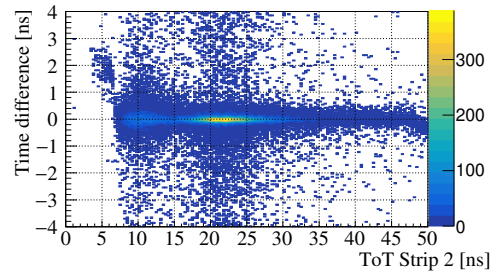
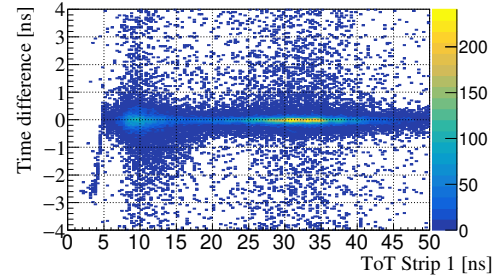


Figure 5: Time difference in the two coordinates as function of the signals' time-over-threshold.

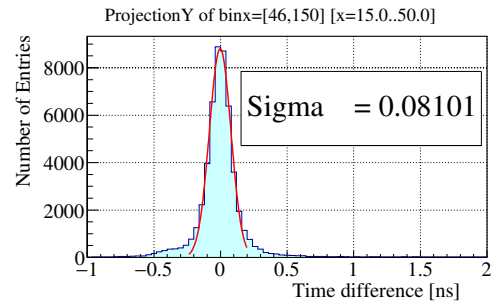


Figure 6: Time difference for pairs of channels that collected signal, one in each sensor.

References

- [1] <https://fair-center.eu/for-users/experiments/cbm.html>
- [2] <https://www-hades.gsi.de>
- [3] C. Sturm et al., *Start of mCBM Commissioning*, CBM Progress Report 2018, doi:10.15120/GSI-2019-01018, 190 (2019)
- [4] J. Pietraszko et al., *Diamonds as timing detectors for MIP: The HADES proton-beam monitor and start detectors*, Nucl. Instr. Meth. Phys. Res. **A618**, 121-123 (2010)
- [5] V. Sola et al., *First FBK Production of $50 \mu\text{m}$ Ultra-Fast Silicon Detectors*, Nucl. Instr. Meth. Phys. Res. **A 924**, 360-368 (2019)

¹ GSI Helmholtzzentrum für Schwerionenforschung GmbH, Darmstadt, Germany, for the CBM and HADES Collaborations. We acknowledge the support given by IKP, providing beam and facilitating us to carry out the experiments.

PAX-project development

A. Pesce for the PAX collaboration

The PAX-project aims to provide a method to produce an intense beam of polarized antiprotons [1]. It was supported by an ERC-Advanced Grant ("POLPBAR") between 2010 and 2016, and it is now in a Joint Research Activity (JRA) of the "STRONG 2020" project. After having successfully performed a spin-filtering test with protons using a transversely polarized hydrogen gas target [2], the PAX Collaboration plans to complete these studies with a test of longitudinal polarization buildup at COSY.

In order to ensure that the beam polarization is oriented in the longitudinal direction in the COSY straight section where the PAX interaction point is located, a superconducting solenoid, a so called "Siberian Snake", has been installed in the opposite straight section of the ring (Fig.1).



Figure 1: A picture of the Siberian Snake installed in COSY.

In preparation of the longitudinal spin-filtering test, the snake commissioning will start at COSY in March 2020 [3]. For this commissioning, a vertically polarized proton beam will be injected into COSY, electron-cooled and accelerated up to a momentum of $520 \text{ MeV}/c$. By ramping the solenoid from zero to 2.7 Tm , the vertical beam polarization will be transferred into the horizontal plane.

In order to cope with the foreseen experimental activities, a large acceptance silicon vertex detector has been realized in collaboration between the University and INFN of Ferrara (Italy) and the FZJ to serve as a beam and target polarimeter in proton-(anti)proton and proton-deuteron internal gas target experiments in the 30 MeV to 200 MeV beam energy range. It will provide an absolute calibration of the atomic Breit-Rabi polarimeter of the polarized target. At the same time it will serve as a beam position monitor in the beam-target interaction region.

The detector is composed of four identical quadrants, mounted in a diamond configuration (Fig.2) around an openable storage cell. Each quadrant consists of three layers of double-sided silicon-strip

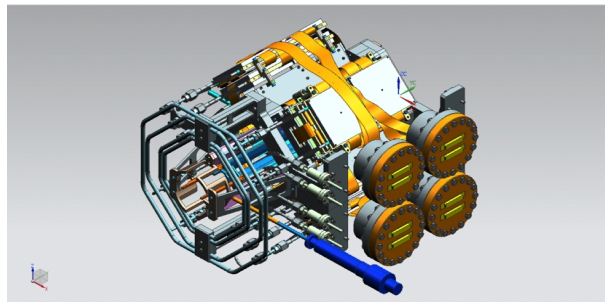


Figure 2: Sketch of the PAX detector assembly.

sensors, mounted inside an aluminum box, and a front-end readout system. Three kinds of $100 \text{ mm} \times 100 \text{ mm}$ silicon sensors are mounted, some of which have been recovered from the HERMES experiment at DESY-HERA. The electronic readout and the silicon sensors are cooled down by two separate cooling circuits.

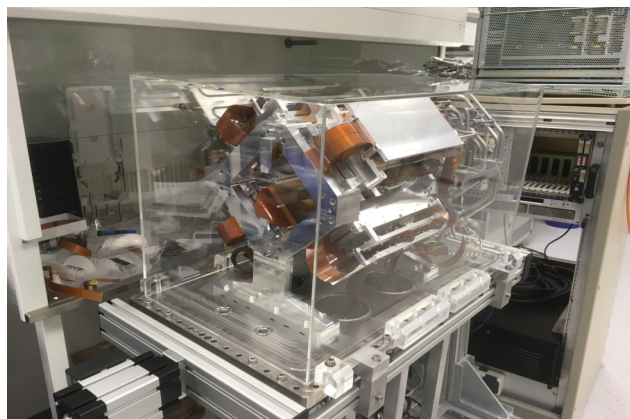


Figure 3: Picture of the fully assembled PAX detector with four complete quadrants.

After a first commissioning at COSY [3] in March 2017, with two complete quadrants, the PAX detector has been fully assembled (Fig.3) and is ready for its final commissioning.

References

- [1] Barone V, et al (2005) Antiproton-proton scattering experiments with polarization. **hep-ex/0505054**
- [2] Augustyniak W, et al (2012) Polarization of a stored beam by spin-filtering. **Phys Lett B 718(1):64 – 69**
- [3] Lenisa P., et al (2019) Low-energy spin-physics experiments with polarized beams and targets at the COSY storage ring. **EPJ Techniques and Instrumentation (2019) 6:2**

A Detailed Single Detector Analysis

A. Andres for the JEDI Collaboration

This report covers a detailed analysis of the spin tune and the horizontal polarization of data, taken during the November/December run 2018. Besides the well understood analysis using the combined-detector method[1], a new single detector analysis is presented, using the turn discrete fourier transform. The discrete Fourier transform provides one amplitude and phase estimator for a macroscopic time interval. The fourier coefficient a_{ν_k} and b_{ν_k} are given by the summation over all detected events N_{ev}

$$a_{\nu_k} = \frac{2}{N_{ev}} \sum_{n=1}^{N_{ev}} \cos(2\pi\nu_k n) \quad b_{\nu_k} = \frac{2}{N_{ev}} \sum_{n=1}^{N_{ev}} -\sin(2\pi\nu_k n) \quad (1)$$

where n denotes the turn number of event and ν_k the scanned spin tune. The amplitude ϵ and the phase ϕ are given by

$$\epsilon = \sqrt{a_{\nu_k}^2 + b_{\nu_k}^2} \quad \phi = \arctan\left(\frac{b_{\nu_k}}{a_{\nu_k}}\right). \quad (2)$$

Calculating and fitting the phase as a function of time while fixing the spin tune $\nu_{s,fix}$ and using the following formula

$$\nu_s(t) = \nu_{s,fix} + \frac{1}{2\pi} \frac{d\phi(n)}{dn} \quad (3)$$

enables to compute the spin tune as a function of time. This method is done for the up- and down detector individually. The results of the spin tune measured by the individual detectors together with the combined detectors method used in[1] are shown in Fig. 1. As it can be seen, the three curves match very

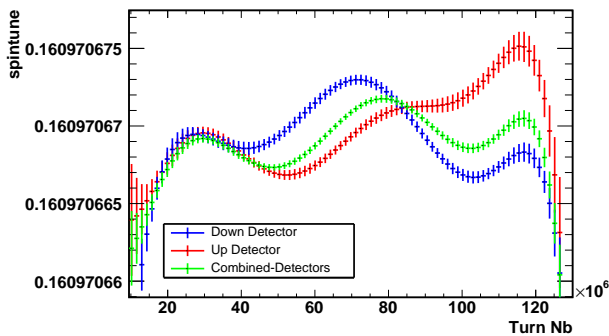


Figure 1: Spin tune as a function of time, calculated with individual detectors and the combined-detector method[1].

well within their uncertainties up to 40×10^6 turns, which is the time of switching on the RF Wien Filter. Afterwards, the apparent spin tune, measured

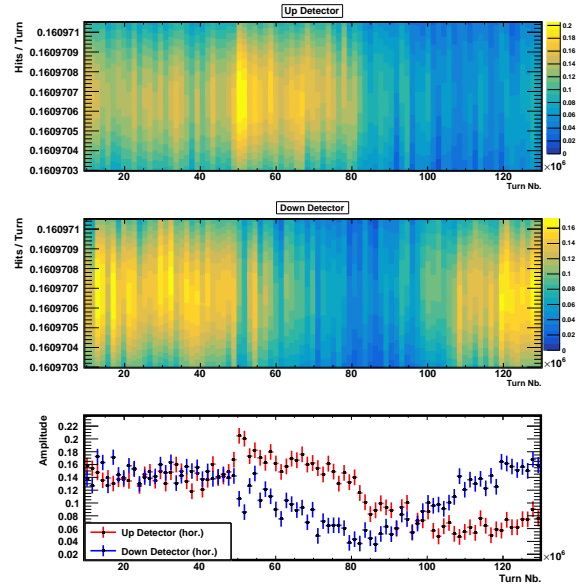


Figure 2: **Upper Plots:** Fourier Spectra around the spin tune, measured by the up- and down detector. **Lower Plot:** Spectra, evaluated at the spin tune, calculated with the combined-detector method.

by the individual detectors deviates from the combined detector method and an oscillating behaviour occurs.

A similar behaviour shows the horizontal polarization, see Fig.2. The first two plots show the Fourier amplitudes according to ϵ in eq. 2. The lower plot shows the amplitude evaluated at the spin tune, with the combined detectors method. Both detectors show the same results within their uncertainties until the RF Wien Filter is switched on. Afterwards, an oscillation pattern is present.

A great advantage of the combined-detector method is its independence of the beam luminosity. As the oscillation occurs, when the RF Wien Filter is switched on, we conclude, that the RF Wien Filter excites unexpected beam oscillations. Therefore, the count rates in the individual detectors change and cause the unexpected results

$$N_{\uparrow,\downarrow} \propto (1 + a \cos(\omega_{WF}t)) \cdot (1 \mp \epsilon \cos(\omega_s t + \phi_s)), \quad (4)$$

where a denotes an arbitrary oscillation amplitude, ω_{WF} the frequency of the beam oscillations and ϵ the horizontal polarization. A new feedback system is in progress to monitor the change of luminosity while data taking.

References

- [1] D.Eversmann et al. (JEDI), *Phys. Rev. Lett.* **115**, 094801(2015).

Controlling Systematic Uncertainties In EDM Searches

A. Aggarwal for the JEDI collaboration

Spin tracking simulations for the planned EDM measurement in storage ring are very important in order to check and control the systematic uncertainties. Keeping in mind the sensitivity of the experiment various effects are important to be considered. One of the major factor is the interaction of the magnetic dipole moment (MDM) and electric quadrupole moment (EQM) with electromagnetic field gradients that can produce an effect of a similar order of magnitude as that expected for an EDM. Spin tracking is done by introducing realistic fields allowing to determine their gradients and extending the Thomas-Bargmann-Michel-Telegdi equation in order to evaluate the real effect of interaction of MDM and EQM with field gradients. It is shown that the effects induced by field gradients do not affect the determination of EDM, but allow precise determination of magnitude of systematic uncertainty.

A novel method was proposed [1] for controlling the systematic uncertainties based on the measurement of EQM which interaction with fields gradients induce the same effect as EDM. Since EQM value is known with good precision, its measurement with the same method as in EDM search would demonstrate control of systematic uncertainties to the required level. In [1] one of the EDM measurement methods (rf Wien filter method) was considered and an analytical solution is given for this case. However, this cannot account for all the effects present in a realistic storage ring. Therefore, the existing spin tracking codes should be extended by including the EQM interaction with field gradients.

Numerical simulations were performed with BMAD software [3] developed by Cornell University. EDM effects are already present in BMAD but the detailed treatment of MDM and EQM interaction with field gradients are not present. Firstly, the BMAD software was modified by adding full spin precession equation including MDM and EQM interaction with field gradients (see e.g. Eq. 2 in ref. [1]). For all magnets mid-plane field profile for a soft edge 2D dipole custom field described as the BMAD custom field in order to set the benchmark. After successful definition of 2D dipole field we are defining field using Enge function. Then it was necessary to modify BMAD tracking to properly treat the custom bending field and so on for other magnets. With these modifications BMAD software allows one to calculate of the field gradients effects on spin precession. One of the scenarios proposed for EDM measurement is Quasi Frozen Spin method [2]. The storage ring is designed for the deuteron beam with a momentum of 1042.24 MeV/c. The symmetric lattice consist of two arc section, each with four identical bending dipoles

with field of $B_d = 1.5 T$. Two arcs sections are separated by straight sections with static Wien filters with electric field $E_w = 12 MV$ and corresponding magnetic field.

The results of [1] and of the present analysis [5] demonstrate that MDM and EQM interaction with field gradients should be considered when analyzing effects for very small EDM values. It was shown that these additional effects could be very useful for studying the systematic uncertainties in high precision EDM measurements. In the considered case it was shown that for somewhat different Wien filter settings EQM effect is by factor 1.78 larger than EDM effect for EDM value of $10^{-29} e \cdot cm$ as shown in figure 1. Therefore reproducing EQM value within known accuracy could pin down the systematic uncertainty to $10^{-32} e \cdot cm$. One specific method of EDM measurement were considered, similar studies should be performed for other proposed methods. Hence simulation codes should be modified with complete T-BMT equation and customized fields. Further plans are to introduce full three dimensional customized fields [4] for all magnets using Enge function.

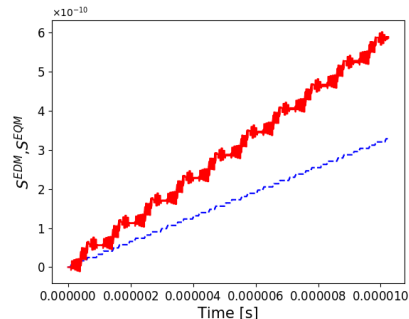


Figure 1: Comparison of vertical spin component for EDM effect (symmetric field) – blue dashed line and for EQM effect (asymmetric field) – red solid line.

References

- [1] A. Magiera, *Phys. Rev. Accel. Beams* **20**, 094001 (2017).
- [2] Y. Senichev *et al.*, Proc. 6th International Particle Accelerator Conference (IPAC15), p. 213, (2015).
- [3] <https://www.classe.cornell.edu/bmad>
- [4] B.D. Muratori *et al.*, *Phys. Rev. Accel. Beams* **18**, 064001 (2015).
- [5] A. Aggarwal *et al.*, Proc. 3rd Jagiellonian Symposium on Fundamental and Applied Subatomic Physics, p. 373, (2020).

Spin Tune Measurements for Electric Dipole Moment Searches

Abhiroop Sen^{a,b}

This report provides a summary of the spin tune measurements for longer cycles (~ 1000 s) during the beam time of April-May 2019. During these cycles, the extraction of the beam by the target is not continuous, but occurs in intervals. Discrete turn Fourier analysis is performed on the data [1]. Taking the up and down detectors separately, the count rates are fourier transformed and a peak is observed in the spectrum around the spin tune frequency [Fig. 1]. Using the fourier coefficients

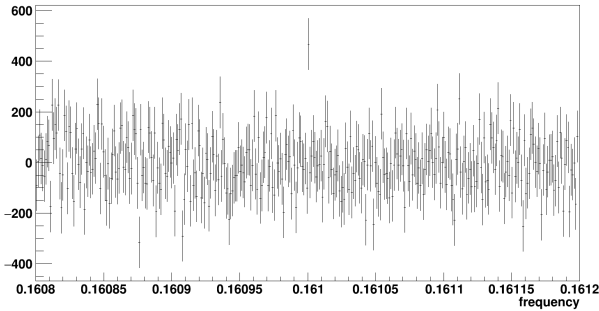


Figure 1: Peak in the Fourier spectrum around the spin tune frequency

$$\begin{aligned} a_{\nu_k} &= \frac{2}{N} \sum_{n_{ev}=1}^N \cos(2\pi\nu_k n_{ev}) \\ b_{\nu_k} &= \frac{2}{N} \sum_{n_{ev}=1}^N -\sin(2\pi\nu_k n_{ev}) \end{aligned} \quad (1)$$

where N is the total number of events, k is the turn number and ν_k is the turn dependent frequency, the amplitude and frequency are calculated as follows

$$\epsilon_k = \sqrt{a_{\nu_k}^2 + b_{\nu_k}^2}, \quad \phi_k = \arctan\left(\frac{b_{\nu_k}}{a_{\nu_k}}\right) \quad (2)$$

The slope $\frac{\partial\phi_k}{\partial k}$ is calculated by fitting a polynomial to the phase plot, and ν_s^0 is the initial spin tune. The spin tune can be calculated using the phase and the relation [Fig. 2]

$$\nu_s(k) = \nu_s^0 + \frac{1}{2\pi} \frac{\partial\phi_k}{\partial k} \quad (3)$$

The uncertainty in the spin tune is calculated using error propagation [Fig. 3]. A polynomial of order two is fitted to the phase $\phi(k) = c_0 + c_1k + c_2k^2$. Therefore, the spin tune according to eq. 3 is

$$\nu_s(k) = \nu_s^0 + \frac{1}{2\pi} (c_1 + c_2k) \quad (4)$$

The uncertainty in the spin tune is then given by

$$\sigma_{\nu_s}^2 = \frac{1}{4\pi^2} (\sigma_{c_1}^2 + 4\sigma_{c_2}^2 k^2 + 4k \text{cov}(c_1, c_2)) \quad (5)$$

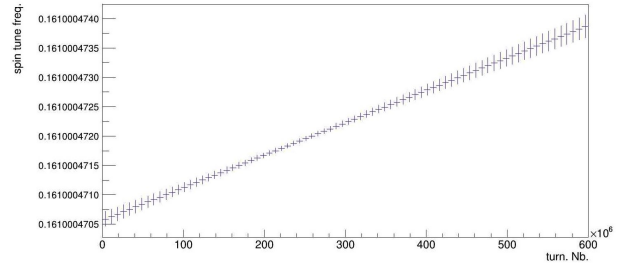


Figure 2: Calculated spin tune

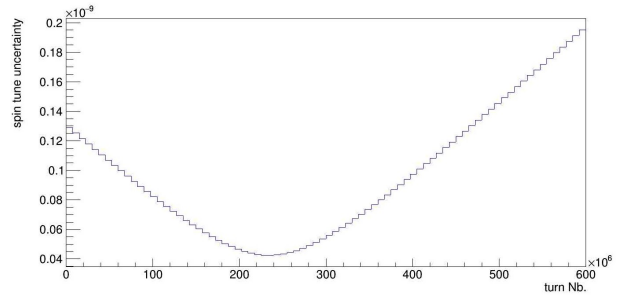


Figure 3: Uncertainty in the spin tune

This analysis is performed separately on each cycle and bunch. Figure 3 shows that the uncertainty in the spin tune measurement has been brought down to the order of 10^{-11} , from the previous limit of 10^{-10} during 100 s cycles. An uncertainty of the order of 10^{-11} is expected from the theoretical error calculation. The uncertainty in the phase calculation is given by $\sigma_\phi^2 = \frac{2}{NP^2}$, where N is the number of events and P is the polarization. If $V(t)$ is the variance in the time that the phases were calculated and N_{bin} is the total number of bins, the uncertainty in the spin tune is given by

$$\sigma_{\nu_s}^2 = \frac{\sigma_\phi^2}{N_{bin}V(t)} \quad (6)$$

Since $V(t) \propto T_{cycle}^2$ and $N_{bin} \cdot N = N_{tot}$,

$$\sigma_{\nu_s}^2 \propto \frac{2}{N_{tot}T_{cycle}^2P^2} \implies \sigma_{\nu_s} \propto \frac{1}{T_{cycle}} \quad (7)$$

Therefore, increasing the length of the cycle by a factor of 10 is expected to bring down the uncertainty in the spin tune by the same factor, which is what is observed.

References

- [1] D. Eversmann (2018) Ph.D thesis

^a Institut für Kernphysik, Forschungszentrum Jülich
^b RWTH Aachen

Extraction of Azimuthal Asymmetries using Optimal Observables

F. Müller, J. Pretz

Azimuthal asymmetries play an important role in scattering processes with polarized particles. This work [1] introduces a new procedure using event weighting to extract these asymmetries. It is shown that the resulting estimator has several advantages in terms of statistical accuracy, bias, assumptions on acceptance and luminosities compared to other estimators discussed in the literature.

The distribution of scattered particles is given by:

$$N(\vartheta, \varphi) = \frac{1}{2\pi} \mathcal{L} a(\vartheta, \varphi) \sigma_0(\vartheta) (1 + \epsilon(\vartheta) \cos(\varphi)). \quad (1)$$

The azimuthal asymmetry one is looking for is denoted by ϵ . The variables in equation 1 are defined in table 1.

variable	meaning
$N(\vartheta, \varphi)$	number of events observed
$\sigma_0(\vartheta)$	unpolarized cross section
ϑ	polar angle
φ	azimuthal angle, $\varphi = 0$ corresponds to positive x -direction
$\epsilon(\vartheta) = PA(\vartheta)$	asymmetry parameter to be determined
P	beam polarization
$A(\vartheta)$	analyzing power
\mathcal{L}	luminosity
$a(\vartheta, \varphi)$	acceptance

Table 1: Definitions of variables used in eq. 1.

The classical way to extract ϵ at a given ϑ is to integrate over a certain range in φ resulting in number of events $N_{L,R}^{\uparrow(\downarrow)}$ for two polarization configurations (\uparrow and \downarrow) in the left (L , $\varphi \approx 0$) and right (R , $\varphi \approx \pi$) part of the detector. Combining these number of events, ϵ can be obtained using for example the cross ratio method [2].

It is easy to understand that this method, based on event counts, does not make optimal use of the data. An event at $\varphi = 0$ or $\varphi = \pi$ carries more information than events further away from these extremes. If one makes the integration range over φ too large one even dilutes the sample with events close to $\pi/2$ and $3\pi/2$ such that the statistical error on ϵ increases when more events are added. This is shown in Figure 1. The solid curve shows the figure of merit, FOM, ($= \sigma_\epsilon^{-2}$, where σ_ϵ is the statistical error on ϵ) as a function of the integration range. At a given φ_{max} all events between $-\varphi_{max}$ and φ_{max} are included in N_L for example. The FOM drops for $\varphi_{max} > 65^\circ$.

From a statistical point of view it is beneficial to weight every event by $\cos(\varphi)$. The analysis is thus

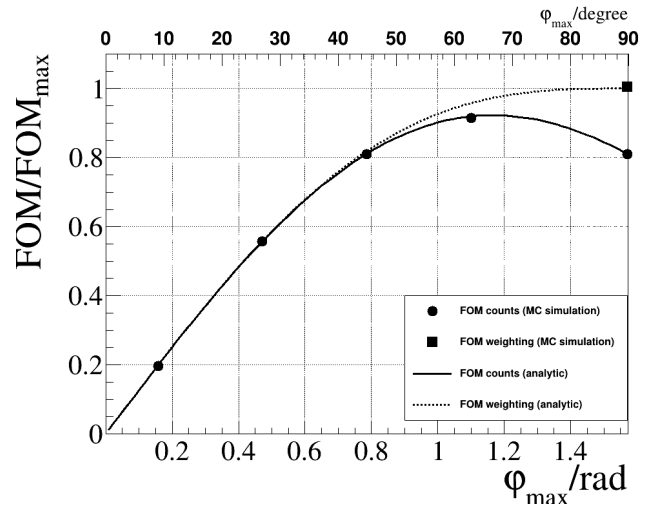


Figure 1: Figure of merit (FOM) for estimators using event counts and event weighting, calculated analytically (lines) and from MC simulation (symbols).

based on

$$\sum_{i=1}^{N^\uparrow} \cos^n(\varphi_i) \quad \text{and} \quad \sum_{i=1}^{N^\downarrow} \cos^n(\varphi_i) \quad , \quad \text{with} \quad n = 0, 1, 2.$$

rather than event counts. In this case the FOM follows the dashed curve in Figure 1.

It can also be shown that using this weighting procedure, the FOM is the same as in the maximum likelihood method reaching the Cramér-Rao limit of the lowest possible statistical error.

Moreover, using event weights has the advantage that no knowledge about the acceptance is required and no correction due to possible difference in luminosity has to be applied. On the contrary, the method even provides information on the azimuthal dependence of the acceptance. The method is easily extendable to more observables, like tensor the polarization.

References

- [1] J. Pretz and F. Müller, “Extraction of Azimuthal Asymmetries using Optimal Observables,” *Eur. Phys. J.*, vol. C79, no. 1, p. 47, 2019.
- [2] G. G. Ohlsen and P. W. Keaton, “Techniques for measurement of spin-1/2 and spin-1 polarization analyzing tensors,” *Nucl. Instrum. Meth.*, vol. 109, pp. 41–59, 1973.

Pellet target development for the JePo polarimeter

O. Javakhishvili and I. Keshelashvili for the JEDI collaboration

One of the key elements of the JEDI experiment at COSY is the new polarimeter (JePo). The JePo is a two layer detector system consisting of a modular inorganic LYSO crystals and ΔE scintillators. The produced light is detected by SiPM arrays. The main requirements are simplicity, interchangeability, long term stability and high resolution[1]. One crucial part of the polarimeter is the target system. In storage ring EDM (srEDM) measurements the requirements for the target are minimal influence on beam particles and vacuum system. Most of the traditional target systems are not suitable for srEDM experiments. Some of the targets either can not use carbon, they significantly worsen vacuum conditions, or they have too high density. As an example, in the current configuration horizontal and vertical carbon block targets are used in JePo. This type of target requires additional beam excitation with white noise to make the small part of the beam particles hit the target. Although a very thin carbon wire could be employed, the density of the wire still will be way too high, leading to high beam losses. In view of all the drawbacks of different types of targets we developed new concept of the ballistic carbon pellet target[1]. The idea is to shoot a small (tens of micron) carbon pellet through the beam (see Figure 1). It will consist of shooter and catcher mechanisms to oscillate the pellet and make it to cross the beam. By controlling the movement of the pellet it will be

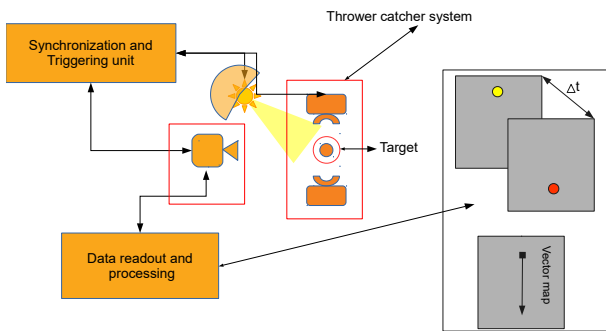


Figure 1: Block diagram of pellet target system

possible to even scan the beam profile at desired position if the DAQ will be synchronized with the pellet movement. In this way the target system will have the least interaction with the beam. Anything using electrical and magnetic fields must be avoided not to disturb the beam. Frequency and speed of the oscillation must be variable to achieve the desired effective target density. The proper monitoring system must be developed, including precise triggering, track reconstruction and data synchronization units, to synchronize the target tracking data with

the other parts of the polarimeter.

The triggering and time-of-flight (TOF) measurement unit consists of two laser and two fast pin photo diodes. The output of the pin diodes are amplified and converted to a digital signal which is fed into the FPGA. It performs TOF measurement and also triggers the CMOS camera. The FPGA extracts tracking information such as flight trajectory from video frames. A fast camera is required for the tracking system to get as much frames as possible. The used FPGA incorporates dedicated ARM core, which can be used to communicate with the target system from a remote computer using the local network. In addition, the target system must be able to read and write data from other parts of the detector and the accelerator using the EPICS. This can be also easily achieved with CPU.

The first version of the triggering system has been developed. It was tested with 0.4 mm metal ball. The output signal is very clean as it is shown on Figure 2. These tests will continue to examine pellets of different sizes, further adjust optics and tune amplifier parameters.

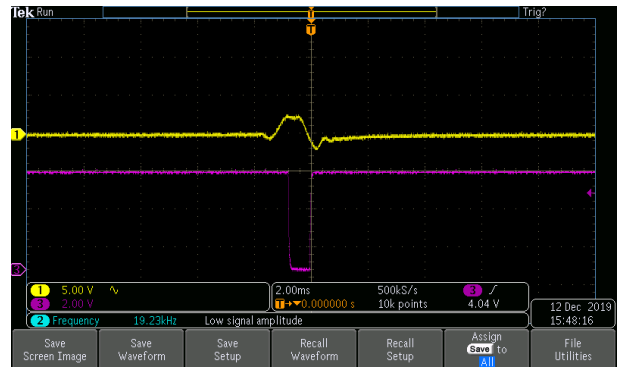


Figure 2: The trigger unit test with 0.4 mm pellet. The yellow line is analog signal from amplifier, the purple line is digital signal pulse which goes in FPGA

References

- [1] I. Keshelashvili et al., "A new approach: LYSO based polarimetry for the EDM measurements", J. Phys. Conf. Ser. 1162, 012029 (2019)

Development of Rogowski beam position monitors

F. Abusaif
for the *JEDI* collaboration

Currently, the Jülich Electric Dipole Moment Investigations (*JEDI*) collaboration is running a precursor experiment for the search for a permanent electric dipole moment of deuterons or protons using the COoler SYnchrotron (COSY) located at the Forschungszentrum Jülich. This precision experiment requires knowing the beam transverse positions along the ring with a good accuracy.

A Rogowski coil is a special type of helical wire wound around a non-magnetic strip [1]. The operation principle of a typical Rogowski coil depends on Ampere's and Faraday's laws [2, 3], where the presence of a time-changing beam results in the formation of an induced signal between Rogowski coil terminals.

A Beam Position Monitor (BPM) based on Rogowski coil is made in a way that the helical geometry is segmented into four equal quadrants lying in the coil's xy plane. This particular geometry is used for easier and direct link between the voltage readouts from quadrants and the transverse positions of an AC beam along the longitudinal axis.

For a COSY beam with a relativistic momentum of 970 MeV/c², the revolution frequency is 750 kHz. An overall revolution frequency of 3 MHz will be required to operate the Rogowski BPM if COSY beam is running in the four bunches mode (with each bunch having a revolution rate of 750 kHz).

A test Rogowski coil has been constructed recently in order to test the possibility of operating the coil at higher frequencies, mainly at the frequency of 3 MHz. A typical Rogowski BPM used for operation at 750 kHz has 445 windings per each quadrant and resonance frequency at 1.2 MHz. Theoretically [4, 5], the inductance of a coil L with a circular cross section is directly proportional to the square of coil's winding number n^2 , while the resonance frequency is inversely proportional to the square root of inductance, meaning that a decrease in n by some factor will result in an increase of the coil self resonance frequency by the same factor. For the test coil, a thick Copper wire (0.5mm) was used to get less number of winding ($n = 164$) and hence higher self resonance frequency.

For getting the maximum possible output from the coil at some fixed beam current, one can also operate the coil at its resonance frequency. Figure 1. shows the voltage frequency curve of the test coil made of 164 turns. An additional parallel capacitor of 15 pF was connected to the coil terminals in order to shift the resonance from 3.356 MHz down to 3 MHz.

Such operational mode, where the coil is operated at its self resonance frequency has to be investigated in

more details in the near future. The stability and reproducibility of electrical response is of great importance in order for the Rogowski BPM sensor to give precise beam positions.

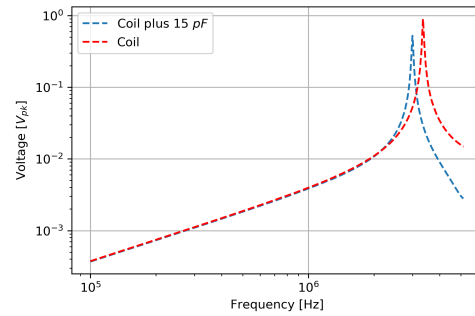


Figure 1: The voltage-frequency response from test Rogowski coil showing the effect of adding a parallel 15 pF capacitor to get the system resonating at 3 MHz.

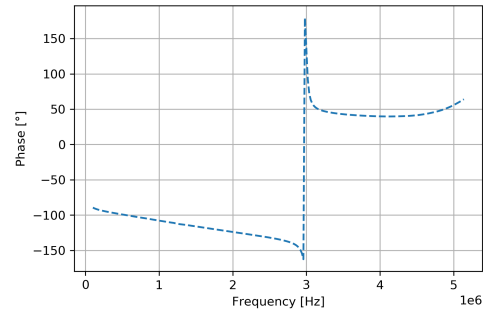


Figure 2: The phase-frequency response from test Rogowski coil connected in parallel with 15 pF capacitor to get the system resonating at 3 MHz.

References

- [1] Samimi, M. H., Mahari, A., Farahnakian, M. A. and Mohseni, H. (2014). *IEEE Sensors Journal*, 15(2), 651-658.
- [2] Tumanski, S. (2007). *Measurement Science and Technology*, 18(3), R31.
- [3] Rogowski, W., Steinhaus, W. *Archiv f. Elektrotechnik* 1, 141-150 (1912). <https://doi.org/10.1007/BF01656479>
- [4] Hashmi, G. M., Lehtonen, M., and ELHAF-FAR, A. (2007). *Pulse*, 1, P2.
- [5] Robles, G., Shafiq, M., and Martínez-Tarifa, J. M. (2018). In *Multidisciplinary Digital Publishing Institute Proceedings* (Vol. 4, No. 1, p. 10).

Progress toward a direct measurement of the deuteron Electric Dipole Moment at COSY

Vera Shmakova on behalf of the JEDI collaboration

One of the major problems of modern particle physics is the inability of the Standard Model to explain the matter-antimatter asymmetry of the Universe. Electric Dipole Moments (EDM) violate both parity and time-reversal symmetry which means that EDMs violate CP-symmetry, while CPT appears to be conserved. A measurement of the EDM of a particle probes new sources of CP-violation. In this report, we present the results of the ‘‘EDM precursor’’ experiment which is seen as a first step towards an experimental program to determine the EDMs of protons and deuterons using a storage ring [1], [2]. According to the Thomas-BMT equation, the spin motion in a ring is described by [3], [4]

$$\begin{aligned} \frac{d\vec{S}}{dt} &= \vec{\Omega} \times \vec{S} = \\ &= -\frac{q}{m}(G\vec{B} + (\frac{1}{\beta^2} - 1 - G)\vec{\beta} \times \vec{E} + \frac{\eta}{2}(\vec{E} + \vec{\beta} \times \vec{B})), \end{aligned}$$

with radial electric field \vec{E} and vertical magnetic field \vec{B} . If there is an EDM, the invariant spin axis in the ring would be tilted in radial direction. In reality, however, there are additional magnetic misalignments, so that the invariant spin axis is tilted in both radial and longitudinal directions. Our goal is to measure the tilt of the invariant spin axis which allows us to obtain an experimental access to the EDM. In order to induce the vertical polarization build-up,

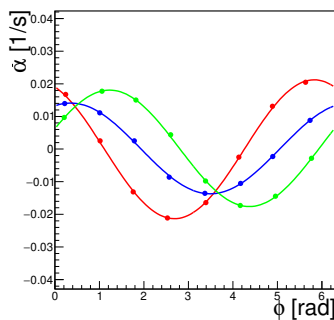


Figure 1: Polarization build-up $\dot{\alpha}$ for Wien filter rotation angle 9.38 mrad around the beam axis, solenoid is on -20.54 mrad (red), -7.45 mrad (blue), 5.63 mrad (green).

the RF Wien filter [2], [5] was operated on one of the harmonics of the spin precession frequency (871 kHz) and the RF phase was locked with the spin precession phase. In this case, a particle passing through the RF Wien filter gets a spin kick in the same direction every turn. In order to obtain a map of the EDM resonance strength, the measurements were performed for different RF Wien filter rotations around

the beam axis and for different settings of a solenoid in the opposite straight section which rotates the invariant spin axis at the RF Wien filter longitudinally. The initial slopes of the polarization build-up ($\dot{\alpha}$) were observed for various phases of the RF Wien filter, resulting in the sinusoidal dependencies, shown in Fig.1. The decoherence of the horizontal polarization [6] was distinguished by simultaneous fitting the time dependencies for full polarizations and slopes of the vertical polarization build-up. The

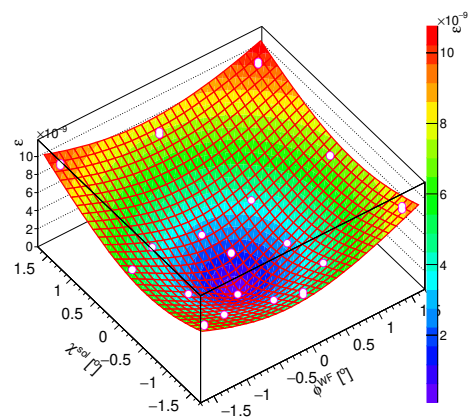


Figure 2: The map for the obtained resonance strength ε^{EDM} [2] for various Wien filter and solenoid settings.

resulting map of all points for the measured EDM resonance strength ε^{EDM} of deuterons with momenta of 970 MeV/c depending on the RF Wien filter rotation angles and solenoid settings is shown in Fig.2. The fit function represents a square root of an elliptic paraboloid, which means there appear quadratic dependencies of the ε^{EDM} for both the RF Wien filter rotations and the solenoid settings. The minimum of the surface corresponds to the orientation of the invariant spin axis at the RF Wien filter.

References

- [1] F. Abusaif *et al.*, [arXiv:1812.08535v2](https://arxiv.org/abs/1812.08535v2) [physics.acc-ph].
- [2] F. Rathmann *et al.*, arxiv.org/abs/1908.00350 [physics.acc-ph].
- [3] T. Fukuyama and A. J. Silenko, *Int. J. Mod. Phys. A* 28 (2013) 1350147.
- [4] A. Saleev *et al.*, *Phys. Rev. ST Accel. Beams* 20 (2017) 072801.
- [5] J. Slim *et al.*, *Nucl. Instrum. Methods Phys. Res. A* 828 (2016) 116.
- [6] N. Hempelmann, PhD Thesis (2018).

Spin tune response to three-steerer bumps to aid elements alignment

A. Saleev for the JEDI Collaboration

Introduction

Searches of electric dipole moments (EDM) of charged particles in pure magnetic rings, such as COSY, or electrostatic and hybrid magnetic-electric storage rings, planned in the future, require new methods to disentangle the EDM signal from the large background produced by magnetic dipole moments. In the JEDI precursor experiment, one major source of systematic background are non-ideal magnetic element alignments that lead to in-plane imperfection magnetic fields.

The EDM signal constitutes a rotation of the spin in the electric field. In an all magnetic ring (COSY), it is the motional electric field $\propto [\vec{\beta} \times \vec{B}]$ along the radial x -axis around which the EDM precesses. As such, an EDM contributes also to a constant tilt of the stable spin axis $\vec{c} = \vec{e}_y + \xi_{\text{edm}} \vec{e}_x$. On the other hand, nonuniform in-plane imperfection magnetic fields tilt the invariant spin axis towards x or z , $\vec{c} = c_y \vec{e}_y + (\xi_{\text{edm}} + c_x^{\text{mdm}}) \vec{e}_x + c_z^{\text{mdm}} \vec{e}_z$. While $c_y \simeq 1$, the projections $c_{x,z}$ depend on the specific location chosen to define the one-turn spin transfer matrix.

Imagine a position-dependent polarimeter to observe polarisation rotation in some location in the ring. The order of the spin rotations in the imperfection fields will be different for different locations of the observation point, thus the resulting axis \vec{c} of the one-turn spin transfer matrix will also be different (see also discussion in ref.[1] Chap.2 Sec.IV).

Misalignments of ring elements which create imperfection fields have been measured at COSY for all magnets. Treating the element alignment as model parameters, the goal of the new study is to verify the model prediction for \vec{c} at different locations of the ring (see [2]) and put constraints on the element alignments. The limit on EDM is then given by the systematical and statistical error of the difference between model prediction and measurement of \vec{c} .

Orbit bumps

The spin tune denotes the number of spin rotations for one turn of a particle in the ring. It can be determined to a very high precision, with a relative error of 10^{-10} during a 100 s long beam cycle [3]. Such precision allowed us to develop a new method, called ‘‘spin tune mapping’’ [4]. In the past we used the compensation solenoids of the high- an low-energy electron coolers to make spin tune shifts and determined the angular orientation of \vec{c} with high precision of $2.8 \cdot 10^{-6}$ radian. Now we propose to use vertical three-steerer closed-orbit bumps to make spin tune

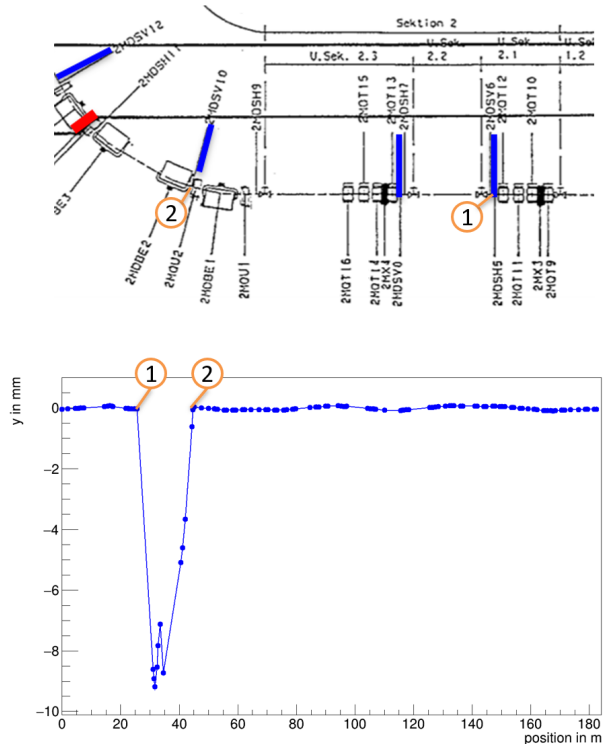


Figure 1: Top: on the scheme of COSY, vertical steerers are marked with blue lines. One of the MXS-family sextupoles is marked with short red line. Bottom: an example of vertical closed orbit when the local three-steerer bump MSV6-MSV8-MSV10 is applied. The pointers (1) and (2) on both pictures correspondingly denote the locations of the first (MSV6) and the last (MSV10) steerer of the bump.

shifts (see Fig.1) and measure the direction of invariant spin axis all around in the ring with different bumps.

Both analytic and lattice models predict that the spin tune shift $\Delta\nu_s$ has a parabolic dependence on the bump amplitude (see Fig. 2). The corresponding analytic result is

$$\cos \pi(\nu_s + \Delta\nu_s) = \cos \pi\nu_s \cos \frac{\psi}{2} - (\vec{c} \cdot \vec{w}) \sin \pi\nu_s \sin \frac{\psi}{2}$$

where $(\vec{c} \cdot \vec{w}) = c_x \sin \alpha - c_z \cos \alpha$ defines the offset of the minimum of a parabola. The angle ψ is proportional to the amplitude of the bump. The components of the invariant spin axis c_x and c_z are defined at the location of last steerer of the bump. The parameter α is specific for each bump, for which COSY-Infinity (see [5]) simulations suggest clustering around $\sim -40^\circ$ or $\sim -65^\circ$. The measurements of each steerer setting for the bump additio-

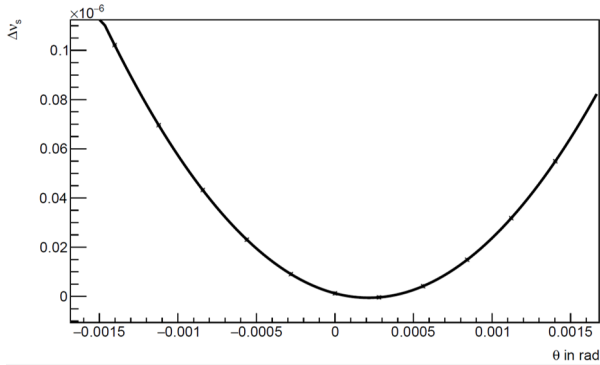


Figure 2: A model prediction of the spin tune shifts for the bump MSV8 - MSV10 - MSV12 with respect to the kick angle θ of the central steerer (COSY-Infinity simulation with COSY lattice). The minimum of parabola is shifted because solenoid field of 0.5 Tmm is introduced in the model at the place of Siberian snake at COSY.

nally against a solenoid field allows to validate the model prediction for non-commuting spin rotations in the bump. This effect is determined independently from the imperfections present in the ring. A superconducting solenoid that was successfully used in the JEDI precursor experiment will be utilized for this purpose.

Chromaticity correction

To set up the high precision spin tune measurement, a long spin coherence time (SCT) of the order of a few hundred seconds is needed. Usually the sextupoles are set up such that vertical and horizontal chromaticities simultaneously vanish [6]. By fine tuning the sextupoles of the MXS and MXG families, one determines the setting where the spin coherence time reaches the optimum. However, when the vertical orbit bump is set up (see Fig. 1), the vertical orbit shift in the sextupoles located within the bump will significantly change the chromaticity and detune the machine setup from the optimum. One such example could be MXS-family sextupole marked as short red line on the top of Fig.1 and located within the bump consisting of consecutive steerers MSV8, MSV10 and MSV12. The central steerer of the bump, MSV10, is marked by pointer (2) on the Fig. 1, while first and last steerers of the bump are denoted by two blue lines without pointers.

For that reason, those particular sextupoles within the bump have to be switched off during the spin tune mapping. To facilitate the optimization of the remaining sextupoles for long SCT, a chromaticity measurement should be set up, based on the recently developed tool for fast betatron tune measurement. Chromaticity is by definition a derivative of the tune with respect to momentum. RF-frequency jumps can be used to change the momentum during the measu-

rement of tune and chromaticity can be determined. Once the chromaticity is mapped with respect to the sextupole strengths, the working point for sextupole settings where chromaticity equals zero is selected, and fine scans for the best SCT can be performed. Simulations using COSY-Infinity are used to provide guidance for the correction.

Outlook

The JEDI Collaboration will have three weeks of beam time for spin tune mapping with steerer bumps at COSY in September 2020. As an outcome of the beam time, a working tool for optimization of magnetic element alignments on the basis of the precision spin dynamics should be produced, which is important for JEDI precursor experiment at COSY and for future storage rings.

In the prototype EDM ring recently proposed by the JEDI Collaboration [7] this method allows to control the systematic background from unwanted magnetic fields. In this case, the difference of spin tunes for clockwise (CW) and counterclockwise (CCW) beams relative to the applied steerer bump magnitudes is directly proportional to the EDM signal and should be consistent for every bump configuration. Inconsistency of the measured spin tune difference maps for CW/CCW beams for all bumps in the ring is an indication of the presence of systematic background.

References

- [1] S. Y. Lee, Spin Dynamics and Snakes in Synchrotrons (World Scientific, 1997) books.google.de/books?id=And2QgAACAAJ
- [2] Rathmann, F., Nikolaev, N.N., Slim, J.: Spin dynamics investigations for the EDM experiment at COSY. *Phys. Rev. Accel. Beams* **23**, 024601 (2020)
- [3] Eversmann, D., et al.: New method for a continuous determination of the spin tune in storage rings and implications for precision experiments. *Phys. Rev. Lett.* **115**, 094801 (2015). DOI 10.1103/PhysRevLett.115.094801
- [4] Saleev, A., et al.: Spin tune mapping as a novel tool to probe the spin dynamics in storage rings. *Phys. Rev. Accel. Beams* **20**, 072801 (2017)
- [5] Berz, M.: Computational aspects of optics design and simulation: COSY INFINITY. *Nucl. Instrum. Meth.* **A298**, 473–479 (1990). DOI 10.1016/0168-9002(90)90649-Q
- [6] Guidoboni, G., et al.: Connection between zero chromaticity and long in-plane polarization lifetime in a magnetic storage ring. *Phys. Rev. Accel. Beams* **21**, 024201 (2018)
- [7] JEDI Collab., Storage Ring to Search for Electric Dipole Moments of Charged Particles Feasibility Study (ArXiv, 2019) <https://arxiv.org/pdf/1912.07881.pdf>

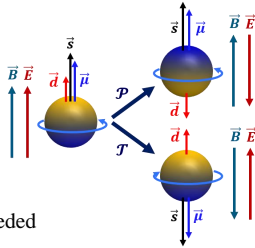


SEARCH FOR ELECTRIC DIPOLE MOMENTS AT COSY IN JÜLICH – SPIN-TRACKING SIMULATIONS USING BMAD

V. Poncza¹, A. Lehrach^{1,2}, Institut für Kernphysik 4, Forschungszentrum Jülich, 52425 Jülich, Germany, ¹also at III. Physikalisches Institut B, RWTH Aachen University ²and JARA-FAME, 52056 Aachen, Germany on behalf of the JEDI Collaboration

Motivation

- Measure **Electric Dipole Moment** (EDM) of charged hadrons at COSY
- **Vertical spin build-up** as a measure of EDM
- EDM-like signals due to **systematic effects**
- **Spin-tracking** simulations needed to disentangle systematic effects from real EDM signal

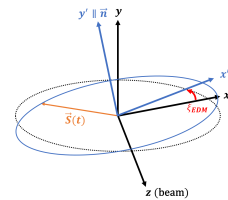


Spin Dynamics

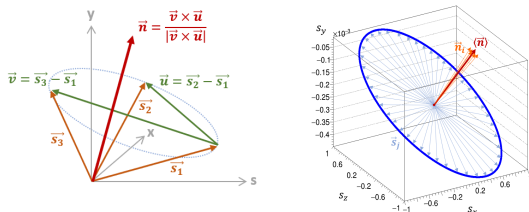
$$\frac{d\vec{S}}{dt} = (\Omega_{MDM} + \Omega_{EDM}) \times \vec{S} = \left(\frac{q}{m} G\vec{B} + \frac{q\eta}{2m} \vec{\beta} \times \vec{B} \right) \times \vec{S}$$

$$\vec{d} = \eta \cdot \frac{q}{2mc} \vec{S} \quad \text{and} \quad \tan(\xi_{EDM}) = \frac{\eta\beta}{2G} \quad [2]$$

- Spin rotates around **invariant spin axis** \vec{n}
- Invariant spin axis is tilted by
 - the **electric dipole moment**
 - **systematic effects** (i.a. misaligned magnets)



Invariant Spin Axis



- Track reference particle for several turns using the Bmad Software Library [1]
- Calculate the normal vector \vec{n}_i for each possible combination of three spin vectors
- The invariant spin axis $\langle \vec{n} \rangle$ is the mean of all normal vectors

benchmarking:

Input: $\eta = 0.0002 \Rightarrow$ theory: $n_x = -0.32127 \cdot 10^{-3}$, $n_z = 0$

Output: $\langle \vec{n} \rangle = \begin{pmatrix} -0.321269108 \cdot 10^{-3} \pm 7.636 \cdot 10^{-9} \\ 0.999999948393 \pm 2.5 \cdot 10^{-12} \\ 2.568 \cdot 10^{-9} \pm 1.6878 \cdot 10^{-8} \end{pmatrix}$

Experimental Situation

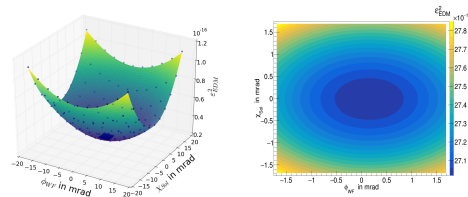
EDM resonance strength: $\varepsilon_{EDM} = \frac{\Omega_{Py}}{\Omega_{rev}}$

$$\varepsilon_{EDM}^2 \propto A \cdot (\phi_{WF} - \phi_0)^2 + B \cdot \left(\frac{\chi_{Sol}}{2 \sin(\pi\nu_s)} + \chi_0 \right)^2 \quad [3]$$

Basic idea:

- Fit point of minimal resonance strength (ϕ_0, χ_0)
- ϕ_0 is a measure of the EDM + systematic effects

Simulation: $\eta = 0$ + magnet misalignments



Simulation: $\phi_0 = 0.15 \pm 0.02$ mrad, $\chi_0 = 0.01 \pm 0.01$ mrad

Measurement: $\phi_0 = -3.7 \pm 0.04$ mrad, $\chi_0 = -6.96 \pm 0.04$ mrad

\Rightarrow unknown longitudinal field components

Summary & Outlook

- The COSY ring is modeled using Bmad
- The implemented method to determine the invariant spin axis is in agreement with theoretical predictions
- Simulating the experimental situation and comparing the results to the measurement show a lack of knowledge of the net longitudinal field in COSY
- Possible sources of longitudinal fields are fringe fields and the narrow positioning of the COSY magnets which will be added to the model

References

- [1] D. Sagan, "Bmad: A relativistic charged particle simulation library", Nuclear Instruments and Methods in Physics Research A, vol. 558, pp. 356-359, 2006.
- [2] T. Fukuyama and A. J. Silenko, "Derivation of Generalized Thomas Bargmann-Michel-Telegdi Equation for a Particle with Electric Dipole Moment", Int. J. Mod. Phys. A28, p.1350147, 2013.
- [3] A. Saleev, N.N. Nikolaev, and F. Rathmann, "JEDI and RF Wien Filter Driven Spin Dynamics", unpublished.

Beam-based alignment at the Cooler Synchrotron (COSY)

Tim Wagner on behalf of the JEDI Collaboration
Forschungszentrum Jülich & RWTH Aachen University

Physics Motivation

Electric Dipole Moment (EDM):

- Fundamental property of a particle, like mass or magnetic dipole moment
- Requires \mathcal{P} and \mathcal{T} $\overset{CP}{=} CP$ violation
- Close connection to matter antimatter asymmetry
- Axions can create oscillating EDM
- Charged particle EDM can be measured in a storage ring. The signal is a build-up of a vertical polarization.

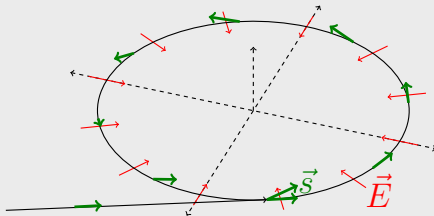


Figure: Basic principle for an EDM measurement. The vertical buildup of the polarization happens due to the interaction of the EDM with the electric field.

- **But:** Orbit distortions lead to a fake signal [1]
→ Improve the orbit
→ Beam-based alignment

Technique

- Use the beam to optimize the beam position inside quadrupole
- Vary quadrupole strength k by $\pm\Delta k$, then observe and minimize orbit change
- Orbit change [2] described by:

$$\Delta x(s) = \left(\frac{\Delta k x(s_0) \ell}{B\rho} \right) \left(\frac{1}{1 - k \frac{\ell \beta(s_0)}{2B\rho \tan \pi \nu}} \right) \times \frac{\sqrt{\beta(s)} \sqrt{\beta(s_0)}}{2 \sin \pi \nu} \cos(\phi(s) - \phi(s_0) - \pi \nu)$$

- Minimized with the following merit function:

$$f = \frac{1}{N_{\text{BPM}}} \sum_{i=1}^{N_{\text{BPM}}} (x_i(+\Delta k) - x_i(-\Delta k))^2$$

$$f \propto (\Delta x(s))^2 \propto (x(s_0))^2$$

- Merit function has the shape of a paraboloid and the minimum is the optimal position in the quadrupole

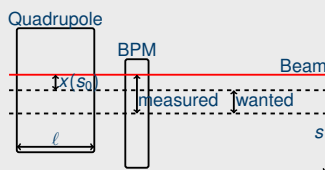


Figure: The optimal beam position is in the center of the quadrupole ($x(s_0) = 0$). When that point is found one can determine the offset between the BPM and the quadrupole.

Results

- Measurement performed for 12 quadrupoles
- Beam moved inside the quadrupoles to different horizontal and vertical positions

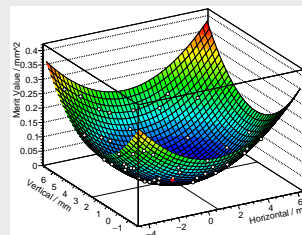


Figure: Example for one measurement of the beam based alignment. The x- and y-axis show the beam position inside the quadrupole and the z-axis shows the evaluated merit function. The white dots are measured points and the red dot is the minimum of the fit, i.e. the optimal position.

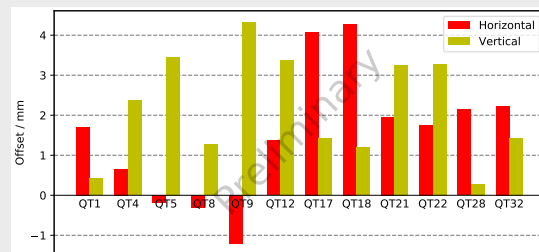


Figure: Preliminary results for all 12 quadrupoles. The optimal position of the beam inside quadrupole is displayed for the horizontal and vertical direction. The optimal position can be used to determine the offset of nearby beam position monitors.

- With these optimal positions inside the quadrupoles the offset for 6 beam position monitors has been calculated
- The new offsets lead to an improvement of the corrected orbit in the accelerator

	Orbit RMS_y	Steerer Current RMS
no offsets	1.21 mm (100%)	2.66 A (100%)
with offsets	1.01 mm (83%)	2.10 A (79%)

- Lower orbit RMS leads to a lower systematic error for an EDM measurement
- Measurement of all 56 quadrupoles in COSY planned in the future to calibrate all BPMs and further improve the orbit

References

- [1] M. S. Rosenthal. "Experimental Benchmarking of Spin Tracking Algorithms for Electric Dipole Moment Searches at the Cooler Synchrotron COSY". PhD thesis. RWTH Aachen University, 2016.
- [2] G. Portmann et al. "Automated beam based alignment of the ALS quadrupoles". In: *Conf. Proc. C950501* (1996), pp. 2693–2695.

Contact: Tim Wagner - t.wagner@fz-juelich.de



Method to search for axion-like particles at storage rings, demonstrated at COSY

Swathi Karanth on behalf of JEDI collaboration
 Institute of Physics, Jagiellonian University, Kraków, Poland

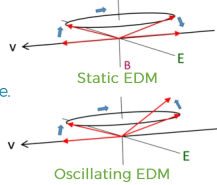


Axions or Axion-Like Particles (ALPs)

Proposed to explain the lack of CP violation in the strong interaction	Candidate for dark matter in the universe
Axions	
Axion-gluon coupling introduces an oscillating Electric Dipole Moment (EDM)	Light mass and weakly coupled to nucleons

Oscillating EDM allows us to search for ALPs in a storage ring.

Search using in-plane polarized deuteron beam at COSY



Assumptions:

- Axion field has large spatial and time coherence.
- Axions are dense and extend beyond the ring
- EDMs oscillate coherently. Phase is unknown.

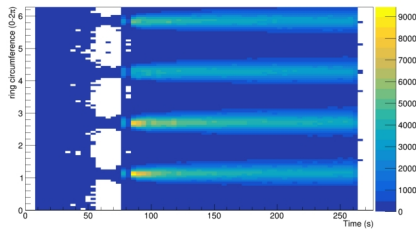
Experimental setup

Unknown phase problem:

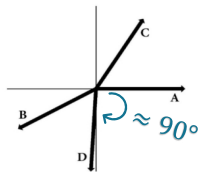
- right frequency + right phase $\Rightarrow P_y$ accumulation \checkmark
- right frequency + wrong phase $\Rightarrow P_y$ accumulation \times

Solution

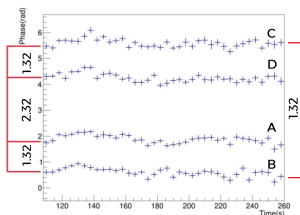
Simultaneous searches with beams having perpendicular polarization.



2D plot of the time evolution of the beam in the ring



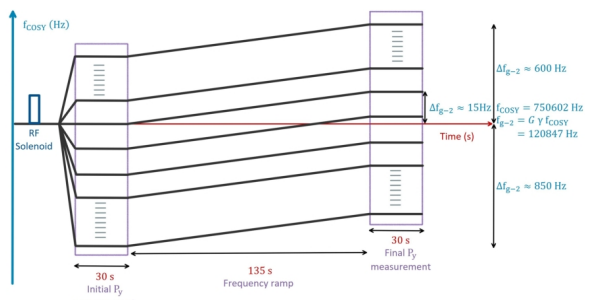
Polarization direction of the 4 bunches in the horizontal plane in lab frame.



Phase measurement verifies the polarization pattern at the detector.

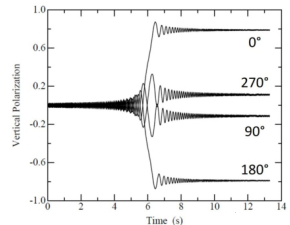
Plan for frequency scanning

Vary the spin precession frequency (f_{g-2}) in search of resonance.
 Ramp speed ≈ 0.1 Hz/s
 Compare initial and final polarization measurements.

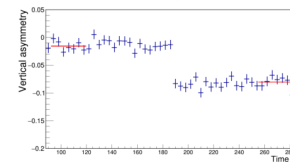


Expected results

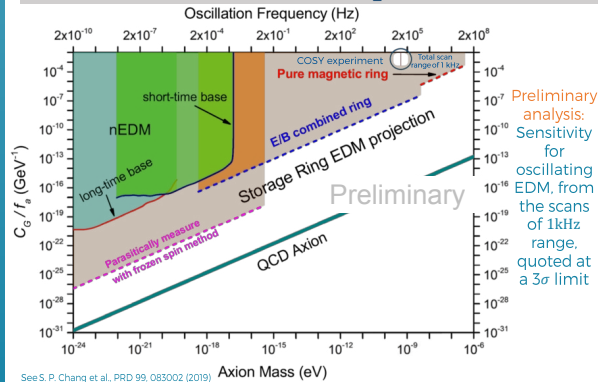
Simulations with a single bunch for 4 different phases 90° apart
 Resonance crossing speed 0.5 Hz/s
 Strength of oscillating EDM $1.6 \times 10^{-21} e \cdot cm$



- Tests with RF Wien filter:
- Generate signal similar to axion.
 - Calibrate polarization jumps.



Results of the first COSY experiment



See S. P. Chang et al., PRD 99, 083002 (2019)

Email: swathi.karanth@doctoral.uj.edu.pl

Controlling Systematic Error In Search For An Electric Dipole Moment



Moment In The Storage Ring



Anjali Aggarwal¹ and Andrzej Magiera¹ on behalf of JEDI collaboration

¹The Marian Smoluchowski Institute of Physics, Jagiellonian University, Kraków, Poland

Abstract

Measurements of electric dipole moment (EDM) for light hadrons with use of a storage ring have been proposed. The expected effect is very small, therefore various subtle effects need to be considered. In particular, interaction of particle's magnetic dipole moment (MDM) and electric quadrupole moment (EQM) with electromagnetic field gradients can produce an effect of a similar order of magnitude as that expected for EDM. Reproducing known EQM value gives the possibility to estimate global systematic uncertainties with the precision necessary for an EDM measurement with the planned accuracy.

Introduction:

- The JEDI Collaboration (Jülich Electric Dipole Moment Investigations) is developing tools for the measurement of permanent (EDMs) for proton and deuteron using storage ring.
- Final precision of 10^{-29} e-cm is expected with the dedicated storage ring.

Motivation:

- The Standard Model (SM) of Particle Physics fails to explain the reason for our very existence since it is not capable to account for the apparent matter-antimatter asymmetry of our Universe as shown in fig. 1.

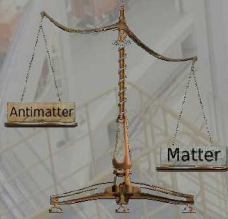


Fig. 1 Matter and anti-matter asymmetry.

"Sakharov conditions"

- Baryon number violation.
- C-symmetry and CP-symmetry violation fig.2.
- Interactions out of thermal equilibrium.

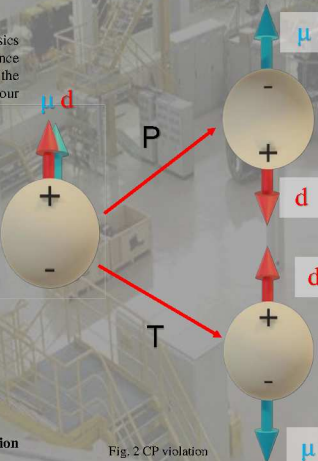


Fig. 2 CP violation

Challenges:

- For spin precession, up to now only interaction of the MDM and EDM with electromagnetic fields were considered only. But for a particle possessing a MDM and/or EQM, additional spin precession occurs due to their interaction with field gradients.
- For magnetic field $1T$ and $D = 10^{-29}$ e-cm of deuteron $\rightarrow S_y = 1.5 \cdot 10^{16}$
- For gradient $\delta B / \delta z = 10$ T/m and MDM of deuteron $\rightarrow S_y = 1.4 \cdot 10^{17}$ and EQM of deuteron $\rightarrow S_y = 4.3 \cdot 10^{16}$.
- The TBMT spin precession equation extended by MDM and EQM interaction with fields derivatives and including the terms generated by EDM [3].

$$\frac{d\vec{s}}{dt} = \frac{e}{mc} \vec{s} \times \left[\left(\frac{g}{2} - 1 + \frac{1}{\gamma} \right) c\vec{B} - \left(\frac{g}{2} - 1 \right) \frac{\gamma c}{\gamma + 1} (\vec{\beta} \cdot \vec{B}) \vec{\beta} - \left(\frac{g}{2} - \frac{\gamma}{\gamma + 1} \right) \vec{\beta} \times \vec{E} \right] + \frac{D}{\hbar} \vec{s} \times \left[\vec{E} - \frac{\gamma c}{\gamma + 1} (\vec{\beta} \cdot \vec{E}) \vec{\beta} - c\vec{\beta} \times \vec{B} \right] + \frac{ge\hbar}{2m^2c^2\gamma + 1} \left[\vec{s} \times (\vec{\beta} \times \vec{v}) \right] \left\{ c\vec{B} - \frac{\gamma c}{\gamma + 1} (\vec{\beta} \cdot \vec{B}) \vec{\beta} - c\vec{\beta} \times \vec{E} \right\} + \frac{Q\gamma}{\hbar(2I - 1)} \left\{ \vec{s} \cdot \vec{v} + \frac{\gamma}{\gamma + 1} \vec{\beta} \times (\vec{\beta} \times \vec{v}) + \vec{\beta} \cdot \frac{\partial}{\partial t} \right\} \left\{ \vec{s} \times \left[\vec{E} - \frac{\gamma}{\gamma + 1} (\vec{\beta} \cdot \vec{E}) \vec{\beta} + c\vec{\beta} \times \vec{B} \right] \right\}$$

Bmad Simulations For Quasi Frozen Spin Ring:

- Baby MAD - (Methodical Accelerator Design). Simulations done so far on Bmad are as follows:
- Ring lattice structure defined, particle tracking, spin tracking,
- Defined customised field for dipoles [4], $B_y = \frac{B_0}{2} \left[\tanh \frac{\pi}{2a} (z + L) - \tanh \frac{\pi}{2a} (z - L) \right]$, and also for Wien filter as shown in fig. 7.
- Field gradients are introduced in the TBMT equation.

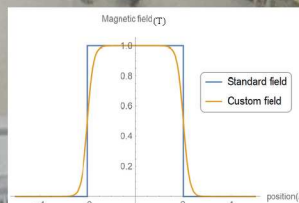


Fig. 7 The standard and customised fields for a dipole magnet.

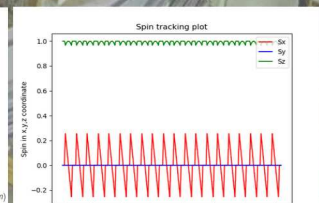


Fig. 8 Spin tracking for symmetric field of Wien filter.

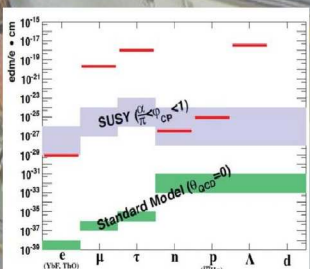


Fig. 4 Prediction from various models and experimental predictions.

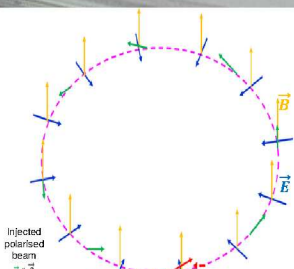


Fig. 5 Basic idea of spin behaviour in storage ring.

Basic Idea For EDM Calculation:

Spin parallel to momentum and z axis, Electric field in x direction and magnetic field in y direction as shown in fig. 5

Spin rotation angle per one revolution for $D = 10^{-29}$ e-cm equals to $3 \cdot 10^{-15}$ rad i.e. 6 degree in year.

- Methods proposed for EDM measurement for charged particle in storage ring are
 - Frozen spin method
 - RF Wien filter method
 - Quasi frozen spin method

All methods are based on build up of vertical polarisation component for initially horizontally polarised beam.

Quasi Frozen Spin Method

- The spin is not frozen with respect to the momentum vector, but continually oscillates with small amplitude around momentum direction.

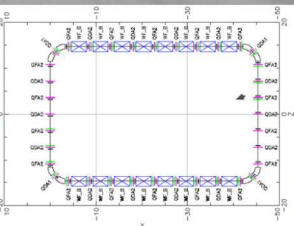


Fig. 6 Quasi frozen spin ring floor plan by BMAD

Systematic Uncertainties:

- Measuring EQM allows to extract value of systematic uncertainties [4].
- Reproducing the known values of EQM in the storage ring measurement would demonstrate that all the systematic uncertainties are well under control and pin down their value by 10^{-24} e-m.

Results and Conclusions:

- For a QFS ring, for the first time the influence of the deuteron EQM ($0.2859 \cdot 10^{-33}$ e.m²) interaction with field gradients on the vertical spin component was analysed.
- Spin tracking was calculated for EDM (10^{-27} e.m) and symmetric Wien filter field as shown in Fig. 8.
- Symmetric field refers to equal field strength ($E = 12$ MV) on both sets of Wien filters (on each straight section of accelerator). Similarly asymmetric field means different field strengths ($E = -12$ MV and -37.6 MV) on both sets.
- For a symmetric field EDM produces vertical polarization and EQM has zero effect. For asymmetric is vice versa.

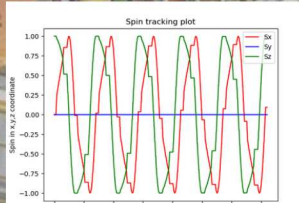


Fig. 9 Spin tracking for EQM and asymmetric field.

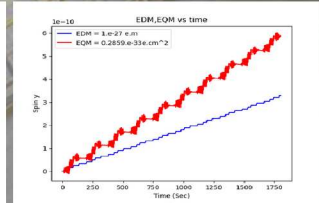


Fig. 10 Comparison of EDM (symmetric field) and EQM (asymmetric field) induced effects on vertical spin component.

Future plans:

- Introduce the full three dimensional customized fields [5] for all magnets including field gradients in order to calculate the real effects of magnetic field on spin precession.
- Method of measurement of EQM to pin down the systematic uncertainties can be used for any lattice.

References:

[1] P. Lenisa, et al., Nuclear Physics News, 2017.
 [2] Y. Senicichev, et al., in Proc. 6th Int. Particle Accelerator Conf. (IPAC'15), May 2015, p. 213.
 [3] R.H. Good, Phys. Rev. 125, 2112 (1962).
 [4] A. Magiera, Phys. Rev. Accel. Beams 20, 094001 (2017).
 [5] B.D. Muratori et al., Phys. Rev. Accel. Beams 18, 064001 (2015).

3rd Jagiellonian Symposium on Fundamental and Applied Subatomic Physics, June 23 – 28, 2019

The OSIRIS source calibration system

A. S. Göttel

The main goal of the JUNO [1] detector, located in Jiangmen, China, is to measure the neutrino mass hierarchy (MH) by detecting reactor anti-neutrinos in liquid scintillator(LS) through inverse beta decay. Moreover JUNO can be used to measure e.g. solar neutrinos through elastic scattering. The success of JUNO strongly depends on the radiopurity of its liquid scintillator. In particular, the concentrations of ^{238}U and ^{232}Th must be kept lower than $10 \times 10^{-15} \text{ g g}^{-1}$ for the MH analysis to work, and if solar neutrinos are to be detected then radiopurity must be at least one order of magnitude stricter.

The **Online Scintillation Internal Radioactivity Investigation System** (OSIRIS) (see Fig. 1) is a pre-detector for JUNO. Its purpose is to monitor JUNO's LS during filling, exploiting the fast Bi-Po time-coincidences of the ^{238}U and ^{232}Th decay chains.

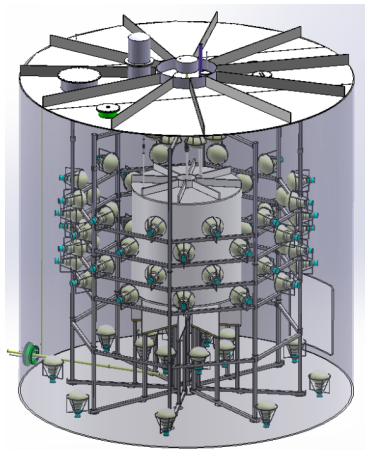


Figure 1: The OSIRIS detector, with the bell shaped calibration unit on top.

Special care must go into the design of OSIRIS's calibration system, to ensure that no contamination of the LS can occur. The calibration will consist of two parts: the Automated Calibration Unit (ACU) and the laser system. The latter is being designed in Tübingen. The ACU itself was provided by the Daya Bay [2] collaboration, and has been re-purposed for the needs of OSIRIS. This effort was mostly made in collaboration with the SJTU in Shanghai. The Software governing the ACU, while still under development, was already greatly overhauled, and the hardware tests so far show promising results.

The ACU is fully automated and will be completely sealed before data-taking begins. Inside of it are three acrylic wheels, used in a revolver-like structure on a stainless steel turntable to lower three different capsules in innermost vessel of the detector. One capsule will contain high-activity radioactive

isotopes emitting gamma rays for monthly energy, and position reconstruction, calibration. The second one will carry a low-activity gamma isotope for continuous monitoring of changes in the LS. Lastly, the third one will carry a LED into the detector which can mimic signals in the LS with a high timing accuracy. The LED will be used to calibrate the high-voltage gain and the timing of the PMTs themselves, to an accuracy better than 1 ns.

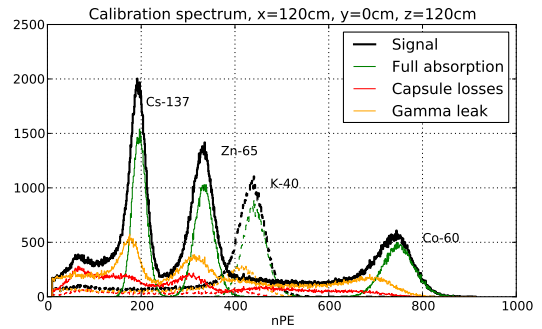


Figure 2: A typical calibration energy spectrum for OSIRIS. The x-axis depicts the number of photoelectrons produced in the PMTs. The solid lines show the spectrum for the high-activity capsule, and the dashed lines for the low-activity one. The different colors show the different effects which contribute to the full signal, shown in black.

The PMTs all around the inner vessel are arranged in a cylindrical fashion (see Fig. 1). This naturally introduces spatial inhomogeneities in the detector response. Since additionally the calibration sources cannot go through the central axis of the detector, for mechanical reasons, they will instead be deployed at a distance of 120 cm from the centre line along the z-axis. This position was chosen using simulations, as it maximises variation in the sampled detector response. A typical (simulated) energy calibration spectrum for OSIRIS can be seen in Fig. 2. In order to account for the different effects which alter the spectrum, specially designed fit functions will be used to extract the Gaussian full-absorption peaks and minimise bias.

References

- [1] F. An et al., Neutrino physics with JUNO, *Journal of Physics G: Nuclear and Particle Physics*, 43(3):030401(2016)
- [2] J. Cao et al., An overview of the Daya Bay reactor neutrino experiment, *Nuclear Physics B*. 908 (2016) 62-73

iPMTs in OSIRIS

M. C. Vollbrecht

The main detector of the JUNO experiment (**J**iangmen **U**nderground **N**eutrino **O**bservatory) is under construction, one of its subsystems will be OSIRIS (**O**nline **S**cintillator **I**nternal **R**adioactivity **I**nteraction **S**ystem). This cylindrical detector is shown in Fig.1 and will be used to screen the scintillator in the JUNO detector for any issues that might affect the sensitivity of JUNO, for example possible contaminations with Uranium or Thorium.

OSIRIS will feature in total 76 20-inch iPMTs (**i**ntelligent **P**hoto**M**ultiplier**T**ubes) to analyse signals originating from the scintillator and the water buffer around it. The newly developed design of the iPMTs combines the PMT and all needed readout plus control devices in such a way that only one Ethernet cable is sufficient to power and run the whole device. Furthermore, there is the possibility to perform waveform reconstructions or baseline regulation on the hardware itself, hence the term "intelligent".

Since the electronics of the iPMTs will be sealed permanently before use, intensive testing of all the internal components and the mechanical sealing procedures of the iPMTs is very important. Many tests and tools have been developed so far, each focusing on different aspects of the iPMTs. A few examples will be given in the following paragraphs:

1. The power supply of the iPMTs is done via PoE (**P**ower **o**ver **E**thernet). PoE uses two cable pairs present in a standard Ethernet cable to deliver power to the device without disturbing possible data transfer happening simultaneously. Since PoE divides devices into different power classes, the needs of an iPMT in terms of power have to be negotiated with the source powering the iPMT. For this reason, a detailed test of the communication between Ethernet switches and the board for PoE communication was performed and possible error sources were eliminated.
2. In order to reconstruct events in the detector, the time information of individual signals has to be known. To synchronize the timestamps that are attached to a recorded signal, an external clock is used as a reference to which the timestamps of the signals are aligned. This reference signal is sent out on a regular basis to ensure precise timing during normal operation. Tests probing this synchronisation technique yielded positive results, the implementation is progressing constantly.

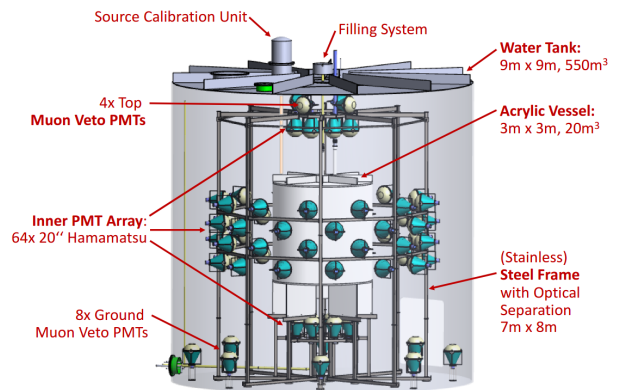


Figure 1: Overview of the OSIRIS detector, ©Prof. M. Wurm.

3. The PMT current signal measurement is done with the VULCAN chip that was designed at the ZEA-2 institute of the Forschungszentrum Jülich. This chip is highly configurable, making it very flexible and powerful. Still, the wide range of possible settings has to be evaluated and the configuration that fits best to the expected signals needs to be selected. Work in that direction is advancing steadily, including cooperative measurements at ZEA-2 as well as at the physics institute IIIB of the RWTH.
4. The glueing procedures which seal the iPMT electronics from the surrounding water in the final application need to be evaluated under realistic circumstances. The sealing of the devices is crucial, since any leak might introduce water to the electronics inside of the iPMTs, or the oil used for cooling the electronics could contaminate the ultra pure water around the iPMTs, thus affecting the sensitivity of OSIRIS. To simulate the working conditions, mechanical tests with the materials used have been performed, further studies, for example pressure tests, are under way.

The installation of the iPMTs in OSIRIS is planned to take place in early 2021, consequently, the iPMT shipment to China will happen in autumn 2020. Until then, many more tests will follow, as well as a thorough cleaning procedure. This step is needed to eliminate a possible contamination of the water surrounding the iPMTs with grease, oil, or simply dust that was present in the air at the time of production. Furthermore, this cleaning should reduce background activity levels by removing natural radiation sources that mimic the signals OSIRIS is sensitive to.

Improved method for obtaining effective quantum efficiency of the Borexino photomultipliers

M. Redchuk

During the last year, significant work has been done to improve and develop a novel approach towards obtaining the effective quantum efficiency (EQE) of the photomultiplier tubes (PMTs) of the Borexino detector, an important parameter in the Borexino Geant4 Monte Carlo (MC) simulation. This parameter determines the amount of light converted to p.e. by each PMT in the simulation, which influences the energy estimators (EE), and ultimately, the reference spectral shapes of different background isotopes and neutrino signals, used in the multivariate fit for the solar neutrino analysis, shown in Fig. 1.

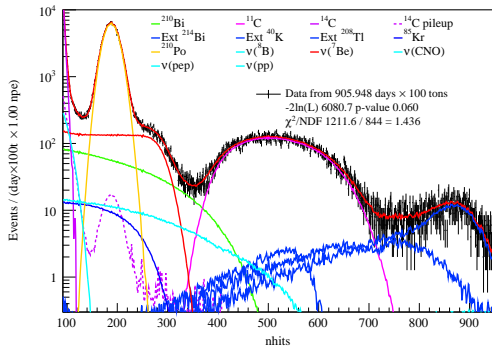


Figure 1: Example of an energy spectrum fit using reference shapes constructed using MC.

The main improvement consists in the development of a new approach to the selection of ^{14}C events, which are used to compute EQE and monitor its time evolution. The blue curve in Fig. 2 shows the original method based on all active PMTs, which results in a wrong selection with unstable increasing energy due to varying and unstable PMT quality, and the loss of PMTs over time.

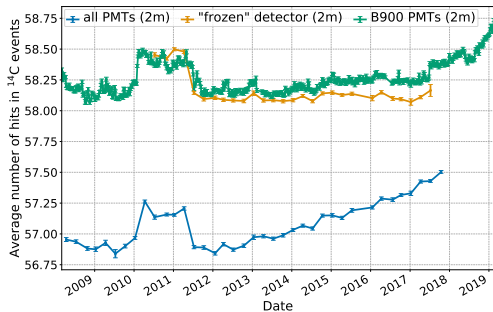
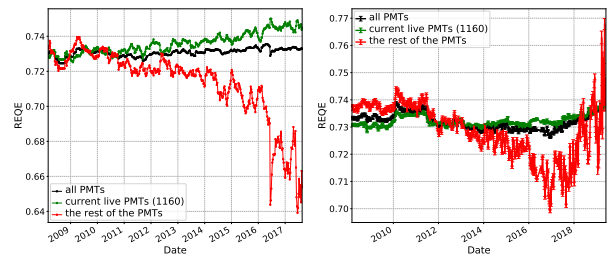


Figure 2: Average ^{14}C energy resulting from all PMTs (blue), preliminary studies (orange) and B900 (green).

In order to avoid this effect, the new method uses the so-called B900 PMTs, selected based on stable

quality and long lifetime. A new EE based only on B900 has been constructed and implemented. As seen in Fig. 2, the resulting ^{14}C selection using this EE (green) is consistent with the preliminary studies (orange), and can be used to calculate EQE of all PMTs, including the non-B900 ones.

The resulting average EQE is shown in Fig. 3b, compared to the previous values shown in Fig. 3a. The new EQE values demonstrate expected stable values for B900 PMTs, which is not the case for old EQE; and the total average EQE which represents the changes in the quality of PMTs correctly.



(a) Old method.

(b) New method.

Figure 3: Average EQE in all active PMTs (black), B900 PMTs (green) and the rest of the PMTs in the given time point (red).

The new method for EQE has been validated using independent studies on the evolution of the effective light yield (ELY), based on ^{210}Po data. As seen from Fig. 4, MC using new EQE inputs (blue) represents the ELY evolution in data (green) better than the old (red).

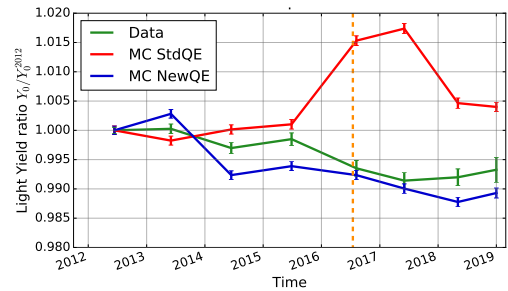


Figure 4: ELY calculated using ^{210}Po data (green) and ^{210}Po MC with old (red) and new (blue) REQE inputs. The beginning of Phase-III is marked with the orange dashed line.

The improved EQE inputs improve the spectral shapes constructed using MC which allows to perform multivariate fit on the latest Borexino Phase-III data (orange dashed line in Fig. 4), aimed at the CNO neutrino measurement.

Modelling liquid scintillator non-linearity in JUNO

Philipp Kampmann

The measurement of the neutrino mass hierarchy by JUNO relies on the precise energy measurement of IBD from the coincident Inverse Beta Decay (IBD) signal, where an antineutrino interacts with a proton and generates a positron and a neutron [1]:

$$\bar{\nu}_e + p \rightarrow e^+ + n \quad (1)$$

The positron can be measured by its energy deposition in the scintillator, followed by its annihilation with an electron of the detector material. The neutron is measured with the energy released by the Deuteron de-excitation after the neutron is captured on a free proton of the detector material. As the neutron thermalizes before it gets captured, the energy depositions from positron and neutron can be divided into the prompt and the delayed event. The initial energy of the electron anti-neutrino, which is needed for the determination of the mass hierarchy, can be fully reconstructed with the measurement of the prompt energy. It is required to reach a relative uncertainty on the energy scale of the prompt event of less than 1% and an energy resolution better than 3% at 1 MeV. This contribution focuses on the description of the energy non-linearity introduced by the scintillation medium.

To describe the energy deposition of the positron, several processes are needed. First, the positron deposits its energy due to positron-electron scattering in the scintillation medium. This is described using the energy loss by Bhabha-scattering [2]. After that, the positron annihilates with an electron of the detector medium. This happens usually at rest after forming positronium. These gamma photons do not directly excite the scintillation medium to produce light. Instead they interact with electrons due to Compton scattering, Rayleigh scattering and the photoelectric effect. These scattered-off electrons deposit their energy then in the scintillator due to electron-electron scattering. This is described by the energy loss via Møller-scattering [2] in this work. For the description of the production of scintillation light (L), the empirical Birks' law is used:

$$L(E) = L_0 \int_0^E \frac{1}{1 + k_B \langle \frac{dE}{dX} \rangle (E')} dE' \quad (2)$$

with L_0 being a normalization constant and k_B being the Birks' material constant. Another non-linear source of light in the detector is Cherenkov light. The production of Cherenkov light by electrons and positrons is considered by the usage of an empirical model.

To obtain the amount and the energies of secondary electrons produced by annihilation gamma photons

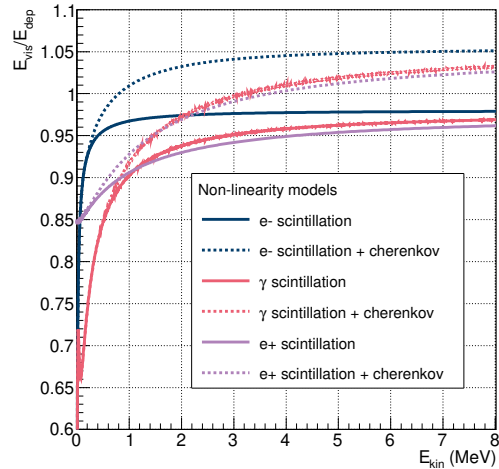


Figure 1: The different resulting non-linearity models for different particles. The positron non-linearity curve describes positrons which annihilate at rest into two photons. The E_{vis}/E_{dep} ratio is normalized to be 1 in the case of no cherenkov light and no quenching. The value of the Birks' constant of $k_B = 0.01 \text{ g/MeV/cm}^2$ is used here.

a calculation procedure was developed. This procedure decides first if Compton scattering or Photoelectric Absorption is performed depending on the relative cross section and the energy of the gamma photon. If Compton scattering occurs, a random angle following the Klein-Nishina differential cross section is drawn and the resulting electron and gamma photon energies are calculated accordingly. If Photoelectric Absorption occurs, the gamma photon is fully absorbed and its full energy is transferred to the electron. Therefore the calculation is performed iteratively until the gamma photon undergoes Photoelectric Absorption. The resulting electron energies are inserted into Birks' law (Eq. 2) to get the full non-linear energy signal of the gamma photons. In the case of positron annihilation at rest into two gamma photons, the energy of each gamma photon is $E_\gamma = 0.511 \text{ MeV}$. The resulting non-linearity curves for electrons, gamma photons and those positrons are shown in Fig. 1. Annihilations in flight or into 3 gamma photons are not included.

References

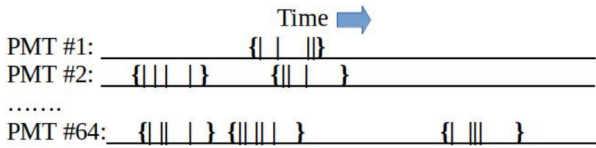
- [1] F. An et al., Neutrino Physics with JUNO, *Journal of Physics G: Nuclear and Particle Physics*, 43(3):030401(2016)
- [2] C. Patrignani et al., *Review of Particle Physics*, *Chin. Phys.*, C14(10):100001 (2016)

Online Event Builder for OSIRIS

R. Liu¹, C. Genster¹

JUNO is a 20 kt liquid scintillator detector under construction in Jiangmen, China, whose goal will be to determine the neutrino mass hierarchy. In order to meet the stringent requirements on the radiopurity of the liquid scintillator, the OSIRIS pre-detector is being designed to monitor the liquid scintillator during the several months of filling the large volume of JUNO. OSIRIS will contain 20 ton of scintillator and will be equipped with 76 20-inch PMTs. The DAQ system will have no global hardware trigger: instead, each PMT will provide a data-stream composed of the waveforms, each containing a gps time stamp. Then, dedicated offline trigger software will organize individual waveforms into events.

For the 64 inner PMTs, 240 ns readout windows are applied on each of them during data taking. The hits inside these readout windows are packaged as single hits inside the PMTs, and these packages will be delivered to the event builder. The picture [1] below shows how it works. After this process, the packages are lined in one single timeline rather than 64 timelines.



“|”: Real hits or dark hits on each pmt.
 “{}”: Readout window of 240 ns.

Figure 1: Workflow for hits packaging of the 64 inner PMTs.

The events will be built and determined by the trigger window settings: (n;dt). Each trigger window will start from one packaged hit and last for time of dt. If there are no less than n hits during one trigger window, then we will have one event triggered. The multiplicity number n and trigger window time dt need to be optimize in later testing process.



Figure 2: Readout windows packaging workflow. The “{” are the start time of each readout windows from different PMTs in Figure 1.

The skeleton structure of the event builder code was first built up by ZEA-2, FZ Jülich. Then the IKP-2 neutrino group, Uni-Mainz neutrino group and RWTH Aachen neutrino group have been working together on modifying and implementing logics and new modes in the codes.

In general the software runs in 4 threads: reader, sorter, selector and writer. Each thread runs as

fast as possible and can access their corresponding data container. There are 4 containers in memory, mainly queues that implemented as doubly linked lists.

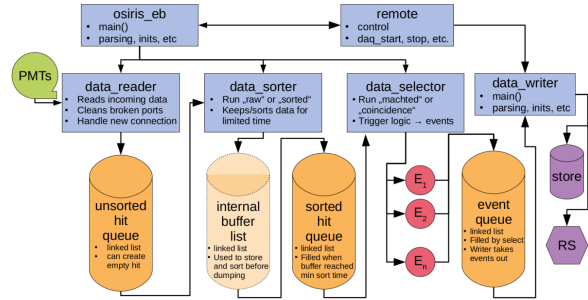


Figure 3: The structure of the event builder [2].

Incoming data arrives at the data reader and is there put into the unsorted hit queue in the order they come in via the network. The data reader also handles new connections and cleans up broken ports.

The data sorter constantly grabs the first item of the unsorted hit queue and puts it into an internal buffer, implemented as a linked list. If the contained data spans more than a given time window, it is sorted and pushed into the sorted hit queue. The sort/collection time should be set in a way that we are sure no more hits are arriving belated into the window to be sorted. This need to be tested in later data runs.

The data selector contains the trigger logic. It constantly grabs the first hit in the sorted queue and applies some trigger logic to be defined by physics later. It is also possible to just write out sorted or matched hits without application of trigger. The output of the data selector are collections of hits packed into a event. In general, this structure contains a header with some information about the trigger followed by a collection of hit-objects. Events are put into the event queue sorted since the input of the data selector is sorted in time and the process takes one hit after another without going back.

The data writer finally just takes events from the event queue and writes them to disk or sends them out to another machine running the RootSorter online analysis.

References

- [1] R. Liu, Progress on Event Builder, JUNO Collaboration meeting talk (14.01.2020).
- [2] C. Genster, Event Builder Overview, (01.2020)

¹Institut für Kernphysik, Forschungszentrum Jülich, Jülich 52428, Germany

Reconstruction with Deep Learning Methods in JUNO

Yu Xu¹

Deep Learning method is now widely used in many fields of high energy physics, including Large Hadron Collider experiments, NOvA and MicroBOONE experiments, due to its potential in the many fields [1]. The principle of deep learning is simple: standard multilayer feedforward networks with as few as one hidden layer using arbitrary squashing functions are capable of approximating any Borel measurable function from one finite dimensional space to another to any desired degree of accuracy, provided sufficiently many hidden units are available [2].

Borel measurable function f : If $f : XY$ is continuous mapping of X , where Y is any topological space, (X, \mathcal{B}) is measurable space and $f^1(V)\mathcal{B}$ for every open set V in Y , then f is Borel measurable function.

In JUNO experiment we need to reconstruct charge and hit time of the FADC waveform first, and then reconstruct the vertex and energy of the event based on the charge and time information. Last, we can do physics analysis based on the event reconstruction.

Waveform Reconstruction

For the waveform reconstruction in JUNO, the main goal is to get the charge and time of hits. For charge, we need to reduce the electronics non-linearity effect. For time, we use Wasserstein distance to evaluate the performance of reconstruction in case there can be multiple hits in one channel.

Wasserstein distance: Let $\Gamma(\mu, \nu)$ denote all joint distributions γ for (X, Y) that have marginal distributions μ and ν , the Wasserstein distance of order p on d dimension Polish metric space R^d is defined by [3]:

$$W_p(\mu, \nu) := \inf_{\gamma \in \Gamma(\mu, \nu)} \left(\int_{R^d \times R^d} d(x - y)^p d\gamma(x, y) \right)^{1/p} \quad (1)$$

I construct a neural network model based to reconstruct the charge and time of hits. As the result of our model, the mean value of Wasserstein distance is 3.74, as shown in Fig. 1. In the mean time, the charge non-linearity is less than 0.5%.

Particle Identification

In the liquid scintillator there is intrinsic difference in the pulse shape of different particles, which allow us to identify the types of the particles with their time profiles in JUNO. In the experiment, the major influence factors are the transit time spread (TTS) effect and PMT dark noise. Considering all above effects, we find that for α/β and e/p discrimination,

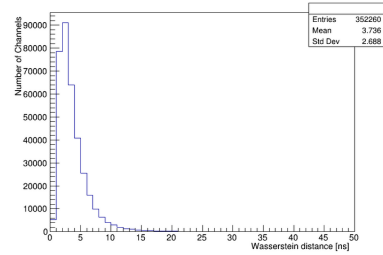


Figure 1: The distribution of Wasserstein distance for over 300 k channels, with the mean value as 3.74 and standard deviation as 2.71.

we are able to select more than 98% signals with less than 1% background remaining. Even for e^+/e^- discrimination, we can still select 50% signals with 5% background remains.

Vertex Reconstruction

For vertex reconstruction we select the information of the triggered PMTs positions, their charges and hit times and then input these information into deep learning model. The resolution of vertex reconstruction on x/y/z axis is around 6 to 7 cm for 1 MeV events. In the whole detector, the non-uniformity is less than 1%.

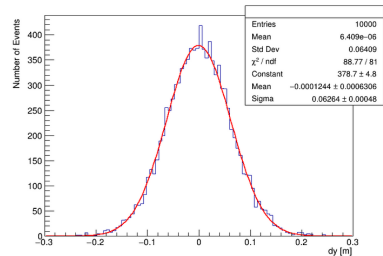


Figure 2: The performance of vertex reconstruction on y axis, with the resolution as about 6.2 cm

Conclusion

We implement deep learning method in JUNO and get some good preliminary results. We currently do the reconstruction independently for the different part of JUNO experiment and we will combine the different part in one global framework in the next step.

References

- [1] A. Kim Albertsson etc, arxiv 1807.02876 (2018)
- [2] B. Kurt Hornik, etc. Neural Networks, 2(5):359 – 366, 1989
- [3] C. Cedric Villani. The Wasserstein distances, pages 93–111, 2009.

Analytical Multivariate Fit and Sensitivity Studies in the Borexino Solar Neutrino Analysis



Ömer Penek^{1,2} and Livia Ludhova^{1,2}
on behalf of the Borexino collaboration



Motivation

Studying ...

... Neutrinos with the Sun

... the Sun with Neutrinos

Oscillation Parameters

ν Magnetic Moment

Deviations from MSW-LMA (New Physics)

Metallicity

Energy Production and Loss

Fusion (pp chain and CNO cycle)

The Borexino Detector

Nylon Outer Vessel
R = 5.5 m
Barrier for Rn from steel, PMTs etc.

Water Tank
R = 9 m, 2.1 kt of Water Shielding, Cherenkov muon veto

Buffer
PC + DMP

Nylon Inner Vessel
R = 4.25 m
~ 300 tons of liquid scintillator (PC/PPO solution)
Fiducial Volume ~100 tons (software cut)

Stainless Steel Sphere
R = 6.85 m
Buffer + Scint. container
PMTs support

208 Outer Detector PMTs

2212 Inward-facing PMTs

High Light Yield ~ 500 p.e. / MeV

High Radiopurity ($^{238}\text{U} + ^{232}\text{Th}$) < 6.64×10^{-19} g/g

Multivariate Analysis Strategy and Likelihood Construction

Multivariate Analysis Strategy

Threefold Coincidence (TFC)

β^+ -decay of ^{11}C
→ Positron Pulse-Shape

1. Split data in TFC-subtracted and TFC-tagged spectra with 92% ^{11}C -tagging efficiency while preserving 64% of the total exposure in the TFC-subtracted spectrum

2. Radial Distribution: Disentangle External Backgrounds

3. e^+/ν Pulse-Shape Parameter: Disentangle the remaining ^{11}C (8%) in the TFC-subtracted spectrum → Orthopositronium (50%) and Annihilation γ s

Pulse-Shape and Radial Distance Distributions

Pulse-Shape (PS): electron and positron like events
PS- L_{ps} : Pulse-Shape Parameter

2D PS vs. Energy

Y-Projection of 2D PS Histogram

Radial Distance: uniform component and external background like events

2D Radial vs. Energy

Y-Projection of 2D Radial Histogram

The N_{ps}^{dLZ} energy estimator is defined as the number of PMTs hit within 400 ns after cluster start time

PDF Construction and Definition of $\mathcal{L}_{MV}(\vec{\theta})$

Poisson(λ, k) = $\frac{\lambda^k}{k!} e^{-\lambda}$

0 = Signal Index and 1 = Background Index

$PDF_{\mathcal{L},0,1}(m_{0,1}, n_{0,1}, k) = \int_0^\infty d\lambda' \text{Poisson}(m_{0,1}, \lambda', k) \text{Poisson}(\lambda', n_{0,1})$

$PDF_{\mathcal{L}}$ = Convolution of RED and BLUE or RED and GREEN Projection

$\mathcal{L}_{MV}(\vec{\theta}) = \mathcal{L}_{sub}^{TFC}(\vec{\theta}) \mathcal{L}_{tag}^{TFC}(\vec{\theta}) \mathcal{L}_{PS}(\vec{\theta}) \mathcal{L}_{Radial}(\vec{\theta})$

Likelihood Construction

$\mathcal{L}_{sub,tag}^{TFC}(\vec{\theta}) = \prod_{i=1}^{N_{bins}} \text{Poisson}(\lambda_i(\vec{\theta}), k_i)$

Scaling Parameter m defined by energy projection (Index s) = fraction of signal/bkg counts with respect to data counts

$m_{0,1s} = \frac{SC_{0,1s}}{TSC_s} \cdot \frac{TDC_s}{RI_{0,1s} + RIN_{0,1s}}$

[T]SC = [Total] Species Counts, [T]DC = [Total] Data Counts, $s \leq P$ = Projection Index
RI[N] = (PS or Radial) Reference Histogram Counts [Bins], λ = Model Bin Content, k = Data Bin Content, $n_{0,1}$ = (Signal/Bkg) Reference Bin Content, $j \leq M$ = Bin Index

$PDF_{PS, Radial}^{\mathcal{L}, tot}(\vec{m}, \vec{n}, k) = \sum_{i=0}^k PDF_0(m_0, n_0, k-i) PDF_1(m_1, n_1, i)$

Likelihood Description for the Pulse-Shape and Radial Distribution

$\mathcal{L}_{PS, Radial}^{tot, calc}(\vec{\theta}) = \prod_{s,j=1}^{P,M} \frac{a_s \lambda_{js}^{k_{js}}(\vec{\theta})}{k_{js}!} e^{-a_s \lambda_{js}(\vec{\theta})}, TDC_s = a_s \sum_{j=1}^M \lambda_{js}(\vec{\theta})$

Multivariate Analytical Fit

Simultaneous Determination of $\nu(pp)$, $\nu(^7\text{Be})$, and $\nu(pep)$ - Fit from 0.19 to 2.93 MeV

$\nu(pp) = 134 \pm 10^{+16}_{-10}$ cpd/100t

$\nu(^7\text{Be}) = 48.3 \pm 1.1^{+0.9}_{-0.8}$ cpd/100t

$\nu(pep)_{HZ} = 2.43 \pm 0.36^{+0.15}_{-0.22}$ cpd/100t

$\nu(pep)_{LZ} = 2.65 \pm 0.36^{+0.25}_{-0.24}$ cpd/100t

$\nu(HZ/LZ) \Leftrightarrow \nu(\text{CNO})$ constraint to High/Low (Metallicity Solar Model)

$^{210}\text{Bi} = 17.5 \pm 1.9$ cpd/100t

$^{210}\text{Po} = 260.0 \pm 3.0$ cpd/100t

$^{11}\text{C} = 26.8 \pm 0.2$ cpd/100t

$^{14}\text{C} = 40 \pm 2$ Bq/100t (constraint)

$^{85}\text{Kr} = 6.8 \pm 1.8$ cpd/100t

$^{208}\text{Tl} = 3.3 \pm 0.1$ cpd/100t

$^{214}\text{Bi} = 1.9 \pm 0.3$ cpd/100t

$^{40}\text{K} = 1.0 \pm 0.6$ cpd/100t

TFC - subtracted

TFC - tagged

Borexino Collaboration, Nature 562 (2018), 505-510

Sensitivity for pep and CNO Neutrinos

$\Delta\chi^2 = -2 \times (\log \mathcal{L}(\theta) - \log \mathcal{L}_{\min}) = \chi^2 - \chi^2_{\min}$

Break $^{210}\text{Bi} - pep - \text{CNO}$ Correlation by fixing the CNO rate to: Fix ratio of pp and pep Rates

$R_{CNO}(HZ) = 4.92 \pm 0.55$ cpd/100t

$R_{CNO}(LZ) = 3.52 \pm 0.37$ cpd/100t

$R_{pp} = 131.1 \pm 1.4$

$R_{pep} = 2.74 \pm 0.04 = 47.8 \pm 0.8$

$\nu(^7\text{Be})$

$\nu(pep)$

$\nu(\text{CNO})$

$Z \geq 5\sigma$ pep Discovery

Best CNO Limit

< 8.1 cpd/100t 95% C.L.

¹Forschungszentrum Jülich, 52425, Jülich, Germany; ²RWTH Aachen University, 52062, Aachen, Germany;

Member of the Helmholtz Association

Contact: o.penek@fz-juelich.de

[1] Borexino Collaboration, Physical Review D 89, 112007 (2014) [2] O. Smirnov Nucl. Inst. Meth. in Physics Research Section A 595, 410 (2008) [3] S. Marocchi, PhD Thesis (2016) [4] Borexino Collaboration, arXiv:1707.09279 [4] Borexino Collaboration, Nature 562, 505-510 (2018)



RWTH AACHEN UNIVERSITY

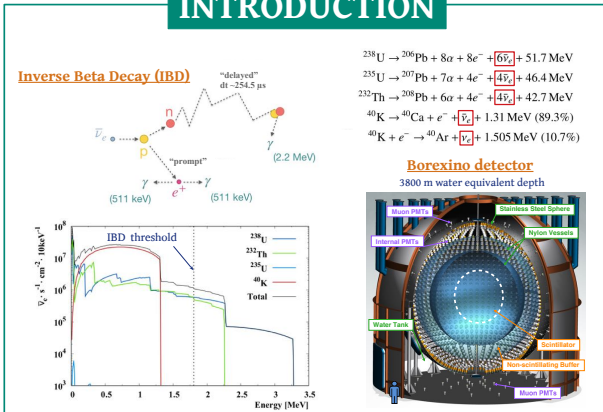
ANALYSIS STRATEGIES FOR THE UPDATED GEONEUTRINO MEASUREMENT WITH BOREXINO

Sindhujha Kumaran^{1,2} for the Borexino Collaboration

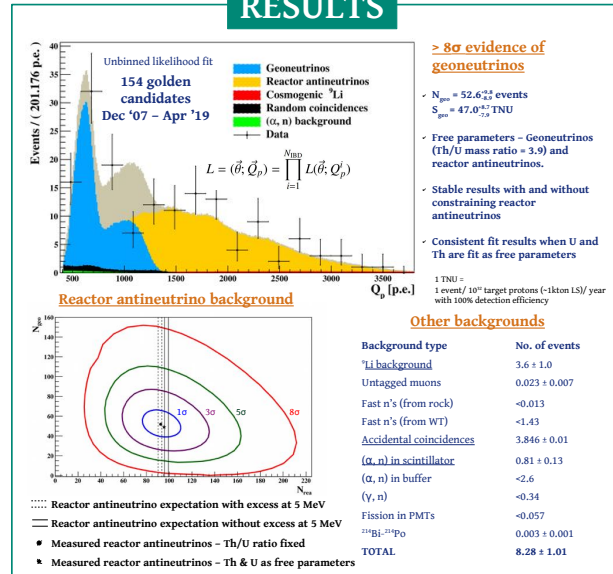


Updated statistics and improved analysis techniques lead to ~18% precision in Borexino's geoneutrino measurement

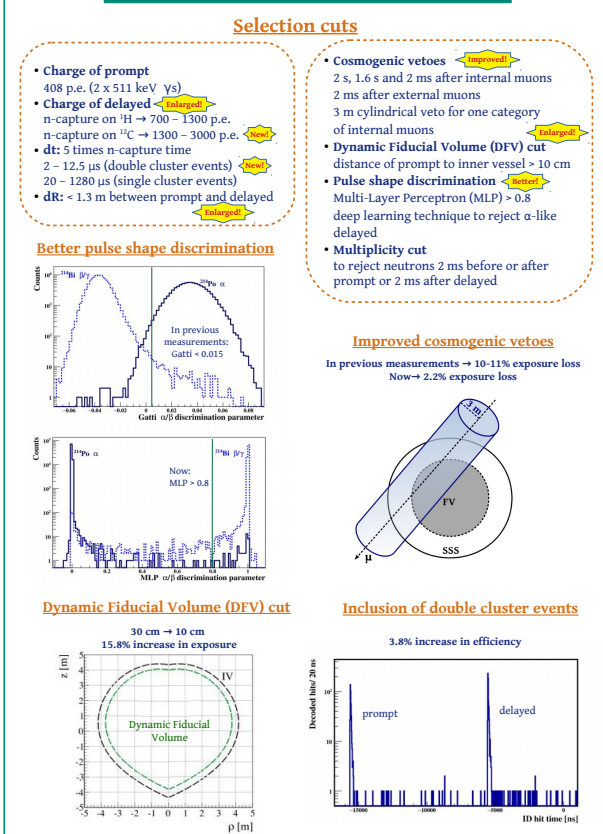
INTRODUCTION



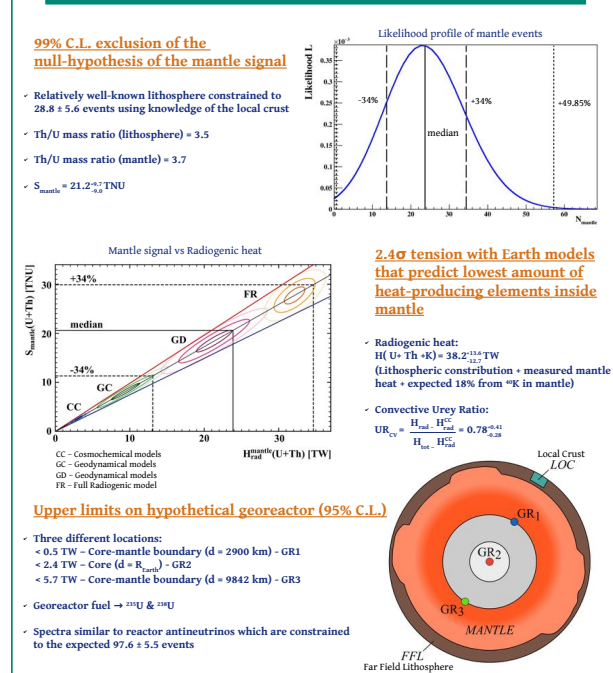
RESULTS



ANALYSIS TECHNIQUES



GEOLOGICAL INTERPRETATIONS



Progress of the Lamb-shift Polarimeter for the Molecular Beam Source in Novosibirsk

L. Huxold^a, R. Engels, M. Büscher^{a,b}, Y. Shestakov^c, D. Toporkov^c

A prototype polarized hydrogen and deuterium molecule beam source has been developed at the Budker Institute of Nuclear Physics (BINP) in Novosibirsk. The Molecular Beam Source (MBS) is based on the Stern-Gerlach principle. First tests indicate a separation of \vec{H}_2 and \vec{D}_2 molecules in different nuclear spin projection states [1]. For verification a measurement of nuclear spin polarization is needed. A Lamb-Shift Polarimeter (LSP) is well suited for this purpose [2]. Therefore, an LSP has been built at the IKP. In 2018 it had been shipped to Novosibirsk and its proper functioning was shown. This year it was successfully used to measure the polarization of an atomic beam and tuning measurements were performed.

Since the magnetic field in the Wienfilter is perpendicular to the nuclear spins of the ions produced in the ionizer, Larmor-precession will occur. The frequency of the precession is given by $\omega_{Larmor} = \hbar^{-1} \cdot g \cdot \mu \cdot B$, with g being the g-factor, μ the magnetic moment of the particle and B the magnetic field strength. Single-electron ions (H_2^+ , HD^+ and D_2^+) behave differently than protons and deuterons. While the nuclear spins of the atomic ions will precess relatively slowly, the electrons of the molecular ions will follow the magnetic field adiabatically. Since the magnetic field of the electron acting on the nuclei is in the order of 10 T, the nuclear spins will follow the electron spin. Therefore, the measured nuclear polarization of the molecules is independent of the magnetic field of the Wienfilter, while for the atomic ions the magnetic field of the Wienfilter should be set such, that the angle by which the nuclear spins are rotated after passing the Wienfilter is known and the measured polarization therefore can be corrected (e.g. 180° and correction factor of -1). Since the angle is the product of Larmor-frequency and time the particle take to pass the magnetic field of the Wienfilter, the angle is velocity dependent. To determine the angle for a given velocity the polarization was measured for different magnetic field strengths. A measurement for protons of an energy of 2 keV is shown in Fig. 1.

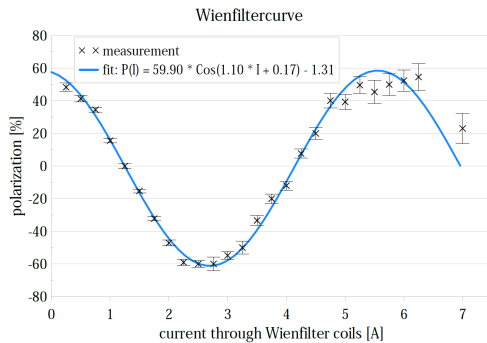


Figure 1: Wienfilter calibration curve for 2 keV protons. At about 2.7 A the polarization vector is rotated by 180°.

Since low intensities are expected, when the ABS is modified to produce a molecular beam, the efficiency of all parts of the LSP have to be optimized. One part to be optimized is the production of metastable atoms from H_2^+ ions in the Cs vapor in the Cs-cell. As shown by Pradel et al. the highest cross section for metastable production from atomic ions is at 550 eV (protons) and 1100 eV (deuterons) [3]. For molecules this might be different. Another factor is the Cs vapor density, which can be adjusted by the temperature of the Cs. A measurement in Novosibirsk showed an optimum for 2 keV H_2^+ at a temperature of 170°C. In Jülich it was tried to perform a more detailed measurement. However, to obtain a sufficient stable ion beam was not always possible and the transportation of the beam through the LSP at different energies interferes with the measurement and seems to dominate it. To estimate the production efficiency of metastable atoms from H_2^+ ions the photomultiplier signal was normalized by the ion current before the Cs-cell. An Example shown in Fig 2.

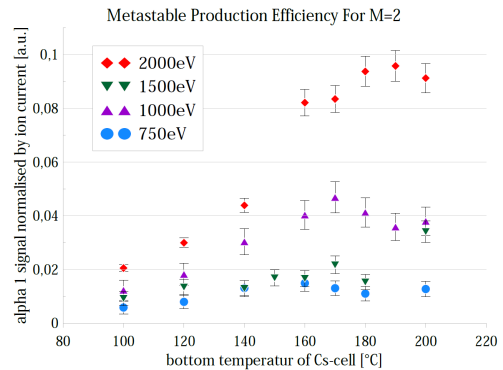


Figure 2: Production efficiency for metastable atoms from H_2^+ ions as function of the temperature on the bottom of the Cs-cell.

In February 2020 measurements with the MBS and the LSP have started. However, the measured signals are too low to differentiate from the background and noise. A new alignment of the MBS, the Ionizer, and the LSP is planned as next step. Furthermore, optimization of the Ionizer are necessary.

References

- [1] D.K. Toporkov et al.; Nucl. Instrum. Meth. A **868** (2017) 15.
- [2] R. Engels et al.; Rev. Sci. Instr. **85** (2014) 103505.
- [3] P. Pradel et al.; Phys. Rev. A **10** (1974) 797.

^a Institute for Laser- and Plasma Physics, Heinrich-Heine University Düsseldorf, Germany

^b Peter Grünberg Institute, Forschungszentrum Jülich, Germany

^c Budker Institute of Nuclear Physics, Russia

Measurement of the nuclear polarization of pulsed H^- and D^- beams produced by the COSY polarized ion source with a Lamb-shift polarimeter

R. Engels, N.-O. Fröhlich, R. Gebel, K. Grigoryev, S. Pütz, and Y. Valdau

Until now the nuclear polarization of the polarized H^-/D^- source at COSY is determined and optimized with the "low-energy polarimeter" behind the cyclotron. This polarimeter is a nuclear-reaction polarimeter based on the elastic scattering of protons with carbon in a thin foil. This reaction implies relatively large differential cross sections and analysing power for the given energy of the cyclotron. Nevertheless, a polarization measurement with this device needs the pre-acceleration of the ions with the cyclotron and takes several minutes. Thus, a faster polarization measurement directly behind the source, i.e. without using the cyclotron, would be very profitable. For this reason a Lamb-shift polarimeter (LSP) was installed in the south hall some years ago. Such a LSP consists of three components: In a cesium cell incoming protons undergo a charge exchange with Cesium vapor to produce metastable hydrogen atoms in the state $2S_{1/2}$. A strong magnetic field preserves the nuclear polarization so that only hyperfine substates with the same proton/deuteron spin than the original protons/deuterons have are populated. In a spinfilter all metastable atoms are quenched into the ground state $1S_{1/2}$. Only special conditions of a longitudinal magnetic field, a radial electric field and a radio-frequency of 1.60975 GHz in the TM_{010} mode inside a cavity will keep one metastable hyperfine substate. By changing the magnetic field two hyperfine substates of the metastable hydrogen atoms/ three hyperfine substates of the metastable deuterium atoms with different nuclear spin can be chosen to transmit through the spinfilter. E.g., at 53.5 mT metastable hydrogen atoms in the hyperfine substate α_1 with the proton spin $m_I = +1/2$ and at 60.5 mT the hyperfine substate α_2 with spin $m_i = -1/2$ will survive. For deuterium these resonances are at 56.5 mT ($m_I = +1$), 57.5 mT ($m_I = 0$) and 58.5 mT ($m_I = -1$). In a quenching chamber the residual metastable atoms are quenched into the ground state with a strong electric field due to the Stark effect. By counting the produced Lyman- α photons the amounts $N_{m_I=+1/2}$ and $N_{m_I=-1/2}$ are registered for hydrogen atoms and the polarization can be calculated by $P_z = \frac{N_{m_I=+1/2} - N_{m_I=-1/2}}{N_{m_I=+1/2} + N_{m_I=-1/2}}$. For deuterium the vector-polarization $P_z = \frac{N_{m_I=+1} - N_{m_I=-1}}{N_{m_I=+1} + N_{m_I=0} + N_{m_I=-1}}$ and the tensor-polarization $P_{zz} = \frac{N_{m_I=+1} + N_{m_I=-1} - 2N_{m_I=0}}{N_{m_I=+1} + N_{m_I=0} + N_{m_I=-1}}$ are determined in the same. Only minor correction factors must be added that can be found in Ref. [1]. At this time LSP's were used for proton/deuteron beams in the kev regime only and, thus, a Helium

gas storage cell was implemented in front of the LSP to strip the electrons of the H^- and D^- . Due to the necessary high gas pressure inside the cell, the incoming beam intensity was reduced so much that less than 1 nA of proton beam reached the LSP. At these conditions polarization measurement were possible, but very difficult and time consuming.

Meanwhile, it has been shown that a Lamb-shift polarimeter is able to measure not just the nuclear polarization of protons/deuterons and in combination with an ionizer of hydrogen/deuterium atoms [1], but even of the corresponding molecules and molecular ions H_2^+ , D_2^+ [2] and HD^+ [3]. For the molecular ions it was shown that the residual electron is stripped in the Cesium cell itself and the protons can again catch an electron from the Cesium to produce metastable hydrogen atoms. This two-step process reduces the efficiency of the production of the metastable atoms compared to a proton beam by a factor of 30-40, but polarization measurements of the molecular ions are possible.

In recent experiments with the LSP at the polarized ion source of COSY the Helium cell was dismantled and the H^-/D^- ions are send directly into the Cesium cell. In Fig. 1 is shown how the ion beam intensity in a Farady cup at the end of the LSP decreases, when the Cesium vapor density is increased due to higher temperatures of the liquid Cesium at the bottom of the cell. In parallel, the amount of Lyman-

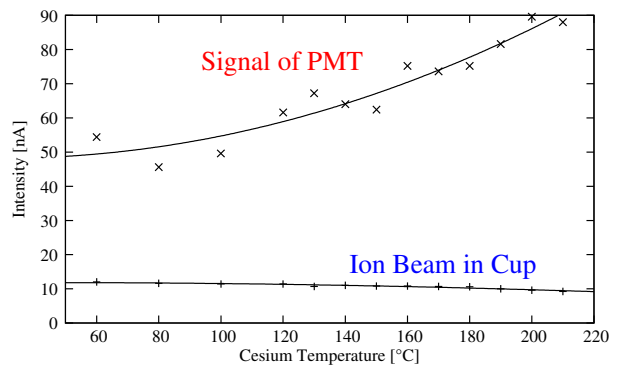


Figure 1: Like expected, the trough-going H^- beam intensity is reduced when the pressure inside the Cesium cell is increased due to higher temperatures of the liquid Cesium. In parallel, the larger amount of beam-Cesium interactions increases the number of metastable atoms that can produce Lyman- α photons registered by the photomultiplier.

α photons was measured as function of the Cesium temperature by switching off the radio-frequency in the spinfilter. With radio-frequency on and a lon-

itudinal magnetic field between the resonances all metastable atoms are quenched inside the spinfilter and only the residual ions in the beam are producing a background signal in the photomultiplier. The difference is shown in Fig. 1. For protons, the optimal Cesium temperature is about 160°C , but the H^- ions prefer higher Cesium vapor densities for the production of the metastable atoms. Nevertheless, the temperature of the actual Cesium cell is limited to 200°C for continuous operation. From this measurements can be deduced that the production of metastable atoms is reduced compared to a proton beam by a factor of about 20, much less in comparison with the Helium-gas stripper cell before.

Even first polarization measurements of the ion beam are now possible. Fig. 2 shows a Lyman- α spectrum of a polarized and an unpolarized H^- beam. Like expected the Lyman- α intensity for the hy-

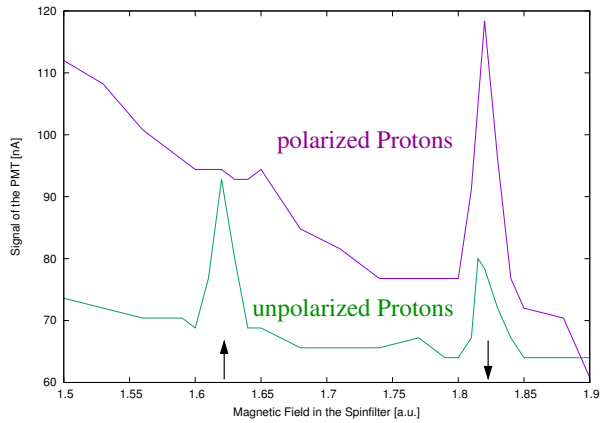


Figure 2: Lyman- α spectra of an unpolarized (green) and a polarized (violet) H^- beam. The equal population of the hyperfine substates with proton spin up and down for the unpolarized case are clearly visible. For the polarized beam the metastable atoms with nuclear spin down are dominating.

perfine substates with nuclear spin up and down is equal for incoming unpolarized ions (green plot). When a negative polarization was switched on at the source, the amount of photons for the resonance of the metastable atoms with spin up is reduced and for spin down increased. The signal-to background ratio is about 1:3 and the background is dominated by the residual ions in the beam. In addition, it is observable that the longitudinal magnetic field of the spinfilter influences the background, i.e. larger fields help to better focus the ions through the apparatus and reduce the background signal. Nevertheless, different focusing of the ions like here for polarized and unpolarized beams have a huge influence on the shape of the background signal.

Fig. 3 shows a first measurement with a polarized D^- beam. Here, Deuterium atoms with spin up are dominating compared to the substates with $m_I = 0$

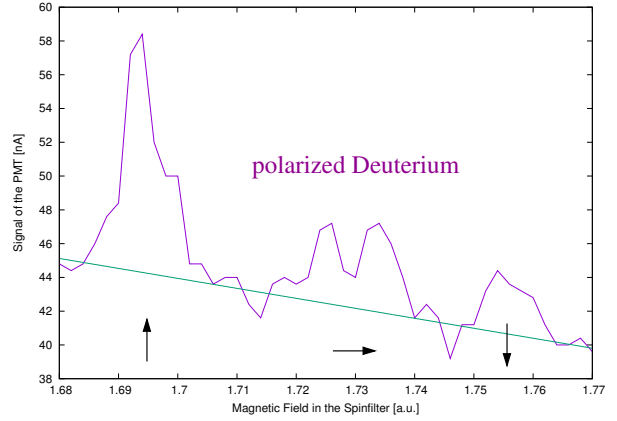


Figure 3: A Lyman- α spectrum of a polarized D^- beam. Here, deuterons with $m_S = +1$ are dominating.

or $m_I = -1$. To calculate the nuclear polarization of Lyman- α spectra of this quality is possible, but on this level not very precise. What is necessary next is to improve the data taking with an automatic system. Then, the necessary settings of the Wienfilter behind the source must be found to adjust the direction of the nuclear spin to be parallel to the beam axis in the LSP. This Wienfilter tuning could be done in first order for the H^- ions, but must be repeated for the D^- beam. Another open question is the necessary magnetic field strength inside the Cesium cell to avoid depolarization of the incoming ions. For protons/deuterons and molecular ions rather small fields above 20 mT are needed to overcome the coupling of the total electron spin J and the nuclear spin I of the metastable atoms. In case of the H^-/D^- ions it must be taken into account that after stripping of the first electron a fast atom in the ground state can exist for a short time inside the Cesium cell. The coupling strength B_c will be 8 times larger compared to the metastable atoms and maybe much higher magnetic fields are needed. If the lifetime of these atoms until the next stripping into a proton/deuteron is short enough, no larger magnetic fields are necessary. Only further measurements can solve this question, but even in the actual status of the LSP a relative tuning of the nuclear polarization is possible before the cyclotron.

References

- [1] R. Engels et al., Rev. Sci. Instr. **74** (2003) 4607.
- [2] R. Engels et al., Rev. Sci. Instr. **85** (2014) 103505.
- [3] R. Engels et al., accepted at Phys. Rev. Lett. (2020).

Production of HD Molecules in Definite Hyperfine Substates

V. Verhoeven, M. Büscher^{a,b}, R. Engels, K. Grigoryev, L. Huxold^b, C. Kannis, L. Kochenda^c, P. Kravtsov^c, Y. Michael, H. Ströher, V. Trofimov^c, A. Vasilyev^c, and M. Vznuzdaev^c

Polarized experiments, e.g. at COSY, use an ABS based on the Rabi apparatus either to produce polarized ion/atomic beams for further acceleration or to feed storage-cell targets. During the last years it was observed that the polarized hydrogen/deuterium atoms in such a storage-cell can recombine into molecules where the nuclear polarization is partially preserved. A collaboration of the University of Cologne, the Petersburg Nuclear Physics Institute and the Research Center Jülich built a dedicated apparatus for further investigations of the different recombination processes on various surfaces. With this setup it was possible to produce polarized H₂ and D₂ molecules with parallel nuclear spins. Depending on the surface materials large polarization values above 0.8 have been obtained. [1]

To produce HD molecules is the next big step in this development. Up to now only polarized solid HD ice has been produced with the 'brute force' method and was used as polarized target, e.g. at the CLAS experiment. An advantage of solid HD is the long lifetime of the polarization, in the order of years. But the polarization values achieved for the proton ($P_z \approx 0.5$) and the deuteron ($P_z \approx 0.27$) are rather small. Moreover, a control of the tensor-polarization P_{zz} is not possible. But for many important fundamental applications the other polarization combinations are needed.

We were now able to produce HD molecules in every possible spin combination. By operating an ABS with a Hydrogen and Deuterium mixture, a beam containing the corresponding atoms in defined hyperfine substates can be generated. When these atoms recombine into HD molecules it is possible to produce any spin isomer of the HD molecules, because the nuclear spins of the hydrogen and the deuterium atoms can be adjusted separately [2].

In the next step the polarized HD molecules will be frozen as ice. The main goal is to build polarized targets for laser-acceleration experiments to produce polarized proton and deuteron beams. Also polarized H₂⁺ and HD⁺ ions in single spin-isomers are a perfect tool for precision spectroscopy of this most simple molecular ions, because the influence of the spin-dependent part of the transition-frequencies can be determined separately. Another option to use these molecules can be the search for a static electric dipole moment (EDM) with oscillating electric fields or even experiments searching for an oscillating nuclear EDM produced by the axion dark matter field. For both methods the use of highly polarized HD molecules is beneficial, because the EDM effect would be proportional to the inverse nucleon charge

z^{-1} that is at minimum for the hydrogen isotopes [3]. One more promising application would be the use as polarized fuel for fusion reactors. Polarized DT (its properties are similar to HD) could be used to improve the efficiency of reactors up to the factor 1.5 or to improve the design in terms of tritium production.

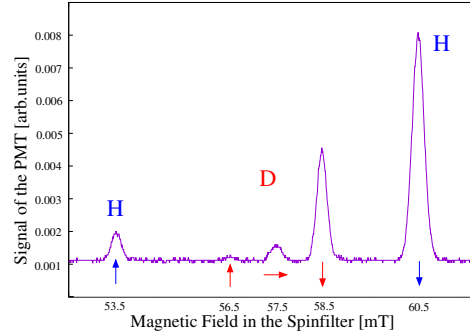


Figure 1: Lyman- α spectrum of HD molecules after recombination on a Fomblin surface. The nuclear polarization deduced from this spectra is $P_z = -0.77 \pm 0.01$ for hydrogen and $P_z = -0.79 \pm 0.01$ and $P_{zz} = +0.69 \pm 0.01$ for deuterium.

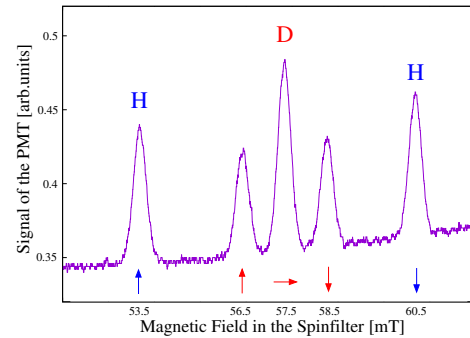


Figure 2: Lyman- α spectrum of HD molecules when unpolarized hydrogen atoms recombine on a gold surface with tensor-polarized deuterium atoms: $P_{zz} = -0.61 \pm 0.01$.

References

- [1] R. Engels et al., Phys. Rev. Lett. **115** 113007 (2015).
- [2] R. Engels et al., accepted at PRL (2020).
- [3] H.B. Tran Tan et al., Phys. Rev. A **99** 013430 (2019).

^a Peter Grünberg Institut, Forschungszentrum Jülich

^b Institut für Laser- und Plasmaphysik, HHU Düsseldorf

^c Petersburg Nuclear Physics Institute, Gatchina, Russia

A new type of laser-induced polarized proton source

C. S. Kannis, J. Böker, M. Büscher^{a,b}, R. Engels, I. Engin^a, O. Felden, R. Gebel, K. Grigoryev, A. Hützen^{a,b}, L. Huxold^b, A. Lehrach, T. P. Rakitzis^c, D. Sofikitis^d, and C. Zheng^a

Stern-Gerlach spin separation and spin-exchange optical pumping are two conventional methods for the production of spin-polarized hydrogen/deuterium (SPH/SPD) atoms/ions. The only drawback of these methods is the low densities they produce, namely $\sim 10^{12}$ [1] and 10^{14} cm^{-3} [2], respectively. A new technique for the production of high-density SPH/SPD involves the molecular photodissociation of hydrogen/deuterium halides. The reported densities exceed 10^{19} cm^{-3} [3]. In this experiment short (150 ps, 10 Hz) circularly polarized UV pulses were used for the molecular photodissociation, i.e. 213 nm for HBr/HCl and 266 nm for DI. The detection of the polarized atoms was possible with the use of a pick-up coil, due to the magnetization quantum beats.

Following this concept we perform an experiment for the production and detection of nuclear-spin polarized protons/deuterons [4]. The experimental setup consists of a Nd:YAG laser (EKSPLA, SL330 series), a nozzle for the molecular gas and a Lamb-Shift polarimeter (LSP). The laser's output can be double, so we are capable to use the fundamental wavelength (1064 nm) and the fifth harmonic (213 nm) simultaneously (see Fig. 1). Fig. 1). The last is needed for

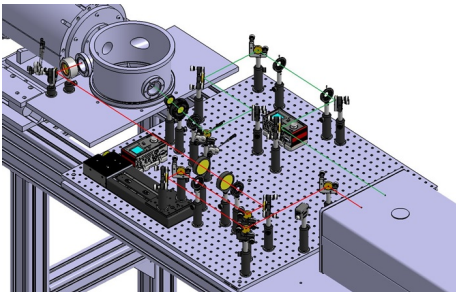


Figure 1: The optical setup: The fifth harmonic of the Nd:YAG laser (green line-213 nm) photodissociates the gas target into the interaction chamber. The fundamental wavelength (red line-1064 nm) aligns the molecular bonds, resulting higher polarization.

the molecular photodissociation process, whereas the other will be used at a latter stage of the experiment for the bond alignment of the molecules, which leads to higher percentage of polarization. The repetition rate is 5 Hz and the pulse duration 170 ps. The nozzle is synchronized with the laser system with the use of a precise trigger delay generator. Thereafter a Lamb-Shift polarimeter is used to measure the polarized hydrogen/deuterium atoms. The main LSP components are: an ionizer, a Wien filter, a Cs vapor cell, a spin filter, and a quenching chamber (a photomultiplier is used for the detection of Lyman- α

photons).

The functions of the LSP components are described elsewhere [5]. At present, we are not able to detect SPH atoms from the photodissociation of HCl, due to the low photodissociation cross-section of the molecule. However we measured the unpolarized background for different values of backing pressure (see Fig. 2). The current signal comes from the diffusive gas and its lifetime is tens of ms. On the other hand, the expected signal from the polarized protons will arrive at the detector much earlier (within 10 μs after the laser pulse) and it will be steeper. These characteristics make it separable from the background signal.

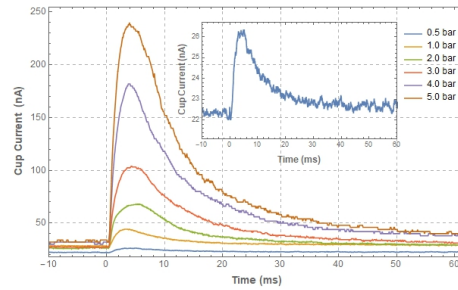


Figure 2: HCl diffusion signal for various values of backing pressure measured by a Faraday cup. Inset: A zoom into the signal at 0.5 backing pressure.

Consequently, we will proceed to a gas change. HBr gas has 500 times larger photodissociation cross-section compared to HCl. This magnification factor is adequate for the detection of SPH atoms from the LSP. In addition, a new holder for the nozzle is prepared, which allows us to adjust the height of the nozzle relative to the laser beam, without changing the direction of the laser beam. For this an extension of the interaction chamber is required which will be implemented soon. As a next step deuterated halides will be used to produce polarized deuteron beams with the same laser system.

References

- [1] E. Steffens et al., Rep. Prog. Phys. **66** (2003) 1887.
- [2] M. Poelker et al., Phys. Rev. A **50** (1994) 2450.
- [3] D. Sofikitis et al., Phys. Rev. Lett. **121** (2018) 083001.
- [4] A. Hützen et al., High Power Laser Sc. Eng., **7** (2019) E16
- [5] R. Engels et al., Rev. Sci. Instr. **74** (2003) 4607.

^a Peter Grünberg Institut (PGI-6), FZ Jülich

^b Institut für Laser-und Plasmaphysik, HHU Düsseldorf

^c Department of Physics, UoC Heraklion, Greece

^d Department of Physics, UoI Ioannina, Greece

A Fast Tune Measurement System for COSY

P. Niedermayer, B. Breitreutz, C. Böhme, V. Kamerdzhiw

Introduction

The aim of the *fast tune* project is to provide a fast, robust and reliable tune measurement system for bunched beams in COSY.

During the upgrade of the beam position measurement system at COSY [1] in 2017 new LIBERA beam position processors [2] were installed. These are able to measure the beam position for each particle bunch individually (bunch-by-bunch measurement). While exciting the betatron oscillations of the beam the horizontal and vertical tune can be extracted from the beam position data by means of a Fourier analysis. This allows for a fast tune measurement with a time resolution of milliseconds. It is also possible to realize a continuous tune monitoring, which is – especially during acceleration of polarized beams – most helpful for machine operation.

Concept and Implementation

The fast tune system consists of two parts, i.e. the beam excitation and the measurement of the resulting beam oscillations.

To excite coherent transverse betatron oscillations [3] of the whole beam, a noise signal is applied to the beam. COSY has two suited sets of electrodes for this purpose. One is the stripline unit [4]. It consists of four electrodes which act as a backward coupler to the particle beam. Each stripline is fed by a 15-watts power amplifier (PA). Since this is not sufficient for a reliable measurement at proton momenta above roughly 1 GeV/c, it is planned to replace them by 100-watts PAs. Using a relays matrix it is possible to switch between horizontal, vertical, or simultaneous excitation.

The other set of electrodes is part of the beam damping system. It already has 150-watts PAs which allow for tune measurement in the full COSY energy range. Depending on the needs of the experiment, either system can be used. The noise signal is generated offline and uploaded to an arbitrary signal generator that feeds the electrodes. For excitation a band-limited noise is used, in a frequency range that covers the betatron sidebands, i.e. typically 0.3 to 0.5 times the revolution frequency. The noise sequence is typically only a few milliseconds long, therefore the impact on the beam (beam loss) is kept to a minimum. While the former *tune* measurement utilizes a frequency sweep that takes up to 1 s and significantly decreases the beam lifetime, the new method can be seen as nearly non-destructive beam diagnostics.

During the beam excitation, the LIBERAs are triggered to acquire the horizontal and vertical position of every single bunch. These bunch-by-bunch (BbB) data are read out and analyzed. Due to the coherent betatron oscillations, the values oscillate around the mean (orbit) value.

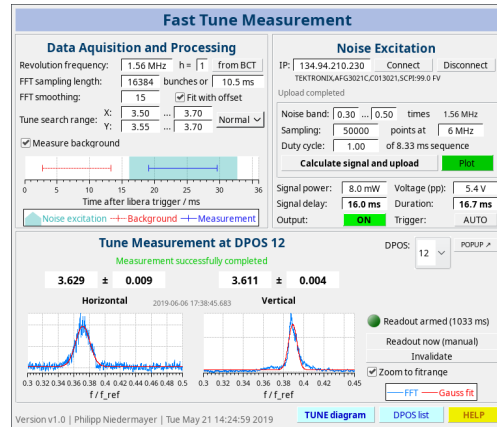


Figure 1: Screenshot of the main user interface

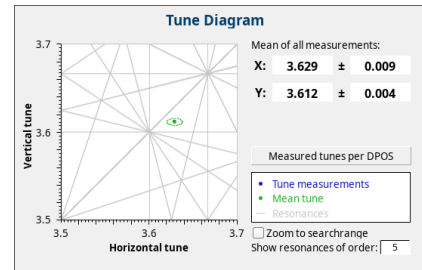


Figure 2: Screenshot of the tune resonance diagram

Its frequency is determined by applying a Fourier analysis to a sufficient amount – typically a couple of thousand – BbB-values. Since the measured data points are one per bunch, the result is already normalized by the revolution frequency. The resonance is clearly visible in the resulting spectrum and fitted by a Gaussian (see fig. 1). The Gauss-fit of the measured data directly leads to the fractional tune, q or $(1 - q)$. For COSY it is known that the tune is in the interval from 3.5 to 3.7, thus the tune is $Q = 4 - f/f_{rev}$.

In principle, the data of one single beam position monitor (BPM) for each plane allows for the calculation of the tunes. But by using several of the 25 available BPMs, it is possible to compare the results of independent systems. Thus, spurious signals – which have been a cause for false results in the past – can easily be detected. Furthermore the precision can be increased by averaging over all measured tunes.

Achievements

The first version of the fast tune system was commissioned in June 2019. It allows for a distinct tune measurement triggered by the COSY timing system at one (or multiple) specific times during the machine cycle. It can especially be used to measure the tune at a certain

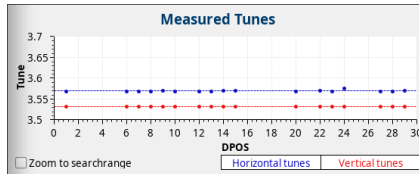


Figure 3: Tunes measured at different BPMs compared

point during the acceleration ramp.

Using the graphical interface (fig. 1) one can set up the noise excitation and configure parameters for data acquisition and processing. The time structure of the measurement setup is shown for convenience. For every BPM the frequency spectrum of the measured data and a Gaussian fit can be displayed. The tune resonance diagram shows the measured tune and resonances to be avoided (see fig. 2). The circle indicates the 1-sigma uncertainty of the measurement. Strong outliers can easily be identified in an overview of all BPM results (fig. 3) and can be deactivated individually.

The fast tune system features:

- Configurable excitation using an arbitrary noise signal
- Minimal beam disturbance due to short (ms) excitation
- Optional background suppression with an additional measurement before the excitation
- Simultaneous measurement with multiple BPMs for enhanced robustness
- Support for coupled tunes and multi-bunch-mode
- High level data integrity and plausibility checks for better reliability
- Live tune resonance diagram

The new fast tune system was introduced to the COSY operators within the frame of a *COSY crew training* held in August 2019. Operation instructions and a documentation were provided both for the user interface and backend.

Latest Results

During the JEDI beamtime from 4th to 6th calendar week in 2020, the system was used for the first time with low intensity deuteron beams. The damping system was used for beam excitation. Since its electrodes are located in the horizontal and vertical plane – and not in the diagonal planes as at the stripline unit – the much stronger vertical signal could be damped additionally with attenuators. Thus, a sufficient excitation of the horizontal plane did not lead to excessive beam loss in the vertical plane.

For beam evaluation, the tune of unpolarized deuterons was repeatedly measured during the ramp to track its movements during acceleration. Furthermore, the 150-watts PAs allowed for tune measurement at the end of cycles with extraction of polarized beams, despite the low beam intensity of several 10^8 particles. Still, the variation of the measured tunes over the single BPMs was smaller

than $6 \cdot 10^{-4}$ in the horizontal, and $3 \cdot 10^{-4}$ in the vertical plane.

Outlook

During commissioning we encountered that the 15-watts amplifiers at the stripline unit, despite adequate for exciting the beam by a frequency sweep, are not powerful enough for noise excitation of proton beams above 1 GeV/c and with less than roughly 10^{10} particles. This is because of the distribution of the spectral power density over a huge bandwidth. This problem is currently being circumvented by using the damping system with its 150-watts PAs for excitation. But already existing 100-watts PAs are being repaired, to make both electrode systems operational for fast tune measurements throughout the whole energy range of COSY.

As the current implementation is based on bunch-by-bunch data it can only be used for bunched beams. It is planned to also support **unbunched beams** by analysing the raw ADC values of the pick-up signal. Therefore two methods are under discussion. Either a fast Fourier transformation of the raw ADC values is done on the LIBERAs itself or the data from the LIBERAs are transferred to the IOC where all data analysis takes place.

The next version of the fast tune system will also support **continuous tune measurements**. It will then be possible to analyse the dynamic processes for example during the acceleration ramp. In a first step only the readout and processing will be modified, leaving the noise excitation in a fixed frequency range, wide enough to accommodate the varying revolution frequency. As a second step one can think of ramping the noise frequency synchronous to the revolution frequency during acceleration. While this will require a noise-sweep which can not be implemented with the present hardware, it will significantly improve the excitation power density per frequency.

Currently we are also preparing a standard tool for **chromaticity measurements** based on the fast tune system. The beam momentum will be changed by means of frequency jumps using the RF-cavity. Using several tune measurements before and after each jump, we can then calculate the chromaticity automatically. The high precision of the fast tune system will allow for a precise chromaticity measurement.

References

- [1] C. Böhme et. al.: *The upgraded beam position measurement system at COSY*. In: Short Reports, Annual Report 2017, Institut für Kernphysik · COSY, Jülich, 2017
- [2] Libera Hadron: www.i-tech.si/products/libera-hadron
- [3] K. Wille: *The physics of particle accelerators: An introduction*. Oxford Univ. Press, 2005
- [4] J. Bojowald et. al.: *Stripline Unit*. In: Annual Report 1991, IKP, Forschungszentrum Jülich, Germany, Jül-2590, Mar.1992

EPICS Integration Status

I. Bekman, C. Böhme, V. Kamerdzhev, S. Merzliakov, P. Niedermayer, K. Reimers, M. Simon, M. Thelen

Abstract

This report gives an overview and status of the COSY systems integrated into EPICS.

EPICS

EPICS (Experimental Physics and Industrial Control System) is an open-source, modular, flexible, scalable CS. It provides a framework for server-client nodes on top of standard network infrastructure via Channel Access protocol. Notable clients are Control System Studio [7] for GUI deployment and EPICS Archiver [8] appliance for state and data logging.

Tune and Fast Tune Measurement

A new tune measurement system based on the LIBERA Hadron beam position monitors has been developed. This new system is described in a dedicated section within this annual report, see [4].

Schottky Spectrum Data Acquisition

The schottky spectrum measurement is regularly used to determine the revolution frequency, side bands and beam distribution in longitudinal phase space. Currently three R&S FSV spectrum analyser are in use. They can be controlled and read out by a dedicated EPICS IOC and CSS user interface. The GUI allows to display the spectra and their evolution in time. Using markers and reference traces transient processes like beam cooling can easily be observed and quantified. Online data analysis directly yields the most important parameters: revolution frequency, frequency spread and momentum spread from a Gaussian fit.

2 MeV Cooler and Ramp Editor

The 2 MeV electron cooler has been recently integrated into the EPICS control system [1]. For operation of the cooler it is most helpful to automate certain processes relative to the timing system. For example it has been wanted to automatically ramp the electron current up and down at the start and end of a machine cycle. Therefore several PVs controlling the electron gun have to be ramped.

A ramp editor has been developed to automate this [2]. The editor allows to define arbitrary waveforms for several PVs by means of points as shown in figure 1. When activated, the software sets the PVs value based on the selected experiments and interpolated according to the COSY timing. Currently

10 slots are available to control PVs. This value can be extended as required.

While the ramp editor has been primarily developed for the high energy electron cooler, it can also be used with any EPICS based system that provides a PV for control. This allows for timing based automation in a reproducible way.

Steerer

For all COSY steerers EPICS based control has been implemented and replacing Tcl/Tk GUI and control system. After period of stabilization the new system has been introduced in daily operation (c.f. figure 2). Code and issue tracking is being practiced according to Development Environment Training. (see [10]). Accessibility of ring steerers via new control system allows us to use new algorithms for optimization or automation, e.g. Orbit Correction or Beam Based Alignment. New algorithms are envisaged to be integrated in the control system, e.g. automated Orbit Response Matrix measurement or Injection Optimization.

BPMs and Liberators

Gain of BPM signal preamplifiers([9], [5]) is controlled via EtherCAT hardware and integrated in EPICS. With the help of EPICS controlled generators delivering test signal to BPM pickups it is possible to perform in-situ calibration. Rapid Electrical-Zero calibration has been implemented to account for device-per-device differences and operation GUI delivered. It considers offsets of physical devices and relative to quadrupole optical axis and minimizes electrical offsets of each pair of pickups via individual gain adjustments. With this method systematic RMS of electrical BPM offsets can be brought down to $\mathcal{O}(10\mu m)$.

Powersupply Monitors (Istwerte)

For all ring magnets EtherCAT-based current value readout for the power supplies has been (or is being) implemented and integrated in EPICS. The current values are being monitored and archived (c.f. figure 3). This allows for rapid online diagnostics, alarming system is envisaged.

Orbit Correction System

With improvements mentioned above and new measurements it has become with the help of Orbit Correction to bring the RMS of actual beam orbit difference to golden orbit down to $\mathcal{O}(1mm)$ in both planes.

An optimization is currently happening within few cycles but is envisaged to speed up with better understanding of the optics model and ORM measurements. [3]

Ionization Profile Monitor

IPM is in operation since 2007. The beam profiles are published from LabView via EPICS and an improved Gaussian fitting procedure (also used in Schottky spectra) has been implemented in an EPICS IOC. The IPM Upgrade is envisaged to incorporate the functionality of LabView control into control system.

Other Systems

Notable systems integrated in EPICS are MWPCs and ionization chambers at extraction, profile grids at injection, beam loss and current monitors in COSY ring as well as both neutral particles "H0" detectors for both electron coolers.

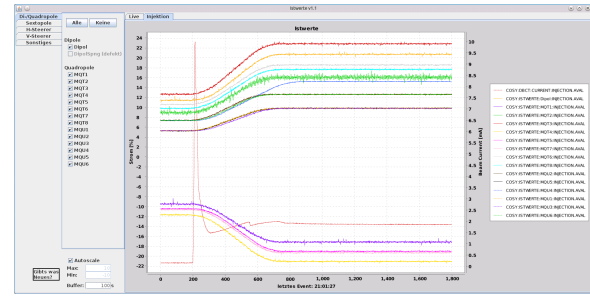


Figure 3: Screenshot of Istwerte Java GUI

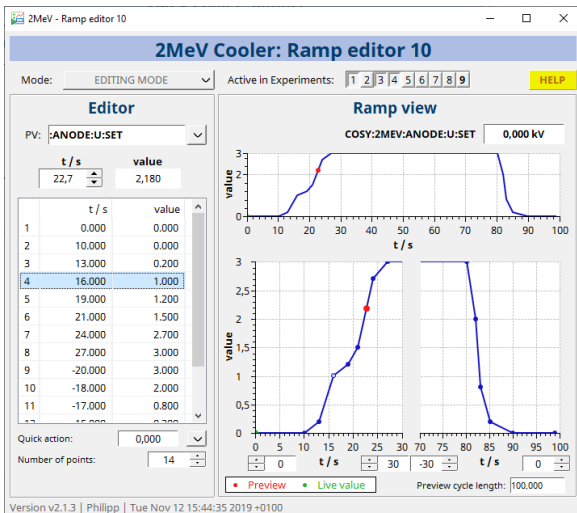


Figure 1: Screenshot of ramp editor CSS GUI

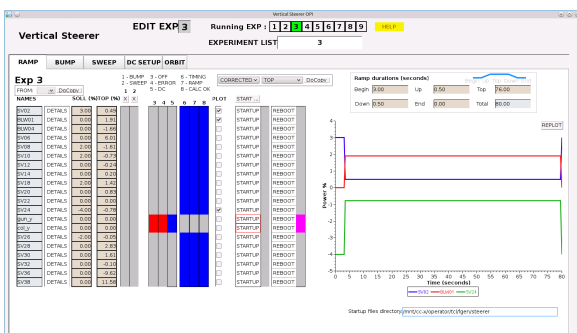


Figure 2: Screenshot of Steerer CSS GUI

References

[1] P. Niedermayer *et al.*, **Recent Developments and Experimental Results From Electron**

Cooling of a 2.4 GeV/c Proton Beam at COSY, in *Proc. COOL'19*, Novosibirsk, Russia, Sep. 2019, pp. 72–76, doi:10.18429/JACoW-COOL2019-FRX01

[2] P. Niedermayer, **Integration of the COSY 2MeV Electron Cooler into EPICS**, in *Annual Report 2018 - Institut für Kernphysik*, Forschungszentrum Jülich, pp. 92–93

[3] C. Böhme *et al.*, **COSY Orbit Control Upgrade**, in *Proceedings of IBIC2017*, Grand Rapids, Michigan, USA, 2017, doi:10.18429/JACoW-IBIC2017-TUPCF20

[4] P. Niedermayer, B. Breitkreutz, C. Böhme, V. Kamerzhiev, **A Fast Tune Measurement System for COSY**, in *Annual Report 2019 - Institut für Kernphysik*, Forschungszentrum Jülich

[5] **"Libera Hadron BPM"**; <https://m.i-tech.si/accelerators-instrumentation/libera-hadron>

[6] **The Experimental Physics and Industrial Control System**, <https://epics-controls.org/>

[7] J. Hatje, M. Clausen, C. Gerke, M. Moeller, H. Rickens, **Control System Studio (CSS)**, in *Proceedings of ICALEPCS 2007*, Knoxville, TN, USA, 2007, pp. 37–39, <https://accelconf.web.cern.ch/accelconf/ica07/PAPERS/MOPB03.PDF>, <http://controlsystemstudio.org/>

[8] M. Shankar, M. Davidsaver, M. Konrad, L. Li **The EPICS Archiver Appliance**, in *Proceedings of ICALEPCS 2015*, Melbourne, Australia, 2015, pp. 761–764, doi:10.18429/JACoW-ICALEPCS2015-WEPGF030

[9] I. Bekman, C. Böhme, V. Kamerzhiev, S. Merzliakov, P. Niedermayer, K. Reimers, **The upgraded beam position measurement system at COSY**, in *Annual Report 2017 - Institut für Kernphysik*, Forschungszentrum Jülich

[10] I. Bekman, C. Böhme, P. Niedermayer, M. Simon, M. Thelen, **Tools for software development at COSY**, in *Annual Report 2014 - Institut für Kernphysik*, Forschungszentrum Jülich

Friction force measurements in stochastic cooling

B. Breitkreutz, N. Shurkhno, R. Stassen, I. Gorelyshev^{1,2}, E. Khabarova^{1,2}, A. Sidorin^{1,2}, A. Shemchuk¹, V. Filimonov¹, C. Dimopoulou³

Direct measurement of the friction force acting on ion distribution function can be fruitful for tuning of the cooling system and comparison of the stochastic and high Voltage electron cooling. Longitudinal component of the friction force in electron cooling is usually measured by Voltage step method. Similar procedure can be performed for measurements of the friction force in the stochastic cooling. For the filter method used at COSY the step in the equilibrium energy can be provided by simultaneous step of the delay Δt_{filter} in the long leg of the comb filter and step of the system delay Δt_{sys}

$$\Delta t_{sys} = \frac{T_{P \rightarrow K}}{T_0} \Delta t_{Filter},$$

determined by $T_{P \rightarrow K}$ - time of flight between pickup and kicker, where T_0 is the revolution period. For example, during the measurement, which result is presented in the Fig. 1, preliminary cooled proton beam was initially accelerated by step of the equilibrium energy, and when the beam reached the new equilibrium (after about 220 s), it was decelerated back to the initial state.

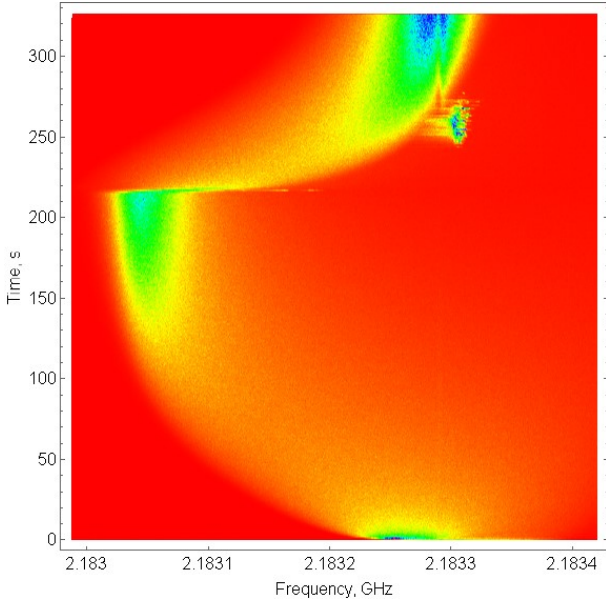


Fig. 1: Waterflow spectrogram of the measurements carried out at the 1400th harmonic of the revolution frequency. The initial proton beam momentum is 2.425 GeV/c, intensity is about $3 \cdot 10^9$ particles, output power of stochastic cooling is about 60 W. Spectrum analyzer saved one spectrum per second.

The particle energy during the process can be calculated from the relative frequency shift from the equilibrium and slip factor of the ring, which was equal to about -0.1 at the measurements. The frequency value is extracted from the measured trace via calculation of the distribution maximum as a function of time. The maximum value E_M satisfies the condition

$$\Psi(E_M, t) \Leftrightarrow \left. \frac{\partial \Psi(E, t)}{\partial E} \right|_{E_M} = 0$$

which corresponds to zero diffusion term in the Fokker-Planck equation (FPE). Ψ is the energy distribution function.

Another characteristic value of the distribution is its mean as known as first raw moment M . Its evolution in terms of FPE is written as

$$\frac{dM}{dt} = \int E \left[-\frac{\partial}{\partial E} (F(E)\Psi(E, t)) + \frac{\partial}{\partial E} \left\{ D(E) \frac{\partial \Psi(E, t)}{\partial E} \right\} \right] dE$$

The first term is the friction force averaged over the distribution:

$$\int -E \frac{\partial}{\partial E} (F(E)\Psi(E, t)) dE = \int F(E)\Psi(E, t) dE = \langle F \rangle_\Psi$$

The second term describes asymmetry of the distribution in respect to the mean value. So the difference in evolutions of the maximum and mean value can be used for estimation of shape and value of the diffusion. Evolution of the maximum and mean values calculated from the trace shown in the Fig. 1 is presented in the Fig. 2. The friction force calculated from two measurement (with opposite sign of the energy step) is presented in the Fig. 3 (line “Meas.byMax”) together with the equivalent force calculated from evolution of the mean value (line “Meas.byMoment”) and friction force calculated on the basis of the Beam Transfer Function measurement (line “Theory”).

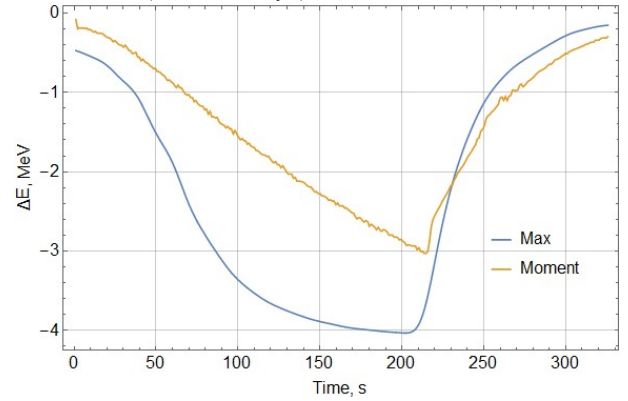


Fig. 2: Evolution of maximum (Max) and mean (Moment) energy distribution function values.

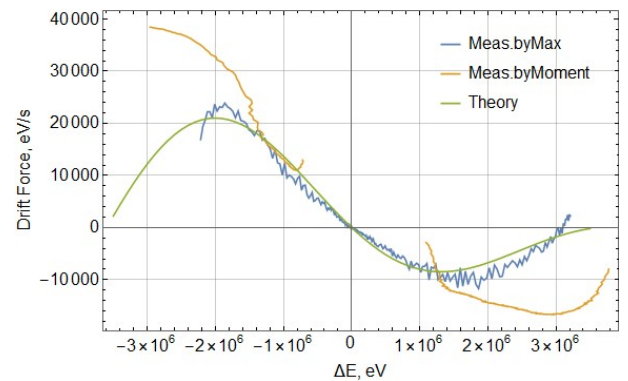


Fig. 3: Comparison of theory and measurements.

References:

[1] I.Gorelyshev et al., PHASE STEP METHOD FOR FRICTION FORCE MEASUREMENT IN FILTER STOCHASTIC COOLING, COOL2019, Novosibirsk

¹ JINR, Dubna

² Saint Petersburg State University, Saint Petersburg

³ GSI, Darmstadt

Introduction

Stochastic cooling system is a feed-forward system, that uses the beam signal measured at a pick-up to correct beam's errors further with the kicker. The hardware delay between the pick-up and the kicker thus synchronizes the kicker's kick with the measured particles and represents the crucial parameter for the performance of the system. The system delay normally should be adjusted within the picosecond accuracy, making the adjustment procedure quite time-consuming, so it could easily last for hours. At the same time the adjustment process itself is straightforward and linear, allowing for automation and considerable speed up. As a part of HESR (FAIR, GSI) stochastic cooling systems construction and tests at COSY (FZ Juelich), we have developed a technique for fast and accurate delay adjustment, a Drift Term Optimization method, allowing a regular adjustment to be performed within a few seconds. The report explains the developed method.

Usual delay adjustment routine

Normally the delay adjustment starts with the open-loop measurements: the vector network analyser excites the kicker and measures the response at the pick-up, so the open-loop measurement represents a product of a beam transfer function (BTF) and a full system's hardware transfer function (HTF):

$$OLM = HTF \times BTF \quad (1)$$

Typical measurements are shown in Fig. 1:

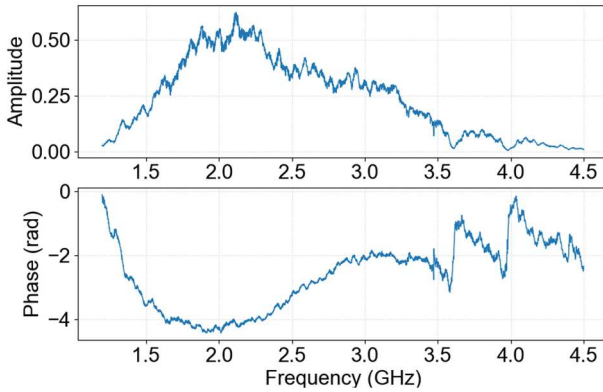


Fig. 1: Amplitude and phase of open-loop measurements.

After processing the equation (1) it can be shown that the phase of the open-loop measurements represents a system's delay error at each harmonic:

$$Arg(OLM) = n\omega_0 T_{PK}^{err} \quad (2)$$

Therefore, to adjust the system's delay, one could minimize the phase of the open-loop measurements for all harmonics in the passband, which represents the traditional adjustment algorithm. Unfortunately, the algorithm won't result in a good delay setting because of a non-linear behaviour of the hardware transfer function. The simple minimized delay error doesn't take the non-

linear amplitude into account, while it is desired to have smaller delay errors for higher amplitude. This leads to a not optimum delay setting and a detuned system, which requires in turn a subsequent time-consuming fine-tuning with the beam.

A several attempts were taken at COSY to develop an algorithm, that would include the amplitude of the system. Eventually they produced a tangibly better results, significantly reducing the time for the fine-tuning, the good delay setting then could be achieved with just a few additional measurements with the beam. But the whole procedure was still time-consuming and difficult to automate, so a further development was desirable.

Drift term optimization method

The process of stochastic cooling is completely described with a following Fokker-Planck equation:

$$\frac{\partial \psi}{\partial t} = -\frac{\partial}{\partial x}(F\psi) + \frac{\partial}{\partial x}\left(D\frac{\partial \psi}{\partial x}\right) \quad (3)$$

where ψ is a particle distribution function, x is parameter of interest (energy, momentum, betatron amplitude), F is a drift or cooling term and D is a diffusion or heating term.

The drift term F describes the cooling effect of the cooling process, while diffusion term D describes noisy heating effects, affecting the cooling (electronic, thermal noises and beam Schottky noise). This implies the fact that the effects of system delay mismatch could be directly seen with the calculation of a drift term only. There's also no need in independent treatment of a transverse drift term since the delay is a longitudinal effect only. The longitudinal drift term in a general form could be written as:

$$F = 2f_0 f_p \frac{Q^2}{A} \frac{e}{E_0 \beta^2} \text{Re} \sum_n \frac{HTF}{1 - OLM} e^{i\Omega T_{pk}} \quad (4)$$

where f_0, f_p – revolution and particle frequencies, Q, A – charge and atomic number of particles, e – elementary charge, E_0, β – nominal particle energy and velocity, n – harmonic number, $\Omega = 2\pi n f_p$, T_{pk} – travel time between pickup and kicker for a given particle.

Since the only interest is the effect of the delay, there is no need in absolute value of the drift term, but only in the quantities affecting its phase, so the following simplified equation could be used for the phase studies:

$$F = f_p \text{Re} \sum_n \frac{\overline{OLM}}{1 - \overline{OLM}} e^{i\Omega T_{pk}} \quad (5)$$

where \overline{OLM} is the open-loop measurements with a normalized amplitude.

This equation could be directly used for the delay study, the plots for slightly detuned system and perfectly adjusted delays are shown in Fig. 2:

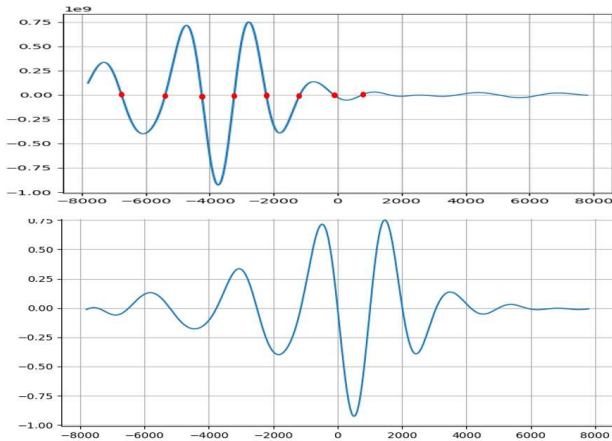


Fig. 2: Normalized drift terms for 0.8 ns delay error (top) and optimal delay (bottom).

From Fig. 2 it is clear what technically should be done in order to get the optimum delay value: the delay should move the appropriate zero of the drift term to the origin. Appropriate means the one, that has the highest amplitudes on both sides of the zero, positive on the left and negative on the right (to accelerate slower particles and to slow down the faster ones). Finding the zero is simple if the initial delay error is not too big, since it is just a point in between maximum and minimum (w.r.t to a sign). But if the delay error is significant, as always happens when adjusting from scratch, the “excitation” on Fig. 2 will shift far from the origin, making it very difficult to find the proper zero, so prior to calculation the phase should be flattened. The optimum delay value then could be found by calculation of a drift term for two arbitrary delay values with further extrapolation.

Eventually the adjustment algorithm comprises only four simple steps:

1. Perform open-loop measurements
2. Normalize the amplitude
3. Flatten phase
4. Find delay that shifts the proper zero the origin

Here only step 1 requires some time for processing, which depends on the vector network analyzer sweeping settings. Steps 2-4 are purely algorithmic and normally evaluate immediately. The algorithm sums over many harmonics (Eq. 5), which works as weighed averaging and therefore it is not very sensitive to small local deviations and noise. Thus, it works effectively even for a very fast sweeps containing not that many points, keeping single delay adjustment time within a second on average.

The method is also very robust since it utilizes the core idioms of stochastic cooling, incarnated in the Fokker-Planck equation. As a demonstration we show open-loop measurements for a system with the kicker (Fig. 3), installed back to front, which accidentally happened during experiments at COSY in 2017. Normally with such a setup one would hardly expect any

cooling at all, but surprisingly it appeared that the phase could be eventually manually adjusted in such a way that the peaks in the amplitude correspond to the flatter phase regions, generally resulting in somewhat reduced bandwidth.

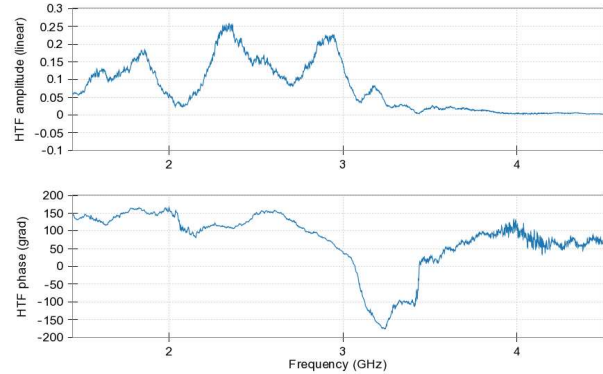


Fig. 3: Amplitude (top) and phase (bottom) of open-loop measurements for the system with inversed kicker.

Even for such an exaggerated example the proposed delay adjustment method works still effectively. The properly adjusted phase is shown in Fig. 4, a strong nonlinearity explains why the regular method of minimizing the phase would fail in this case:

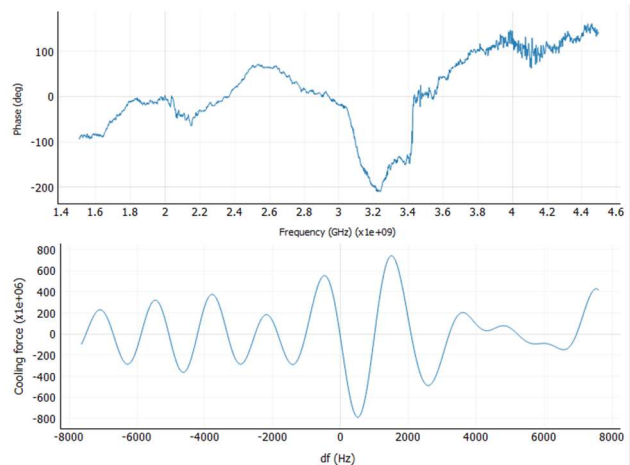


Fig. 4: Phase (top) and drift term for optimum delay setting for the system with inversed kicker.

Conclusion

The new Drift Term Optimization method for the system delay adjustment of the stochastic cooling systems was developed and experimentally tested at COSY. The method appears to be fast, accurate and robust and is considered for using at the FAIR facility.

Electrostatic deflector studies with small-scale electrodes

K. Grigoryev¹

The search for electric dipole moments (EDMs) of charged particles in storage rings requires development of dedicated electrostatic deflector elements. Designed in Ref [1], JEDI prototype-ring consists of more than 50 electric deflectors of 1 m length with the 60 mm spacing and the electric fields of 10 MV m^{-1} .

The high-voltage test stand was used to study scaled-down electrode prototypes of different materials, profiles and polishing at the gap distances of 1 mm to 0.05 mm. The first electrode prototypes were made from stainless-steel and mechanically polished. The second set of electrodes from the stainless-steel was TiN coated. For further tests two sets from aluminium were produced. The electrodes surface roughness was measured in ZEA using white light interferometer with $50 \mu\text{m}$ lateral step size and a height resolution of 3 nm (the values are shown in the Fig. 1).



Figure 1: Surface roughness of the electrodes.

For the precise positioning, each measurement started by mechanically setting of the distance between the electrodes to zero. The first high-voltage tests were performed with the uncoated stainless-steel electrodes. The discharges mainly happened in the small gaps between the electrodes. No discharge was observed at a distance of 10 mm which leads to the $E_{\text{max}} \approx 4.1 \text{ MV m}^{-1}$.

The measured minimal dark currents were compatible with zero to tenths of a picoampere (see Fig. 2). The maximum values of the electric field E_{max} , shown in the Fig. 3, are taken at the measurement points when the dark current was still compatible with zero within errors. The measurements showed that with half-sphere electrodes of 10 mm radius at distances of less than a millimeter, electric fields above the required values of $E = 17 \text{ MV m}^{-1}$ could be reached.

Mechanically polished stainless-steel electrodes at distances less than a millimeter demonstrate that electric fields close to the breakdown limit in ultra-high vacuum can be reached [2].

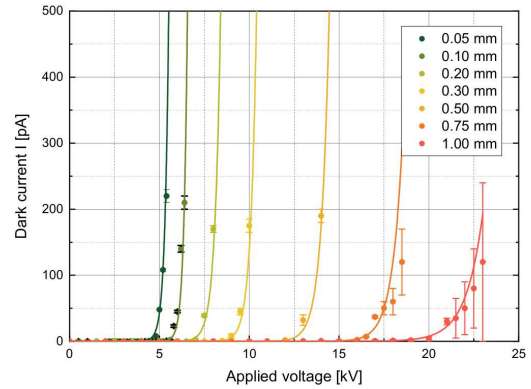


Figure 2: Dark current measured using stainless-steel uncoated electrodes at the distances $S = 0.05$ to 1 mm.

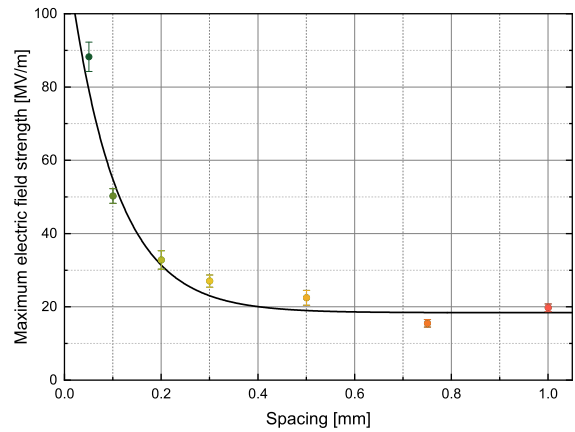


Figure 3: Maximum electric field strength from Fig. 2 as function of spacing between the electrodes. For the individual points the same colors as in Fig. 2 were taken. The line is drawn to guide the eye.

The maximum electric fields obtained in the measurements using scaled-down electrodes look promising. They are clearly above the required values for an electrostatic deflector of 10 MV m^{-1} for the JEDI prototype-ring. The improvement of the HV breakdown capability using different electrode materials and coatings as well as gas conditioning will be further investigated in the future using real-size deflector elements of a length $\ell = 1020 \text{ mm}$ at distances of $S \approx 20 - 120 \text{ mm}$ between the plates individually connected to 200 kV power supplies.

References

- [1] F. Abusaif, et.al., arXiv:1812.08535 (2019).
- [2] K. Grigoryev, et.al., Rev. Sci. Instrum. 90, 045124 (2019).

Status Monitoring System for the Polarised Source of COSY

Frank Dahmen, Nils-Oliver Fröhlich, Ralf Gebel, Christian Weidemann, and Yury Valdau

The source of polarised H^- and D^- ions is one of the most crucial system for the polarised COSY physics program. Setting up the polarised source is time consuming and any malfunction of the subsystem can lead to a long shut down for the repair after which a subsystem has to be setup from the beginning. Hence, it is extremely important to monitor status of the system and fast react on a possible malfunctions of individual components to realize uninterrupted operation of the source.

The Colliding Beam Source (CBS) of COSY consist of the three main subsystems: the CS-Gun - source of neutral Cs atoms, the Atomic Beam Source (ABS) - source of polarised neutral H^0 and D^0 atoms, and the charge exchange and extraction region. The Cs-ions are produced by a high temperature ionisation in the so-called Cs-Gun. Positive ions are then accelerated using electric field applied to a set of electrodes and focused by a triplet of quadrupole magnets. Shortly in front of extraction and charge exchange region positive ions are neutralized in Cs-steam in the neutraliser. On the opposite side of the CBS polarised atoms of H^0 and D^0 are produced in the atomic beam source by means of permanent 6-pole magnets and RF-transition units. In the charge exchange region, polarised neutral atoms collide with neutral Cs atoms and get ionised. Negatively charged hydrogen or deuterium atoms get deflected in the extraction region into the cyclotron beam transport line while positively charged Cs ions get deflected into the opposite direction in a Cs-Cup for diagnostic.

To work with such a low energy beams exceptional stability of the high voltage and vacuum system is needed. Furthermore, a high temperature Cs-ioniser and neutralizer should be permanently temperature stabilized, which make the system even more sensitive to the external effects.

The polarised source control system is PLC based and has relatively advanced interlock capabilities, which allow to avoid possible dangerous situations. However, interlock system can only bring the system in a safe condition switching the power supplies off and closing the vacuum valves, which imply a new source beam development and hence relatively long interruption for the experiment. To avoid this a new polarised source status monitoring system has been developed.

The status monitoring system for the CBS is based on Taslink system [1], which already has been used since a long time for status monitoring of the COSY transformers. The system consists of: a client, a small PC card located next to the source PLC system and except up to 16 logical signals, and a server, which communicate with different clients over the network and is connected to the normal telephone network. In case of CBS interlock or vacuum systems generate a logic signal at one input of the Taslink client, a telephone voice message can be send

to the person on shift. The person on shift should accept the message using a telephone code (55), otherwise the message will be send again in a predefined number of times. The web-based software on the server allows to set individually reaction on the signals from clients, change person on shift, and communication ways (SMS, e-mail, telephone message) [2].

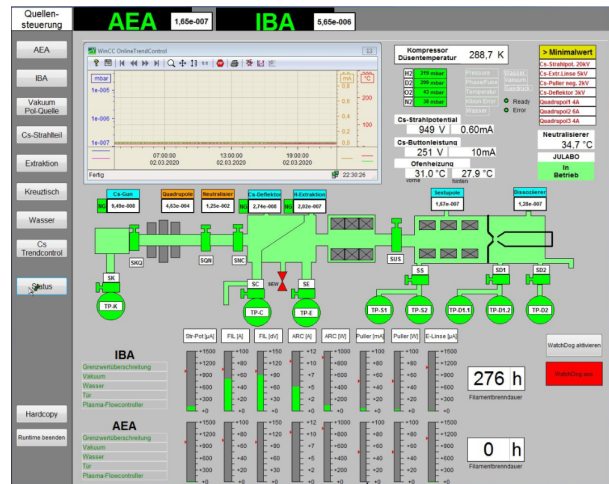


Figure 1: The status page of the sources PLC control system. During operation of polarised source a picture is stored in the elog every half an hour.

Besides status monitoring system a special software on PLC PC is running which stores a screenshot for this PC every half an hours. This allows, without remote access to the PLC PC, a monitoring of the polarised source status. Since PICOSkope software, used for the monitoring of a source diagnostic parameters, is running on the same PC, screenshot storage also allows to monitor a development of the CBS parameters remotely. In the Fig. 1 a source monitoring SPS page stored in the elog is presented. Regular maintenance of the polarised source and permanent monitoring of the polarised source status using presented status monitoring systems allows to increase reliability of the system and reduce down time of the source during the experiments. All those factors together, made a six month long polarised beam company at COSY for the JEDI experiment in 2019 possible.

References

- [1] <https://www.tas.de/produkte-services/uebertragungstechnik/alarmuebertragungseinrichtung-tas-link-iii>
- [2] <http://134.94.180.122/arutel/index.php>

Status of the NESP beam line

Frank Dahmen, Olaf Felden, Ralf Gebel, Karl Reimers, Marius Rimmler, Nils-Oliver Fröhlich, and Yury Valdau

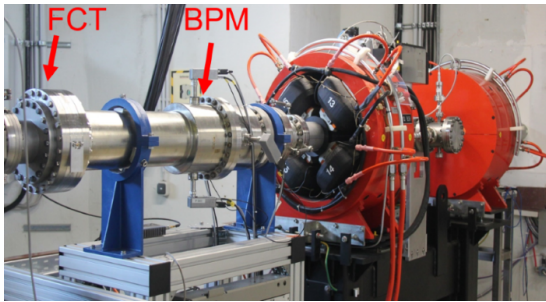


Figure 1: The picture of the NESP beam line in Big Karl hall. The Fast Current Transformer and Beam Position Monitor for beam diagnostic are marked as FCT and BPM, respectively. Two quadrupole magnets QN1 and QN2 (constructions colored red) are also presented.

A new beam line between cyclotron and former Big Karl hall was build and equipped with diagnostic elements and a duplet of quadrupole magnets. At the NiederEnergyStrahlungPlatz (NESP) low energy beams of protons, deuterons, H^- , and D^- ions up to injection energies of COSY (45 and 75 MeV for the H^- , D^- ions, respectively) are available. The energies of protons and deuterons can be reduced down to 10, 20, 30, and 40 MeV from the maximal values using a graphite degrader installed in the cyclotron bunker.

One of the main advantages of NESP experimental place is the relatively large Big Karl hall, available for the installation of the experimental equipment, which make neutron production experiments using a cyclotron beam feasible [1]. On the other hand, the maximal integral DC current delivered at NESP is presently limited by 10 nA due to the absence of the radiation shielding in vertical direction in the experimental hall.

In the Fig. 1 a NESP beam line in the Big Karl hall commissioned during High Brilliance neutron Source (HBS) experiment in June 2019 is presented. It consist of two quadrupoles QN1 and QN2, for beam focusing, and the Fast Current Transformer (FCT) and Beam Position Monitor (BPM) for none destructive beam diagnostic. Depending on the requirements of the experiment a standard COSY profile monitor (MWPC) [2] or a beam cup can be installed at the end of the beam line. The FCT and BPM are readout using Lock-In Amplifier based DAQ discussed in Ref. [3]. This allows beam current measurement and position monitoring up to minimal DC currents of 3 nA.

In the Fig. 2 typical beam profile measurements done at the end of the NESP beam line using a beam profile monitor is presented. Information about the beam size, extracted from such measurements, has been used for beam size optimization during the HBS beam time. The goal of optimization was to reach minimal beam size in both

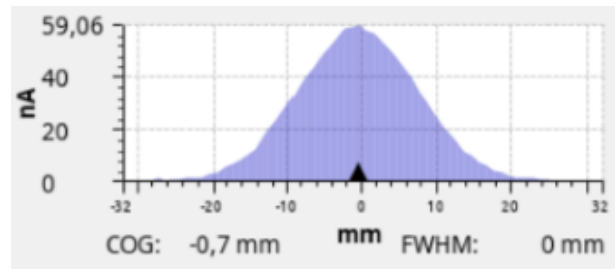


Figure 2: Vertical 45 MeV beam profile measured with beam profile monitor at NESP target place. On the vertical axis is beam current measured in Ampere, on horizontal axis beam size in millimeters.

planes simultaneously.

In the Table 1 results of beam development done within this beam time are summarized. During the beam size optimization at NESP, all other magnets in Injection Beam Line (IBL) were switched off. Only dipole D11 was used, to deflect the beam in the direction of NESP after the extraction from the cyclotron and energy degradation. The time and date in Table 1 correspond to the time when analyzed beam profile measurements took place. The beam width was determined from the picture and hence represent a first approximation of the beam profile σ with possible error of ± 1.5 mm. The values of the magnet currents are taken from the electronic logbook, while for the 10 MeV-beam values are reconstructed using information from the power supply current monitoring system.

Vertical and horizontal beam sizes of the 45 MeV beam at NESP with switched off QN1 and QN2 quadrupoles are relatively close to the sizes expected directly at the exit of the cyclotron. Nevertheless, the H^- beam can be additionally focused at NESP using QN1 and QN2. Usage of the degrader for the beam energy reduction significantly increase beam size, as one can conclude from comparison of determined beam sizes measured at 40 and 45 MeV without focusing. However, this effect can be partly compensated using quadrupoles in NESP beam line. The beam profile of the degraded proton beam at 10 MeV was only measurable with optimized quadrupole currents in QN1 and QN2 and, as one can conclude from the Table 1, is already relatively large at 20 MeV. The values of the magnet currents summarized in the Table 1 can be used as a first approximation of the beam line parameters for the experiments at NESP.

In summer 2019, NESP beam line was commissioned during HBS beam time. Used none destructive beam diagnostic instruments are operational with low intensity DC beams available at NESP. Installation of the two quadrupoles next to the target place allows to significantly improve quality of the degraded cyclotron beams available in Big Karl hall.

Energy [MeV]	Date	Time	σ_X [mm]	σ_Y [mm]	D11 [%]	QN1 [%]	QN2 [%]
10	30.06	13:44	20	19	28	20	-29
20	27.06	15:09	18	17	31.3	22	-27
20	27.06	10:47	22	22	31.3	off	off
30	27.06	16:54	16	15	34.7	23	-34
40	30.06	13:31	13	11	38.6	25	-35
40	26.06	14:54	23	23	38.6	off	off
45	19.06	16:06	8	9	-39	17	-32
45	30.06	18:44	13	11	-38.8	off	off

Table 1: Magnet currents and transversal beam sizes measured during HBS beam time in June 2019. The σ_X and σ_Y are the beam profile half width approximated from the measurements done at specified time and date. The currents of the D11 dipoles and quadrupoles QN1 and QN2, installed in Big Karl hall, are given in percent. Measurements at 45 MeV are done with H^- beam. All other focusing magnets, besides QN1 and QN2, in Injection Beam Line were switched off during this studies.

References

- [1] https://www.fz-juelich.de/jcms/jcms-2/EN/Forschung/High-Brilliance-Neutron-Source/_node.html
- [2] P. Niedermayer, user manual for MWPC, available via <https://gitlab.cce.kfa-juelich.de/BCC/MWPC/css-gui/blob/master/documentation/manual.pdf>
- [3] Yu. Valdau et al., "Development of High Resolution Beam Current Measurement System for COSY-Jülich", IBIC2016 Conference proceedings, DOI:10.18429/JACoW-IBIC2016-TUPG41.

Proton induced neutron yield measurements of different CANS targets

M. Rimmler, M. Strothmann, P. Zakalek

For Compact Accelerator-driven Neutron Sources (CANS), the target material providing the largest neutron yield depends on the energy of the sub-100 MeV primary proton beam. Simulations based on the TENDL database [1] suggest that low-Z materials, e.g. Beryllium and Vanadium, generate more neutrons at proton beam energies below 20 MeV while high-Z materials, e.g. Tantalum, generate more neutrons at proton beam energies above 20 MeV [2]. In order to improve the reliability of the underlying databases for future CANS projects, the neutron yield was measured experimentally for Beryllium, Vanadium and Tantalum for 10 MeV, 20 MeV, 30 MeV, 40 MeV, 45 MeV protons from the cyclotron JULIC at the NiederEnergieStrahlPlatz (NESP). The primary neutron yield is indirectly determined through the measurement of the 2.23 MeV gamma ray of hydrogen induced by thermal neutron capture in a polyethylene (PE) moderator surrounding the targets. The gamma rays were measured with an energy sensitive Ga-Detector positioned at 1 m distance from the PE. The detector efficiency and neutron to gamma conversion rate is determined by the measurement of the gamma spectrum of a known AmBe neutron source. A picoamperemeter directly measures the number of protons impinging the target which can be extrapolated for background runs without target with additional non-destructive current measurements with the Beam Position Monitor (BPM) and Fast Current Transformer (FCT) [3].

In order to obtain proton beam energies at NESP below the 45 MeV JULIC design energy, a tuneable carbon degrader shortly after extraction of the beam from JULIC is used. Scattering of protons from the degrader increases the beam size which results in the generation of background neutrons from the vacuum tube and other parts along the beam line. This increases the background when measuring the neutron yield of different targets. Therefore an additional quadrupole doublet was installed in the NESP area [4]. With focusing of the beam, the background was reduced by one order of magnitude as shown in Figure 1.

The reduction of background in the gamma spectrum allowed to perform the neutron yield measurements with shorter run times down to half an hour each for both the measurement with target and the background measurements compared to 3.5 hours each for both measurements without focused beam.

Figure 2 shows the preliminary results for the proton induced neutron yield measurements with different CANS targets, i.e. Beryllium, Tantalum and Vanadium for energies from 10 MeV to 45 MeV.

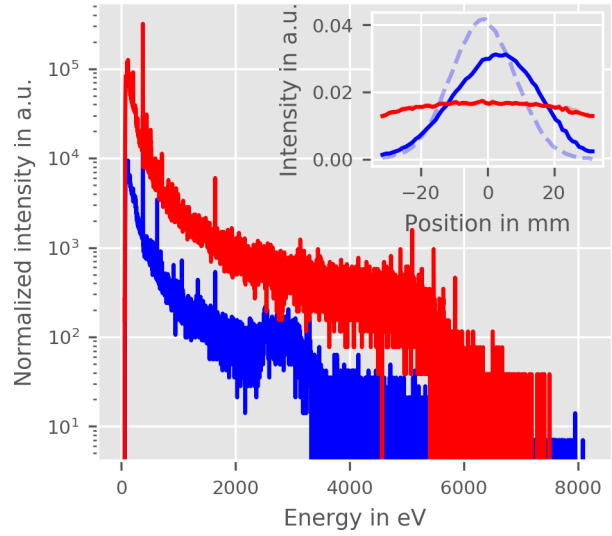


Figure 1: Comparison of gamma spectra recorded during background measurement for 10 MeV for optimized beam size with focusing quadrupoles (blue) and non optimized beam size (red). The inset shows the optimized and non optimized horizontal beam profile (blue and red, respectively). The dashed and shaded lines show the vertical beam profile. The non optimized vertical beam profile coincides with the non optimized horizontal beam profile.

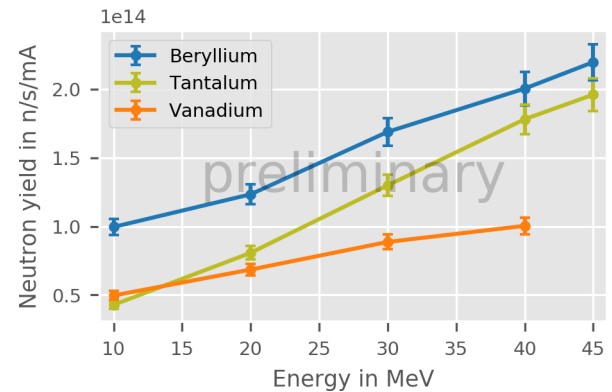


Figure 2: Proton induced neutron yield (p,n) measurements from Beryllium, Tantalum and Vanadium targets for proton energies from 10 MeV up to 45 MeV.

The measured total neutron yields are corrected with MCNP simulations of the experiment. This gives information about the neutrons that escape the PE moderator such that they are invisible for the gamma detector. It is important to compare the number of escaped neutrons during a measurement with a target at a specific energy to the number

Target	Energy in MeV	Neutron yield in 10^{14} n/s/mA [2]	Measured neutron yield in 10^{14} n/s/mA
Beryllium	10	0.072	1.00 ± 0.06
	20	0.28	1.23 ± 0.07
	30	0.58	1.69 ± 0.10
	40	1.07	2.01 ± 0.12
	45	1.37	2.20 ± 0.13
Vanadium	10	0.072	0.50 ± 0.03
	20	0.48	0.69 ± 0.04
	30	1.18	0.89 ± 0.05
	40	2.11	1.00 ± 0.06
Tantalum	10	0.005	0.43 ± 0.03
	20	0.29	0.81 ± 0.05
	30	1.17	1.30 ± 0.08
	40	2.68	1.78 ± 0.11
	45	3.68	1.96 ± 0.12

Table 1: Comparison of energy- and target-dependent neutron yield in n/s/mA for the simulations in [2] and the measurement at NESP as shown in Figure 2.

of escaped neutrons during the measurement with the AmBe calibration source. The ratio of neutrons that do not escape the moderator in both scenarios applies as a correction factor to the measured total neutron yield. Furthermore, one has to investigate additional reaction channels in the target that generate neutrons to isolate the neutron yield dominated by the (p,n) reaction. For this reason, we correct for neutrons generated through the most dominant further reaction channel, i.e. (n,2n).

In Figure 2, one can see that Beryllium dominates strongly at energies below 20 MeV which is contradictory to simulations that suggest Vanadium to have a larger or equal neutron yields in this energy range as shown in Table 1. Moreover, Figure 2 shows that the crossover of neutron yields between Beryllium and Tantalum is shifted to higher energies than 45 MeV whereas in the simulations it occurs at roughly 20 MeV[2].

In conclusion, the experimental results obtained from the proton induced neutron yield measurements at NESP recommend to use Beryllium as a target material below 45 MeV in order to obtain the largest neutron yield at CANS facilities. The indirect measurement of the neutron yield via prompt gamma rays from a PE moderator with optimized proton beam focusing at all accessible energies represents a fast method to characterize CANS targets regarding the total proton induced neutron yield.

References

- [1] A. J. Koning, D. Rochman, J.-Ch. Sublet, N. Dzysiuk, M. Fleming, S. van der Marck, Nucl. Data Sheets, 155, 1-55 (2019)
- [2] P. Zakalek, P.-E. Doege, J. Baggemann, E. Mauerhofer, Thomas Brückel, The European Physical Journal Conferences 231:03006 (2020)

- [3] Yu. Valdau et al., IBIC2016 Conference proceedings, 434-437 (2017)
- [4] F. Dahmen, O. Felden, R. Gebel, K. Reimers, M. Rimpler, N.-O. Froehlich, Yu. Valdau, Status of the NESP beam line, Institute for nuclear physics Juelich annual report 2019

Efficiency measurements of a mesitylene based cold moderator system

M. Strothmann, M. Rimmler, P. Zakalek

Neutron scattering instruments operated at Compact Accelerator based Neutron Sources (CANS) require specific neutron energy spectra [1] which is realized with the usage of optimized moderator systems. Typical moderator materials to provide low energy neutron spectra are methane, hydrogen and mesitylene at cryogenic temperatures [2]. Mesitylene has the advantage that it is more radiation resistant than methane and easier to handle than hydrogen. It was investigated at 20 K [3], at 90 K and 300 K [4] and shows promising performances. The exact performance of a moderator system depends on the moderator geometry, the moderator material and the temperature. Experimental validations of MCNP simulations are therefore necessary. Measurements with a new designed cold moderator system based on mesitylene have been done to characterise the performance of mesitylene as cold moderator material in the NESP area of the COSY facility. The half transparent drawing in Fig. 1 shows the dimensions of the mesitylene volume inside the aluminium moderator vessel with attached thermal bridge to the cryocooler.

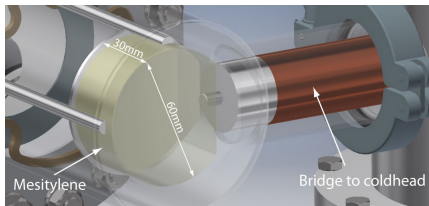


Figure 1: Drawing of moderator assembly with attached cold finger.

An overview of the measurement setup is sketched in Fig. 2. A 5 mm thick Ta target disk was aligned in an 45° angle to the beamline. A pulsed 45 MeV proton beam from the cyclotron JULIC with pulse widths of $200 \mu\text{s}$ and $500 \mu\text{s}$ and frame lengths of 30.3 ms, 50 ms and 80 ms has been used to measure the high energy region with high intensity as well as the low energy region. The mesitylene vessel was mounted inside a polyethylene block which pre-moderates the hot neutrons to thermal energies (25 meV). The mesitylene was cooled by a cold finger cryocooler to temperatures between 10 - 180 K. The neutron energy spectra were measured by a time-of-flight setup with a 7 m long neutron guide as a flight path. For the neutron detection, ^3He tube detectors were used which were mounted inside a shielding of borated polyethylene to reduce the background.

Fig. 3 shows the measured neutron spectra for temperatures between 22 K and room temperature. Although the neutrons are under moderated, visible

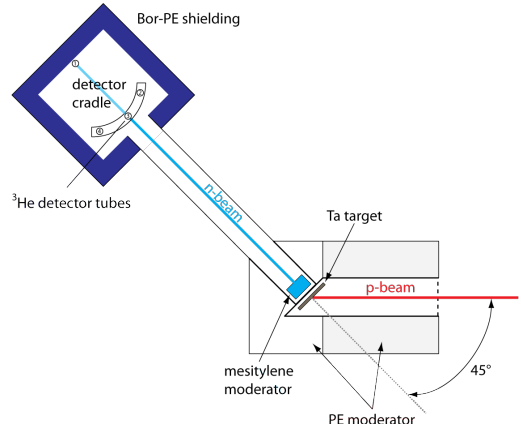


Figure 2: Sketch of measurement setup.

by the broadening of the peak and the shoulder to smaller wavelengths, a lowering of the moderator temperature shifts the spectra significantly to lower energies and increases the number of neutrons with long wavelengths. This is an important figure of merit with respect to the application in CANS instrumentation and the performed measurements gives a gain factor of ~ 20 . Mesitylene is a good cryogenic moderator material which shows good properties for the usage at CANS.

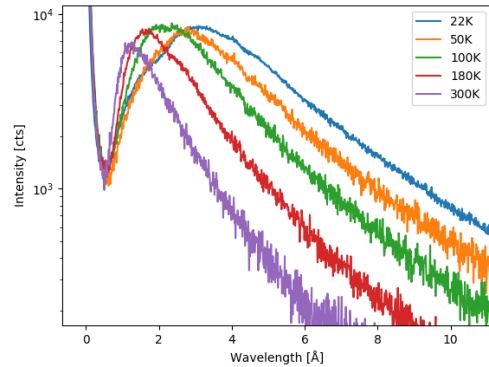


Figure 3: Plot of measured neutron spectra for mesitylene temperatures between 22 K and 300 K.

References

- [1] P. Zakalek, et al. Proceedings, 13th Heavy Ion Accelerator Technology Conference 18 (2019) 117
- [2] M. Huerta Parajon, et al., Physics Procedia 60 (2014) 74
- [3] K. Nünighoff, et al., Eur. Phys. J. A. 38 (2008) 115
- [4] F. Cantargi, et al., Nucl. Instrum. Methods Phys. Res., B 248 (2006) 340

Real time impedance monitoring for extraction magnets



C. Klinkenberg, A. Leimbach, S. Weber (BK GuT)
 I. Bekman, C. Böhme, J. Böker, C. Ehrlich, J. Hetzel, M. Simon, M. Thelen (IKP-4)
 F. Frenzel, C. Poulwey (P-Z)
 14 January 2019

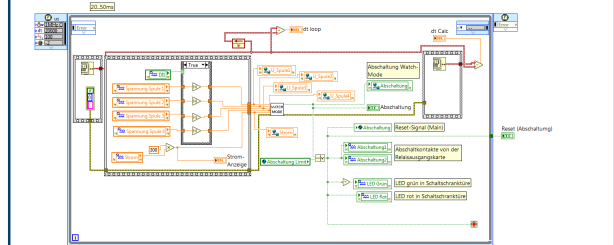
Magnetic extraction septum

Magnetic extraction septum

- The extraction septum consists of two magnets connected in series.
- The maximum current through the septum is 2750 A.
- Monitoring systems protect the magnetic septum from overheating.
- Without protection the coils are thermally destroyed after a burn-out time of 1.2 s.

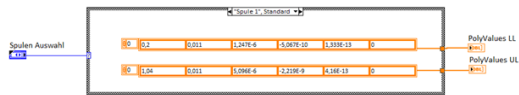


Software - LabVIEW



LabView

- graphical software development
- programmed in several VI's



Coil database

- Each coil has its own characteristic constants for the switch-off polynomials.

Polynomials for the shutdown calculation

Polynomials

- The two vectors show the coefficients P1 for the lower polynomial and P2 for the upper polynomial.
- Polynomials are represented as 4th order polynomials.
- The voltages are described as a function by the polynomials. Tolerance to the lower shutdown limit is 20%, the upper limit is 4%.

$$P1 = \begin{pmatrix} 0.2 \\ 0.011 \\ 1.247 \times 10^{-6} \\ -5.067 \times 10^{-10} \\ 1.333 \times 10^{-13} \\ 0 \end{pmatrix}$$

$$P2 = \begin{pmatrix} 1.04 \\ 0.011 \\ 5.096 \times 10^{-6} \\ -2.219 \times 10^{-9} \\ 4.16 \times 10^{-13} \\ 0 \end{pmatrix}$$

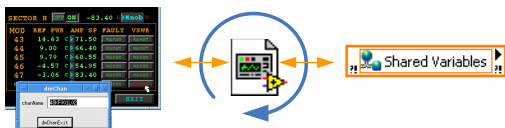
Hardware – National Instruments



Assemblies

- CompactRIO Controllers 9045 are modular, high-performance embedded controllers for rapid development and deployment into industrial control and monitoring applications.
- 5 special I/O modules are used for all measurements.

EPICS



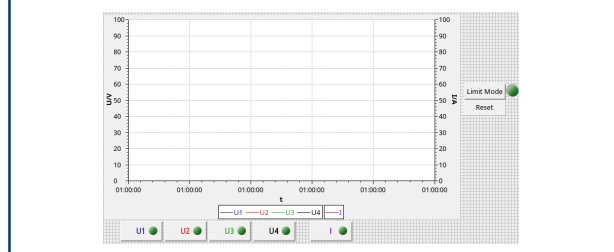
Process Variables (PVs)

I/O Server

Shared Variables

EPICS PVs	VI names
COSY:SME:1:lowercoil_voltage	U_Spule1
COSY:SME:1:uppercoil_voltage	U_Spule2
COSY:SME:2:lowercoil_voltage	U_Spule3
COSY:SME:2:uppercoil_voltage	U_Spule4
COSY:SME:current	Strom
COSY:SME:fault	Abschaltung
COSY:SME:reset	Reset
COSY:SME:enable_limitmode	Limit Freigabe
COSY:SME:enter_limitmode	Enter Limit

Visualization



Outlook

- In future, the system will monitor the injection septum at the HESR.
- The biggest difference to the system used in COSY is the bipolar current direction through the injection magnet.
- The monitoring system is already prepared for this with an additional input for selecting the current direction.

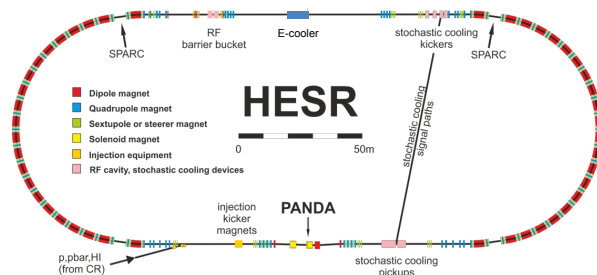


Experimental studies of stochastic cooling system for HESR

N. Shurkhno, Forschungszentrum Jülich

The High Energy Storage Ring (HESR) of the FAIR project at GSI Darmstadt will be very important for different scientific programs due to the modularized start version of FAIR. Stochastic cooling is one of the key components to fulfil the requirements of the different experiments. COSY accelerator at Forschungszentrum Jülich is well suited to test the performance of the HESR stochastic cooling hardware at different energies and variable particle numbers. All three stochastic cooling systems with first original pickup and kicker of the HESR cooling system have been installed into the COSY. The results of the last stochastic cooling beam time is presented, including the first use of GaN based amplifiers and optical hollow fiber-lines in a stochastic cooling system.

- **HESR requires cooling** for accumulation of particles and fulfillment of beam requirements for experiments
- **Stochastic cooling** consists of three 2-4 GHz systems for 3-dimensional cooling, each uses new developed sensitive pick-ups and kickers, custom made GaN power amplifiers and optical hollow fiber as long transmission lines.

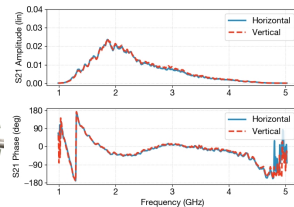


Stochastic cooling system

The new slot-ring pick-ups and kickers were specially developed for HESR, they provide high sensitivity, modular structure and simultaneous operation of all 3 degrees of freedom. First pickup and kicker of the HESR stochastic cooling system have been installed into the COSY accelerator at FZ Jülich and cooling in all degrees of freedom have been obtained. The tedious setup of the cooling systems is performed automatically with developed adjustment algorithms within ~1 min frame.

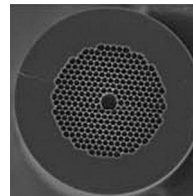


Pick-up for the stochastic cooling system of HESR inside a tank



Open-loop measurements for horizontal and vertical sum signals

Unique new hardware



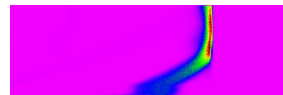
Hollow optical fibers (NTK PCF-1550) with GRIN lenses were used for all three systems as feeders to minimize system delay and dispersion



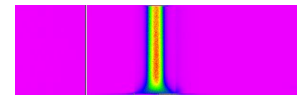
Custom made 100W power amplifiers were crafted by Nanowave Tech Inc. to optimize gain, phase and group delay for best cooling performance

Cluster target experiments

One of the main tasks for stochastic cooling at HESR is to preserve the beam during cluster-target experiments at PANDA. During 2018 first experiments with original cluster target were successfully carried out at COSY. (Target thickness is 7.4×10^{14} atoms/cm²).



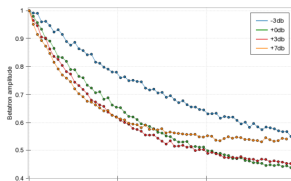
Beam with target, no cooling. Fast energy loss and emittance growth. The whole beam lost within ~5 min.



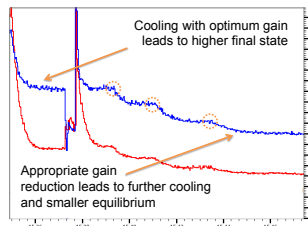
Beam with target and stochastic cooling. Fast cooling, beam losses stopped, stable equilibrium.

Cooling with variable gain

Achieving small final emittances and energy spread is always a trade-off in stochastic cooling: the faster is the cooling - the larger is the final equilibrium state. Since both cooling speed and final state depend on system gain, one solution is to properly adjust the gain (power amplification) during cooling. The result of an algorithmic step adjustment of the system gain is shown below.



Transverse stochastic cooling with different gains



Cooling with optimum gain leads to higher final state
Appropriate gain reduction leads to further cooling and smaller equilibrium



Recent Extensions of JULIC for HBS investigations



IKP at Forschungszentrum Jülich

At the Forschungszentrum Jülich (FZJ) the energy variable cyclotron JULIC is used as injector of the Cooler Synchrotron (COSY) and for irradiations of different types. Recently a new target station inside Big Karl Experimental area close to the cyclotron bunker was built. It offers space for complex detector and component setups for nuclear and neutron related experiments. It is mainly used for tests of new target materials, neutron target development and neutron yield investigations.



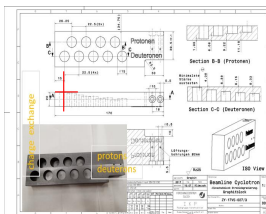
JULIC

Routinely 45 MeV H⁺ and 75 MeV D⁺

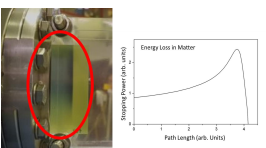
- Pole diameter 3.3 m / 700 t iron
- 20 – 30 MHz ($\eta=3$)
- 22.5 – 45 MeV/A
- $\langle B \rangle_{max} = 1.35$ T, $B_{pole} = 1.97$ T
- 2 – 4.5 keV/A injection
- 3 ion sources
 - 2 multicusp
 - pol CBS
- Pre-accelerator of COSY



Position of energy degrader and dipole magnet to obtain optimal experimental conditions in Big Karl area with reduced neutron background.

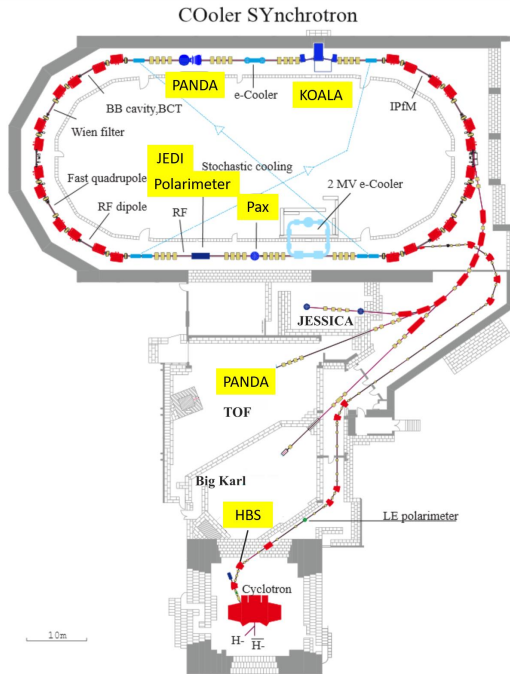


Frameless graphite energy degrader for fixed energies of 10, 20, 30 and 40 MeV for protons and deuterons.

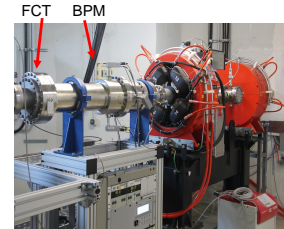


Measurement of the penetrating depth into PMMA using gafchromic® films and comparison with SRIM-calculation to validate the proton energy.

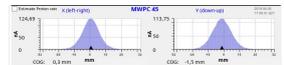
COSY facility



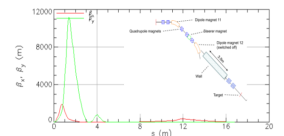
- COoler Synchrotron, 3.7 GeV/c
- Polarized protons and deuterons
- Beam cooling
 - electron cooling
 - stochastic cooling
- Development and Test of FAIR related components
 - accelerator components (BB Cavity, BCT, IPM...)
 - detectors and modules (PANDA, KOALA, CBM...)



Beamline with Quadrupoles, Beam Position Monitoring System (BPM) and Fast Current Transformer (FCT) in Big Karl area.

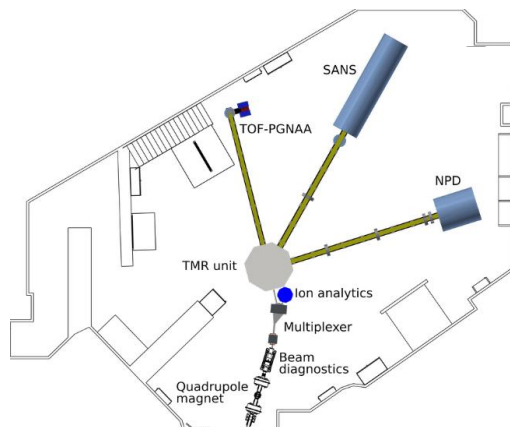


Beam profile taken with MWPC. The beam size regarding the experimental needs is ~15 mm FWHM.

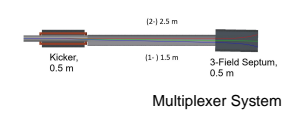


Beam Transport calculation results for optimized β -functions and beam size.

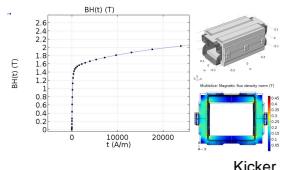
Outlook - HBS JULIC Neutron Platform



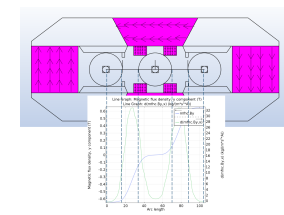
- Development, testing and operation of components of pulsed accelerator based neutron sources
 - targetry and neutron provision,
 - moderator development and optimization of the TMR unit.
- Test of Proton beam transport devices
 - beam control and dynamics,
 - beam multiplexing or beam dump systems
- Design, construction and operation of versatile neutron instruments
 - for neutron scattering purposes,
 - neutron analytics



Multiplexer System



Kicker



Septa Magnet

Multiplexer system with fast kicker deflecting the beam up to 40° into a dedicated septa magnet to separate the beam to three target stations.

Member of the Helmholtz Association

Simulations for the proposed K-Long Facility at Jefferson Lab

K. Luckas, J. Ritman and S. Schadmand

The proposed K-Long Facility in Hall D at the Thomas Jefferson National Laboratory is an extension to the GlueX spectrometer [1]. Figure 1 shows the scheme for the beamline to produce a secondary K_L^0 -beam, which hits the liquid hydrogen or deuterium target within the GlueX detector.

The K_L^0 -beam facilitates the access to strange resonances, called hyperons. This work presents a feasibility study to measure the $\Sigma(1670)^+$, a well-established resonance. A sample of 5.0×10^5 events of the channel $K_L^0 p \rightarrow \Sigma(1670)^+ \rightarrow \Lambda \pi^+ \rightarrow \pi^+ \pi^- p$ is simulated and analysed with the standard GlueX software. To simulate the $\Sigma(1670)^+$ -resonance, the beam momentum distribution is convoluted with a Breit-Wigner function with a mass parameter of $M = 1670$ MeV and a width of $\Gamma = 60$ MeV [2] in a custom generator. This generated data sample is processed through a GEANT4 simulation of the complete GlueX detector setup.

The first task in the event reconstruction is to assign particle species to the measured charged tracks, based on information from the specialised PID detectors, including the Time-of-Flight and BCAL timing, as well as dE/dx measurements, e.g. by the central drift chamber. As the distributions of these variables for the positive particles overlap, more than one particle species is allowed for each track. In this study, it was found that the reconstruction efficiencies of the individual particles are 68 % (proton), 81 % (π^+), and 25 % (π^-). Here, the significantly smaller efficiency of the negatively charged pions is caused by their low momentum, as lower momentum particles spiral in the drift chambers.

After the particle identification, different cuts are performed in order to apply an event selection. The four vector of the Λ -baryon is determined from the measured four vectors of π^- and p. A cut on the invariant mass with a total width of 14 MeV centered around the physical mass of 1115 MeV is used to select Λ -baryons. To suppress events, that are induced by a possible beam contamination, a cut on the squared missing mass of $Xp \rightarrow \Lambda \pi^+$ is introduced. The distribution of this missing mass can be described by a normal distribution, yielding a mean

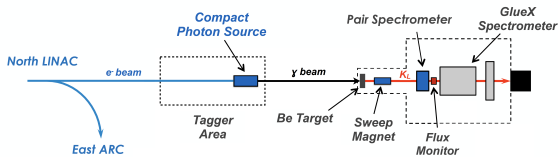


Figure 1: Beamline of the KLF experiment [3].

of $\mu = 0.25$ GeV² and a width of $\sigma = 0.016$ GeV². Based on this, events within a range of $\pm 2\sigma$ centered around the physical mass of the K_L^0 were selected for the further analysis. It was found, that the missing mass can clearly be used, to distinguish signal reactions from reactions induced by photons, or neutrons. A fit to the measured charged tracks determines the location of the interaction point. In order to reduce combinatorics and background events, it is required, that this interaction point lies within the target volume.

Finally, the overall reconstruction efficiency is approximately 6 %, where the main losses are caused by the soft pion momentum. As shown in Fig. 2, the reconstructed and generated kinetic beam energy distributions are in good agreement with each other. Accordingly, the reconstruction of the given resonance is clearly feasible with the detector setup. In conclusion, the KLF experiment will offer great opportunities in strange and multi-strange baryon spectroscopy.

A complementary study of radiative decays of hyperons within the GlueX experiment will be performed in the forthcoming year.

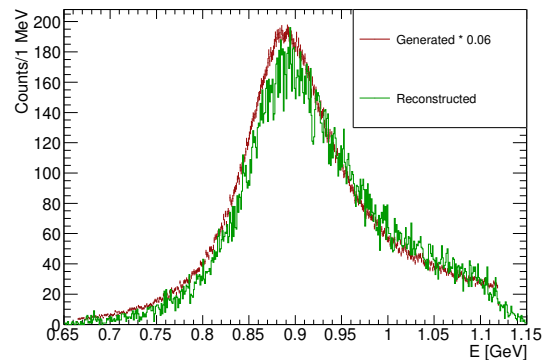


Figure 2: Comparison of reconstructed and generated kinetic beam energy. The generated (red) distribution is scaled by a factor 0.06

References

- [1] S. Adhikari et al. [GlueX Collaboration], The GlueX beam line and detector, in progress
- [2] M. Tanabashi et al. (Particle Data Group), Phys. Rev. D 98, 030001 (2018)
- [3] Strange hadron spectroscopy with secondary KL beam in Hall D, Spokespersons: M. J. Amarian, M. Bashkanov, S. Dobbs, J. Ritman, J. R. Stevens, and I. I. Strakovsky (KLF Collaboration), JLab C2-12-19-001, Newport News, VA, USA, 2019

Search for four quark exotic states with charm and strange quark content

Ashish Thampi and Elisabetta Prencipe

The $J/\psi\phi$ invariant mass system is suitable to search for $c\bar{c}s\bar{s}$ exotic states. We propose to perform such an analysis using the whole Belle data set collected at the centre of mass energy of the $\Upsilon(4S)$, corresponding to 772 million $B\bar{B}$ pairs. We prepared an analysis strategy for the reconstruction of our decay of interest.

- $B^\pm \rightarrow J/\psi\phi K^\pm$ (charged mode)
- $B^0 \rightarrow J/\psi\phi K^0$ (neutral mode)

The J/ψ is reconstructed from e^+e^- or $\mu^+\mu^-$ within the mass range of $2.95 < M_{ee} < 3.16$ GeV/c^2 and $3.06 < M_{\mu\mu} < 3.13$ GeV/c^2 . The J/ψ mass window is decided from a similar study already done in the BABAR experiment. The ϕ is reconstructed from K^+K^- . The mass window $1.0045 < M_{KK} < 1.0390$ GeV/c^2 was decided by optimizing the figure of merit, FOM .

$$FOM = \frac{N_{sig}}{\sqrt{N_{sig} + N_{bkg}}}$$

The B mesons were selected by applying the cuts on the following kinematic variables, beam constrained mass ($M_{bc} > 5.27$ GeV/c^2) and energy difference ($|\Delta E| < 0.03$ GeV). After reconstructing the B meson, the best B candidate is selected by minimizing the χ^2 value.

$$\chi^2 = \chi_v^2 + \left(\frac{M_{ll} - m_{J/\psi}}{\sigma_{J/\psi}}\right)^2 + \left(\frac{M_{KK} - m_\phi}{\sigma_\phi}\right)^2 + \left(\frac{M_{bc} - m_B}{\sigma_B}\right)^2,$$

where χ_v^2 is obtained by fitting the vertex of all charged tracks. M is the reconstructed mass, m is the nominal mass and σ is the mass resolution.

We studied the reconstruction efficiency as a function of the invariant masses ($J/\psi\phi$, $J/\psi K$, ϕK) and also for the different experiment runs in Belle. The average reconstruction efficiency is 17.6% for the charged mode and 7.9% for the neutral mode.

The analysis scheme can be validated by reproducing the branching fraction of the decay of interest through the Monte Carlo study. The branching fraction used for the Monte Carlo generation is 5.2×10^{-5} for the charged mode and 9.4×10^{-5} for the neutral mode. To measure the branching fraction we allowed the M_{bc} to vary and fit it using a Gaussian for signal events and an Argus function for background events. We calculate the branching fraction as,

$$B.F. = \frac{N_{sig}}{N_{B\bar{B}} \times eff \times b.f.}$$

where N_{sig} is the number of signal events we obtained from fitting, $N_{B\bar{B}}$ is the total number of $B\bar{B}$ pairs, eff is the reconstruction efficiency and $b.f.$ is product of the secondary branching fractions of the B decay.

In Belle the data is collected as different experiment runs, labelled from 07 to 65. We have corresponding MC data for each experiment run. For each experiment run the branching fraction is calculated and the weighted average is $(5.4 \pm 0.1) \times 10^{-5}$ for the charged mode and $(9.4 \pm 0.1) \times 10^{-5}$ for the neutral mode. This confirms that the reconstruction scheme we developed is consistent with the input values for the MC data.

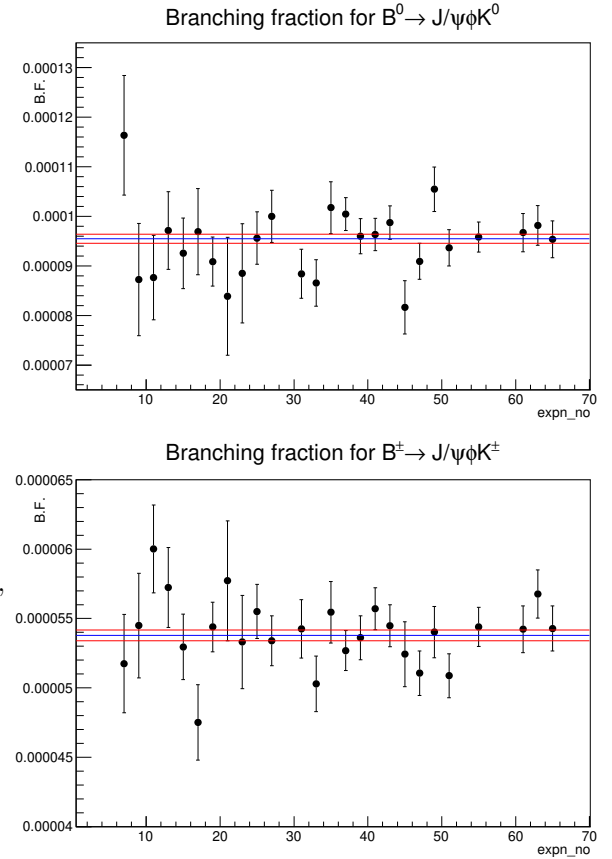


Figure 1: Branching fraction for the neutral decay $B^0 \rightarrow J/\psi\phi K^0$ (top) and the charged decay $B^\pm \rightarrow J/\psi\phi K^\pm$ (bottom) for experiments from 07 to 65

We investigated the possible background sources from B decays. We will use real data from the Belle experiment after the reconstruction scheme is approved in order to study the invariant mass distribution of the $J/\psi\phi$, $J/\psi K$ and ϕK systems for the resonant states announced by the LHCb collaboration.

Search for Exotic States with the combined BaBar and Belle Data Sets.

D. Meleshko, E. Prencipe, J. Ritman, A. Thampi and T. Tysak

The BaBar and Belle experiments collected together an integrated luminosity of 1.5 ab^{-1} . They are not collecting data any longer since a decade, but one can use the combined data sets collected at $\Upsilon(nS)$ by these two e^+e^- detectors to challenge measurements of branching ratios, cross sections, search for very rare decays which with the only BaBar or the only Belle would be not possible, for example the analysis of the $D_s^+ D_{s0}(2317)^{*-}$ invariant mass system in the continuum, *e.g.* $e^+e^- \rightarrow D_s^+ D_{s0}(2317)^{*-} X$, that also could allow improvements on the width measurement of the $D_{s0}(2317)^{*-}$.

For those analyses where soft pions are involved, *e.g.* those involving the $D_{s0}(2317)^{*-} \rightarrow D_s^- \pi^0$, where most of the photons have $p_T < 500 \text{ MeV}/c$, BaBar and Belle offer for the time being a unique opportunity to perform a precision study of the width and lineshape. According to theoretical studies, the interpretation of the $D_{s0}(2317)^{*-}$ depends on the width measurement. Up to now only an upper limit of 3.8 MeV at the 90% confidence level for the $D_{s0}(2317)^{*-}$ width has been measured, on an analysis performed by BaBar in 2003 with integrated luminosity equal to 91 fb^{-1} . With a 15 times higher statistics a great improvement is expected in this measurement. There is evidence that both BaBar and Belle reach the sub-MeV range for the resolution of the width, which is not achieved by any other running experiment.

This analysis has started with the Belle data sets. During summer 2019 two master students visited IKP1 from the University of Kyiv and participated to this project. We present in Fig. 1 the first analysis results: validation on the whole data set is performed by fitting the D_s^+ and $D_{s0}(2317)^{*-}$ mesons after a cut-based analysis which follows the BaBar guideline for the analysis of $e^+e^- \rightarrow D_s^+ \pi^0 X$. The fit result shows an improvement in the mass resolution of $D_{s0}(2317)^{*-}$, which now is estimated to be 7.3 MeV compared to the previous published value of 8.6 MeV. The improvement is obtained by using more sophisticated tracking and particle identification tools, together with higher statistics.

In case an enhancement compatible with the X(4140) and the X(4274), which were observed in the $J/\psi\phi$ invariant mass, is confirmed in the continuum, a search for hexaquark states with cs quark content could be performed. Predictions for a ccc -hexaquark state have been made from D.L. Canham, where the S-wave X(3872)D scattering cross section is evaluated in the $D^0 D^{*0} \bar{D}^0$ invariant mass system, with $X(3872) \rightarrow D^0 \bar{D}^{*0}$. Building a similarity between the X(4140) and the X(3872) states, one could interpret the X(4140) as the *strange* counterpart of the X(3872). Here the preliminary result of the reconstruction of the X(3872) in the analysis $e^+e^- \rightarrow 4D^{(*)}X$ in the continuum is reported on MC (Monte Carlo) sample, showing the $X(3872) \rightarrow D^0 \bar{D}^{*0}$. If a signal compatible with the X(3872) is observed in this channel in the

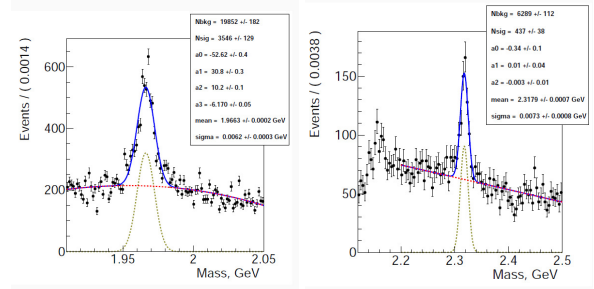


Figure 1: Preliminary plot of the invariant mass distributions on data performed at Belle for (left) the $K^+K^-\pi^-$ system in the analysis $e^+e^- \rightarrow D_s^+ D_{s0}(2317)^{*-} X$ in the continuum and (right) the $D_s^+ \pi^0$ system in the same physics channel, in which the 2 peaks corresponding to the D_s^+ and $D_{s0}(2317)^{*-}$ mesons are clearly visible.

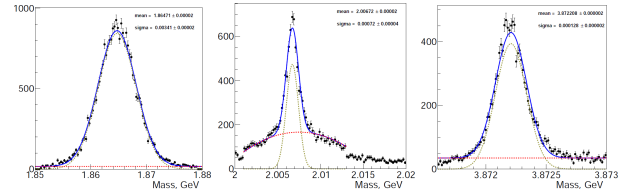


Figure 2: Preliminary plots of the invariant mass distributions on signal MC performed at Belle for (left) the $D^0 \rightarrow K^-\pi^+$ in the $e^+e^- \rightarrow D^0 \bar{D}^{*0} \bar{D}^0 X_C$ analysis in the continuum; (middle) the $D^{*0} \rightarrow D^0 \gamma$ and $D^{*0} \rightarrow D^0 \pi^0$; and (right) the $X(3872) \rightarrow D^0 \bar{D}^{*0}$ system in the same physics channel.

continuum, this would be the first observation. The goal of this analysis is to look for the X(3872), measure the cross section of the process, and look for resonant states eventually in the invariant mass system of 3 $D^{(*)}$ mesons. Preliminary results on a MC signal sample are reported in Fig. 2.

Results of the analysis $B \rightarrow J/\psi\phi K$ are shown in detail in an individual report by Ashish Thampi.

In summary, the study of the analysis of the $c\bar{c}s\bar{s}$ exotics with BaBar and Belle combined data sets started. From first feasibility studies it looks promising. We expect an improvement of a factor up to 7 times in the measurement of the $D_{s0}(2317)^{*-}$ width, and an important contribution in the study of the invariant mass distribution of $D_s^+ D_{s0}(2317)^{*-}$ and $J/\psi\phi$, which will help in understanding the nature of the exotic states already seen by LHCb through B decays, and investigate eventually new enhancements in that invariant mass systems, in different production mechanisms.

This project is supported by DFG - grant n. 1722, and JENNIFER2 under the Horizon2020 program - grant n. 822070.

D. Alfs, D. Grzonka, K. Kilian, T. Seifick and J. Ritman

P-349 Experiment

The goal of the P-349 experiment is to test whether antiprotons produced in high-energy pp collisions are polarized [1]. Polarization will be measured from the left-right asymmetry in the $\bar{p}p$ scattering in the CNI region. The assumed number of antiproton events collected during 21 days of measurement was equal to $2.2 \cdot 10^8$ and about $2 \cdot 10^5$ useful antiproton scattering events were expected. Details of the experimental method can be found in [1].

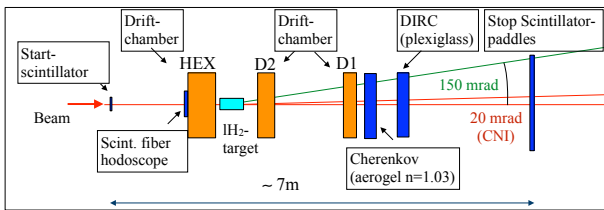


Figure 1: Experimental setup for measurements performed in 2014 and 2015.

Event selection

All events with signals in the START and STOP detectors and no signal in the Aerogel Cherenkov detector were registered and further event selection was performed offline. A considerable number of events show two particles passing through the setup (see Fig. 2). These are not analyzable due to undefined drift times in the drift chambers and not separable photon distributions in the DIRC. Therefore in the first step events with a single hit in START and STOP scintillators are selected resulting in the rejection of about 85% of the collected events.

In the next step the minimum requirement for a three dimensional track reconstruction is imposed: at least two hits in the vertical wire planes and at least one for each inclined plane. Furthermore, events with hits from more than 21 cells are rejected due to rapidly increasing number of combinations in the track finding. Application of these conditions for the D1 and D2 drift chambers results in a few percent of collected events remaining for further analysis

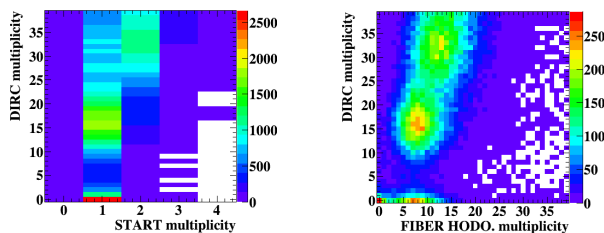


Figure 2: Correlation of multiplicities. Left: START and DIRC. Right: Scintillating fiber hodoscope and DIRC.

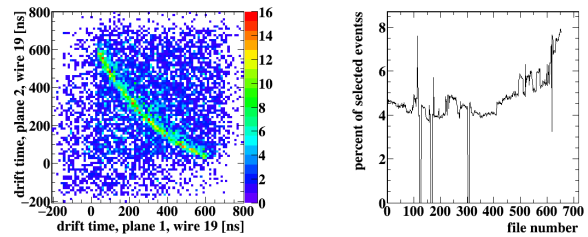


Figure 3: Left: Correlation of drift times in subsequent planes of D1 which (several uncorrelated signals). Right: Percent of events remaining after imposing cuts on START detector, STOP detectors and conditions for track reconstruction in D1 and D2 (2015 measurement).

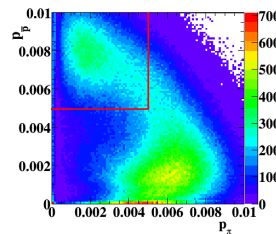


Figure 4: Results of the MC supported PID for 2015 data. Events within the red square are antiproton candidates.

(see Fig. 3, right). The efficiency of the track finding procedure for the selected events is about 65%. The last step is the selection of antiprotons in the reconstructed event sample by the distribution of Cherenkov photons in the DIRC, which exhibits a detection efficiency of above 90% in the beam area. Particle reconstruction in the Plexiglas DIRC results in $7.8 \cdot 10^5$ antiproton candidates (see Fig. 4). The details of track reconstruction, drift chamber calibration and particle identification with Plexiglas DIRC are described in [2].

Summary and outlook

The number of collected antiproton events is smaller than expected and insufficient to determine antiproton polarization. For further measurements an improved setup was prepared. The new system was operated at CERN, but due to problems with the DAQ and various detector components, only a few days of useful data could be taken which does not drastically increase the actual statistics. Another measurement with this setup is planned at CERN, and it will be preceded by detailed tests at COSY with polarized proton beam.

References

- [1] D. Grzonka, et al., Acta Phys. Polon. B 46 191 (2015), CERN-SPSC-2014/SPSC-P349 (2014).
- [2] D. Alfs, et.al., Annual Reports 2017 and 2018, IKP/COSY.

Jül-4423 • April 2020
ISSN 0944-2952

Mitglied der Helmholtz-Gemeinschaft

